Design and evaluation of immunotherapeutic imaging for cancer vaccination

Heleen Dewitte

Pharmacist

Thesis submitted to obtain the degree of
Doctor in Pharmaceutical and Medical Sciences

Proefschrift voorgedragen tot het bekomen van de graad van
Doctor in de Farmaceutische en de Medische Wetenschappen

2015

Faculteit Farmaceutische Wetenschappen

Dean:
Prof.dr.apr. Jan Van Bocxlaer

Promoter:
Prof.dr.apr. Stefaan De Smedt

Co-promoter:
Dr.apr. Ine Lentacker

Faculteit Geneeskunde en Farmacie

Dean:
Prof.dr. Alain Dupont

Promoter:
Prof.dr. Karine Breckpot

Members of the Evaluation Committee:

Chairman:

Prof.dr. **Jean-Paul Remon**	Ghent University

Secretary:

Prof.dr. **Stefaan De Smedt** (promoter)	Ghent University

Members of the Reading Committee:

Prof.dr. **Karine Breckpot** (promoter)	Vrije Universiteit Brussel
Prof.dr. **Michel Versluis**	University of Twente
Prof.dr. **Johan Grooten**	Ghent University

Members of the Examination Committee:

Dr. **Ine Lentacker** (co-promoter)	Ghent University
Prof.dr. **Bruno De Geest**	Ghent University
Prof.dr. **Daisy Vanrompay**	Ghent University
Prof.dr. **Patrick Segers**	Ghent University
Prof.dr. **Ayache Bouakaz**	Université François-Rabelais, Tours
Dr. **Clemens Bos**	UMC Utrecht

Getekend door Michiel Jaques

Ghent, February 10th 2015

The promotors:

Prof.dr.apr. Stefaan De Smedt

Prof.dr. Karine Breckpot

The author:

Apr. Heleen Dewitte

The co-promotor:

Dr.apr. Ine Lentacker

TABLE OF CONTENTS

ABBREVIATION LIST

5-FU	5-Fluorouracil
ACUC	Animal care and use committee
ALARA	As low as reasonably achievable
ANOVA	Analysis of variance
APC	Antigen presenting cell
APC	Allophycocyanin
ATP	Adenosine triphosphate
BBB	Blood brain barrier
BCA	Bicinchoninic acid
BM-DC	Bone marrow-derived dendritic cell
BSA	Bovine serum albumin
CD	Cluster of differentiation
CEUS	Contrast-enhanced ultrasound
CFSE	Carboxyfluorescein succinimidyl ester
CI	Confidence interval
CLSM	Confocal laser scanning microscopy
CPMG	Carr-Purcell-Meiboom-Gill
CPP	Cell-penetrating peptide
CPS	Cadence pulsed sequencing
CT	Computed tomography
CTL	Cytotoxic T lymphocyte
DAMP	Danger-associated molecular pattern
DC	Dendritic cell
DIC	Differential interference contrast
DLS	Dynamic light scattering
DOPC	1,2-dioleoyl-*sn*-glycero-3-phosphocholine
DOPE	1,2-dioleoyl-*sn*-glycero-3-phosphoethanolamine
DOTAP	1,2-dioleoyl-3-trimethylammonium-propane
DOX	Doxorubicin
DPPC	1,2-dipalmitoyl-*sn*-glycero-3-phosphocholine
DSPE	1,2-distearoyl-*sn*-glycero-3-phosphoethanolamine
eGFP	Enhanced green fluorescent protein
ELISA	Enzyme-linked immunosorbent assay
EMA	European medicines agency
EPR	Enhanced permeability and retention

ER	Endoplasmatic reticulum
FBS	Fetal bovine serum
FCI	FetalClone™ I
FCS	Fetal calf serum
FDA	Food and drug administration
FITC	Fluorescein isothiocyanate
Flt3L	FMS-related tyrosine kinase 3 ligand
FOV	Field-of-view
FSC	Forward scatter
GC	Glycated chitosan
GFP	Green fluorescent protein
GM-CSF	Granulocyte-macrophage colony-stimulating factor
GOT	Glutamic oxaloacetic transaminase
HIFU	High-intensity focused ultrasound
HSP	Heat shock protein
i.d.	Intradermal
IF	Impact factor
IFN	Interferon
IL	Interleukin
IP-10	Interferon gamma-induced protein 10
LDH	Lactate dehydrogenase
LoD	Limit of detection
LPS	Lipopolysaccharide
MB	Microbubble
M-CSF	Macrophage colony-stimulating factor
MFI	Mean fluorescence intensity
MHC	Major histocompatibility complex
MI	Mechanical index
MIG	Monokine induced by gamma interferon
MMP	Matrix metalloproteinase
MoDCs	Monocyte-derived dendritic cell
MP	Microparticle
MPLA	Monophosphoryl lipid A
MTT	Methyl thiazol tetrazolium
NBD	phosphatidylethanolamine-N-(7-nitro-1,3-benzoxadiol-4-yl)
NIR	Near infrared
NK	Natural killer
NMR	Nuclear magnetic resonance

NP	Nanoparticle
ODN	Oligodeoxynucleotide
OVA	Ovalbumin
PAM	Pam_3CSK_4
PAMP	Pathogen-associated molecular pattern
PBMC	Peripheral blood monocytes
PBS	Phosphate buffered saline
PE	Phycoerythrin
PEG	Polyethylene glycol
PEI	Polyethylene imine
PET	Positron emission tomography
PFC	Perfluorocarbon
PFCE	Perfluoro-15-crown-5-ether
PFH	Perfluorohexane
PLA	Poly-lactic acid
PLG	Poly(lactic-*co*-glycolic)
PLGA	Poly(lactic-*co*-glycolic) acid
PnP	Peak negative pressure
PRF	Pulse repetition frequency
PRR	Pathogen recognition receptor
REML	Restricted maximum likelihood
RES	Reticuloendothelial system
RF	Radiofrequency
RLU	Relative light unit
ROI	Region of interest
s.c.	Subcutaneous
SD	Standard deviation
siRNA	Short interfering RNA
SLN	Sentinel lymph node
SONAR	Sound navigation and ranging
SPECT	Single-photon emission computed tomography
SPF	Specific pathogen free
SPIO	Superparamagnetic iron oxide
TAA	Tumor-associated antigen
TAM	Tumor-associated macrophage
TCEP	Tris(2-carboxyethyl)phosphine hydrochloride
TCR	T cell receptor
TE	Echo time

TEM	Transmission electron microscopy
TGF-β	Transforming growth factor β
Th	Helper T lymphocytes
TI	Thermal index
TIPS	Therapy and imaging probe system
TLR	Toll-like receptor
TNF	Tumor necrosis factor
tPA	Tissue plasminogen activator
TR	Repetition time
T_{reg}	Regulatory T cell
TriO	Trimix + ovalbumin mRNA
US	Ultrasound

Aim and outline of this thesis

Despite ongoing efforts to find new drugs and tools in the battle against cancer, it remains one of the leading causes of morbidity and death worldwide. A more recent treatment approach, cancer immunotherapy, harnesses the patient's own immune system to fight the tumor. Ever since, cancer immunotherapy is booming and various novel therapeutic moieties emerge based on the adoptive transfer of *ex vivo* modified immune cells, or on the delivery of recombinant proteins for the induction or blockage of specific pathways involved in immunity. This field is moving fast, new targets are virtually being discovered daily, various immunotherapeutics have made their way into clinical trials and even some of them have been granted approval for clinical use in patients. As a result, immunotherapy was named "*Breakthrough of the year 2013*" by Science Magazine.

One of these immunotherapeutic strategies is the use of dendritic cell-based vaccines. Here, the key initiators of immune responses, the dendritic cells, are modified *ex vivo* so that they start presenting tumor antigens and evoke specific antitumor immunity. Although promising results are accumulating, these cellular vaccines face a number of problems which are mainly associated with their cumbersome and patient-specific production. In addition, when these modified cells are injected as a vaccine, they often experience difficulties to reach their anatomical target sites *in vivo*.

To address these issues, the aim of this thesis is to design biomaterial solutions to overcome these problems associated with current cancer vaccines. More specifically, we will develop theranostic strategies that allow the induction of anticancer immunity by targeting dendritic cells, while simultaneously providing real-time feedback *via* non-invasive diagnostic imaging techniques.

Chapter 1 provides a general introduction to the two main topics that are addressed in this thesis. Firstly, an overview of current cancer immunotherapy is given, including a summary of how dendritic cells can evoke antitumor immune responses. Moreover, the rational design of biomaterials that can be used for this purpose will be discussed. Secondly, the concept of therapeutic imaging will be introduced. The two key diagnostic imaging techniques employed in this thesis, magnetic resonance imaging and ultrasonography, will be highlighted. The application of contrast agents for both imaging methods is addressed, as well as how these diagnostic agents can be used for therapeutic imaging.

Importantly, when novel cancer vaccination strategies are investigated, the initial experiments are usually performed on *in vitro* cultured cells. However, it is crucial to realize that the use of *in vitro* model dendritic cells is associated with a number of limitations. The effects of small variations in cell culture circumstances on the way these cells behave *in vitro* will therefore be discussed in **Chapter 2**.

Taking these pitfalls into account, we will evaluate two different kinds of therapeutic imaging methods for immunotherapy. In **Chapter 3**, the use of liquid perfluorocarbon droplets as imageable antigen-delivery systems is explored. This way, we aim to produce traceable dendritic cell vaccines which could allow non-invasive tracking of the migration and faith of the injected antigen-laden dendritic cells *in vivo* using fluorine MRI.

This strategy, however, still requires the *ex vivo* modification of dendritic cells, and therefore does not solve all the issues associated with cellular vaccines. For that reason, a second therapeutic imaging strategy will be implemented for immunotherapy: the use of microbubbles for ultrasound-guided, ultrasound-triggered delivery of antigens and immune adjuvants to dendritic cells *in vivo*. Therefore, in **Chapter 4**, we will develop mRNA-loaded microbubbles for the ultrasound-mediated delivery of antigen-coding mRNA, and evaluate their potential in dendritic cell cultures *in vitro*. In **Chapter 5**, these microbubbles will be further modified to carry antigen mRNA as well as adjuvant mRNA for the simultaneous transfection and immunomodulation of dendritic cells. Furthermore, we will evaluate whether cells that were modified in this way, can indeed trigger antitumor immunity *in vivo*. Finally, **Chapter 6** will provide a first step towards the immediate *in vivo* application of this transfection strategy. For this, we aim to investigate if these theranostic mRNA-loaded microbubbles can reach the lymph nodes upon subcutaneous injection, and whether their migration can be visualized *via* contrast-enhanced ultrasonography.

Chapter 1

A general introduction to cancer immunotherapy and therapeutic imaging

Parts of this chapter were accepted for publication as:

Heleen Dewitte[1], Rein Verbeke[1], Karine Breckpot[2], Stefaan C. De Smedt[1], Ine Lentacker[1], Nanoparticle design to induce tumor immunity and oppose the immunosuppressive tumor microenvironment. *Nano Today*, ***In press*** (2015).

[1]Laboratory for General Biochemistry and Physical Pharmacy, Department of Pharmaceutical Sciences, Ghent University, Ottergemsesteenweg 460, 9000 Ghent, Belgium

[2]Laboratory of Molecular and Cellular Therapy, Department of Biomedical Sciences, Medical School of the Vrije Universiteit Brussel (VUB), Laarbeeklaan 103, 1090 Jette, Belgium

ABSTRACT

Over the years, research in the field of cancer immunotherapy has flourished, bringing about crucial breakthroughs, but at the same time revealing the drawbacks of current *ex vivo* approaches that put a break on the successes obtained with cellular vaccines. This chapter focuses on how immunotherapy can be induced by targeting dendritic cells, and how nano- and micromaterials can be designed for this purpose.

In addition, an overview of therapeutic imaging is provided, highlighting the strengths of imageable and image-guided drug delivery using MRI and ultrasound. The basic principles of both imaging techniques are addressed and the evolution in the design of contrast agents and relevant therapeutic imaging moieties is described.

PART 1: CANCER IMMUNOTHERAPY

CANCER IMMUNOTHERAPY ON THE RISE

Cancer is still one of the leading causes of death in the Western world, and besides the enormous impact is has on the patients (both physically, mentally and financially), it is also a major challenge for society. For example, for 2008, the American Cancer Society calculated the total economic impact of premature death and disability from cancer worldwide was $895 billion, not including direct medical costs (www.cancer.org)[1]. In addition, current treatments such as surgery, radiotherapy and chemotherapy have their limits. Especially the occurrence of metastatic disease has a detrimental impact on the patient's prognosis. As a result, novel treatment strategies are being investigated and explored. One of these new approaches is cancer immunotherapy, where the patient's immune system is enlisted in the battle against the tumor. It holds a number of important advantages over current therapies, including its selectivity, the fact that it is a systemic approach that can tackle both the primary tumor as well as metastatic lesions and the build-up of an immunological memory which could offer long-term protection against relapse.

The initial idea of exploiting the immune system to combat cancer, originated in the early 1800s, when Dr. Wiliam Coley achieved (limited) antitumor effects by injecting microbe-derived toxins[2]. Since then, the field of cancer immunotherapy has evolved drastically, mainly due to a number of crucial breakthroughs in our understanding of the complex function of the immune system, a number of which are listed in **Figure 1**.

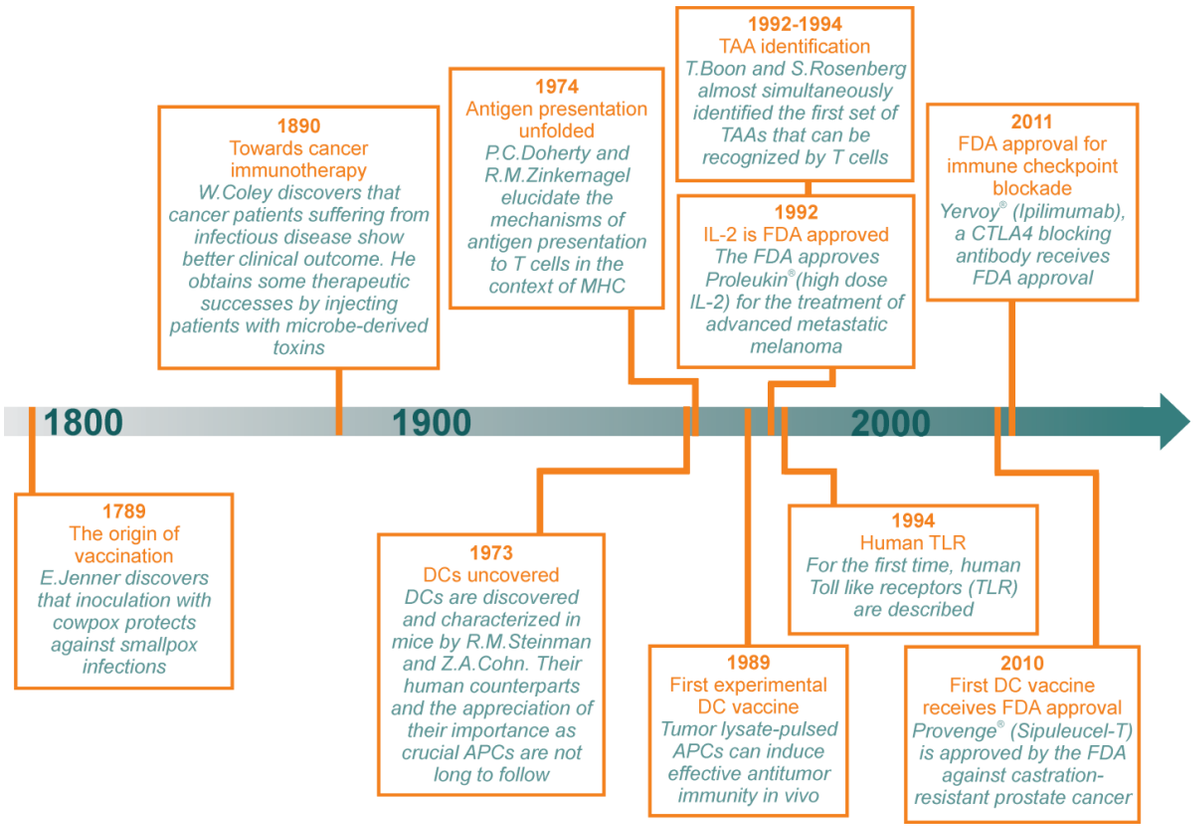

Figure 1. Timeline overview of important discoveries and milestones that have shaped cancer immunotherapy today[3-7].

An essential step forward was the identification of dendritic cells (DCs) as the initiators of immunity. These cells form a bridge between innate and adaptive immunity by capturing antigens and efficiently presenting them to T cells in specialized molecules called major histocompatibility complexes (MHCs). Depending on the intracellular location of the antigenic protein, presentation will occur either in MHC-I, for cytoplasmic proteins, or in MHC-II for exogenous antigens, which have been endo- or phagocytosed by the cell. Once the antigen-MHC complexes are translocated to the DC surface, the presented antigen can be recognized by $CD8^+$ or $CD4^+$ T cells in case of MHC-I or MHC-II presentation, respectively. Importantly, these antigen-presenting cells (APCs) are unmatched in their capacity to activate naïve antigen-specific T cells: DCs are the only cell type that can provide the necessary co-stimulatory signals (e.g. ligation of CD86 or CD80 on the DC surface to CD28 on the T cell membrane), chemokines (e.g. IP-10 and MIG) and cytokines (e.g. type I IFN and IL-12) required for T cell stimulation. This way, DCs can initiate proliferation and differentiation of antigen-specific $CD8^+$ T cells into cytotoxic T lymphocytes (CTLs), and $CD4^+$ T cells into helper T cells (Th)[4]. An overview of the ways DCs present antigens and induce T cell responses is presented in **Figure 2**.

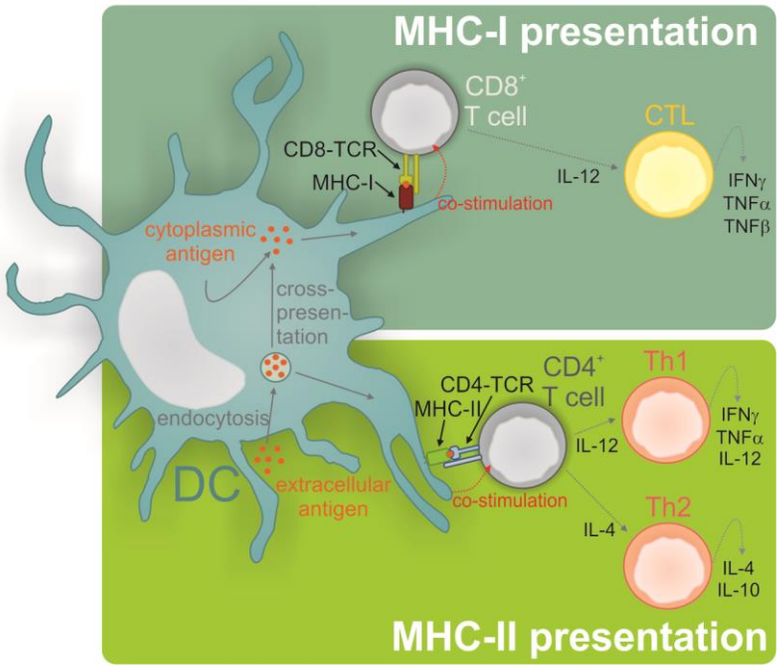

Figure 2. Antigen presentation and T cell activation by DCs.

Cytoplasmic antigens (e.g. proteins produced within the cell's cytoplasm) are cleaved into peptides which can be presented in MHC-I complexes at the DC surface. There, they can be recognized by antigen-specific $CD8^+$ T cells. When these cells receive co-stimulation from the DCs, they will become activated and differentiate into CTLs. Engulfed extracellular antigens on the other hand, are presented in MHC-II. The antigens can then be recognized by the T cell receptors (TCRs) of $CD4^+$ T cells. Upon activation, these differentiate into Th1 or Th2 cells, depending on the local cytokine environment. Through cross-presentation, a process that exclusively occurs in potent APCs, extracellular antigens can be diverted towards MHC-I presentation.

In the meanwhile, researchers were looking into the Achilles' heel of tumor cells. For long, the existence of tumor-associated antigens (TAAs), which are selectively or preferentially expressed by tumor cells, was presumed but not proven. As early as 1905, Clowes and Baeslack reported that immunity occurred in mice that spontaneously recovered from their tumor burden[8]. This was further evidenced by Gross' experiments in 1943, who proved that somehow the immune system of mice was capable of recognizing and rejecting implanted tumors[9]. However, it was only in the early 1990s that the first sets of human TAAs against which CTL responses could be mounted, were actually identified[10, 11].

Taken together, the weak spots of tumor cells and the strengths of our immune system were exposed. By combining these novel insights, the road to the development of new therapeutic strategies that exploit the patient's immune system to selectively recognize and destroy tumor cells was paved.

DENDRITIC CELL-BASED IMMUNOTHERAPY

The identification of DCs as the initiators of immunity made them interesting targets in cancer immunotherapy. Not so long after their discovery, the first report on DC-based vaccination was published[12]. In DC-based vaccination, DCs are modified to present TAAs to T cells, resulting in TAA-specific CTL activation. The production of such cellular vaccines requires loading of the DCs with TAAs, after which the cells need to be matured, in order to become potent APCs.

With regards to the antigen-loading of DCs, various strategies have already been explored. The earliest studies made use of tumor lysates as a source of antigen. Later on, based on the identification and sequencing of TAAs, recombinant antigens or antigen-derived peptides were produced and passively pulsed into DCs. More recently, researchers have moved on to the use of viral vectors for the delivery of DNA or RNA encoding TAAs[13, 14]. Due to safety issues associated with the use of these pathogen-based delivery systems, the use of non-viral carriers for the delivery of DNA and RNA is currently under investigation.

After antigen-loading, the DCs are exposed to maturation stimuli. These can be pathogen or danger-associated molecular patterns (PAMPs and DAMPs respectively), that can bind to the DCs' pathogen recognition receptors (PRRs) and initiate an intracellular cascade resulting in the production of pro-inflammatory cytokines, increased antigen-presentation and augmented expression of co-stimulatory molecules (e.g. CD40, CD80, CD86) and chemokine receptors (e.g. CCR7). The mature antigen-presenting DCs can then be injected as therapeutic cancer vaccines. The initial results were promising, and in 2010, years of research in this field were rewarded by the food and drug administration (FDA) approval of the first DC-based vaccine: Provenge® (Sipuleucel-T, marketed by Dendreon)[15]. **Figure 3** is a schematic representation of how these DC-based vaccines are generally produced.

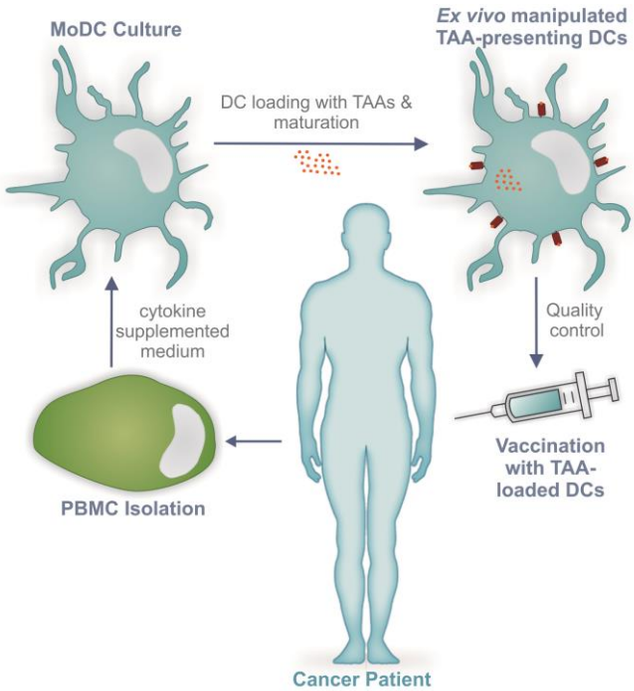

Figure 3. Production of *ex vivo* generated DC-based cancer vaccines.
Peripheral blood monocytes **(**PBMCs) are collected from a cancer patient *via* leukapheresis. By culturing these cells with cytokines, they can be differentiated into monocyte-derived DCs (MoDCs). These can subsequently be loaded with TAAs and maturation stimuli after which the mature antigen-presenting DCs can be reinfused as a therapeutic vaccine.

Although DC vaccine research is flourishing, a number of important drawbacks hinder the applicability of current DC-based vaccines. First of all, and this might even be the most limiting factor, all the modification steps described above (*i.e.* antigen-loading and maturation), are performed on isolated cells *in vitro*. This way, the production of these vaccines is labor-intensive. In addition, working with isolated cells makes these therapeutics patient-specific. For every other patient, cell isolation, antigen-loading and maturation needs to be repeated, which adds to the production costs of the vaccines. To give an illustration, the costs for a full round of Provenge® treatment are currently set at $93,000 (~ €70,000), not including hospital and physician fees. Thirdly, it was shown that upon subcutaneous injection of the cellular vaccine, DC survival and migration towards the lymph nodes, where T cell activation occurs, is poor. Merely 5% of the transferred cells are capable of reaching the lymphatics, requiring the use of large numbers of antigen-modified cells in order to establish therapeutic effects[16]. As a result, only cells that can be isolated in sufficient numbers can be employed. For primary plasmacytoid or “conventional” DCs, this is a challenge, therefore researchers have chosen for a long time to use monocyte-derived DCs (MoDCs). These cells are obtained by isolating a patient’s peripheral blood monocytes (PBMCs) and culturing them with cytokines (GM-CSF with or without IL-4) to stimulate their differentiation into MoDCs. These cells, however, do not show

the same phenotypic properties as most of the lymphoid-resident DCs, but rather correspond to "*emergency DCs*" which are usually only detected at sites of inflammation[17]. This, together with loss of activation of the cells once injected, and insufficient cytokine production by the *in vitro* modulated cells, has sparked interest to find ways of loading antigens into various circulating DCs subsets *in vivo*[18, 19].

ADVANTAGES OF PARTICULATE SYSTEMS FOR DC VACCINATION IN VIVO

The search for *in vivo* antigen-delivery techniques promptly resulted in the production of nanoparticles (NPs) and microparticles (MPs) to carry antigenic material towards DCs in the skin or the lymphatics, since the use of particle structures offers many important benefits over the delivery of free antigen. Before describing the advantages of particulate vaccines, it should be noted that a number of prerequisites will determine whether these particulate cancer vaccines are indeed able to induce potent immune responses *in vivo*.

A first important point is that many novel antigen-delivery systems are still entirely evaluated *in vitro* on murine or human DCs that were generated from bone marrow or blood precursor cells, respectively. Indeed, a thorough characterization of the materials with respect to their capacity to encapsulate antigen and/or adjuvant, their stability, uptake by DCs and antigen-transfer to these cells is routinely performed *in vitro*. However, purely *in vitro* testing comes with a number of pitfalls. First of all, it should be noted that *in vitro* generated DCs need to be considered as models for a complex *in vivo* situation where numerous types of DCs exist[20-22]. In addition, for murine bone marrow-derived DCs, it was reported that slight variations in cell culture protocol resulted in large variation in the phenotype of the generated cells, as well as in their capacity to respond to particulate antigen[23]. Moreover, *in vitro* experiments evaluating the particle's characteristics and uptake by DCs are often exclusively performed in serum-free media, making it even more difficult to draw conclusions on their *in vivo* behavior. Therefore, *in vitro* validation of new carriers should comprise proof of the compatibility of the carrier with biological fluids with respect to particle aggregation, size and antigen release kinetics. For example, cationic particles are often used for electrostatic binding of antigenic protein or nucleic acids encoding antigens. Without additional surface modifications, such as grafting polyethylene glycol (PEG) chains on the outer particle surface to provide the particle with a hydrophilic shield that reduces the particles' surface charge, these structures tend to quickly aggregate upon contact with serum proteins. This can result in premature antigen release and a change in particle size, which leads to different cellular uptake and antigen transfer kinetics[24, 25].

Secondly, the aim of antigen-loaded particles is to deliver the antigenic material to APCs so they can induce potent antitumor immune responses. Importantly, evidence emerged indicating that potent immune responses can only be mounted when antigens are presented to T cells by mature DCs. In fact, where mature DCs stimulate antitumor immunity, antigen-presentation by their immature counterparts will rather lead to tolerance and suppression of effector antigen-specific T cells[26, 27]. The process of DC maturation is complex, finally resulting in a complete shift of the cell's function towards antigen presentation. Thus, fully mature DCs are characterized by (a) combined up-regulation of numerous co-stimulatory molecules (e.g. CD40, CD80, CD86), (b) cytokine production (e.g. IL-12p70 and IL-6) and (c) increased migratory capacities for their translocation to the T cell areas of the lymph nodes. Only when all of these processes occur simultaneously, are DCs considered as fully mature and are they expected to be able to mount potent antitumor immune responses. Thus, an *in vivo* applicable particulate system for DC vaccination should not only deliver antigen, but also exhibit immune adjuvant effects and induce complete maturation of the antigen-loaded DCs. Whether NPs and MPs as such possess intrinsic adjuvant activity is a recurring topic of discussion. Thorough comparisons of the various reports are difficult to make due to the plethora of confounding factors (e.g. particle size, surface charge, production methods, additional surface modifications) that prevent unbiased conclusion-drawing. Hence, the opinions on carrier-related auto-adjuvancy remain divided: cationic liposomes might induce surface charge density-related DC activation[28-30], others show exactly the opposite, pointing towards enhanced adjuvancy of neutral or anionic liposomes [31]. Similar debates arose for Poly(lactic-*co*-glycolic) acid (PLGA) capsules, another commonly investigated antigen-carrier. Whereas Sharp et al. pointed out that PLGA could induce significant cytokine production[32], many other researchers could not observe any PLGA-induced DC maturation or cytokine secretion[33]. For most particles, however, it is clear that stimulation of DC maturation by including adjuvants will result in the production of more effective particulate vaccines. Of note, it was demonstrated that it is crucial to deliver antigen and adjuvant to the same intracellular compartment to obtain both $CD4^+$ and $CD8^+$ T cell activation[34]. Schlosser and colleagues investigated the effect of delivering antigenic protein and adjuvant (CpG oligodeoxynucleotides (ODNs), a toll-like receptor 9 (TLR9) agonist or Poly(I:C), a known TLR3 agonist) packaged in separate PLGA microspheres, or co-formulated within the same microsphere. As expected, co-encapsulation of antigen with a TLR agonist significantly improved antigen (cross-)presentation and induction of potent CTL responses *in vivo*[35]. Similar results demonstrating the need for physical association of antigen, carrier and adjuvant were obtained for liposomal NPs by Zaks et al.[36]. Therefore, particles should be co-formulated with both antigen and PRR agonists (often TLR agonists). In this way, a three-component system is produced, containing (a) a target antigen, which will steer the immune responses towards the cancer cells, (b) an immune potentiator to enhance the antigen-specific

immune responses, and (c) a suitable particulate carrier to deliver antigen and adjuvant to the DCs at the site of interest.

Thirdly, choosing a potent adjuvant is crucial, and this could also become a pitfall in particle design. Firstly, it is important to consider that not all TLRs are expressed by all DC subsets. Therefore, rational design and adjuvant selection based on the subset of DCs that will be targeted by the particulate vaccine *in vivo* are key. Moreover, the cellular location of the TLR which is targeted by the adjuvant-particle composite can also play a role. This is exemplified by the work of Bal and colleagues, who evaluated liposomal formulations containing either Pam_3CSK_4 (a TLR2-1 agonist) or CpG ODNs (a TLR9 agonist). They observed that the delivery of adjuvants to endosomal TLRs, such as TLR3, 7, 8 and 9 benefit more from the liposomal delivery than adjuvants to TLRs that are located on the cell surface. As a result, liposomal encapsulation of CpG ODNs resulted in prominently better results over liposomal Pam_3CSK_4[37]. Furthermore, there are differences in TLR expression on mouse and human DC subsets. For instance, TLR9, receptor to the popular adjuvant CpG ODNs, is absent on most human DC subtypes[38]. Careful and critical interpretation of immunological effects observed in mouse models is therefore warranted. An overview of the TLRs, their cellular location and commonly used agonists is given in **Figure 4**.

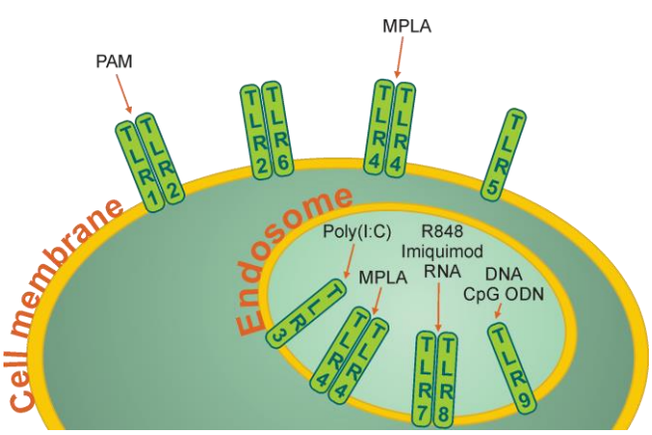

Figure 4. Cell membrane and endosomal TLRs can ligate to a variety of agonists.
By using these agonists as immune adjuvants, DC maturation can be induced and antigen-presentation and stimulation of antigen-specific T cells becomes possible.
(Abbreviations: PAM = Pam_3CSK_4; MPLA = monophosphoryl lipid A)

Taking the pitfalls of *in vitro-in vivo* translation and the requirement for simultaneous antigen and adjuvant delivery into account, the following sections will describe the advantages of different biomaterials for vaccination purposes, and the different strategies that are used to enhance the particulate's immunogenicity. An overview of different carrier-antigen-adjuvant combinations that have been designed and evaluated, is listed in **Table 1**.

Table 1: Particulate carriers for simultaneous antigen and adjuvant delivery to DCs *in vivo*.

Passive DC targeting and the loophole of cross-presentation.

Carrier	Particle-related advantages	Antigenic cargo	Combined immune adjuvants
PLGA	Antigen release rate can be modified by tweaking the ratio of glycolic acid to lactic acid	Protein	CpG ODNs[35, 39, 40] Poly(I:C)[35, 39] Poly(I:C) combined with resiquimod (R848)[41] R848[40]
		Tumor lysate	CpG ODNs[42]
		Peptide	MPLA[43] CpG ODNs[44]
		pDNA	GpG + IL-10 siRNA[45] Poly(I:C) + IL-10 siRNA[45]
Liposomes	Easy modification and production Possible auto-adjuvancy (depending on the liposome's physicochemical properties)[29, 37, 46]	Protein	MPLA[47] non-coding DNA[36] CpG ODNs[36, 37, 48, 49] Poly(I:C)[36, 49, 50] TDB (C-type lectin ligand)[49] PAM3CSK4 (PAM)[37] Cationic lipid (3,5-didodecycloxybenzamidine, TRX)[30]
		Peptide	Non-coding DNA[36] CpG ODNs[36, 51] Poly(I:C)[36]
Cubosomes	Increased encapsulation compared to liposomes	Protein	MPLA + imiquimod[52]
Gold NPs	NP size is easy to control Tracking *via* computed tomography (CT) imaging	Protein	CpG ODNs[53, 54]
Bacterial magnetic particles	Enhanced gene delivery by magnet application Auto-adjuvant effects	pDNA	Auto-adjuvant[55]
Polymeric micelles	High protein loading capacity Auto-adjuvant effects	Protein	Auto-adjuvant[56] Poly(I:C)[56]

A first advantage of formulating antigens in particles, is that by packaging the antigenic material in larger constructs, antigens are passively targeted towards phagocytic APCs and can be considered for cross-presentation. In general, exogenous antigenic material that is taken up by DCs *via* phagocytosis or endocytosis will end up in the MHC-II presentation pathway, leading to the activation of Th cells. Cytoplasmic proteins, on the other hand, can be presented in MHC-I and result the induction of CTLs. Cross-presentation acts as a loophole in these pathways, allowing exogenous antigens to be redirected towards MHC-I (as previously depicted in **Figure 2**). How exactly phagocytosed or endocytosed antigens find their way into MHC-I presentation remains vague, although increasing evidence demonstrates the involvement of phagosomes, early endosomes and autophagosomes[57-59]. By formulating antigens into NPs and MPs, these cross-presentation-competent organelles can be targeted, resulting in activation of both CTLs (*via* MHC-I) and long-lasting memory T cells (*via* MHC-II)[60]. The role of particulate delivery systems in governing antigen-presentation can be illustrated by the research of Stano et al. They elegantly showed that the use of solid-core NPs where antigen is attached to the particle surface, preferentially leads to $CD4^+$ T cell activation, whereas administration of NPs that encapsulate the antigen within their watery core primarily results in $CD8^+$ responses. As a result, the authors propose co-administration of both antigen-loaded particles since these result in superior immune responses with both $CD4^+$ and $CD8^+$ properties[61]. Additional modifications can be made to nanoparticulate vaccines to promote cross-presentation. An example is the inclusion of pH-sensitive polymers into liposomes. After endocytic uptake, the reduced endosomal pH will activate the fusogenic potential of these polymers, causing disruption of the endosomal membrane and cytoplasmatic delivery of the antigenic material. In this way, antigen presentation *via* the MHC-I pathway is stimulated, and enhanced CTL induction could be achieved[30, 62]. Of course, this specifically applies for protein antigen delivery. When antigen-encoding DNA or RNA are delivered, this problem completely turns upside down, as the cytolpasmatic protein production upon nucleic acid delivery will favor the MHC-I presentation pathway. Here, strategies that target the produced antigens to the MHC-II pathway (e.g. *via* attachment of lysosome-targeting sequences) in order to call for T cell help can be applied[63].

Protection of antigen integrity and tuning antigen-release kinetics.

Secondly, encapsulating antigens in particles protects them from premature degradation and enables modulation of the antigen delivery kinetics. Antigens that are packaged within NPs or MPs are shielded from digestive enzymes (proteases and nucleases) that are ubiquitous in blood and interstitial fluid. This is especially important for the delivery of nucleic acids (*i.e.* DNA or RNA encoding tumor antigens) to DCs, which are much more prone to premature degradation. The kinetics of antigen presentation were also shown to exert a major effect on the strength, duration and memory of the induced immune responses. For example, Johansen

and colleagues showed that dose-escalating antigen contact resulted in much stronger $CD8^+$ T cell responses compared to single-shot antigen delivery[64]. Therefore, particles that result in a burst release of the antigenic material upon engulfment by DCs, will induce less pronounced immune responses compared to sustained release particles. This was evidenced by Demento et al., who compared immune response induction by liposomal (fast release) versus slow release PLGA-based protein delivery. Indeed, mice vaccinated with liposomes exhibited lower and shorter-lived antibody titers and a lower frequency of memory T cells compared to PLGA-vaccinated mice. Similar observations were made when slow and fast-release PLGA particles were compared[65]. Thus, tweaking the release kinetics of the encapsulated antigen can augment antitumor immunity. As a result, clever modifications to basic polymer and liposome structures to ensure longer antigen-retention and controllable antigen release have been reported. For example, Moon et al. created covalent crosslinks between different bilayers of multilamellar liposomes in order to slow down the release of antigen[47]. Another considerable option to achieve longer-term antigen presentation by DCs, is to use nucleic acid-based vaccines instead of protein or peptide vaccines. In addition to favoring MHC-I antigen presentation, as discussed in the previous section, genetic vaccines can prolong the duration of antigen presentation and subsequently the activation of CTLs. This was demonstrated in a comparative study of Liao et al. where a sustained period of antigen presentation was measured after RNA transfection, whereas peptide pulsed DCs rapidly lost their ability to present the antigen[66]. Interestingly, the delivery of mRNA has been shown to generate more rapid and longer lasting antigen presentation compared to DNA, making mRNA an interesting source of antigen[67].

Multifaceted antigen-delivery vehicles.

In addition, particle design is not limited to the mere creation of an antigen-delivery structure. NPs and MPs can be equipped with tracer molecules, or can be constructed from materials that allow *in vivo* imaging of injected antigen-loaded particles. Imaging and tracking the migration of these multifaceted particles from the injection site to the draining lymph nodes can provide initial feedback on the vaccine efficacy. For instance, Lee et al. described the production of gold NPs that could be covalently loaded with a model protein antigen and CpG ODNs. Upon injection of the resulting 23 nm particles in the rear footpads of mice, their migration to the popliteal and inguinal nodes could be followed using computed tomography (CT)[53]. To date, however, not many research groups have reported on such multimodal particulate vaccines yet. The reason for this, is that up to now, traceable particles have been mainly designed to determine the fate and migratory capacities of *ex vivo* modified antigen-loaded DCs. The focus on *in vivo* DC targeting is a more recent development in cancer immunotherapy, which gives us reason to believe that reports on new multifaceted particles aiming for *in vivo* modification and migration trafficking are expected to follow.

Alternative biomaterial-based strategies.

Another possibility is to target DCs towards the antigens, rather than vice versa. For this, Ali and coworkers designed a poly-lactide-*co*-glycolic (PLG) matrix that releases GM-CSF in order to recruit DCs into the scaffold *in vivo*. Importantly, the authors showed that the number of DCs that could be attracted in this way, resembles the amount of *ex vivo* modified DCs that are routinely injected as a cellular vaccine. Upon DC infiltration into the scaffold, the cells can come in contact with entrapped tumor lysate as a source of antigen, and CpG ODNs as immune stimulants. By fine-tuning the GM-CSF release kinetics from the polymer matrix, the antigen-loaded mature DCs can be released from the scaffold and migrate to the lymph nodes to allow T cell induction[68, 69]. This discovery has led to the design of alternative immune priming centers that aim to attract and *in vivo* modulate DCs[70].

PART 2: THERAPEUTIC IMAGING

INTRODUCTION

Therapeutic imaging agents, also called "*theranostics*" integrate an imageable and a therapeutic moiety into a single agent[71, 72]. This can be interpreted quite broadly. First of all, theranostics could be drug or gene delivery systems that can be followed *in vivo via* one or another medical imaging technique. This way, the biodistribution of the drug can be visualized, providing feedback on whether or not the therapeutic reaches its target site after administration. Such theranostics are especially useful during the development of novel biomaterials, where the effect of different modification strategies (e.g. PEGylation, attachment of targeting ligands) can be rapidly evaluated *in vivo*. Secondly, there is the possibility to produce controlled release theranostics, where the release of the drug or gene from the particulate carrier can be followed *in vivo*. For example, ThermoDox® (developed by Celsion), a thermosensitive liposomal formulation that contains doxorubicin (DOX, a chemotherapeutic) has also been formulated to contain a gadolinium-based magnetic resonance imaging (MRI) contrast agent. After intravenous injection of these theranostic liposomes, heat was applied locally at the tumor site to trigger DOX release. As in addition to the DOX, the MRI contrast agents are also let out of the liposomes, the drug release kinetics could be monitored non-invasively using MRI[73]. A third option is to develop a theranostic that provides visual information on the stage of the disease (e.g. characterization of a tumor mass) and treats it at the same time. Lastly, and related to the previous possibility, theranostics could allow treatment and at the same time visual follow-up of the treatment effects. In other words, the imaging moiety could allow real-time feedback on the effects of the co-delivered therapeutic.

Medical imaging techniques

Thus, in addition to delivering therapeutics, theranostic compounds act as contrast agents which can be detected *via* a non-invasive biomedical imaging technique. An overview of different diagnostic imaging techniques and their most common contrast agents is provided in **Table 2**[74]. Although each technique has its advantages and disadvantages, it is important to note that computed tomography (CT), positron emission tomography (PET) and single-photon emission computed tomography (SPECT) require the use of ionizing radiation. In contrast, MRI and ultrasonography make use of electromagnetism and high-frequency acoustic waves,

respectively. Hence, these two imaging techniques are associated with improved patient and operator safety and they do not produce radioactive waste.

Table 2. Overview of the clinically used diagnostic imaging techniques.

Imaging Technique	Principle	Costs	Spatial resolution	Temporal resolution	Contrast agents
Computed Tomography (CT)	Ionizing radiation (X-rays)	Moderate	+	+/-	Iodine, Barium
Positron Emission Tomography (PET)	Ionizing radiation (γ-rays)	High	-	+/-	Radioactive tracers (e.g. ^{18}F, ^{11}C, ^{13}N, ^{15}O, ^{68}Ga)
Single-Photon Emission Computed Tomography (SPECT)	Ionizing radiation (γ-rays)	High	-	-	Radioactive tracers (^{99m}Tc, ^{131}I, ^{123}I, ^{111}In)
Magnetic Resonance Imaging (MRI)	Electro-magnetism	High	+	-	Paramagnetic metal chelates (e.g. gadolinium complexes or tetraazacycloalkanes) or superparamagnetic nanoparticles (iron oxide, ^{1}H), perfluoro-carbons (^{19}F)
Ultra-sonography	Acoustic waves	Low	+/-	+	Microbubbles

As this thesis focuses on the use of non-ionizing diagnostic imaging techniques, the following sections will elaborate on the principles behind MRI and ultrasonography, and which theranostics can be designed for these imaging methods.

THERAPEUTIC IMAGING WITH MRI

The principles behind MRI

The first principle that lies at the basis of MRI is the concept of nuclear magnetism. In 1925, Uhlenbeck and Goudsmit hypothesized that as protons and neutrons rotate over their axis, they have an intrinsic angular momentum or "spin"[75]. Since pairs of spins tend to cancel out, only atoms that consist of an odd number of protons and neutrons will have a net spin (e.g. $^{1}H_{1}$, $^{19}F_{6}$, $^{31}P_{15}$). Since protons have an electrical charge, their continuous rotation will create a current loop and thus, a magnetic moment (μ). Thus, when spinning nuclei are influenced by an external magnetic field, they will act like little magnets. As an example, for the ^{1}H nucleus, which only consists of 1 proton, the application of an external external magnetic field (B) will cause the spinning protons to attempt to align either parallel (spin up) or antiparallel (spin down) to the applied magnetic field, as shown in **Figure 5A**. Just like the *Zeeman effect* in atomic energy levels, both states have different energy levels, with the parallel state being a low energy level, and the antiparallel state a high energy level.

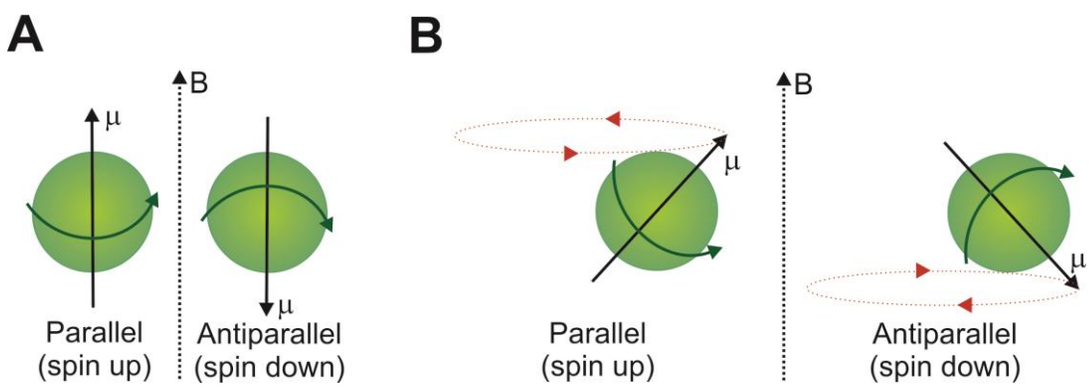

Figure 5. The orientation of spinning nuclei in an external magnetic field.
(A) Spinning nuclei will attempt to align their magnetic moments, μ, parallel or antiparallel to an externally applied magnetic field, B. (B) In fact, the magnetic moment rather precesses around the magnetic field in a certain angle.

However, this alignment is not complete, causing the nuclei to precess about the axis of the applied magnetic field under a certain angle, as shown in **Figure 5B**. The frequency at which this precession occurs, is called the Larmor frequency. Importantly, the Larmor frequency depends on both the magnitude of the external magnetic field, as well as on the type of nucleus. However, as these nuclei can be part of different molecules, they can be present in environments with different electron densities. This will influence their resonance frequency, resulting in a chemical shift (expressed in ppm). An example is provided in **Figure 6**.

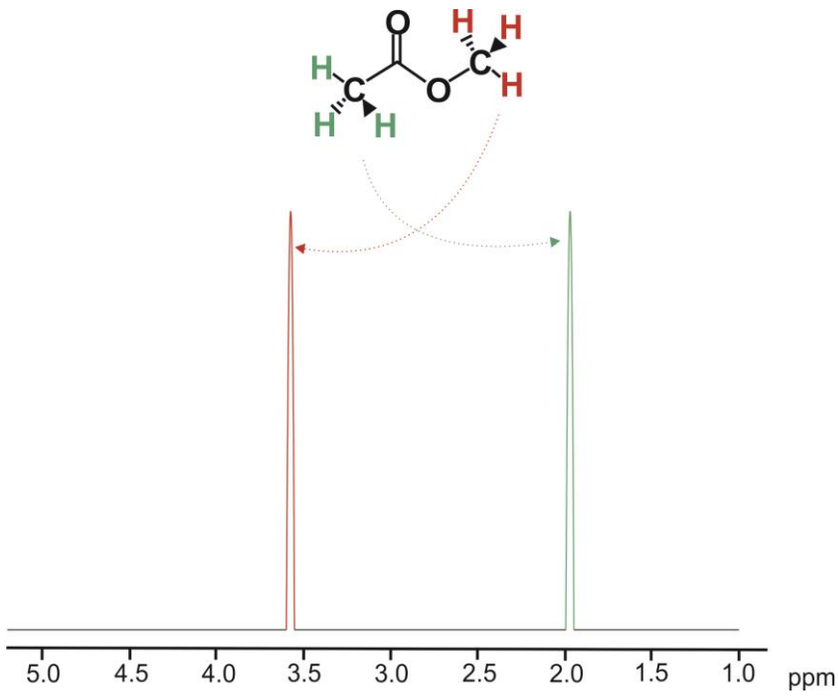

Figure 6. ^{1}H nuclear magnetic resonance (NMR) spectrum for methyl acetate. Methyl acetate contains 6 ^{1}H atoms. As these are present in 2 different chemical environments (indicated in either green or orange), this results in two separate peaks at different chemical shifts in the ^{1}H NMR spectrum. As the number of ^{1}H atoms in each environment is the same (3), both peaks have the same area under the curve.

When applying a radiofrequency (RF) pulse at this Larmor frequency, the spinning nuclei will absorb the added energy, causing them to flip from the low parallel to the high antiparallel energy state. After switching off the RF emission, the excited atoms will relax back to the more energetically favorable parallel state, thereby emitting a RF signal that can be detected by a receiver coil. This relaxation occurs gradually. Depending on the chemical environment in which the excited nuclei are present, they will require a certain amount of time before they release the absorbed energy and return to their ground state. Thus, the T_1 relaxation time is the time needed for 63% of the excited atoms to return to the parallel state. Depending on the chemical environment in which the protons are spinning, this can either be longer or shorter. In addition, the RF pulses will cause the atoms to no longer spin randomly, but in phase. The time needed for the atoms to return to the random spin state and cause a 63% decrease of the signal, is the T_2 relaxation time. When protons are very close together, they will cause them to experience a slightly higher or lower magnetic field, and hence a slightly different T_2 relaxation time.

In order to transform these RF signals into an interpretable image, ^{1}H MRI makes use of a magnetic field gradient instead of a static magnetic field. An example of the magnetic field density generated by different MRI coils is given in **Figure 7**. As the magnetic field will be different at different locations, this can be used to generate differences in the resonance frequency and phase, which can then be used to encode for the location of a particular and hereby pinpoint the origin of the emitted RF signal. Most of the ^{1}H atoms in the human body are present in H_2O and lipid molecules. Hence, ^{1}H MRI basically images the distribution of water and fat molecules at different anatomical locations.

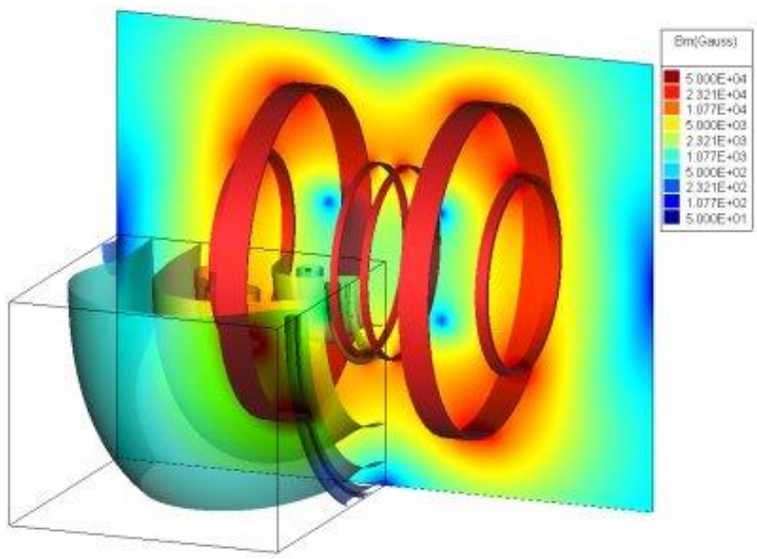

Figure 7. Magnetic field density around MRI coils.
Image reproduced from http://www.integratedsoft.com/Applications/Magnetic-Applications/MRI

Images can either be T_1 or T_2 weighted, which means that differences in either one (or both) of these relaxation times are used to provide the contrast. Interestingly, for a lot of malignancies, different T_1 relaxation times were reported for healthy tissue compared to tumor tissue. For example, breast tumors have a T_1 of 367 ± 79 ms whereas the corresponding healthy tissue has a T_1 of 1080 ± 8 ms[76]. This way, T_1 weighted MRI is generally used to provide anatomical information, and is a powerful tool in the diagnosis of malignancies. Similarly, T_2 relaxation times also differ between tissues, allowing T_2 weighted imaging. This usually requires longer scanning times compared to T_1 weighted imaging, but enables functional imaging. Importantly, different contrast agents need to be selected when using T_1 or T_2 weighted MRI.

^{1}H MRI contrast agents

In ^{1}H MRI, contrast agents can be used to either enhance the natural contrast between two adjacent tissues, or to provide additional dynamic information. There are two main principles on which contrast enhancement could be based. Firstly, contrast agents could change the spin density, *i.e.* the proton density. However, this cannot be modified in ^{1}H MRI. Alternatively, agents can change the T_1 and T_2 relaxation times. Most contrast agents influence both relaxation times but may have a predominant effect on one of them. This way, ^{1}H MRI contrast agents are subdivided into T_1 and T_2 weighted agents.

T_1 weighted contrast agents most frequently are paramagnetic substances, such as Gd^{3+} chelates. These contain a large number of unpaired electrons (7 for Gd^{3+}), which will extensively influence the chemical environment of neighboring ^{1}H atoms. Hence, their T_1 relaxation time is reduced. As a result, the shortened relaxation time will allow rapid return to the thermal equilibrium in rapid excitation-relaxation sequences, thereby enhancing the total intensity of the signal (positive contrast agents)[77]. This type of contrast agents is often used in MRI angiography[78] as illustrated in **Figure 8**, or for the detection of the break-down of natural barriers like the blood brain barrier around brain tumors. .

Figure 8. Gd^{3+} enhanced MR angiography of the head.

MRI protocols that make use of differences in T_2 relaxation time are based on the detection of the signal decay. Thus, contrast agents that speed up this signal decay will locally reduce the overall signal intensity, as such creating dark spots on the MR images (negative contrast agents). Examples are superparamagnetic materials, such as superparamagnetic iron oxide particles (SPIO)[79]. Their superparamagnetic properties will locally disturb the created magnetic field, which provokes the signal dephasing of neighboring protons and as such accelerates the signal decay.

Both T_1 and T_2 weighted contrast agents have been used for the development of theranostics. For example, self-assembled NPs consisting of a SPIO core and a PEI-containing shell have been produced to deliver minicircle DNA, whilst allowing MRI imaging of gene delivery[80]. Similarly, various particulates have been developed and evaluated based on SPIO or Gd^{3+} for MRI-imageable delivery of various drugs or nucleic acid therapeutics[81-83].

^{19}F MRI

As described in the previous sections, ^{1}H MRI, where the distribution of water in the different tissues is imaged, is a commonly used technique in diagnostic medicine, as it provides detailed information on tissue anatomy, pathology and functionality. However, when it comes to specificity when performing contrast-enhanced MRI, there is always the issue of improving the contrast-to-tissue ratio. As the human body is filled with ^{1}H atoms, the differences that need to be created by the contrast agents are substantial, which often compels clinicians to use high doses of these contrast agents. To respond to this, Holland and colleagues shifted their focus towards detecting ^{19}F instead of ^{1}H in 1969[84]. In comparison to ^{1}H, the resonance frequency, sensitivity and signal-to-noise ratio of ^{19}F are merely slightly lower. However, as almost all the fluorine in the human body is immobilized in bone and teeth structures, which makes it invisible to MRI detection methods. Thus, ^{19}F MRI allows selective imaging of fluorine-containing contrast agents at a negligible tissue background[85].

Following the development of ^{19}F MRI, 5-fluorouracil (5-FU), a widely used cytostatic drug was suddenly upgraded from a therapeutic to a theranostic compound[86]. However, as this molecule only comprises 1 single fluorine atom, high tissue concentrations were needed to detect this agent at a sufficient signal-to-noise ratio. Thus, to obtain acceptable image quality, obtaining high local concentrations of ^{19}F nuclei will be crucial. To achieve this, perfluorocarbons (PFCs) proved to be ideal contrast agents. They are metabolically inert, offer a high density of ^{19}F nuclei per molecule and have well-defined safety profiles[87-91]. Some PFCs have gained FDA approval as artificial oxygen carriers due to their ability to dissolve high amounts of various gases (Fluosol®, marketed by Green cross corporation but taken off the market after problems with the storage of the emulsion formulation) or as an aid during eye surgery (Vitreon®, marketed by Vitrophage). Due to their very low surface tension, liquid PFCs usually remain cohesive, and are therefore difficult to formulate as stable emulsions. In order to overcome this hurdle, different lipid and polymer coats have been designed to stabilize the PFC droplets in an aqueous environment[92-94].

This has resulted in the marketing of Cell Sense (CS-1000 by Celsense Inc.), a PFC formulation designed for cell labeling. This way, it has been used by researchers who are developing cellular vaccines (including DC vaccines) and stem cell therapeutics, in order to track the fate of the transplanted cells with high specificity *in vivo*[92]. Especially for DC-based

vaccines, being able to track whether or not the cellular vaccines migrate from the injection site to the draining lymph nodes could provide crucial information that could help predict the therapeutic outcome. An example of DC vaccine tracking using ^{19}F MRI is shown in **Figure 9**. Thus, PFCs have made it as ^{19}F MRI contrast agents, but to date, their use as theranostics has not yet been intensely investigated.

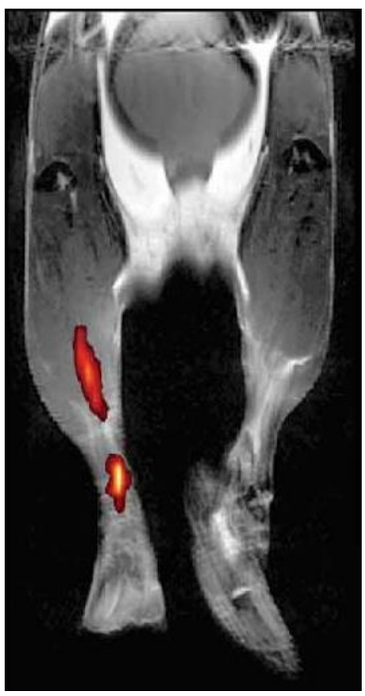

Figure 9. ^{19}F MRI tracking of the migration of PFC-loaded DCs in a mouse model. After subcutaneous injection of the PFC-loaded DCs in tip of the hind foot pad, the migration of a fraction of these cells to the popliteal lymph node could be observed. Image reproduced from Ahrens et al.[92]

THERAPEUTIC IMAGING WITH ULTRASONOGRAPHY

Another imaging technique that does not require the use of ionizing radiation and has the advantages of providing good spatial and temporal resolution at a low cost, is ultrasonography. More importantly, recent advances in the development of microbubbles as ultrasound contrast agents have initiated the research into microbubble theranostics for ultrasonography. The following sections will highlight the principles that lie at the basis of medical imaging and drug delivery using ultrasound and microbubbles. First of all, an overview of how ultrasound came to be an established value for diagnostic and therapeutic applications in the clinic, will be provided. With the rise of microbubbles as FDA-approved ultrasound contrast agents, the last sections will elucidate the principles behind microbubble and ultrasound-triggered drug delivery and recent progress in microbubble design for this purpose will be reviewed.

The history of ultrasound

As is the case for many inventions, the applications for which ultrasound has been used evolved over the years, influenced by the spirit of age. The following sections will briefly discuss the course of events that has led to the courant use of ultrasound for non-clinical and (pre)clinical applications.

(1) Piezoelectricity and echolocation

Ultrasound research was set in motion by the brothers Pierre and Jacques Curie, who discovered piezoelectricity as early as 1880. The phenomenon of piezoelectricity occurs in certain crystals (e.g. quartz and Rochelle salt), which are electrically polarized under mechanical stress[95]. When also the converse effect for these materials was deduced, the possibility to transform mechanical pressure into electricity and vice versa opened new avenues. Similar to the way that striking a tuning fork will lead to a vibration that is propagated through air and can be heard as sound, applying electrical energy to a piezoelectric element can cause it to rapidly vibrate. These vibrations have a certain frequency (in Hz) and result in the creation of a pressure wave, as shown in **Figure 10A**. Depending on the frequency of the vibrations, the waves are classified as sound (20 Hz-20 kHz, *i.e.* within the range of human hearing), infrasound (<20 Hz) or ultrasound (>20 kHz). When such sound waves propagate, the high and low pressure areas they create will displace particles in the medium. Thus, the medium is compressed when the pressure is high, and rarefraction occurs when the pressure is low (**Figure 10B**).

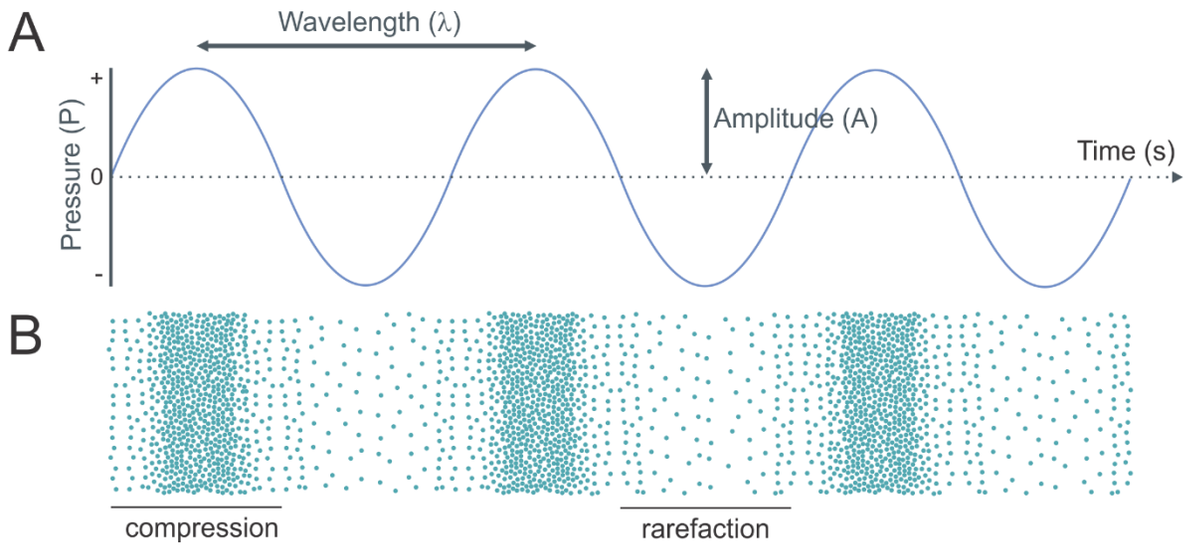

Figure 10. Features of ultrasound waves.

By applying electrical energy to a piezoelectric crystal, vibrations are induced that propagate through the medium as pressure waves with a specific wavelength and amplitude (A). This results in the alternating compression and rarefaction of the medium through which the acoustic wave propagates (B).

This principle saw its first use after the Titanic tragedy in 1912, when researchers proposed that by using sound and listening to echoes, distant icebergs could be detected[96]. The physical principles behind echo detection are explained in **Box 1**. Almost immediately, the first patents describing iceberg echolocation were filed. However, it took two years before the first SONAR (SOund Navigation And Ranging) system was actually assembled. Reginald Fessenden emitted low-frequency sound (~540 Hz) and used a separate receiver to detect underwater icebergs at about 3 km distance. The use of ultrasound for echolocation and the development of transducers capable of both emitting as well as receiving ultrasound waves, was made possible by Paul Langevin, a former student of Pierre Curie. He aligned multiple quartz crystals, allowing the generation and detection of ultrasound at a higher frequency of 40 kHz. Thus, the first ultrasound transducer was a fact.

In the run-up to the First World War, the application of ultrasound-based echolocation-technology changed: it became a powerful military tool to detect enemy submarines. This way, the first German U-boat sunk after SONAR detection using Langevin's hydrophone in 1916. Further perfection of the transducer design allowed the generation of higher sound frequencies which significantly increased the distances at which submarines could be located (to up to 1300 m). Despite a lot of patent disputes, Paul Langevin is still considered to be one of the founders of ultrasonics[97].

Box 1. The physics behind iceberg echolocation explained.

When a sound wave travels through a medium, the density of the medium (ρ) and the speed of sound in that medium (c) will determine the acoustic impedance of that medium (Z).

$$Z = \rho \times c$$

When the wave travels through medium 1 (with an impedance of Z_1) and then hits medium 2 with a different acoustic impedance (Z_2), a part of the ultrasound wave is reflected as an echo. The amplitude of the reflected echo is determined by the acoustic impedance mismatch between the two media as shown in the following formula:

$$R = \frac{Z_2 - Z_1}{Z_2 + Z_1}$$

With respect to the iceberg localization (see figure below): the amplitude reflection coefficient of an ultrasound wave that travels through water (Z_{water} = 1.48 MRayl) before it encounters an iceberg (Z_{ice} = 3.5 MRayl), is 41%, as calculated below:

$$R = \frac{3.5MRayl - 1.48MRayl}{3.5MRayl + 1.48MRayl} = 0.41$$

Depending on the distance between the ship that sent out the echo and the iceberg, the time it takes for the echo to return to the ship will be longer or shorter, for more or less distant icebergs, respectively.

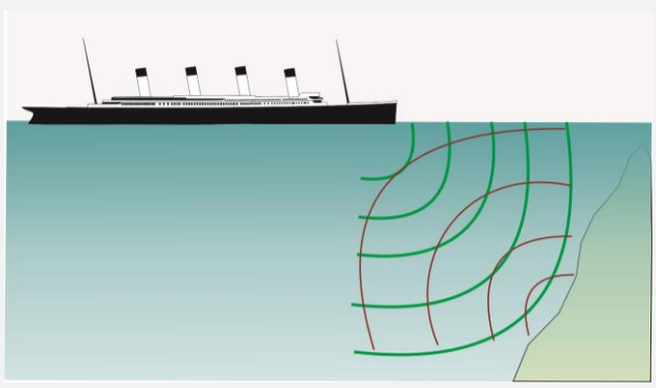

(2) The dawn of ultrasound in diagnostic medicine

At the cradle of medical ultrasound applications was Karl Theodore Dussik in 1946. He developed what he called “hyperphonography”, a transmission-based imaging technique. He applied ultrasound waves at one side of the head of a patient, which was partially submerged in water (**Figure 11A**), and recorded the intensities of the waves at the other side of the head. When the waves passed through the tissue, depending on the acoustic impedance and the speed of sound in the tissues (as listed in **Table 3**), differences in attenuation (*i.e.* loss of

amplitude due to scattering or absorption of the transmitted wave) were created. This way, Dussik could produce 2D black-and-white images as exemplified in **Figure 11B**. Unfortunately, what Dussik thought were the cerebral ventricles and irregularities that he ascribed to the presence of brain tumors, he had not taken the attenuation of ultrasound by the skull into account. Nevertheless, Dussik's research did inaugurate the application of ultrasound in diagnostic medicine[98].

Table 3. Density and acoustical properties of different tissues and materials.

Tissue or material	Density (g cm^{-3})	Speed of Sound (m s^{-1})	Acoustic impedance (MRayls)
Water	1	1480	1.48
Blood	1.055	1575	1.66
Fat	0.95	1450	1.38
Liver	1.06	1590	1.69
Kidney	1.05	1570	1.65
Heart	1.045	1570	1.64
Bone	1.9	4080	7.75
Air	0.0001	335	0.0004

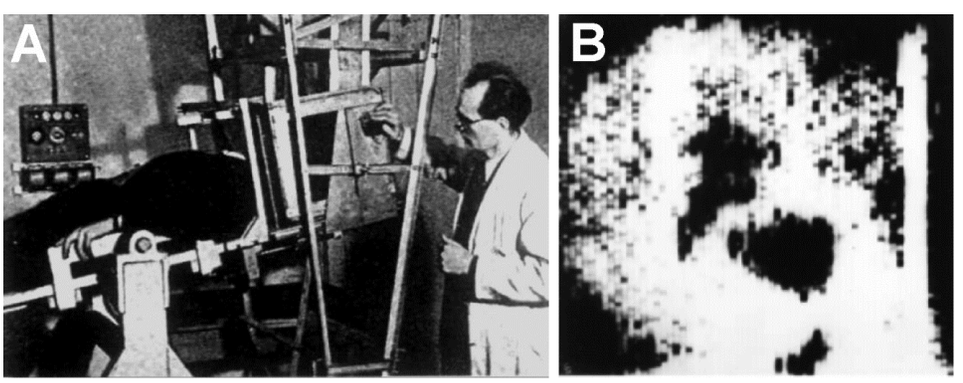

Figure 11. Ultrasound imaging by Karl Theodore Dussik.
(A) The ultrasound apparatus developed by Karl Theodore Dussik to detect brain tumors. (B) Pathological hyperphonogram of the brain recorded by Dussik. Black areas were thought to be enlarged ventricles, exhibiting a low degree of attenuation. (Figure 11B was adapted from Edler and Lindström[99])

This concept was later picked up by Douglass Howry and Joseph Holmes who replaced the transmission detection by the detection of ultrasound echoes. Similar to the echolocation used in SONAR, pulsed ~2.5 MHz ultrasound waves will be reflected at the interface of tissues with a difference in acoustic impedance. Resulting echoes were then detected by the same transducer and converted into black-and-white images. They even further improved the applicability of ultrasound imaging by designing moving transducers that eliminated "false"

echoes and by developing more compact transducers for direct-patient contact, no longer making it necessary to submerge the patients in water[100, 101].

Since then, we have come a long way: black-and-white turned into grayscale imaging, 2D into 3D and even 4D, and the variety in tissues that could be imaged at improved resolution increased rapidly. Advances in image analysis, transducer design and the development of small transportable devices and the merging of different technologies, made ultrasound imaging – in all its forms – one of the standard diagnostic instruments in medicine today.

(3) The microbubble era

In 1968, Gramiak and Shah made a remarkable observation. When imaging the aortic root, they observed a "cloud of echoes" during the injection of saline[102]. These echoes were later ascribed to the presence of small air bubbles in the saline solution. The large difference in acoustic impedance between air (Z_{air} = 0.0001 MRayl) and blood (Z_{blood} = 1.66 MRayl) will indeed cause the generation of echoes by each of these small bubbles (at an amplitude reflection coefficient of nearly 100%). The potential of using such microbubbles as ultrasound contrast agents was almost immediately recognized. Especially for echocardiography, there was an unmet need for ways to get better contrast between blood and the heart muscle (which both have almost identical acoustic impedances: Z_{blood} = 1.66 MRayl; Z_{heart} = 1.64 MRayl, resulting in an amplitude reflection coefficient of merely 0.6%). If one would be able to safely inject microbubbles in the bloodstream, thus increasing the echogenicity of blood in comparison to heart, contrast-enhanced echocardiography could provide clinicians with a highly potent diagnostic tool to non-invasively detect cardiac irregularities. Thus, the use of these small air bubbles as ultrasound contrast agents was initiated[103].

The first contrast agents that were used in this way, were solutions like agitated saline or glucose, which provided extremely short-lived contrast enhancement. To prolong the lifespan of the air bubbles, the dissolution of the gas into the blood needed to be reduced. This was done by equipping the gas bubbles with a thin stabilizing shell, which most frequently consisted of proteins such as albumin (e.g. Albunex®)[104, 105]. Additional improvements were made by replacing the air by hydrophobic gasses, as these are less soluble in blood and will thus generate longer-circulating microbubbles. These second generation microbubble agents were based on sulphur hexafluoride or PFC gas cores, stabilized by lipid (soft-shelled agents) or polymer (hard-shelled agents) shells[106-108]. Moreover, shielding microbubble uptake by phagocytic cells, which is commonly done by including a polyethylene glycol (PEG) corona, resulted in even longer contrast agent circulation times[109]. The overall size of microbubble contrast agents ranges from 0.5 to 10 µm, as this allows sufficient echogenicity (which improves with increasing microbubble size) as well as safety. Below the maximum size of 10 µm microbubbles will be small enough to pass through the microvasculature without causing

embolisms. In addition, the use of inert gasses for the microbubble core and biodegradable, biocompatible shell materials makes microbubbles safe for intravenous applications. A short overview of the composition of some commercially available microbubbles that are approved for clinical use, can be found in **Table 4**.

Table 4. Commercially available microbubbles approved for diagnostic use.

Contrast agent	Manufacturer	Gas core	Shell composition
Definity®	Bristol-Myers Squibb	Perfluorobutane	Phospholipids, PEG5000
Optison®	GE Healthcare	Perfluoropropane	Human serum albumin
Sonazoid®	GE Healthcare	Perfluorobutane	Egg phosphatidylserine
SonoVue® (Lumason™ in the USA)	Bracco	Sulfur Hexafluoride	Phospholipids, PEG4000

Interestingly, besides their echogenicity, microbubbles also exhibit other features that make them particularly appealing for medicinal purposes. Most prominently, the microbubble gas cores will respond to the ultrasound pressure waves by linearly oscillating in response to the high and low pressure peaks of the passing ultrasound waves. As shown in **Figure 12**, in this linear behavior, the amplitude of compression and rarefaction are equal. The way these microbubbles behave, depends on a number of ultrasound- and microbubble-related parameters: ultrasound power (related to the acoustic pressure) and frequency, and microbubble type (gas core and shell elasticity) and size. If the frequency of the transmitted ultrasound wave matches the eigenfrequency of the microbubble, the amplitude of the oscillations reaches a maximum. When this is the case, the microbubbles oscillate nonlinearly, resulting in relatively larger microbubble expansion compared to compression, which heavily impacts the echoes they generate upon ultrasound exposure[110].

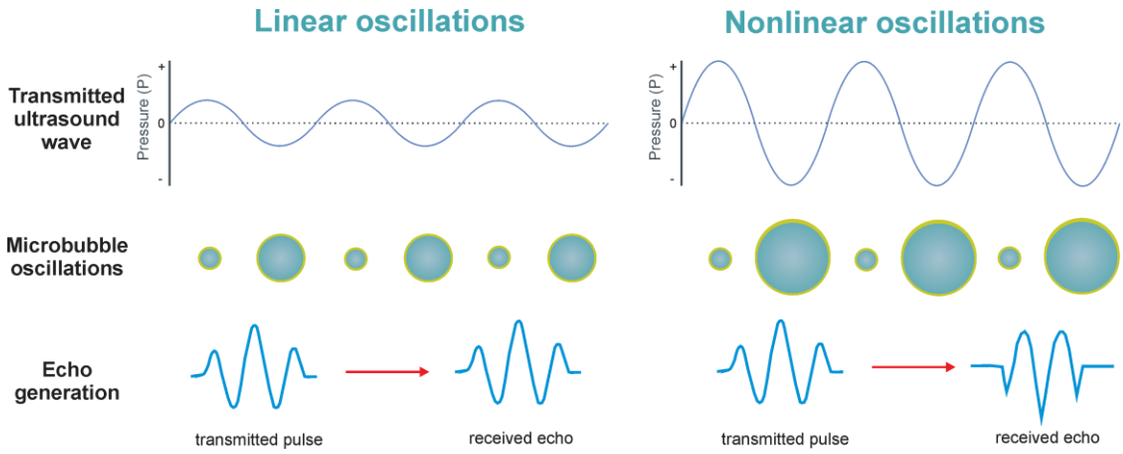

Figure 12. Linear and non-linear microbubble behavior.

Ultrasound-exposed microbubbles will oscillate. Depending on the frequency and the acoustical pressure, the microbubbles can exhibit linear (left panel) and nonlinear (right panel) behavior, resulting in the generation of different echoes.

More specifically, nonlinear movements will result in the generation of second-order harmonic echoes[111, 112]. This means that when an ultrasound pulse is emitted at a certain frequency (f_0), the reflected microbubble echo will not only be at this fundamental frequency, but also at a second harmonic frequency (*i.e.* twice the fundamental frequency, $2f_0$) as depicted in **Figure 13**. Thus, microbubble echoes will be mainly nonlinear, whereas biological tissues rather behave linearly. As a result, selectively looking at nonlinear echo signals allows specific detection of microbubbles while cancelling out tissue-derived echoes. Thus, strategies such as pulse-inversion or amplitude-modulation allow selective harmonic contrast imaging, thereby significantly augmenting the contrast-to-tissue ratio of ultrasound images[111].

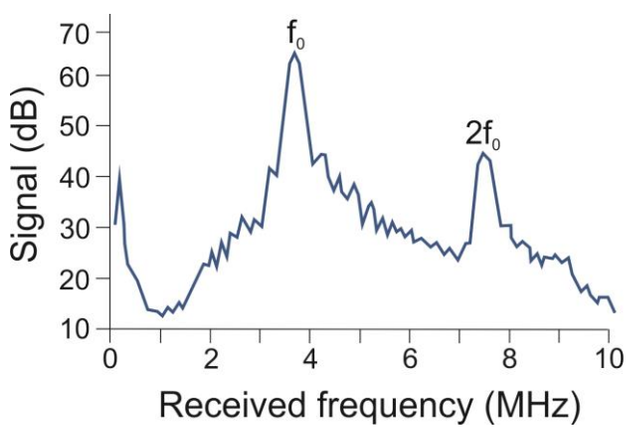

Figure 13. Microbubble harmonic signal generation.

Microbubbles that oscillate in response to a 4 MHz ultrasound wave will produce echoes at various frequencies, including an intense echo at the fundamental frequency (f_0) and second harmonic frequencies ($2f_0$). Image adapted from Lindner et al.[110]

Taken together, contrast-enhanced ultrasound imaging (CEUS) became an established diagnostic moiety in echocardiography. Even though the number of applications approved by the FDA is still limited, research indicates that it could be particularly useful for imaging liver disease as well as for the characterization of tumors. An overview of courant clinically applied ultrasound imaging techniques is provided in **Table 4**.

Table 4. Clinically used ultrasound imaging techniques.

Technique	Principle	Example
B-mode imaging	Echoes from different tissue interfaces are collected and brought together as a 2D image. Each pixel represents one echo, where the brightness of the pixel is directly proportional to the echo intensity.	
Doppler imaging	Echoes derived from moving structures (often blood) are detected at different frequencies than the frequency of the transmitted wave, depending on the direction (towards or away from the transducer) and speed of movement. This information is converted into color images showing movement towards the transducer in red, and movement away from the transducer in blue. Intensity mapping is used to point out the flow velocity. Microbubbles can be used to enhance the signal.	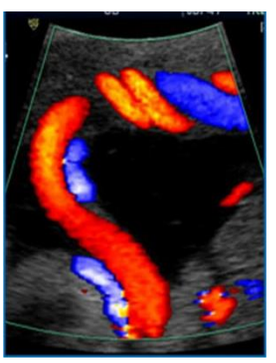
Contrast-enhanced ultrasound imaging (CEUS)	Microbubbles enhance blood echogenicity to improve contrast between e.g. heart muscle and blood. Tissue signal cancellation can be done to allow harmonic imaging and improve the contrast-to-tissue ratio.	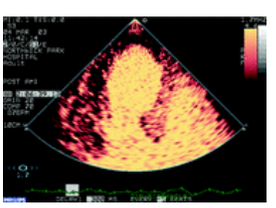

Currently, microbubble contrast agents are moving beyond their exclusive use as vascular contrast agents. Recent studies revealed that when these contrast agents are injected subcutaneously or intradermally, they migrate away from the injection site *via* the lymphatics[113, 114]. More importantly, when microbubbles were injected around the tumor, they could be tracked all the way to the sentinel lymph node. This is the first lymph node that drains material coming from the tumor tissue, and hence this is the first location at risk to harbor metastasis[115-121]. As a result, staging the sentinel lymph node to determine whether or not it contains disseminated cancer cells is a routinely performed procedure in oncology[122]. Using CEUS to determine which node is the sentinel node could be an improvement over the currently used methods, as these are either not patient-friendly (e.g. the injection of a blue dye) or require the use of radioactive tracers.

Assessing and utilizing ultrasound-mediated bio-effects

It is important to keep in mind that ultrasound waves are energy waves. Therefore the risk of inducing bio-effects should always be taken into consideration. For ultrasound, these bio-effects can be subdivided into two main categories, namely mechanical and thermal bio-effects[123].

(1) Mechanical bio-effects

Mechanical bio-effects are classified based on the mechanical index (MI), a safety parameter derived by Apfel and Holland[124]. It is calculated using the following formula, where PnP is the peak negative pressure and F_c is the center frequency of the applied ultrasound wave.

$$MI = \frac{PnP}{\sqrt{F_c}}$$

Mechanical bio-effects are mainly related to cavitation of injected microbubble contrast agents, but also of spontaneously occurring microbubbles[125, 126]. Firstly, when microbubble contrast agents are injected and ultrasound is applied (e.g. for CEUS imaging), microbubbles act as artificial cavitation nuclei. This means that already at relatively low MIs, microbubbles will oscillate, as previously described. As long as the MI is low (<0.5), the cavitation will remain stable, which means that the microbubbles will keep shrinking and expanding whilst generating linear and harmonic echoes (**Figure 14A**). However, when the MI is higher, the microbubble movements become unstable, and the inertia of the fluid that surrounds the cavitating microbubble will eventually cause it to collapse and fragment into smaller microbubbles (**Figure 14B**). Microbubble implosion is a rather violent phenomenon that can be associated with tissue damage and haemorrhage.

When no microbubbles are used, cavitation will only occur at higher MIs. At an MI >1.9, the large peak negative pressures will cause oscillation of naturally occurring gas nuclei. Continuous ultrasound exposure might then result in additional gas influx into the oscillating bubble, causing it to grow in size (**Figure 14C**). Once more, depending on the size of the expanding bubble, the cavitation can rapidly become unstable, eventually leading to microbubble implosion and local bio-effects. Overall, to prevent this mechanical tissue-damage, the FDA limited the MI output of clinical ultrasound scanners to 1.9, although caution is already warranted at lower MI (starting from MI >1), since gas-rich tissues such as the liver and kidney will exhibit nucleation and cavitation already at lower acoustical pressures.

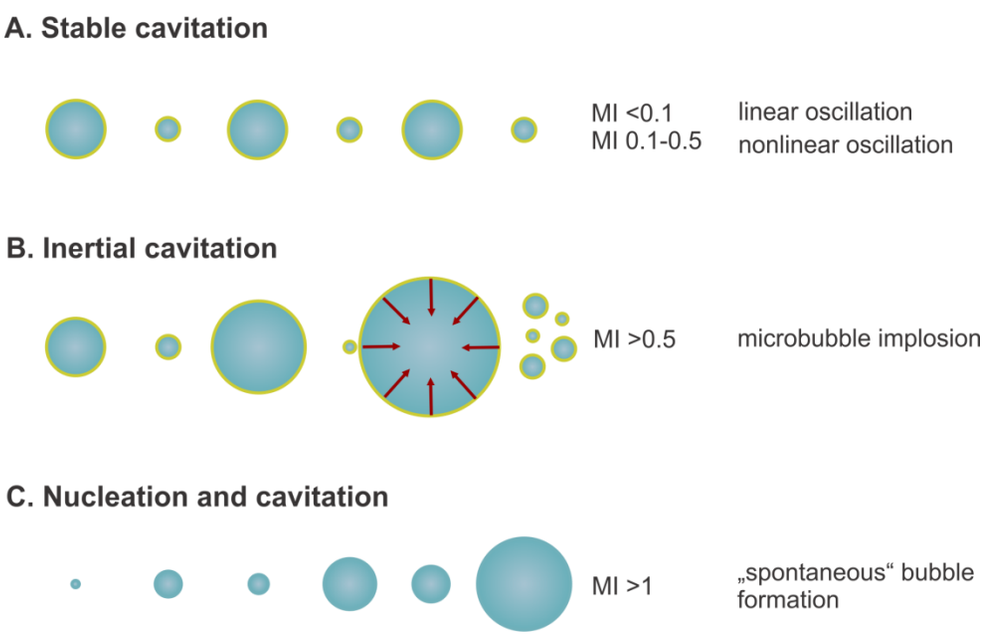

Figure 14. Mechanical bio-effects of ultrasound.

Microbubble contrast agents cavitate in response to ultrasound waves. When the MI is low, the cavitation is stable (A) but when the MI increases, the microbubble oscillations become unstable, and the microbubbles can collapse (B). At even higher MI, these effects can occur without the injection of microbubble contrast agents. Then, natural cavitation nuclei can give rise to oscillating bubbles in ultrasound-exposed tissue (C).

(2) Thermal bio-effects

In addition to mechanical effects, ultrasound energy can partly be absorbed by the exposed tissue, and is converted into heat. As a result, the temperature can locally rise, leading to thermal bio-effects. The risk of these effects can be estimated using the thermal index (TI)[127]. This value is calculated as the ratio between the total acoustic power (W_p) to the estimated power needed to raise the tissue temperature by 1°C (W_{deg}, depends on the tissue type). Overall, procedures that limit the rise in temperature to 1.5°C are generally considered as safe[128].

$$TI = \frac{W_p}{W_{deg}}$$

(3) Utilizing ultrasound-mediated bio-effects for therapy

The described mechanical and thermal bio-effects encompass safety risks. To avoid tissue damage, clinicians are therefore advised to keep ultrasound exposure as low as reasonably achievable (ALARA), even though there have not been concrete indications that adverse events due to mechanical damage occur during ultrasound imaging (that is without the presence of microbubble contrast agents) in humans[123, 128]

On the other hand, the occurrence of these bio-effects can be used to our advantage in both diagnostic and therapeutic medicine. Ultrasound has not only proven its benefit in imaging as explained in the previous sections, it also lies at the basis of a number of other treatments which are currently used in the clinic. This way, mechanical bio-effects are used for lithotripsy and root canal cleaning, whereas thermal bio-effects are applied for physiotherapy and thermal tissue ablation.

Lithotripsy. Low frequency ultrasound shock waves can induce mechanical disruption of kidney and gallbladder stones, as first demonstrated by Chaussy in 1980[129]. By using ultrasound to fragment larger stones into smaller ones that can easily pass through the urinary tract or the bile duct, surgical intervention can be avoided. However, severe side effects have been associated with this technique, as the high intensity non-focused shockwaves can also cause rupture of blood vessels and inflammation[130].

Sonothrombolysis. Blood clots that occlude blood vessels can have sever effects such as ischemic stroke. To avoid morbidity and mortality, it is crucial to dissolve the thrombus as soon as possible, which is mainly done by intravenous injection of thrombolytic drugs (e.g. tissue plasminogen activator (tPA)). It was shown that the use of ultrasound-mediated cavitation can improve enzymatic fibrinolysis by enhancing tPA penetration into the thrombi, thus allowing a reduction of the tPA dose. Several clinical studies using intravascular or transcranial transducers have shown that sonothrombolysis has a good safety profile and a significant therapeutic benefit. Moreover, the use of microbubbles to lower the cavitation threshold and increase cavitation-induced damage to the clot, is currently under investigation[131-133].

Root canal cleaning. For successful endodontic treatment, it is crucial to remove necrotic material, debris and micro-organisms from the tooth's root canal before filling it. Therefore, the root canal is thoroughly irrigated and cleaned. Quite often, this tedious task needs to be repeated due to the incomplete bacteria removal. By inserting a small ultrasound needle tip into the root canal during irrigation, acoustic streaming and cavitation can be induced, resulting in "activation" of the irrigant. This way, significant improvements in root canal cleanliness were observed[134, 135].

Physiotherapy. Soft tissue injuries such as tendon and muscle wounds, often benefit from local heat application. Thus, non-focused ultrasound has been used since the early 1950s for the treatment of sports injuries.

Sonophoresis/Phonophoresis. The ultrasound gel that is used to conduct the ultrasound between the transducer and the patient, can be supplied with anti-inflammatory or analgesic drugs. Ultrasound application can then promote transdermal drug delivery[136].

High Intensity Focused Ultrasound (HIFU). By using focused transducers to locally deposit high amounts of energy in a small volume, tissue can be ablated *via* either mechanical or thermal bio-effects depending on the ultrasound settings used. Generally, HIFU makes use of lower frequency ultrasound (0.8-3.5 MHz) focused to a volume of 1-3 x 8-15 mm. By moving the focal point over the tissue, larger areas can be ablated, often under MRI guidance[137]. The working principle can either be thermal or mechanic. For most therapeutic applications in the clinic, thermal HIFU is used. Here, longer ultrasound pulses result in the accumulation of energy and local heating to over 80°C, causing tissue necrosis and coagulation. Thermal HIFU has been clinically used as an alternative to surgery and other thermal ablation techniques (e.g. cryoablation and RF ablation) for the treatment of breast cancer legions, uterine fibroids and prostate cancer[138]. Alternatively, when shorter pulses and higher frequencies are used, the local heating will be less pronounced and cavitation will become the most prominent phenomenon. This is called mechanical HIFU. Although it is less capable of completely destroying the target tissue, it has been reported to result in immunogenic cell death, accompanied by the release of amongst others heat shock proteins (HSPs) and the infiltration of antigen-presenting cells. Thus, mechanical HIFU could spark immune responses against malignancies[139]. Here too, microbubbles are being explored to lower the threshold for these mechanical effects and to increase the extent of tissue damage[140]. In addition to the use of HIFU for tissue ablation, it is also under investigation to locally trigger the release of chemotherapeutics which are packaged in thermosensitive liposomes. For example, ThermoDox® (thermoliposomal doxorubicin, developed by Celsion) and HIFU are currently being investigated for the treatment of metastatic liver cancer[141, 142].

Opening the blood brain barrier. Another application for microbubbles and ultrasound, which is still in its preclinical phase, is the temporary disruption of the blood brain barrier (BBB). The BBB is one of the hardest barriers to conquer, as it is designed to sustain the brain homeostasis. The tight connections between brain endothelial cells therefore form a strong impediment for the action of drugs that have their target in the brain (e.g. chemotherapeutics for brain tumors, or therapeutics against schizophrenia or Alzheimer's disease)[143]. One of the strategies to temporarily overcome this barrier, is the application of low frequency ultrasound that can be delivered non-invasively and under MRI-guidance, through the skull[144]. Here too, microbubbles can be used to promote cavitation, resulting in the disruption of the BBB for about 4h, allowing passage of small molecule drugs[145, 146], genes[147] and even cell therapeutics (e.g. neural stem cells and immune cells)[148-150].

(1) Sonoporation

As previously described, microbubbles respond to transmitted ultrasound waves by oscillating, and this can cause mechanical bio-effects. Importantly, stable as well as unstable microbubble movements, can affect the integrity of neighboring cell membranes. As shown in **Figure 15**, stably cavitating microbubbles can (A) push or pull at the cell membrane during their expansion or compression, respectively. In addition, (B) the acoustic radiation force can drive microbubble transport towards or even through the cell membrane, or (C) fluid microstreams generated during microbubble oscillations create shear stress that can disrupt the plasma membrane. In addition, and even more pronounced, imploding microbubbles can also affect cell membranes by (D) creating shockwaves or (E) liquid jets. All these bio-effects can create pores in adjacent cell membranes. This phenomenon is called sonoporation[151].

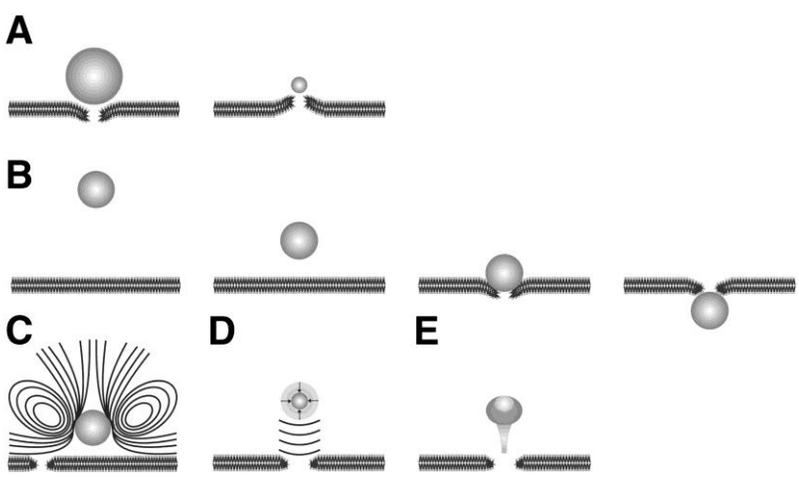

Figure 15. Bio-effects of microbubbles on neighboring cell membranes.
Stably cavitating microbubbles can temporarily permeate cell membranes *via* pushing or pulling (A), acoustic radiation force microbubble displacement (B) or by creating microstreamings in the surrounding fluid (C). Unstable cavitation and resulting microbubble collapse can create shock waves (D) or fluid jets (E). This figure was reproduced from Lentacker et al.[151].

These pores are small and short-lived: if moderate acoustic pressures are used, pore sizes are generally between a few tens to a few hundreds of nanometers, and they are sealed within milliseconds to seconds[152, 153]. The mechanisms through which this membrane repair occurs are not yet fully elucidated. Current theories include patching of the lipid membrane using membrane components derived from intracellular vesicles that are exocytosed, or the stimulation of endocytosis, which results in the removal of the pores from the cell membrane[154, 155].

(2) Implications for drug and gene delivery

Since microbubbles in combination with ultrasound can lead to spatio-temporally controlled cell membrane poration, this could present advantages for ultrasound-triggered drug delivery. By allowing drugs or genes to enter the cell *via* the created pores, direct cytoplasmic entry of the compounds is allowed, circumventing the normal endocytic pathway, as shown in **Figure 16**. This is particularly interesting since one of the problems with passive drug uptake by cells is that endosomes fuse with lysosomes, resulting in the digestion of the endocytosed components[156]. Therefore, methods that allow drugs to directly enter the cytosplasm will avoid premature degradation and increase the therapeutic effect of the delivered drugs. As a consequence, sonoporation is currently under investigation as a strategy to improve drug and gene delivery. Indeed, it was shown that when drugs or genes were co-injected with commercially available microbubbles, enhanced uptake and therapeutic effects could be observed *in vitro* and *in vivo*[157, 158].

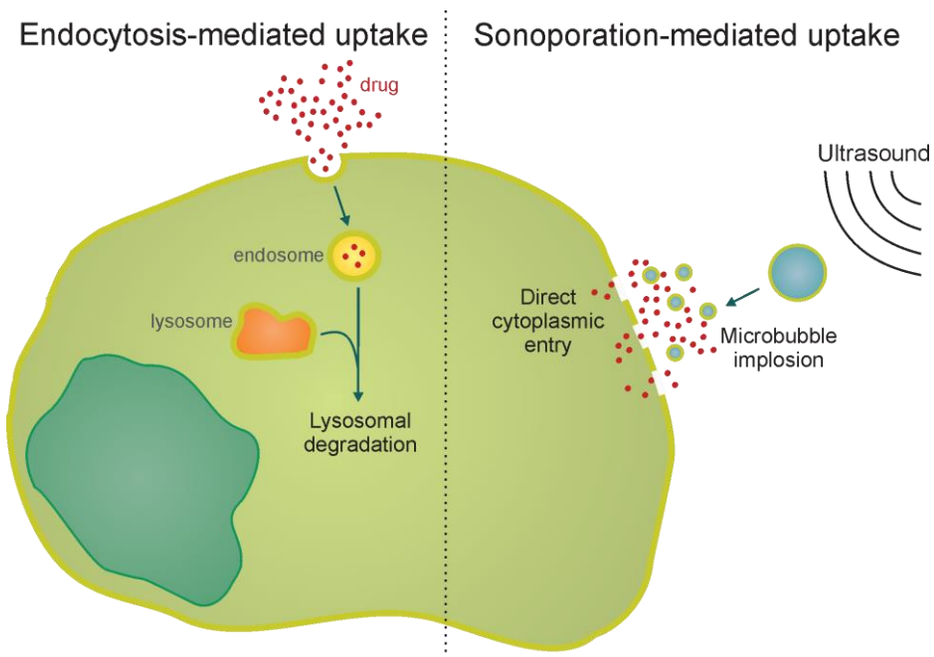

Figure 16. Endocytosis and sonoporation-mediated uptake of drugs.
When drugs are taken up by cells, this normally occurs *via* endocytosis, where the cell membrane invaginates and forms endosomes, which contain extracellular material. These endosomes will fuse with lysosomes, resulting in the digestion of the engulfed components (left panel). When microbubbles and ultrasound induce sonoporation, drugs can enter the cell through the created pores and immediately end up in the cytoplasm, thus avoiding endolysosomal degradation (right panel).

The effects of sonoporation-mediated drug delivery can even be enhanced by loading the drugs or genes onto the microbubbles, as this offers various advantages. First of all, by physically coupling the active components to the microbubbles, ultrasound-induced microbubble implosion will not only locally permeate cell membranes, it will at the same time

result in a local drug release. This has a double benefit: (1) before microbubble implosion, the microbubble-bound drugs or genes are protected against degradation by digestive enzymes (e.g. proteases or nucleases) in the blood, and (2) the coupled drugs or genes are shielded from unwanted uptake in other regions than the target site. Thus, the risk of adverse events can be reduced. What is more, by locally releasing the drug at the exact same location where the cell membranes are perforated, the local high drug concentrations at the pore sites will result in an even better drug uptake. This was evidenced by the work of Lentacker et al., who proved that transfection using pDNA-loaded microbubbles and ultrasound resulted in a 10-fold improvement over the use of naked DNA together with microbubbles and ultrasound *in vitro*[159]. In this way, selectively improving drug uptake at the region of interest could allow a reduction of the total drug dose, which could improve the therapeutic window of the delivered therapeutic agent. Lastly, drug-loaded microbubbles could allow image-guided drug delivery. This way, low MI CEUS could be used to visualize the drugs after injection, and when they reach the target site, higher MI ultrasound pulses can be delivered to locally burst the bubbles, cause sonoporation and promote intracellular drug delivery. Hence, ultrasound-guided, ultrasound-triggered drug and gene delivery could be possible[160].

(3) Loading microbubbles with therapeutics

Loading microbubbles with drugs or nucleic acids can be done in different ways, as summarized for lipid microbubbles in **Figure 17**. First of all, drugs can be incorporated inside the microbubble shell, either by dissolving the drug in an oil layer within the microbubble, or by formulating it in the lipid or polymer shell[161, 162]. The amount of drug that can be loaded in this way, however, is limited as the microbubble coating is generally quite thin (a few nanometers for lipid bubbles and 2-500 nm for polymer bubbles). Secondly, cationic microbubbles have been formulated, which can be electrostatically loaded with nucleic acids (mainly plasmid DNA)[163-165]. Here, the loading capacity is determined by the charge of the microbubble, which is driven by the number of cationic lipids which can be incorporated without impacting lipid packing and microbubble stability[166]. Lastly, and most interestingly, NPs containing drugs or genes can be attached to the surface of microbubbles *via* avidin-biotin bridges or *via* covalent thiol-linkages. This technique has the advantage of a relatively high loading capacity, as demonstrated by Geers et al. who estimated that about 600-1300 drug-loaded liposomes could be covalently coupled to a single lipid-coated microbubble[167]. Moreover, a wide range of therapeutic agents have been linked to microbubbles in this way, including liposomes containing cytostatic drugs (e.g. doxorubicin)[167-169] and nucleic-acid containing NPs (e.g. pDNA or siRNA lipoplexes)[159, 170, 171].

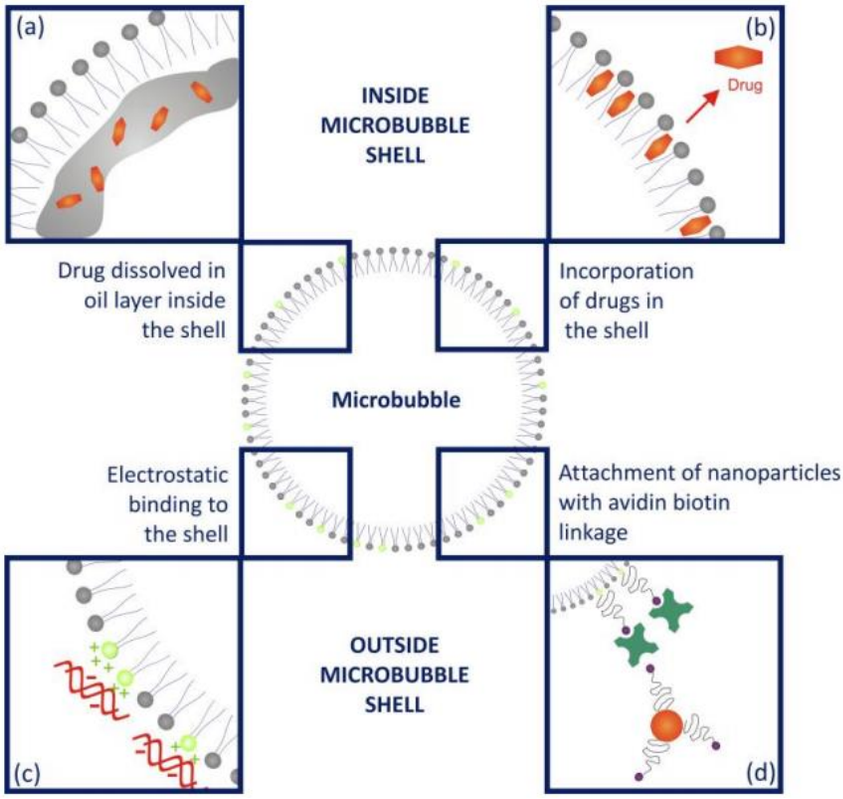

Figure 17. Strategies for drug and gene loading of (lipid) microbubbles.

Drugs can be loaded by (a) dissolving the drug in an oil layer within the microbubble; (b) incorporating drugs within the microbubble shell; (c) electrostatically binding anionic components such as nucleic acids to cationic microbubbles; (d) attaching drug- or gene-containing nanoparticles to the surface of functionalized microbubbles.

Image reproduced from Lentacker et al.[172]

CONCLUSIONS

With respect to immunotherapy, we have come a long way from beginning to understand how the immune system can protect us from danger to realizing how we can harness it in the battle against cancer. By the day, our knowledge on effector cells, stimulatory and suppressive cytokine signaling pathways and potential therapeutic targets expands. However, the number of reports where particles are described that deliver both tumor antigens and immunostimulants to DCs *in vivo* is still limited. To gap the bridge between what we already know about the induction of immunity, and the development of suitable biomaterials, close collaboration between material scientists and immunologists is probably key.

From the therapeutic imaging point of view, theranostics are multifunctional agents that merge imageable and therapeutic moieties. The ability to image drug distribution and release, or to be able to simultaneously treat and follow-up treatment have made them trending topics of investigation. Especially the development of theranostics for imaging techniques that do not require the use of ionizing radiation, such as MRI (^{1}H and ^{19}F) and ultrasonography, could be clinically relevant for visual treatment feedback. How exactly these can be implemented and lifted from theranostics to immunotheranostics will be investigated in the following chapters.

ACKNOWLEDGEMENTS

Heleen Dewitte is a doctoral fellow of the Institute for the Promotion of Innovation through Science and Technology in Flanders, Belgium (IWT-Vlaanderen). Ine Lentacker and Karine Breckpot are postdoctoral fellows of the Research Foundation-Flanders, Belgium (FWO-Vlaanderen). This project was funded through the FWO grant G016513N.

REFERENCES

1. Johnston, K. et al. Economic impact of healthcare resource utilisation patterns among patients diagnosed with advanced melanoma in the United Kingdom, Italy, and France: Results from a retrospective, longitudinal survey (MELODY study). *European Journal of Cancer* **48**, 2175-2182 (2012).
2. Coley, W.B. The treatment of malignant tumors by repeated inoculations of erysipelas. With a report of ten original cases. 1893. *Clinical Orthopaedics and Related Research*, 3-11 (1991).
3. Zinkernagel, R.M. & Doherty, P.C. Restriction of in vitro T cell-mediated cytotoxicity in lymphocytic choriomeningitis within a syngeneic or semiallogeneic system. *Nature* **248**, 701-2 (1974).
4. Steinman, R.M. & Cohn, Z.A. Identification of a Novel Cell Type in Peripheral Lymphoid Organs of Mice. *Journal of Experimental Medicine* **137**, 1142-1162 (1973).
5. Nomura, N. et al. Prediction of the coding sequences of unidentified human genes. I. The coding sequences of 40 new genes (KIAA0001-KIAA0040) deduced by analysis of randomly sampled cDNA clones from human immature myeloid cell line KG-1 (supplement). *DNA research : an international journal for rapid publication of reports on genes and genomes* **1**, 47-56 (1994).
6. Lakhani, S. Early Clinical Pathologists - Jenner,Edward (1749-1823). *Journal of Clinical Pathology* **45**, 756-758 (1992).
7. Kawakami, Y. et al. Cloning of the Gene Coding for a Shared Human-Melanoma Antigen Recognized by Autologous T-Cells Infiltrating into Tumor. *Proceedings of the National Academy of Sciences of the United States of America* **91**, 3515-3519 (1994).
8. Clowes, G.H.A.B., F. W. . Further evidence of immunity against cancer in mice after spontaneous recovery. *Medical News* **87**, 968-971 (1905).
9. Gross, L. Intradermal Immunization of C3H Mice against a Sarcoma That Originated in an Animal of the Same Line. *Cancer Research* **3**, 326-333 (1943).
10. Vanderbruggen, P. et al. A Gene Encoding an Antigen Recognized by Cytolytic Lymphocytes-T on a Human-Melanoma. *Science* **254**, 1643-1647 (1991).
11. Coulie, P.G., Van den Eynde, B.J., van der Bruggen, P. & Boon, T. Tumour antigens recognized by T lymphocytes: at the core of cancer immunotherapy. *Nature reviews. Cancer* **14**, 135-46 (2014).
12. Shimizu, J. et al. Induction of Tumor-Specific Invivo Protective Immunity by Immunization with Tumor Antigen-Pulsed Antigen-Presenting Cells. *Journal of Immunology* **142**, 1053-1059 (1989).
13. Breckpot, K., Heirman, C., Neyns, B. & Thielemans, K. Exploiting dendritic cells for cancer immunotherapy: genetic modification of dendritic cells. *Journal of Gene Medicine* **6**, 1175-1188 (2004).
14. Larocca, C. & Schlom, J. Viral Vector-Based Therapeutic Cancer Vaccines. *Cancer Journal* **17**, 359-371 (2011).
15. Small, E.J. et al. Placebo-controlled phase III trial of immunologic therapy with sipuleucel-T (APC8015) in patients with metastatic, asymptomatic hormone refractory prostate cancer. *Journal of Clinical Oncology* **24**, 3089-3094 (2006).
16. de Vries, I.J.M. et al. Effective migration of antigen-pulsed dendritic cells to lymph nodes in melanoma patients is determined by their maturation state. *Cancer Research* **63**, 12-17 (2003).
17. Villadangos, J.A., Heath, W.R. & Carbone, F.R. Outside looking in: the inner workings of the crosspresentation pathway within dendritic cells. *Trends in Immunology* **28**, 45-47 (2007).
18. Wimmers, F., Schreibelt, G., Skold, A.E., Figdor, C.G. & De Vries, I.J. Paradigm Shift in Dendritic Cell-Based Immunotherapy: From in vitro Generated Monocyte-Derived DCs to Naturally Circulating DC Subsets. *Frontiers in immunology* **5**, 165 (2014).
19. Benteyn, D., Heirman, C., Bonehill, A., Thielemans, K. & Breckpot, K. mRNA-pulsed dendritic cell vaccines *Expert review of vaccines* **submitted** (2014).
20. Henri, S. et al. The dendritic cell populations of mouse lymph nodes. *Journal of Immunology* **167**, 741-748 (2001).
21. Villadangos, J.A. & Schnorrer, P. Intrinsic and cooperative antigen-presenting functions of dendritic-cell subsets in vivo. *Nature Reviews Immunology* **7**, 543-555 (2007).

22. Shortman, K. & Naik, S.H. Steady-state and inflammatory dendritic-cell development. *Nature reviews. Immunology* **7**, 19-30 (2007).
23. Dewitte, H. et al. Choose your models wisely: How different murine bone marrow-derived dendritic cell protocols influence the success of nanoparticulate vaccines in vitro. *Journal of Controlled Release* **195**, 138-146 (2014).
24. Marchini, C. et al. Structural Stability and Increase in Size Rationalize the Efficiency of Lipoplexes in Serum. *Langmuir* **25**, 3013-3021 (2009).
25. Wang, R.R., Xiao, R.Z., Zeng, Z.W., Xu, L.L. & Wang, J.J. Application of poly(ethylene glycol)-distearoylphosphatidylethanolamine (PEG-DSPE) block copolymers and their derivatives as nanomaterials in drug delivery. *International Journal of Nanomedicine* **7**, 4185-4198 (2012).
26. Larsson, M. et al. Requirement of mature dendritic cells for efficient activation of influenza A-specific memory CD8(+) T cells. *Journal of Immunology* **165**, 1182-1190 (2000).
27. Lutz, M.B. & Schuler, G. Immature, semi-mature and fully mature dendritic cells: which signals induce tolerance or immunity? *Trends in Immunology* **23**, 445-449 (2002).
28. Ma, Y.F. et al. The role of surface charge density in cationic liposome-promoted dendritic cell maturation and vaccine-induced immune responses. *Nanoscale* **3**, 2307-2314 (2011).
29. Perrie, Y., Kastner, E., Kaur, R., Wilkinson, A. & Ingham, A.J. A case-study investigating the physicochemical characteristics that dictate the function of a liposomal adjuvant. *Human vaccines & immunotherapeutics* **9**, 1374-81 (2013).
30. Yoshizaki, Y. et al. Potentiation of pH-sensitive polymer-modified liposomes with cationic lipid inclusion as antigen delivery carriers for cancer immunotherapy. *Biomaterials* (2014).
31. Yanasarn, N., Sloat, B.R. & Cui, Z. Negatively Charged Liposomes Show Potent Adjuvant Activity When Simply Admixed with Protein Antigens. *Molecular Pharmaceutics* **8**, 1174-1185 (2011).
32. Sharp, F.A. et al. Uptake of particulate vaccine adjuvants by dendritic cells activates the NALP3 inflammasome. *Proceedings of the National Academy of Sciences of the United States of America* **106**, 870-875 (2009).
33. Fischer, S. et al. The preservation of phenotype and functionality of dendritic cells upon phagocytosis of polyelectrolyte-coated PLGA microparticles. *Biomaterials* **28**, 994-1004 (2007).
34. Blander, J.M. & Medzhitov, R. Toll-dependent selection of microbial antigens for presentation by dendritic cells. *Nature* **440**, 808-812 (2006).
35. Schlosser, E. et al. TLR ligands and antigen need to be coencapsulated into the same biodegradable microsphere for the generation of potent cytotoxic T lymphocyte responses. *Vaccine* **26**, 1626-1637 (2008).
36. Zaks, K. et al. Efficient immunization and cross-priming by vaccine adjuvants containing TLR3 or TLR9 agonists complexed to cationic liposomes. *Journal of Immunology* **176**, 7335-7345 (2006).
37. Bal, S.M., Hortensius, S., Ding, Z., Jiskoot, W. & Bouwstra, J.A. Co-encapsulation of antigen and Toll-like receptor ligand in cationic liposomes affects the quality of the immune response in mice after intradermal vaccination. *Vaccine* **29**, 1045-1052 (2011).
38. Kadowaki, N. et al. Subsets of human dendritic cell precursors express different toll-like receptors and respond to different microbial antigens. *Journal of Experimental Medicine* **194**, 863-869 (2001).
39. Lee, Y.R. et al. Biodegradable Nanoparticles Containing TLR3 or TLR9 Agonists Together with Antigen Enhance MHC-restricted Presentation of the Antigen. *Archives of Pharmacal Research* **33**, 1859-1866 (2010).
40. Ilyinskii, P.O. et al. Adjuvant-carrying synthetic vaccine particles augment the immune response to encapsulated antigen and exhibit strong local immune activation without inducing systemic cytokine release. *Vaccine* **32**, 2882-2895 (2014).
41. Tacken, P.J. et al. Targeted delivery of TLR ligands to human and mouse dendritic cells strongly enhances adjuvanticity. *Blood* **118**, 6836-6844 (2011).
42. Mueller, M., Reichardt, W., Koerner, J. & Groettrup, M. Coencapsulation of tumor lysate and CpG-ODN in PLGA-microspheres enables successful immunotherapy of prostate carcinoma in TRAMP mice. *Journal of Controlled Release* **162**, 159-166 (2012).

43. Zhang, Z. et al. Induction of anti-tumor cytotoxic T cell responses through PLGA-nanoparticle mediated antigen delivery. *Biomaterials* **32**, 3666-3678 (2011).
44. Fischer, S. et al. Concomitant delivery of a CTL-restricted peptide antigen and CpG ODN by PLGA microparticles induces cellular immune response. *Journal of Drug Targeting* **17**, 652-661 (2009).
45. Pradhan, P. et al. The effect of combined IL10 siRNA and CpG ODN as pathogen-mimicking microparticles on Th1/Th2 cytokine balance in dendritic cells and protective immunity against B cell lymphoma. *Biomaterials* (2014).
46. Giddam, A.K., Zaman, M., Skwarczynski, M. & Toth, I. Liposome-based delivery system for vaccine candidates: constructing an effective formulation. *Nanomedicine* **7**, 1877-1893 (2012).
47. Moon, J.J. et al. Interbilayer-crosslinked multilamellar vesicles as synthetic vaccines for potent humoral and cellular immune responses. *Nature Materials* **10**, 243-251 (2011).
48. Slutter, B., Bal, S.M., Ding, Z., Jiskoot, W. & Bouwstra, J.A. Adjuvant effect of cationic liposomes and CpG depends on administration route. *Journal of Controlled Release* **154**, 123-130 (2011).
49. Milicic, A. et al. Small Cationic DDA:TDB Liposomes as Protein Vaccine Adjuvants Obviate the Need for TLR Agonists in Inducing Cellular and Humoral Responses. *Plos One* **7** (2012).
50. Nordly, P. et al. Immunity by formulation design: Induction of high CD8(+) T-cell responses by poly(I:C) incorporated into the CAF01 adjuvant via a double emulsion method. *Journal of Controlled Release* **150**, 307-317 (2011).
51. Li, W.M., Dragowska, W.H., Bally, M.B. & Schutze-Redelmeier, M.-P. Effective induction of CD8+ T-cell response using CpG oligodeoxynucleotides and HER-2/neu-derived peptide co-encapsulated in liposomes. *Vaccine* **21**, 3319-3329 (2003).
52. Rizwan, S.B. et al. Cubosomes containing the adjuvants imiquimod and monophosphoryl lipid A stimulate robust cellular and humoral immune responses. *Journal of Controlled Release* **165**, 16-21 (2013).
53. Lee, I.H. et al. Imageable Antigen-Presenting Gold Nanoparticle Vaccines for Effective Cancer Immunotherapy In Vivo. *Angewandte Chemie-International Edition* **51**, 8800-8805 (2012).
54. Tao, Y., Ju, E.G., Li, Z.H., Ren, J.S. & Qu, X.G. Engineered CpG- Antigen Conjugates Protected Gold Nanoclusters as Smart Self- Vaccines for Enhanced Immune Response and Cell Imaging. *Advanced Functional Materials* **24**, 1004-1010 (2014).
55. Tang, Y.S. et al. Bacterial magnetic particles as a novel and efficient gene vaccine delivery system. *Gene Therapy* **19**, 1187-1195 (2012).
56. Luo, Z.C. et al. Cationic polypeptide micelle-based antigen delivery system: A simple and robust adjuvant to improve vaccine efficacy. *Journal of Controlled Release* **170**, 259-267 (2013).
57. Belizaire, R. & Unanue, E.R. Targeting proteins to distinct subcellular compartments reveals unique requirements for MHC class I and II presentation. *Proceedings of the National Academy of Sciences of the United States of America* **106**, 17463-17468 (2009).
58. Kasturi, S.P. & Pulendran, B. Cross-presentation: avoiding trafficking chaos? *Nature Immunology* **9**, 461-463 (2008).
59. Li, H., Li, Y., Jiao, J. & Hu, H.-M. Alpha-alumina nanoparticles induce efficient autophagy-dependent cross-presentation and potent antitumour response. *Nature Nanotechnology* **6**, 645-650 (2011).
60. Mukai, Y. et al. Induction of Endoplasmic Reticulum-Endosome Fusion for Antigen Cross-Presentation Induced by Poly (gamma-Glutamic Acid) Nanoparticles. *Journal of Immunology* **187**, 6249-6255 (2011).
61. Stano, A., Scott, E.A., Dane, K.Y., Swartz, M.A. & Hubbell, J.A. Tunable T cell immunity towards a protein antigen using polymersomes vs. solid-core nanoparticles. *Biomaterials* **34**, 4339-4346 (2013).
62. Chang, J.S., Choi, M.J., Cheong, H.S. & Kim, K. Development of Th1-mediated CD8+effector T cells by vaccination with epitope peptides encapsulated in pH-sensitive liposomes. *Vaccine* **19**, 3608-3614 (2001).
63. Bonehill, A. et al. Messenger RNA-electroporated dendritic cells presenting MAGE-A3 simultaneously in HLA class I and class II molecules. *Journal of Immunology* **172**, 6649-57 (2004).

64. Johansen, P. et al. Antigen kinetics determines immune reactivity. *Proceedings of the National Academy of Sciences of the United States of America* **105**, 5189-5194 (2008).
65. Demento, S.L. et al. Role of sustained antigen release from nanoparticle vaccines in shaping the T cell memory phenotype. *Biomaterials* **33**, 4957-4964 (2012).
66. Liao, X.S. et al. Transfection of RNA encoding tumor antigens following maturation of dendritic cells leads to prolonged presentation of antigen and the generation of high-affinity tumor-reactive cytotoxic T lymphocytes. *Molecular Therapy* **9**, 757-764 (2004).
67. Melhem, N.M., Gleason, S.M., Liu, X.D. & Barratt-Boyes, S.M. High-level antigen expression and sustained antigen presentation in dendritic cells nucleofected with wild-type viral mRNA but not DNA. *Clinical and Vaccine Immunology* **15**, 1337-1344 (2008).
68. Ali, O.A., Huebsch, N., Cao, L., Dranoff, G. & Mooney, D.J. Infection-mimicking materials to program dendritic cells in situ. *Nature Materials* **8**, 151-158 (2009).
69. Ali, O.A., Emerich, D., Dranoff, G. & Mooney, D.J. In Situ Regulation of DC Subsets and T Cells Mediates Tumor Regression in Mice. *Science translational medicine* **1** (2009).
70. Singh, A. et al. An injectable synthetic immune-priming center mediates efficient T-cell class switching and T-helper 1 response against B cell lymphoma. *Journal of Controlled Release* **155**, 184-192 (2011).
71. Terreno, E., Uggeri, F. & Aime, S. Image guided therapy: The advent of theranostic agents. *Journal of Controlled Release* **161**, 328-337 (2012).
72. Svenson, S. Theranostics: Are We There Yet? *Molecular Pharmaceutics* **10**, 848-856 (2013).
73. Negussie, A.H. et al. Formulation and characterisation of magnetic resonance imageable thermally sensitive liposomes for use with magnetic resonance-guided high intensity focused ultrasound. *International Journal of Hyperthermia* **27**, 140-155 (2011).
74. Studwell, A.J. & Kotton, D.N. A Shift From Cell Cultures to Creatures: In Vivo Imaging of Small Animals in Experimental Regenerative Medicine. *Molecular Therapy* **19**, 1933-1941 (2011).
75. Bederson, B. Essay: Samuel Abraham Goudsmit (1902-1978). *Physical Review Letters* **101**, 010002 (2008).
76. Damadian, R., Zaner, K., Hor, D. & Dimaio, T. Human Tumors Detected by Nuclear Magnetic-Resonance. *Proceedings of the National Academy of Sciences of the United States of America* **71**, 1471-1473 (1974).
77. Caravan, P., Ellison, J.J., McMurry, T.J. & Lauffer, R.B. Gadolinium(III) chelates as MRI contrast agents: Structure, dynamics, and applications. *Chemical Reviews* **99**, 2293-2352 (1999).
78. Zhang, H.L., Maki, J.H. & Prince, M.R. 3D Contrast-enhanced MR angiography. *Journal of Magnetic Resonance Imaging* **25**, 13-25 (2007).
79. Na, H.B., Song, I.C. & Hyeon, T. Inorganic Nanoparticles for MRI Contrast Agents. *Advanced Materials* **21**, 2133-2148 (2009).
80. Wan, Q. et al. Self-assembled magnetic theranostic nanoparticles for highly sensitive MRI of minicircle DNA delivery. *Nanoscale* **5**, 744-752 (2013).
81. Lee, G.Y. et al. Theranostic Nanoparticles with Controlled Release of Gemcitabine for Targeted Therapy and MRI of Pancreatic Cancer. *ACS nano* **7**, 2078-2089 (2013).
82. Amiri, H. et al. Alzheimer's Disease: Pathophysiology and Applications of Magnetic Nanoparticles as MRI Theranostic Agents. *ACS chemical neuroscience* **4**, 1417-1429 (2013).
83. Feshitan, J.A., Vlachos, F., Sirsi, S.R., Konofagou, E.E. & Borden, M.A. Theranostic Gd(III)-lipid microbubbles for MRI-guided focused ultrasound surgery. *Biomaterials* **33**, 247-255 (2012).
84. Holland, G.N., Bottomley, P.A. & Hinshaw, W.S. F-19 Magnetic-Resonance Imaging. *Journal of Magnetic Resonance* **28**, 133-136 (1977).
85. Ruiz-Cabello, J., Barnett, B.P., Bottomley, P.A. & Bulte, J.W.M. Fluorine (F-19) MRS and MRI in biomedicine. *Nmr in Biomedicine* **24**, 114-129 (2011).
86. Wolf, W. et al. F-19 Nmr Spectroscopic Studies of the Metabolism of 5-Fluorouracil in the Liver of Patients Undergoing Chemotherapy. *Magnetic resonance imaging* **5**, 165-169 (1987).
87. Ahrens, E.T., Feili-Hariri, M., Xu, H., Genove, G. & Morel, P.A. Receptor-mediated endocytosis of iron-oxide particles provides efficient labeling of dendritic cells for in vivo MR imaging. *Magnetic Resonance in Medicine* **49**, 1006-1013 (2003).

88. Sever, A. et al. Percutaneous removal of sentinel lymph nodes in a swine model using a breast lesion excision system and contrast-enhanced ultrasound. *European Radiology* **22**, 545-550 (2012).
89. Helfer, B.M. et al. Functional assessment of human dendritic cells labeled for in vivo (19)F magnetic resonance imaging cell tracking. *Cytotherapy* **12**, 238-250 (2010).
90. Himmelreich, U. et al. A responsive MRI contrast agent to monitor functional cell status. *Neuroimage* **32**, 1142-1149 (2006).
91. Krafft, M.P. Fluorocarbons and fluorinated amphiphiles in drug delivery and biomedical research. *Advanced Drug Delivery Reviews* **47**, 209-228 (2001).
92. Ahrens, E.T., Flores, R., Xu, H.Y. & Morel, P.A. In vivo imaging platform for tracking immunotherapeutic cells. *Nature biotechnology* **23**, 983-987 (2005).
93. Bonetto, F. et al. A novel (19)F agent for detection and quantification of human dendritic cells using magnetic resonance imaging. *International Journal of Cancer* **129**, 365-373 (2011).
94. Srinivas, M. et al. Customizable, multi-functional fluorocarbon nanoparticles for quantitative in vivo imaging using F-19 MRI and optical imaging. *Biomaterials* **31**, 7070-7077 (2010).
95. Mould, R.F. Pierre curie, 1859-1906. *Current oncology* **14**, 74-82 (2007).
96. Hunt, J.C.R. Lewis Fry Richardson and his contributions to mathematics, meteorology, and models of conflict. *Annual Review of Fluid Mechanics* **30**, XIII-+ (1998).
97. Lewiner, J. Langevin,Paul and the Birth of Ultrasonics. *Japanese Journal of Applied Physics Part 1-Regular Papers Short Notes & Review Papers* **30**, 5-11 (1991).
98. Shampo, M.A. & Kyle, R.A. Karl Theodore Dussik--pioneer in ultrasound. *Mayo Clinic proceedings* **70**, 1136 (1995).
99. Edler, I. & Lindstrom, K. The history of echocardiography. *Ultrasound in Medicine and Biology* **30**, 1565-1644 (2004).
100. Holmes, J.H., Howry, D.H., Posakony, G.J. & Cushman, C.R. The ultrasonic visualization of soft tissue structures in the human body. *Transactions of the American Clinical and Climatological Association* **66**, 208-25 (1954).
101. Donald, I., Macvicar, J. & Brown, T.G. Investigation of Abdominal Masses by Pulsed Ultrasound. *Lancet* **1**, 1188-1194 (1958).
102. Gramiak, R. & Shah, P.M. Echocardiography of the aortic root. *Investigative radiology* **3**, 356-66 (1968).
103. Nanda, N.C. History of Echocardiographic Contrast Agents. *Clinical Cardiology* **20**, 7-11 (1997).
104. Ismail, S. et al. Albunex(R) Microbubbles Mimic Red-Blood-Cell Transit through the Human Myocardium. *Circulation* **88**, 163-163 (1993).
105. Sponheim, N. et al. Albunex(R) - a New Ultrasound Contrast Agent. *International Conference on Acoustic Sensing Imaging*, 103-108 (1993).
106. Bokor, D. Diagnostic efficacy of SonoVue. *American Journal of Cardiology* **86**, 19g-24g (2000).
107. Schneider, M. SonoVue, a new ultrasound contrast agent. *European radiology* **9**, S347-S348 (1999).
108. Clark, L.N. & Dittrich, H.C. Cardiac imaging using Optison. *American Journal of Cardiology* **86**, 14g-18g (2000).
109. Hernot, S. & Klibanov, A.L. Microbubbles in ultrasound-triggered drug and gene delivery. *Advanced Drug Delivery Reviews* **60**, 1153-1166 (2008).
110. Lindner, J.R. Microbubbles in medical imaging: current applications and future directions. *Nature Reviews Drug Discovery* **3**, 527-532 (2004).
111. Burns, P.N. Harmonic imaging with ultrasound contrast agents. *Clinical Radiology* **51**, 50-55 (1996).
112. Sijl, J. et al. "Compression-only" behavior: A second-order nonlinear response of ultrasound contrast agent microbubbles. *Journal of the Acoustical Society of America* **129**, 1729-1739 (2011).
113. Lurie, D.M., Seguin, B.D., Schneider, P.D., Verstraete, F.J. & Wisner, E.R. Contrast-assisted ultrasound for sentinel lymph node detection in spontaneously arising canine head and neck tumors. *Investigative radiology* **41**, 415-421 (2006).
114. Wisner, E.R. et al. Sentinel node detection using contrast-enhanced power Doppler ultrasound lymphography. *Investigative radiology* **38**, 358-365 (2003).

115. Sever, A. et al. A novel approach to identify sentinel lymph nodes using microbubbles and contrast enhanced ultrasound in preoperative breast cancer patients. *Journal of Clinical Oncology* **27** (2009).
116. Sever, A., Jones, S., Weeks, J., Mills, P. & Jones, P. Successful outpatient identification of the sentinel lymph node with ultrasound using microbubbles in breast cancer patients: final results. *British Journal of Surgery* **97**, 28-28 (2010).
117. Sever, A.R. et al. Preoperative Sentinel Node Identification With Ultrasound Using Microbubbles in Patients With Breast Cancer. *American Journal of Roentgenology* **196**, 251-256 (2011).
118. Sever, A.R., Mills, P., Jones, S.E., Mali, W. & Jones, P.A. Sentinel node identification using microbubbles and contrast-enhanced ultrasonography. *Clinical Radiology* **67**, 687-694 (2012).
119. Goldberg, B.B. et al. Contrast-enhanced ultrasound imaging of sentinel lymph nodes after peritumoral administration of Sonazoid in a melanoma tumor animal model. *Journal of ultrasound in medicine : official journal of the American Institute of Ultrasound in Medicine* **30**, 441-53 (2011).
120. Goldberg, B.B., Merton, D.A., Liu, J.B., Murphy, G. & Forsberg, F. Contrast-enhanced sonographic imaging of lymphatic channels and sentinel lymph nodes. *Journal of ultrasound in medicine : official journal of the American Institute of Ultrasound in Medicine* **24**, 953-65 (2005).
121. Goldberg, B.B. et al. Sentinel lymph nodes in a swine model with melanoma: contrast-enhanced lymphatic US. *Radiology* **230**, 727-34 (2004).
122. Swartz, M.A. & Skobe, M. Lymphatic function, lymphangiogenesis, and cancer metastasis. *Microscopy Research and Technique* **55**, 92-99 (2001).
123. Abbott, J.G. Rationale and derivation of Mi and Ti - A review. *Ultrasound in Medicine and Biology* **25**, 431-441 (1999).
124. Apfel, R.E. & Holland, C.K. Gauging the Likelihood of Cavitation from Short-Pulse, Low-Duty Cycle Diagnostic Ultrasound. *Ultrasound in Medicine and Biology* **17**, 179-185 (1991).
125. Church, C.C. Spontaneous homogeneous nucleation, inertial cavitation and the safety of diagnostic ultrasound. *Ultrasound in medicine & biology* **28**, 1349-64 (2002).
126. Dalecki, D. Mechanical bioeffects of ultrasound. *Annual Review of Biomedical Engineering* **6**, 229-248 (2004).
127. Bigelow, T.A. et al. The Thermal Index Its Strengths, Weaknesses, and Proposed Improvements. *Journal of Ultrasound in Medicine* **30**, 714-734 (2011).
128. Barnett, S.B. et al. International recommendations and guidelines for the safe use of diagnostic ultrasound in medicine. *Ultrasound in Medicine and Biology* **26**, 355-366 (2000).
129. Chaussy, C. & Schmiedt, E. Shock wave treatment for stones in the upper urinary tract. *The Urologic clinics of North America* **10**, 743-50 (1983).
130. Miller, D.L. et al. Overview of Therapeutic Ultrasound Applications and Safety Considerations. *Journal of Ultrasound in Medicine* **31**, 623-634 (2012).
131. Barlinn, K. & Alexandrov, A.V. Sonothrombolysis in Ischemic Stroke. *Current Treatment Options in Neurology* **15**, 91-103 (2013).
132. Saqqur, M. et al. The Role of Sonolysis and Sonothrombolysis in Acute Ischemic Stroke: A Systematic Review and Meta- analysis of Randomized Controlled Trials and Case- Control Studies. *Journal of Neuroimaging* **24**, 209-220 (2014).
133. Birnbaum, Y. et al. Microparticle-containing oncotic solutions augment in-vitro clot disruption by ultrasound. *Thrombosis Research* **98**, 549-557 (2000).
134. van der Sluis, L.W.M., Versluis, M., Wu, M.K. & Wesselink, P.R. Passive ultrasonic irrigation of the root canal: a review of the literature. *International endodontic journal* **40**, 415-426 (2007).
135. Plotino, G., Pameijer, C.H., Grande, N.M. & Somma, F. Ultrasonics in endodontics: A review of the literature. *Journal of Endodontics* **33**, 81-95 (2007).
136. Machet, L. & Boucaud, A. Phonophoresis: efficiency, mechanisms and skin tolerance. *International Journal of Pharmaceutics* **243**, 1-15 (2002).
137. Kennedy, J.E. High-intensity focused ultrasound in the treatment of solid tumours. *Nature Reviews Cancer* **5**, 321-327 (2005).
138. Ter Haar, G. & Coussios, C. High intensity focused ultrasound: Physical principles and devices. *International Journal of Hyperthermia* **23**, 89-104 (2007).
139. Hu, Z. et al. Investigation of HIFU-induced anti-tumor immunity in a murine tumor model. *Journal of translational medicine* **5** (2007).

140. Peng, S. et al. Clinical utility of a microbubble-enhancing contrast ("SonoVue") in treatment of uterine fibroids with high intensity focused ultrasound: A retrospective study. *European Journal of Radiology* **81**, 3832-3838 (2012).
141. Grull, H. & Langereis, S. Hyperthermia-triggered drug delivery from temperature-sensitive liposomes using MRI-guided high intensity focused ultrasound. *Journal of Controlled Release* **161**, 317-327 (2012).
142. Hijnen, N., Langereis, S. & Grull, H. Magnetic resonance guided high-intensity focused ultrasound for image-guided temperature-induced drug delivery. *Advanced Drug Delivery Reviews* **72**, 65-81 (2014).
143. Broman, T. On Basic Aspects of the Blood-Brain Barrier. *Acta Psychiatrica Et Neurologica Scandinavica* **30**, 115-124 (1955).
144. Burgess, A. & Hynynen, K. Drug delivery across the blood-brain barrier using focused ultrasound. *Expert Opinion on Drug Delivery* **11**, 711-721 (2014).
145. Hynynen, K., McDannold, N., Vykhodtseva, N. & Jolesz, F.A. Noninvasive MR imaging-guided focal opening of the blood-brain barrier in rabbits. *Radiology* **220**, 640-646 (2001).
146. Nhan, T. et al. Drug delivery to the brain by focused ultrasound induced blood-brain barrier disruption: Quantitative evaluation of enhanced permeability of cerebral vasculature using two-photon microscopy. *Journal of Controlled Release* **172**, 274-280 (2013).
147. Huang, Q. et al. Effective Gene Transfer into Central Nervous System Following Ultrasound-Microbubbles-Induced Opening of the Blood-Brain Barrier. *Ultrasound in Medicine and Biology* **38**, 1234-1243 (2012).
148. Burgess, A. et al. Targeted Delivery of Neural Stem Cells to the Brain Using MRI-Guided Focused Ultrasound to Disrupt the Blood-Brain Barrier. *Plos One* **6** (2011).
149. Alkins, R. et al. Focused Ultrasound Delivers Targeted Immune Cells to Metastatic Brain Tumors. *Cancer Research* **73**, 1892-1899 (2013).
150. Konofagou, E.E. Optimization of the Ultrasound-Induced Blood-Brain Barrier Opening. *Theranostics* **2**, 1223-1237 (2012).
151. Lentacker, I., De Cock, I., Deckers, R., De Smedt, S.C. & Moonen, C.T. Understanding ultrasound induced sonoporation: Definitions and underlying mechanisms. *Advanced Drug Delivery Reviews* **72C**, 49-64 (2014).
152. Zhou, Y., Cui, J.M. & Deng, C.X. Dynamics of sonoporation correlated with acoustic cavitation activities. *Biophysical Journal* **94**, L51-L53 (2008).
153. Zhou, Y., Kumon, R.E., Cui, J.M. & Deng, C.X. The Size of Sonoporation Pores on the Cell Membrane. *Ultrasound in Medicine and Biology* **35**, 1756-1760 (2009).
154. Reddy, A., Caler, E.V. & Andrews, N.W. Plasma membrane repair is mediated by Ca2+-regulated exocytosis of lysosomes. *Cell* **106**, 157-169 (2001).
155. Draeger, A., Monastyrskaya, K. & Babiychuk, E.B. Plasma membrane repair and cellular damage control: The annexin survival kit. *Biochemical Pharmacology* **81**, 703-712 (2011).
156. Luzio, J.P. et al. Lysosome-endosome fusion and lysosome biogenesis. *Journal of Cell Science* **113**, 1515-1524 (2000).
157. Li, T.L., Tachibana, K., Kuroki, M. & Kuroki, M. Gene transfer with echo-enhanced contrast agents: Comparison between Albunex, Optison, and Levovist in mice - Initial results. *Radiology* **229**, 423-428 (2003).
158. Tsunoda, S. et al. Sonoporation using microbubble BR14 promotes pDNA/siRNA transduction to murine heart. *Biochemical and Biophysical Research Communications* **336**, 118-127 (2005).
159. Lentacker, I. et al. Lipoplex-loaded microbubbles for gene delivery: A Trojan horse controlled by ultrasound. *Human Gene Therapy* **18**, 1046-1046 (2007).
160. Geers, B., Dewitte, H., De Smedt, S.C. & Lentacker, I. Crucial factors and emerging concepts in ultrasound-triggered drug delivery. *Journal of Controlled Release* **164**, 248-255 (2012).
161. Phillips, L.C., Klibanov, A.L., Wamhoff, B.R. & Hossack, J.A. Localized ultrasound enhances delivery of rapamycin from microbubbles to prevent smooth muscle proliferation. *Journal of Controlled Release* **154**, 42-49 (2011).
162. Kooiman, K. et al. Oil-filled polymer microcapsules for ultrasound-mediated delivery of lipophilic drugs. *Journal of Controlled Release* **133**, 109-118 (2009).

163. Sun, R.R., Noble, M.L., Sun, S.S., Song, S. & Miao, C.H. Development of therapeutic microbubbles for enhancing ultrasound-mediated gene delivery. *Journal of Controlled Release* **182**, 111-120 (2014).
164. Vannan, M. et al. Ultrasound-mediated transfection of canine myocardium by intravenous administration of cationic microbubble-linked plasmid DNA. *Journal of the American Society of Echocardiography* **15**, 214-218 (2002).
165. Wang, D.S. et al. Cationic versus Neutral Microbubbles for Ultrasound-mediated Gene Delivery in Cancer. *Radiology* **264**, 721-732 (2012).
166. Ferrara, K., Pollard, R. & Borden, M. Ultrasound microbubble contrast agents: Fundamentals and application to gene and drug delivery. *Annual Review of Biomedical Engineering* **9**, 415-447 (2007).
167. Geers, B. et al. Self-assembled liposome-loaded microbubbles: The missing link for safe and efficient ultrasound triggered drug-delivery. *Journal of controlled release : official journal of the Controlled Release Society* **152**, 249-56 (2011).
168. Lentacker, I., Geers, B., Demeester, J., De Smedt, S.C. & Sanders, N.N. Design and Evaluation of Doxorubicin-containing Microbubbles for Ultrasound-triggered Doxorubicin Delivery: Cytotoxicity and Mechanisms Involved. *Molecular Therapy* **18**, 101-108 (2010).
169. Cool, S.K. et al. Coupling of drug containing liposomes to microbubbles improves ultrasound triggered drug delivery in mice. *Journal of controlled release : official journal of the Controlled Release Society* **172**, 885-93 (2013).
170. Lentacker, I. et al. New strategies for nucleic acid delivery to conquer cellular and nuclear membranes. *Journal of Controlled Release* **132**, 279-288 (2008).
171. Vandenbroucke, R.E., Lentacker, I., Demeester, J., De Smedt, S.C. & Sanders, N.N. Ultrasound assisted siRNA delivery using PEG-siPlex loaded microbubbles. *Journal of Controlled Release* **126**, 265-273 (2008).
172. Lentacker, I., De Smedt, S.C. & Sanders, N.N. Drug loaded microbubble design for ultrasound triggered delivery. *Soft Matter* **5**, 2161-2170 (2009).

Chapter 2

Choose your models wisely: How different murine bone marrow-derived dendritic cell protocols influence the success of nanoparticulate vaccines *in vitro*

This chapter is published as:

Heleen Dewitte[1,*], Rein Verbeke[1,*], Karine Breckpot[2], Roosmarijn E. Vandenbroucke[3], Claude Libert[3], Stefaan C. De Smedt[1] and Ine Lentacker[1]. Choose your models wisely: How different murine bone marrow-derived dendritic cell protocols influence the success of nanoparticulate vaccines *in vitro*. *Journal of Controlled Release,* **195**, 138-146 (2014).
(DOI: 10.1016/j.jconrel.2014.06.024)

[*]Both authors contributed equally to this work

[1]Laboratory for General Biochemistry and Physical Pharmacy, Faculty of Pharmaceutical Sciences, Ghent University, Ottergemsesteenweg 460, 9000 Ghent, Belgium

[2]Laboratory of Molecular and Cellular Therapy, Department of Biomedical Sciences, Medical School of the Vrije Universiteit Brussel (VUB), Laarbeeklaan 103, 1050 Jette, Belgium

[3]Inflammation Research Center, VIB, Technologiepark 927, 9052 Ghent, Belgium

ABSTRACT

Dendritic cell (DC)-based cancer vaccination has shown great potential in cancer immunotherapy. As a result, novel nanoparticles that aim to load DCs with tumor antigens are being developed and are evaluated *in vitro*. For this, murine bone marrow-derived DCs (BM-DCs) are most commonly used as model DCs. However, many different protocols exist to generate these cells. Therefore, we investigated to what extent different BM-DC culture protocols impact on the immunobiology of the cells, as well as their response to particulate antigens. We evaluated four different BM-DC protocols with two main variables: bovine serum and cytokine combinations. Our results show distinct differences in yield, phenotypical maturation status and the production of immune stimulatory and immune suppressive cytokines by the different BM-DCs. Importantly, we demonstrate that the antigen-loading of these different BM-DCs *via* transfection with mRNA lipoplexes results in large differences in transfection efficiency as well as in the capacity of mRNA-transfected BM-DCs to stimulate antigen-specific T cells. Thus, it is clear that the BM-DC model can have significant confounding effects on the evaluation of novel nanoparticulate vaccines. To take this into account when testing novel particulate antigen-delivery systems in BM-DC models, we propose to (1) perform a thorough immunological characterization of the BM-DCs and to (2) not only judge a particle's potential in cancer vaccination based on transfection efficiency, but to include an evaluation of functional end-points such as T cell activation.

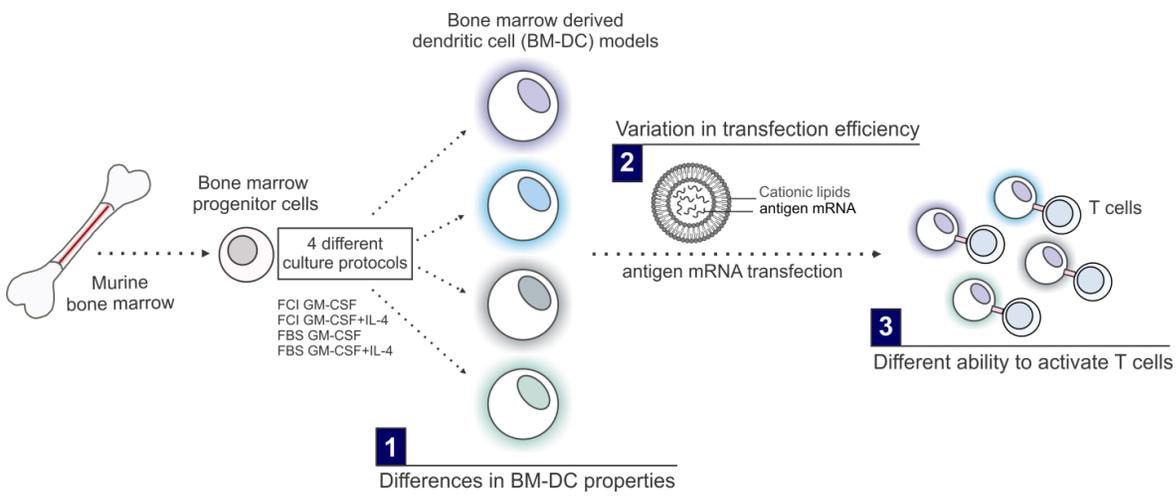

INTRODUCTION

As discussed in **Chapter 1**, novel nanoparticulate vaccines are being developed to deliver tumor associated antigens (TAAs) and immune adjuvants to dendritic cells (DCs) *in vivo*. In search of novel strategies for effective TAA-loading of DCs to combat cancer or viral infections, experiments are generally performed on *in vitro* generated DCs. The main reason for this is the low number of *in vivo* DCs that can be isolated from different tissues[1-3]. As a result, different protocols were established for the *in vitro* production of DCs, generated from murine bone marrow precursors or from the peripheral blood monocytes found in human blood[4-7]. By culturing these murine and human monocytic precursors for a number of days in the presence of appropriate cytokines, their differentiation into murine bone marrow-derived DCs (BM-DCs), and human monocyte-derived DCs (MoDCs) will be induced. This way, convenient DC models for *in vivo* studies of the DC functionality, phenotype, immunogenic potential and antigen-presentation capacity were established. Importantly, these models gained in popularity among researchers who are developing novel particulate systems for the delivery of protein or nucleic acid antigens to DCs. However, it should be noted that even though these methods result in the generation of large numbers of cells with DC-like properties, they do not seem to correspond to any of the DC subsets that under normal circumstances populate the mouse lymph nodes. Instead, they rather, but not completely, resemble "*emergency*" or "*inflammatory*" DCs that only occur in inflamed lymph nodes[8-10]. Therefore, *in vitro* generated monocyte-derived DCs need to be considered as simplified models for a complex *in vivo* situation, and conclusions from experiments using these cells should be drawn with the necessary caution.

An additional critical factor that complicates the use of DCs *in vitro*, is the plethora of protocols that are available for the generation of these cells. The differentiation of bone marrow into BM-DCs can be achieved with either GM-CSF (granulocyte-macrophage colony-stimulating factor) alone or in combination with IL-4 (interleukin-4), but also other factors, including Flt3L (FMS-related tyrosine kinase 3 ligand) or IL-3 have been employed at different concentration ratios[8, 11, 12]. Changing the cocktail and concentrations of cytokines can result in major differences in DC phenotype. In addition, other factors such as cell culture medium, the timeframe for DC generation from bone marrow precursors, additional purification steps, mouse age and especially growth factors that are present in the sera that are routinely added to the culture medium may decide the type of BM-DCs that are produced. Obviously, these differences make it difficult to compare results obtained in different *in vitro* models. For one, the variability of BM-DCs generated *via* different protocols has already lead to substantial debate on an immunological level. For instance, Lutz et al. observed major differences in the immune stimulating properties of BM-DCs based on the serum and cytokine cocktails used during their differentiation from bone marrow cells[13, 14].

Importantly, this variability in BM-DC protocols can also be observed in research on novel antigen-delivery systems. In recent years, numerous reports on the design of novel biomaterial systems to deliver antigenic material to DCs, packaged in nano- and microparticles have been published. These delivery vehicles are becoming increasingly complex, often packaging antigen-coding nucleic acid sequences (plasmid DNA and mRNA) instead of proteins or peptide antigens and aiming for controlled or triggered antigen-delivery to antigen-presenting cells[15-17]. In the initial evaluation of these particles, BM-DCs are often used as model DCs. And here as well, a vast diversity in the BM-DC generation protocols is observed. We hypothesize that these changes in the culture protocols for BM-DCs *in vitro* have important repercussions for their response to particulate antigens, and that a careful choice of the BM-DC protocol is warranted in order to give newly designed delivery systems a full chance of success.

In this chapter, we aim to investigate the effect of using four differently generated model DCs on their immunological properties, as well as their response to particulate antigen. More specifically, we chose to use lipoplexes containing antigen-coding mRNA. mRNA is particularly interesting for the delivery of antigens to DCs, as it offers several advantages: (a) by introducing antigen mRNA, the antigenic protein will end up in the DC cytoplasm and will therefore preferentially be presented in MHC-I which results in de induction of $CD8^+$ T cells; (b) by introducing the nucleic acid sequence encoding an entire protein, immune responses against multiple epitopes can be induced; (c) mRNA is translated in the cytoplasm and therefore does not need to cross the nuclear membrane, in contrast to plasmid DNA and (d) mRNA is not considered as a gene therapeutic, as it does not encompass the risk of genomic integration[18]. For these reasons, we used particles consisting of mRNA complexed to cationic lipids, and evaluated their use in different BM-DC models.

MATERIALS AND METHODS

Dendritic cell culture

Primary murine BM-DC cultures were generated from C57BL/6 mice. Female C57BL/6 mice were purchased from Harlan Laboratories and housed in an SPF facility according to the regulations of the Belgian law and the local Ethical Committee. Mice were euthanized and bone marrow was flushed from the hind limbs. The red blood cells in the resulting single cell suspension were lysed (Pharm Lyse Buffer, BD Biosciences, Erembodegem, Belgium) and the collected cells were seeded in 100 mm Not TC-Treated polystyrene Culture Dishes (Corning®, Amsterdam, The Netherlands) at $2x10^6$ cells ml^{-1} in 15 ml. The cell culture medium used was RPMI 1640 (Gibco-Invitrogen, Merelbeke, Belgium) supplemented with penicillin/streptomycin/L-glutamine (1%, Gibco-Invitrogen) and β-mercaptoethanol (50 μM, Gibco-Invitrogen) and 5% serum. Two different types of serum were used: Fetal Bovine Serum

(FBS 5%, Batch n°RSE30013, HyClone™, Pierce, Rockford, IL, USA) and FetalClone™ I (FCI 5%, Batch n°AXD36551, HyClone™). To promote differentiation of the monocytes into BM-DCs, cytokines were added: GM-CSF alone (20 ng ml^{-1}, Peprotech, Rock Hill, NJ) or a combination of GM-CSF (10 ng ml^{-1}) with IL-4 (10 ng ml^{-1}, Peprotech). On day 3 of the culture, an additional 15 ml complete cytokine-supplemented culture medium containing GM-CSF (40 ng ml^{-1}) or GM-CSF and IL-4 (both at 20 ng ml^{-1}) was added. On day 5, all cells were collected by centrifugation (5min at 300 *g*), resuspended in the appropriate culture medium at 10^6 cells ml^{-1} and seeded in 24 well plates for experiments ($5x10^5$ cells per well). For every experiment, 1 single batch of bone marrow cells was used to generate the 4 different BM-DC cultures in order to exclude bias due to animal-related effects.

Cell yield, viability and purity

At day 5, when the cells were collected from the petri dishes, cell yield was determined by counting the collected cells with trypan blue exclusion of dead cells (Sigma-Aldrich, Bornem, Belgium). DC purity and cell viability were evaluated the next day, *via* anti-CD11c-allophycocyanin (APC) surface staining (eBiosciences, Vienna, Austria) and a SYTOX® green nucleic acid stain (Molecular Probes/Invitrogen, Merelbeke, Belgium), respectively. The cells were collected from the wells, washed in FACS buffer (phosphate buffered saline (PBS, Gibco-invitrogen), supplemented with 5% bovine serum albumin, BSA (Sigma-Aldrich, Bornem, Belgium)) and incubated with a staining buffer containing both the antibody and 45 nM SYTOX® green for 30min at 4°C. After additional washing steps, the cells were analyzed by flow cytometry using a FACSCalibur and CellQuest Pro software (BD Biosciences).

Microscopy

Transmission microscopy images of the cells obtained *via* the different BM-DC generation protocols were recorded using a Nikon C1si confocal laser scanning module attached to a motorized Nikon TE2000-E inverted microscope (Nikon Benelux, Brussels, Belgium), equipped with a Plan APO 40x DIC water immersion objective lens (Nikon) and suitable optical elements to obtain differential interference contrast (DIC) transmission images. For this, the cells were seeded in 35 mm MatTek glass bottom culture dishes (MatTek Corporation, MA, USA) on day 5 of the culture, and imaged on day 6.

BM-DC phenotype analysis

The effect of different sera or cytokine combinations on the DC phenotype was investigated by examining the expression of the maturation markers CD40, CD86 and MHC-II on the DC surface. For this, the cells (at day 6 of the culture) were either untreated, or supplemented with *Escherichia coli*-derived lipopolysaccharide (1 µg ml^{-1} LPS, Sigma-Aldrich)

to induce maturation. 24h after LPS addition, the cells were collected, washed with flow buffer and surface stained for the DC marker CD11c-APC in combination with staining for either CD40-phycoerythrin (PE), CD86-PE or MHC-II-fluorescein isothiocyanate (FITC) (all BD Bioscience) for 30min at 4°C. After additional washing steps, the cells were analyzed by flow cytometry.

mRNA

Luciferase, eGFP, and ovalbumin (OVA) mRNA were produced by *in vitro* transcription from pBlue-Luc-A50, pGEM4Z-GFP-64A and pGEM-Ii80tOVA plasmids[19]. The plasmids were purified using a QIAquick PCR purification kit (Qiagen, Venlo, The Netherlands) and linearized using *Dra* I (for the pBlue plasmid) or *Spe* I (for the pGEM plasmids) restriction enzymes (Promega, Leiden, The Netherlands). Linearized plasmids were used as templates for the *in vitro* transcription reaction using the T7 mMessage mMachine kit (Ambion, Life Technologies, Ghent, Belgium). The resulting capped and polyadenylated mRNAs were purified by DNase I digestion, LiCl precipitation and washed with 70% ethanol. The mRNA concentration was determined by measuring the absorbance at 260 nm. mRNAs were stored in small aliquots at -80°C at a concentration of 1 µg μl^{-1}.

mRNA lipoplexes

Cationic liposomes, containing 50% DOTAP (1,2-dioleoyl-3-trimethylammonium-propane) and 50% DOPE (1,2-dioleoyl-*sn*-glycero-3-phosphoethanolamine) (both Avanti Polar Lipids, Alabaster, AL) were prepared by transferring the appropriate amounts of lipids, dissolved in chloroform into a round-bottom flask. To prepare fluorescent mRNA lipoplexes, 1 mol.% CholEsteryl-BODIPY® FL C12 (Molecular Probes/Invitrogen) was added. The chloroform was evaporated under nitrogen and the resulting lipid film was rehydrated in RNase-free water (Ambion) to obtain a final lipid concentration of 1 mg ml^{-1}. The resulting DOTAP/DOPE liposomes were sonicated for 15min in a bath sonicator (Branson Ultrasonics, Dansbury, USA), after which they were mixed with mRNA to obtain mRNA lipoplexes at a cationic lipid-to-mRNA charge (N/P) ratio of 10 in OptiMem® (Gibco-Invitrogen). The produced liposomes and lipoplexes were subjected to a size and zeta potential quality control prior to use, using a Malvern Zetasizer nano-ZS (Malvern Instruments Ltd, Worcestershire, UK).

mRNA lipoplex loading and transfection of DCs

Uptake and transfection efficiency of mRNA lipoplexes were evaluated in the four differently generated BM-DCs. Lipoplex loading was performed on BM-DCs at day 6 in 24 well plates. The cell culture medium was removed and the mRNA lipoplexes, dispersed in OptiMem® were added for 2h at 37°C (1 µg mRNA per well, N/P=10). For uptake experiments, fluorescent

mRNA lipoplexes containing luciferase mRNA were used. After the 2h incubation period, the cells were collected, washed with FACS buffer and extracellular fluorescence was quenched using trypan blue (1:1 diluted in FACS buffer for 5 min at RT). Then, the cells were washed, surface stained for CD11c-APC and the uptake of fluorescent mRNA lipoplexes was evaluated by flow cytometry. The transfection efficiency of the lipoplexes was evaluated using eGFP mRNA, and after the 2h incubation of the BM-DCs with the particles in OptiMem®, the cells were re-cultured in the appropriate cell culture media. After 24h incubation at 37°C, the eGFP-transfected cells were collected, surface stained for CD11c-APC and expression of eGFP was analyzed by flow cytometry. Untreated cells served as a negative control.

In vitro T cell activation assay

In order to assess the potential of the BM-DCs to prime antigen-specific $CD8^+$ T cells, an *in vitro* OT-I activation assay was performed. In this assay, OVA lipoplex transfected DCs were co-cultured with OT-I cells, which have a transgenic T cell receptor that recognizes the MHC-I restricted OVA-peptide SIINFEKL. Untreated and eGFP-transfected DCs served as negative controls. As a positive control, DCs loaded with SIINFEKL peptide (1 µg ml^{-1}, Eurogentec, Seraing, Belgium) were used. 5h after transfection, the cells were matured for 2h with LPS. Then, the DCs were collected, washed, and seeded per 10^4 DCs in a U-bottom 96 well plate (Falcon, BD Bioscience), for co-incubation with 10^5 OT-I cells (derived from the spleens of OT-I transgenic mice, Charles River). After 5 days, the cells were collected, surface stained for CD8-APC (BD Pharmingen) and the T cell activation marker CD25-PE (MACS Miltenyi, Leiden, The Netherlands) and analyzed by flow cytometry.

ELISA

Supernatants of untreated and LPS-stimulated DCs were screened for the presence of IL-10 and IL-12p70. Supernatants of DC-T-cell co-cultures were assayed for lFNγ and IL-2. Cytokine concentrations were measured *via* ELISA (all Ready-SET-Go!® ELISA kits, eBioscience) according to the manufacturer's instructions.

Statistical analysis

All data are presented as mean ± standard deviation (SD). Presented data are representative for at least 3 independent experiments performed on cells derived from the bone marrow of different donor mice, except for the uptake experiments. Statistical analyses were performed using a one-way ANOVA with Bonferroni correction.

RESULTS

DC yield, purity and viability

We tested a limited number of variations that are commonly encountered in murine BM-DC generation protocols. Based on previous results, we chose to use BM-DCs at day 6 of the culture as this, in our hands, results in the largest cell yield and the lowest percentages of mature DCs in untreated samples. A first variable is the cytokine combination that is used to induce differentiation into BM-DCs. Initially, co-supplementation with GM-CSF and IL-4 was used, whereas more recent studies are performed on cells that were generated with GM-CSF alone. In order to investigate the influence of IL-4, we generated BM-DCs with cytokine supplementation of GM-CSF in the presence or absence of IL-4. A second important parameter is the serum that is added to the BM-DC culture medium as a source of nutritional and growth factors. In general, using different batches of fetal bovine serum (FBS) is known to cause variation in cell viability and growth rates due to large batch-to-batch variation in the levels of both defined and undefined growth factors present. Besides batch differences, varying types of serum have been used and tested for BM-DC generation. Therefore, we chose to use two different types of sera within the cell culture medium: regular FBS and FetalClone™ I serum (FCI). According to the manufacturers' information, the latter is supplemented with additional growth factors, but contains lower levels of certain immunosuppressive growth factors such as transforming growth factor beta-1 (TGF-β1). By changing these two parameters, we obtained four different protocols for the generation of BM-DCs and first investigated the influence of these parameters on cell yield, cell viability and DC purity.

A first observation after 6 days of culturing murine bone marrow cells in the four different culture media, was the difference in cell number. When the growth media are supplemented with FCI, expansion of the cell number is observed, with an 80% increase in cell count when GM-CSF is used alone, and 40% increase when a combination of GM-CSF and IL-4 is used. In the case of FBS-supplementation, on the other hand, the cell number decreases after 6 days of culture, resulting in a 40% and even 60% reduction in cell count when cultured when GM-CSF alone or combined with IL-4, respectively.

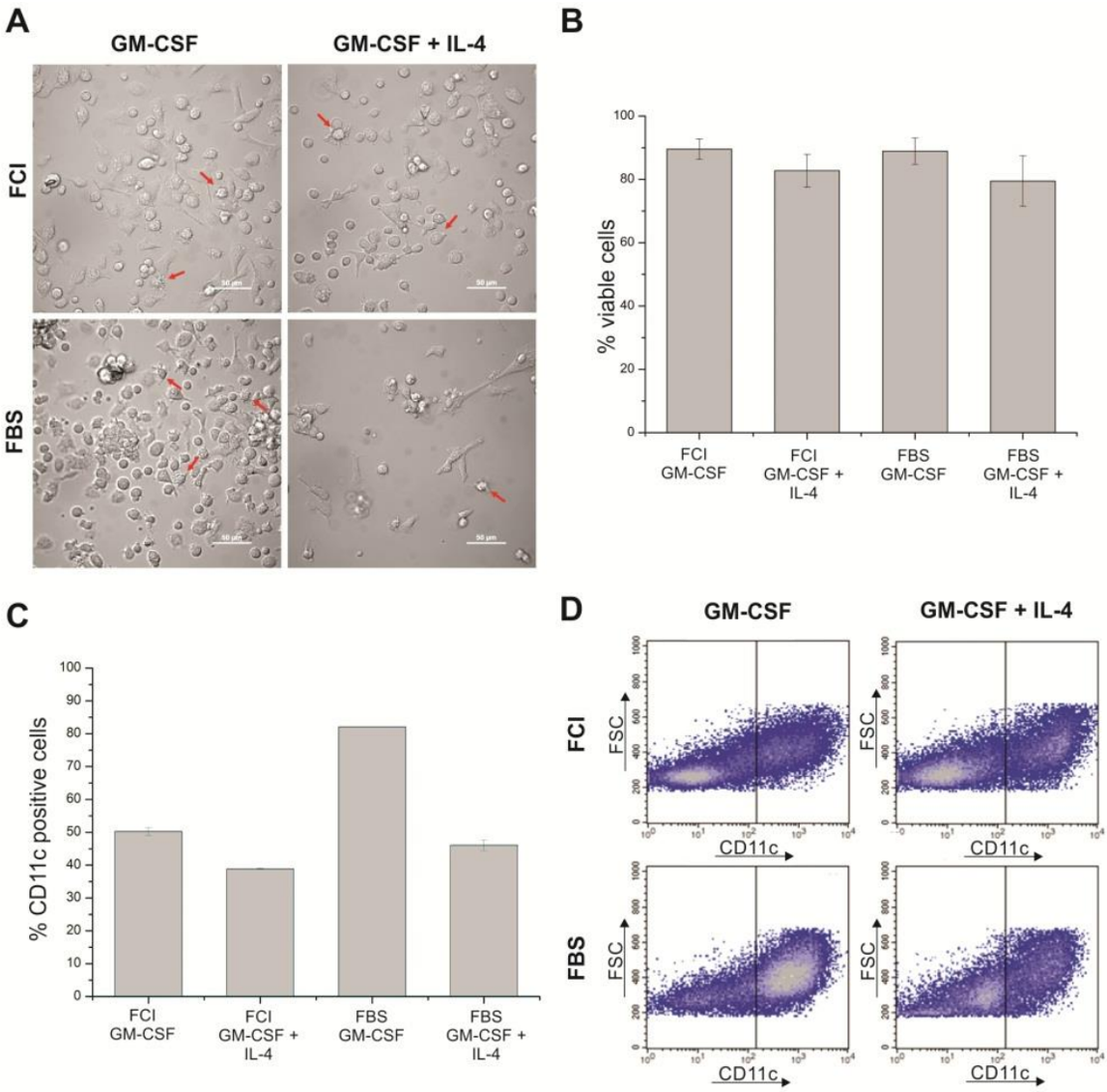

Figure 1: Morphology, viability and purity of different BM-DC cultures.

Images show (A) Transmission microscopy images of BM-DCs generated *via* the four different protocols on day 6 of the culture. Red arrows indicate cells with a DC-like appearance; (B) Graphic representation of cell viability measured *via* SYTOX® green nucleic acid staining (n=3); (C) Graph showing the purity of the BM-DC cultures based on staining for CD11c (n=6), with representative scatterplots shown in (D). There were no significant differences between the BM-DC cultures with respect to cell viability (B). Regarding the DC purity (C), the observed differences were all statistically significant (p<0.001).

In all cases, the resulting cell population is quite heterogeneous, as can be seen in transmission microscopy images in **Figure 1A**. These show that in all four BM-DC cultures, the cells can grow both adherent to the petri dish surface, as well as suspended within the culture medium. In addition, the size and shape of the cells can largely vary. In all populations, a fraction of the cells display a DC-like appearance, with dendrites protruding from the cell membranes. To evaluate the viability of the cells after 6 days of culture, a SYTOX® green nucleic acid stain

was performed. As shown in **Figure 1B**, although there is a trend towards lower cell viability when IL-4 is added to the medium, the observed differences were not significant, and for all protocols tested, the percentage of viable cells exceeded 80%.

In order to determine exactly how many BM-DCs can be obtained from each of the four culture circumstances, the cells were surface stained for the DC maker CD11c and analyzed by flow cytometry. The results in Figure 1C and 1D indeed support the microscopic ascertainments, indicating that a portion of the cells in the population expresses CD11c and can therefore be identified as BM-DCs. A percentage of CD11c positive cells over 80% can be reached when cells are cultured in medium supplemented with FBS and GM-CSF alone, whereas the DC purity in the other cultures is limited to 50%. When these purity results are combined with the differences in total cell yield at day 6 of the culture, FCI-supplemented medium will provide the largest number of DCs, and GM-CSF alone is superior over a combination of GM-CSF and IL-4.

Often, researchers selectively collect either the suspension or the adherent fraction to use in their experiments. In our hands, $CD11c^+$ BM-DCs were found at high percentages in both suspension and adherent fractions, therefore, we chose to collect and use all cells for further experiments.

DC phenotype

An important phenotypical parameter that can provide information on the immunological properties of BM-DCs, is their maturation status. During maturation, DCs shift in function from antigen-uptake to antigen-presentation, a process that is accompanied by increased expression of different molecules that are required for effective antigen-presentation. As their presence is a crucial prerequisite for DCs to become effective T cell activators, we evaluated to what extent well-known maturation markers CD40, CD86 and MHC-II are present on the surface of the BM-DCs generated *via* the different protocols. For this, both untreated (blank) and BM-DCs where maturation was induced by co-incubating them with bacteria-derived lipopolysaccharide (LPS) were surface stained for both the DC marker CD11c and the different maturation markers.

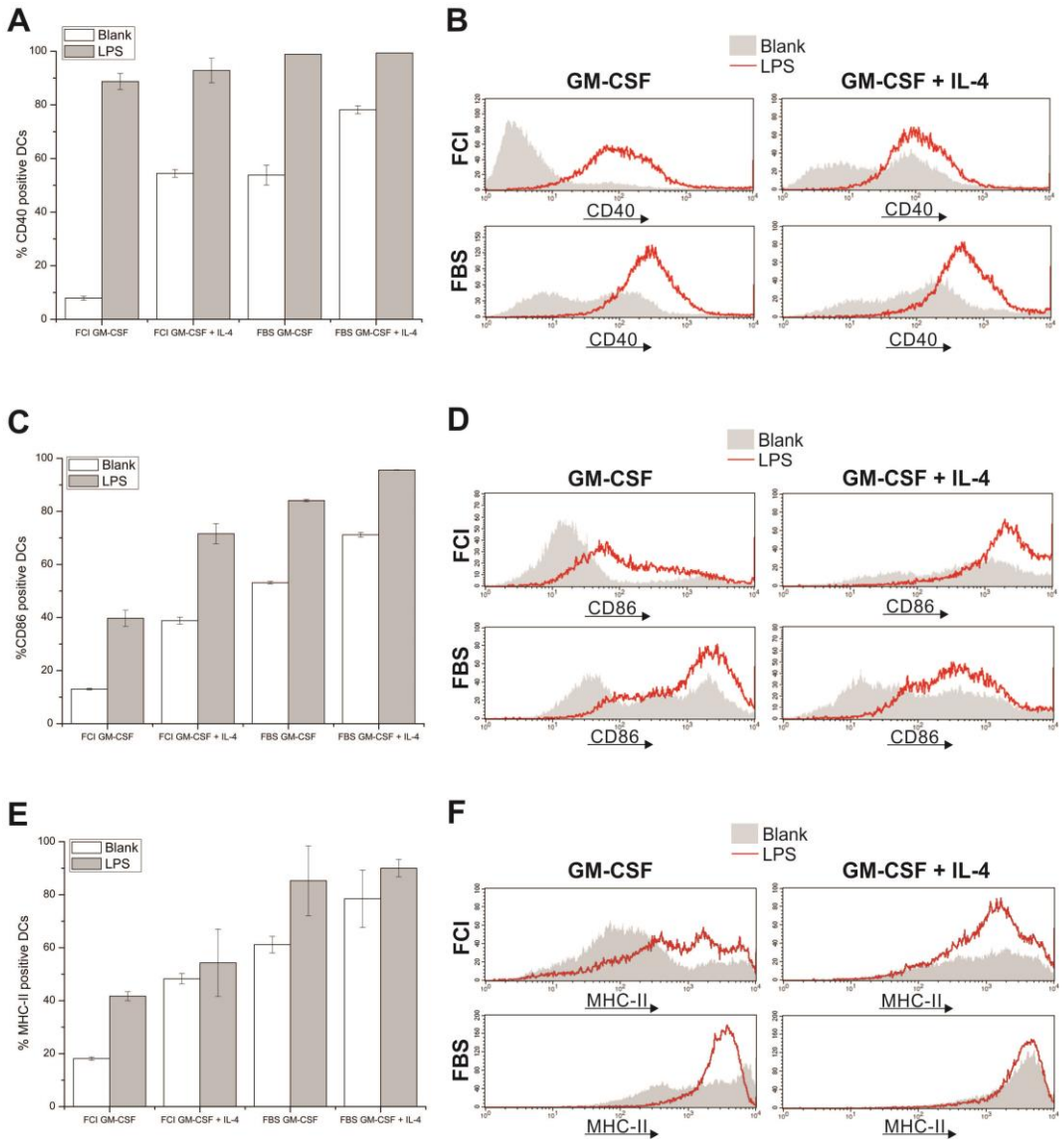

Figure 2. Expression of maturation markers by blank and LPS-stimulated DCs. Untreated (blank) and LPS-stimulated DCs (LPS) were analyzed for the expression of different maturation markers. DCs were gated based on CD11c staining. Images show (A) percentages of CD40 expressing DCs with (B) representative histograms; (C) percentages of CD86 expressing DCs with (D) representative histograms and (E) percentages of MHC-II expressing DCs with (F) representative histograms. (*n*=3)

The results of flow cytometric analysis can be found in **Figure 2**. In the case of the blank DCs, the same trends could be observed for all maturation markers tested. First of all, BM-DCs generated in the presence of IL-4 exhibit a more mature phenotype, which evidences that IL-4 enhances the maturation process. Secondly, changing the serum in the cell culture media also has a significant effect on the phenotype of the generated BM-DCs. In general, supplementation with FBS results in increased maturation marker expression compared to FCI. For effective activation of effector cytotoxic T lymphocytes by DCs, a fully mature DC phenotype is crucial. Even more so, numerous researchers have reported that antigen presentation by immature or partially mature DCs will induce antigen-specific tolerance rather than immunity[20]. Therefore,

we studied the phenotypical properties of the different BM-DC cultures after overnight incubation with LPS, a known toll-like receptor 4 (TLR4) ligand, which is expected to induce complete maturation. Indeed, in all of the BM-DC populations, there is a marked increase in the maturation marker expression level. However, these maximal levels vary gravely. Especially for of BM-DCs cultured with FCI and GM-CSF alone, the percentage of fully mature CD86 and MHC-II expressing cells is limited to 40%, whereas percentages over 90% can be reached when FBS is used. For CD40 expression, differences between the different LPS-stimulated BM-DCs are less pronounced.

Besides expression of molecules needed for antigen presentation and T cell activation on the DC surface, the cells also produce cytokines that can skew T cell responses towards immunity or tolerance. We evaluated the production of two different cytokines by means of ELISA assays: the inflammatory cytokine IL-12p70, which is crucial for the activity of effector T cells and natural killer cells and on the other hand, the immune suppressive cytokine IL-10. As shown in **Figure 3A**, the production of IL-12p70 corresponds nicely to the maturation marker expression by the cells. IL-4 addition as well as utilization of FBS for the culture medium will enhance the IL-12p70 production. The production of IL-10, which is a mediator of immune tolerance, also points towards a preferable situation when FBS and a combination of GM-CSF and IL-4 are used, as these both lead to a significant reduction in IL-10 production (**Figure 3B**).

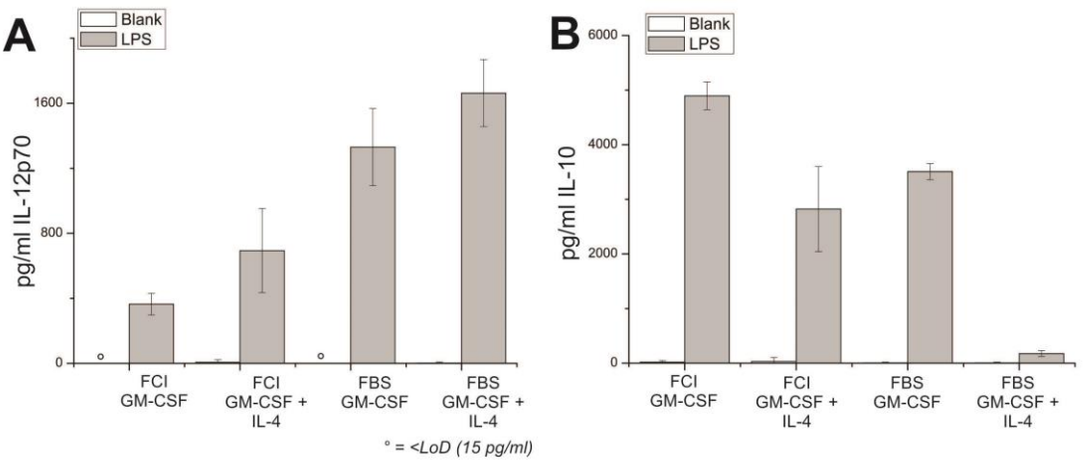

Figure 3. Cytokine expression by untreated and LPS-stimulated DCs.

DC culture supernatants were collected after 24h of incubation in blank or LPS-supplemented culture medium. The supernatants were assayed for the immunostimulatory cytokine IL-12p70 (A) as well as the immune suppressive IL-10 (B). Graphs are summaries of 2 independent experiments (*n*=6).

mRNA lipoplex uptake and transfection potential

The previous experiments have exposed large differences in BM-DC yield, phenotype and cytokine production, when the cells are cultured *via* different protocols. Importantly, all of these protocols have been used to generate BM-DCs for the evaluation of novel antigen-delivery systems designed for potential use in DC-based vaccination. Therefore, we wanted to investigate to what extent the choice of BM-DC model could influence the results obtained with particulate antigens. As a model antigen-delivery system, we chose mRNA lipoplexes, since mRNA is becoming increasingly investigated as a source of antigen, and this requires more of the DCs' own machinery for translation and presentation of the antigens, compared to the use of protein- or peptide-antigens[21]. For the evaluation of such nucleic acid vaccines *in vitro*, transfection efficiency is employed as one of the main parameters and this can make or break the chance for further success. Therefore, we investigated if changes in the BM-DCs culture protocols influence the uptake and transfection potential of mRNA lipoplexes.

We prepared DOTAP/DOPE-lipoplexes with a cationic lipid-to-mRNA charge (N/P) ratio of 10. At this N/P ratio, complete complexation of mRNA is observed. This was supported by zeta potential measurements, which exhibited a drop in surface charge, from 64 ± 6 mV for the cationic liposomes to 51 ± 7 mV after mRNA complexation to the lipids. mRNA complexation resulted in a ~ 1.5 fold increase in mean particle size, as determined by dynamic light scattering (DLS) measurements. Mean particle sizes for liposomes and lipoplexes were 177 nm and 274 nm with a polydispersity index of 0.3 for both particles.

Overall, DCs exhibiting a more mature phenotype are expected to be less efficient in endocytosis and phagocytosis. This can be related to their function: mature DCs focus on antigen presentation, rather than antigen uptake[22]. To evaluate to what extent this affects mRNA lipoplex uptake by the cells, we incubated the different BM-DC cultures with fluorescently labeled mRNA lipoplexes. After 2h of incubation, we evaluated the internalization of the mRNA lipoplexes by means of flow cytometry. We observed an efficient uptake of the nanoparticles by the cells: in all BM-DC models tested, the percentage of lipoplex-loaded CD11c-positive cells was over 96%. However, when looking at the amount of intracellular mRNA lipoplexes, we could observe large differences in the mean fluorescence intensity (MFI) between the different BM-DC models, as shown in **Figure 4A**. As could be expected, the extent of nanoparticle uptake nicely correlated to the phenotypical maturation of the cells: more mature cells were less efficient in engulfing the fluorescent mRNA lipoplexes.

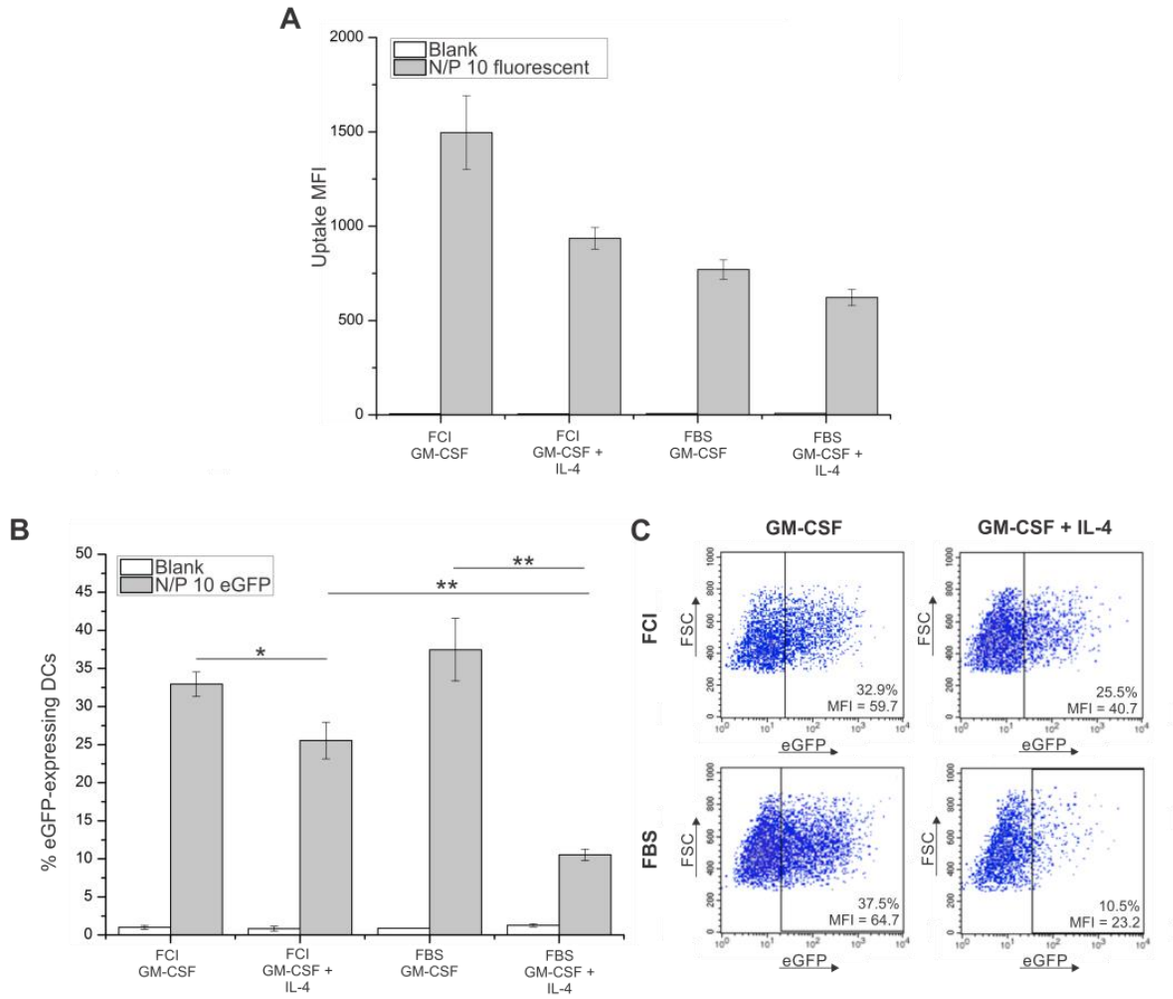

Figure 4. Uptake and transfection efficiency of mRNA lipoplexes.

(A) MFI of BM-DCs after 2h incubation with fluorescently labeled mRNA lipoplexes. Untreated cells served as blanks (n=6). (B) percentages of eGFP transfected DCs 24h after incubation with mRNA lipoplexes. Representative flow cytometry scatterplots are shown in (C). DCs were gated based on CD11c surface staining.

Data represent mean ± SD. (*n*=3, *p<0.05, **p<0.01).

In order to evaluate and to compare the efficiency of mRNA lipoplexes to transfect the different generated BM-DCs, mRNA encoding enhanced green fluorescent protein (eGFP) was used. eGFP mRNA lipoplexes were added to the cells as described in the materials and methods section. After overnight incubation, DCs were surface stained for CD11c and levels of eGFP expression were evaluated by flow cytometry. The results of the flow cytometry analysis are presented in **Figure 4B-C**. Each DC culture was significantly transfected, but transfection efficiencies differed greatly from one culture to another, ranging from minimally 10% and maximally 37%. Clearly the choice of the BM-DC generation protocol highly influences the transfection efficiency of mRNA lipoplexes. Interestingly, for both sera tested the addition of IL-4 resulted in a significant reduction in transfection. Furthermore, this was more profound in the FBS-supplemented culture, which would suggest an additional influence of FBS-supplemented

medium compared to FCI-containing medium. When GM-CSF was used alone, no significant difference in transfection efficiency was observed between the DCs cultured in FBS or FCI.

In vitro T-cell activation

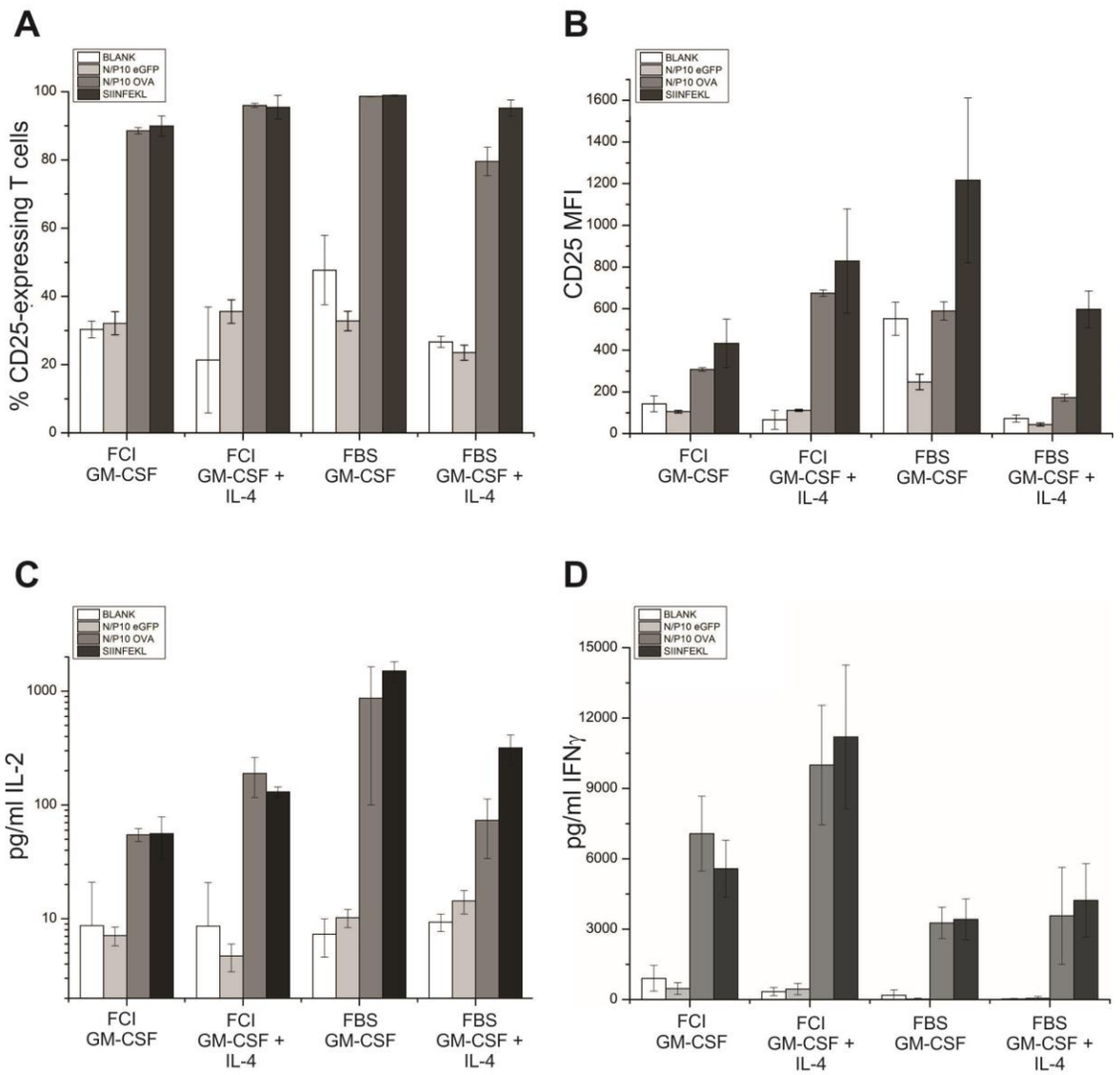

Figure 5. Antigen-specific T cell activation by mRNA lipoplex transfected DCs. OT-I T cells were co-cultured with DCs transfected with eGFP or OVA mRNA. Blank and SIINFEKL-loaded DCs served as negative and positive controls respectively. After 5 days, T cell activation was evaluated by measurement of CD25 expression and cytokine measurements. Figures show (A) % of CD25 positive OT-I T cells with (B) corresponding CD25 mean fluorescence intensity (MFI); (C) IL-2 production and (D) IFNγ production. *n*=3 for all experiments. (Statistical analysis is given in Figure 6)

The key feature of DCs is their capacity to activate antigen-specific T cells, and to induce their differentiation into effector T cells. Since cancer immunotherapy mainly focuses on the induction of CTL responses directed against the tumor cells, we wished to evaluate the potential of different BM-DCs, loaded with mRNA lipoplexes, to induce antigen-specific $CD8^+$ T cell activation. For this, we performed an OT-I T cell activation assay. OT-I cells carry a transgenic CD8 T cell receptor which specifically recognizes the MHC-I restricted OVA peptide SIINFEKL. Therefore, if these OT-I cells are stimulated by mature DCs that present SIINFEKL in the context of MHC-I, these cells will be activated. This activation is accompanied by an increased expression of CD25 on the T cell surface.

As demonstrated in **Figure 5A**, all BM-DCs that were loaded with SIINFEKL peptide (positive control) were capable of inducing expression of CD25 in over 90% of OT-I cells. Changing cytokines or serum merely has a slight influence on the percentage of CD25 positive OT-I cells after 5 days of co-culture. When antigens were loaded into the DCs *via* mRNA lipoplexes, CD25 expression is comparable to the SIINFEKL positive control, indicating extensive antigen presentation in MHC-I by the mRNA-transfected BM-DCs. Only in the BM-DCs cultured with both GM-CSF and IL-4 in FBS-containing medium, mRNA-transfection results in a lower CD25 expression on OT-I T cells. The differences between the different BM-DC protocols are more prominent when the amount of CD25 expressed by the cells is studied, rather than the percentage of CD25-positive cells. For this, we looked at the MFI of the CD25-PE stain on the OT-I cells. The results in **Figure 5B** demonstrate that a higher CD25 expression could be detected in co-cultures of OT-I cells and OVA transfected BM-DCs either generated with FCI and GM-CSF + IL-4 or generated with FBS and GM-CSF alone. The lowest CD25 expression was observed with FBS and GM-CSF + IL-4 supplemented BM-DCs (**Figure 5B**).

Upon activation, the T cells can start proliferating, which often coincides with the production of IL-2. Moreover, if $CD8^+$ T cell activation leads to differentiation into CTLs, the cells will start secreting IFNγ, a type II interferon that enhances the CTL activity. Therefore, we measured the secretion of IL-2 and IFNγ in the DC-T cell co-culture supernatant *via* ELISA. The IL-2 production can be partly linked with the expression of CD25, pointing towards superior T cell activation by BM-DCs either cultured with GM-CSF and IL-4 in FCI-supplemented medium or with GM-CSF alone in FBS-supplemented medium. Importantly, the most remarkable differences were observed in the IFNγ production. Overall, BM-DCs cultured in FCI containing medium could double the IFNγ secretion by OT-I T cells compared to BM-DCs cultured with FBS. A more detailed statistical analysis of the results in this section can be found in **Figure 6**.

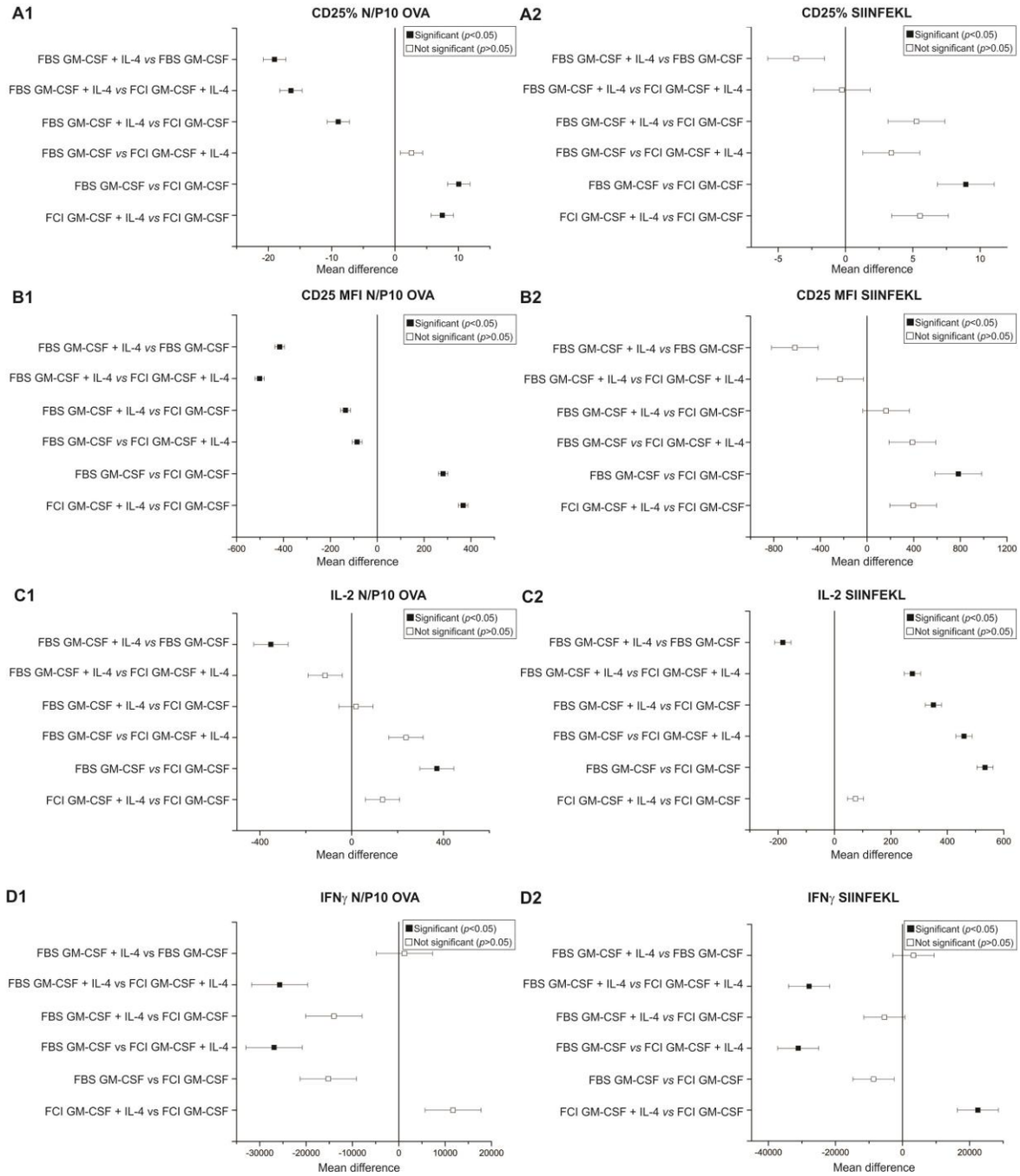

Figure 6. Statistical analysis of T cell activation by transfected DCs.

The results of the T cell activation experiments in Figure 5 were statistically analyzed with a one-way ANOVA followed by Bonferroni correction. Graphs show the mean difference with standard errors between the results obtained in different BM-DC cultures for: (A) % CD25 positive OT-I cells after stimulation with OVA-lipoplex transfected DCs (A1) or SIINFEKL-loaded DCs (A2); (B) the CD25 MFI on OT-I cells after stimulation with OVA-lipoplex transfected DCs (B1) or SIINFEKL-loaded DCs (B2); the secretion of IL-2 after stimulation with OVA-lipoplex transfected BM-DCs (C1) or SIINFEKL-loaded DCs (C2); (D) for the secretion of IFNγ after stimulation with OVA-lipoplex transfected DCs (D1) or SIINFEKL-loaded DCs (D2).

DISCUSSION

BM-DCs are extensively used as *in vitro* model systems to investigate DC immunobiology, as well as for the evaluation of novel particulate vaccines. Due to large variation in protocols to generate BM-DCs from bone marrow precursors[23, 24], we hypothesized that the validation of novel antigen-delivery nanoparticles might be influenced by the BM-DC culture that is used for their evaluation. Several studies reported on a number of crucial factors that can impact the yield, purity and phenotype of BM-DCs generated[13, 25]. Based on the work of Lutz et al., main variables are (a) mouse properties, (b) growth factors and (c) serum supplementation[13]. To exclude the first variable, we opted to consistently use female C57BL/6 mice at 7 weeks of age. With regard to the two other variables, we screened recent literature on nanoparticulate vaccines to find out which growth factor combinations and sera are most widely used. Most researchers evaluate novel nanoparticles in BM-DCs grown in RPMI medium supplemented with GM-CSF alone (20 ng ml^{-1}), or with IL-4 (10 ng ml^{-1}) in addition to GM-CSF (10 ng ml^{-1}). As for the serum, Lutz and Rossner described this to be the most important factor influencing the type of BM-DCs generated[13]. Therefore we chose to work with two different types of bovine serum: FBS and FCI.

After 6 days of culturing red blood cell-depleted murine bone marrow cells in the different cell culture media, the percentage of $CD11c^+$ DCs ranges from 39 to 80%. The highest BM-DC purity can be reached when FBS serum and GM-CSF alone are used. In accordance with previous reports, addition of IL-4 to the medium reduces the yield and purity of the BM-DCs[25]. It should be noted that other factors, such as the duration of the BM-DC culture or the implementation of additional, and often quite complex, purification steps, can result in cultures with larger percentages of $CD11c^+$ cells[4, 23, 26]. Often, cells growing adherent to the culture dishes are excluded in order to increase BM-DC purity. In our hands, however, for all culture media tested, the adherent cell fraction contained a substantial portion of CD11c-expressing BM-DCs. This confirms previous results obtained by Li and Lu, who showed that there is no reason to discard adherent cells in BM-DC cultures as junk cells[27]. Overall, practically all BM-DC protocols will finally result in a cell population containing a (large) fraction of $CD11c^+$ BM-DCs as well as a fraction of non-DCs. These two subpopulations are expected to behave differently with regard to e.g. endocytotic capacity, maturation marker expression and cytokine production. Therefore, in order to assess the impact of novel nano- and micromaterials on DCs *in vitro*, it is important to selectively investigate the response of $CD11c^+$ cells, rather than the total cell population. Assays where no further selection or gating of CD11c-expressing cells is possible (e.g. cell counts, many cytotoxicity assays, DC-T cell co-cultures, other assays performed on the total population), can be impacted by these large variations in BM-DC purity. This should be taken into account in the design and set-up of new experiments.

Substantial differences in surface marker expression can also exist within the CD11c-positive population. This was made obvious by performing antibody staining against maturation markers CD40, CD86 and MHC-II, where we demonstrated the presence of both immature as well as mature BM-DCs in all cultures. Importantly, addition of IL-4 increases the proportion of mature DCs. This can be explained by the induction of "spontaneous" maturation of generated BM-DCs, which is known to be enhanced by the presence of IL-4[23, 28, 29]. In addition, replacing FBS by FCI induces a significant reduction of maturation marker expression by the BM-DCs. In a study of Lutz et al., high serum levels of the liver enzymes glutamic oxaloacetic transaminase (GOT) and lactate dehydrogenase (LDH) have been correlated with high percentages of mature cells[13]. For the batches of FBS and FCI we used, this correlation was not observed: the FCI used contained high levels of both liver enzymes, whereas merely a small fraction of the DCs exhibited a mature phenotype. Even though the effect of the serum compound is prominent, the complexity of these bovine products makes it difficult to pinpoint the exact cause of the observed maturation-differences.

In nanoparticle research, a first step towards success is the efficient uptake of the nanomaterials by the target cells. In the case of DCs, their internalization capacity is closely related to their maturation status: although mature DCs are still capable of performing receptor-mediated endocytosis, aspecific endocytosis as well as phagocytosis and macropinocytosis are markedly reduced in mature DCs compared to their immature counterparts[22]. This was also evidenced by the mRNA lipoplex uptake experiment, showing less extensive mRNA lipoplex uptake by BM-DCs that exhibit a more mature phenotype. Therefore, ideally, antigen-containing nanoparticles should be evaluated in immature BM-DCs. However, a striking observation was the reduced maturation capacity of the more immature BM-DC subsets. For example, BM-DCs cultured with FCI and GM-CSF alone, exhibit the lowest portion of mature DCs in untreated samples, but upon TLR4 ligation maximally 40% of the BM-DCs will up-regulate CD86 and MHC-II. In contrast, well over 80% of BM-DCs generated in the presence of FBS medium, will up-regulate these markers upon LPS stimulation. This reduced responsiveness to maturation stimuli is nicely confirmed by cytokine measurements, showing that these specific BM-DCs also produce low levels of immune stimulatory IL-12p70 and high levels of the immune suppressive IL-10. Such phenotypical properties are expected to impact the immune responses that can be induced by these specific DCs. In addition, it is important to consider that for DC vaccines to be effective, efficient antigen-presentation by fully mature DCs is required. Since different reports have made clear that co-formulation of antigens and maturation stimuli will result in superior immune responses, the purpose of nanoparticulate vaccines has shifted from mere antigen delivery to dual-modality particles that should simultaneously load DCs with antigens and induce maturation of DCs[30, 31]. Therefore, immune stimulants such as the TLR ligands CpG and poly(I:C) have been incorporated into nanoparticulate vaccines[32]. As these dual-modality particles aim to induce complete maturation, it would undoubtedly be disadvantageous to

evaluate them in a maturation-resistant BM-DC model. Therefore, a careful choice and characterization of the BM-DC model for the intended purpose is required.

In addition to immunological properties, we wished to assess to what extent nanoparticulate vaccines can lead to different results when tested in one BM-DC culture versus another. For this, we chose to work with mRNA lipoplexes, since mRNA is an increasingly investigated source of antigen in novel DC vaccines[21]. When DCs are loaded with nucleic acid sequences encoding tumor antigens, the transfection efficiency is used as a critical measure for the amount of antigen delivered, and hence the main criterion to evaluate new nanoparticulate vaccines. An assessment of the transfection efficiency of mRNA lipoplexes in our 4 different models, revealed large differences, ranging from 10% to 37% mRNA expressing BM-DCs, even though the exact same nanoparticles were used. If transfection efficiency is the main parameter, it is now clear that the model BM-DC used for transfection experiments is a confounding factor. Do we then use the right means of scoring novel transfection-based particulate vaccines? First of all, it should at all times be kept in mind that the final end-point of the vaccine is to elicit antigen-specific T cell responses. And this is probably not a question of numbers. As reviewed by Gilboa et al., high efficiency transfection of DCs with antigen does not necessarily correlate with improved immune stimulatory effects[33]. In addition, it was previously suggested that no analytical method can compare to the sensitivity of T cells to detect presented antigens[34, 35]. Therefore, as a concluding experiment, we evaluated to what degree the observed transfection efficiencies could lead to activation of antigen-specific $CD8^+$ T cells *in vitro*. After co-culturing naïve OVA-specific $CD8^+$ T cells with mRNA lipoplex-loaded BM-DCs, significant antigen-specific T cell activation could be observed in all models. However, the differences observed in the extent of T cell activation point towards influences of both phenotypical parameters as well as variations in transfection efficiency. For instance, BM-DCs grown in FCI and GM-CSF-supplemented medium showed low expression of molecules involved in antigen presentation (MHC-II) and T cell activation (CD86 and IL-12p70). As a result, even after efficient loading with antigen-mRNA, merely low T cell stimulation could be detected. A similar reasoning is valid for phenotypically superior BM-DCs (e.g. BM-DCs resulting from culture with FBS in the presence of IL-4), where a markedly low transfection efficiency is the likely cause for the deficient activation of T cells.

CONCLUSIONS

To conclude, *in vitro* data obtained with novel nanoparticles are not exclusively the result of the nanoparticle's capacity to load DCs with antigenic material. Although BM-DCs are routinely used as a model for *in vivo* DCs, they should always be considered as simplified models for a complex *in vivo* situation. By screening a limited number of parameters, we were able to demonstrate extensive differences in BM-DC yield and immunological properties.

Moreover, we showed that the BM-DC model in which novel nanoparticles are tested, acts as an important confounding factor in both transfection efficiency and T cell activation assays. This not only makes it hard to evaluate the potential of novel nanoparticles for DC vaccination purposes, but also renders it difficult to compare results obtained in different research groups using different BM-DC models. We wish to stress that our aim was not to identify an optimal BM-DC protocol, but to expose the bias of the model on the functional outcome of the nanoparticle. Therefore, we propose to: (1) include a thorough immunological characterization of the BM-DCs model used; (2) in addition to transfection efficiency, always evaluate functional end-points, such as T cell activation. Only if these two criteria are met, can the impact of the model's confounding effect be assessed, and can the true value of a novel particulate vaccine be revealed.

ACKNOWLEDGEMENTS

The authors would like to thank Sandra Van Lint and Laura Wayteck for their assistance with the OT-I proliferation assay. They further wish to thank Carlo Heirman, Elsy Vaeremans and Petra Roman for their help with the mRNA production. Heleen Dewitte is a doctoral fellow of the Institute for the Promotion of Innovation through Science and Technology in Flanders, Belgium (IWT-Vlaanderen). Ine Lentacker and Karine Breckpot are postdoctoral fellows of the Research Foundation-Flanders, Belgium (FWO-Vlaanderen). This project was funded through the FWO grant G016513N.

REFERENCES

1. Brocks, C., Graefe, H., Frenzel, H., Pries, R. & Wollenberg, B. Isolation of human myeloid dendritic cells from tumor tissue and peripheral blood. *In vivo* **20**, 239-42 (2006).
2. Pena-Cruz, V. et al. Extraction of human Langerhans cells: a method for isolation of epidermis-resident dendritic cells. *Journal of immunological methods* **255**, 83-91 (2001).
3. Jacome-Galarza, C.E., Lee, S.K., Lorenzo, J.A. & Aguila, H.L. Identification, characterization, and isolation of a common progenitor for osteoclasts, macrophages, and dendritic cells from murine bone marrow and periphery. *Journal of bone and mineral research : the official journal of the American Society for Bone and Mineral Research* **28**, 1203-13 (2013).
4. Inaba, K. et al. Generation of large numbers of dendritic cells from mouse bone marrow cultures supplemented with granulocyte/macrophage colony-stimulating factor. *The Journal of experimental medicine* **176**, 1693-702 (1992).
5. Romani, N. et al. Proliferating dendritic cell progenitors in human blood. *The Journal of experimental medicine* **180**, 83-93 (1994).
6. Tuyaerts, S. et al. Current approaches in dendritic cell generation and future implications for cancer immunotherapy. *Cancer immunology, immunotherapy : CII* **56**, 1513-37 (2007).
7. Lutz, M.B. & Rossner, S. Factors influencing the generation of murine dendritic cells from bone marrow: The special role of fetal calf serum. *Immunobiology* **212**, 855-862 (2007).
8. Shortman, K. & Naik, S.H. Steady-state and inflammatory dendritic-cell development. *Nature reviews. Immunology* **7**, 19-30 (2007).
9. Villadangos, J.A. & Schnorrer, P. Intrinsic and cooperative antigen-presenting functions of dendritic-cell subsets in vivo. *Nature Reviews Immunology* **7**, 543-555 (2007).
10. Satpathy, A.T., Wu, X.D., Albring, J.C. & Murphy, K.M. Re(de)fining the dendritic cell lineage. *Nature Immunology* **13**, 1145-1154 (2012).
11. Brasel, K., De Smedt, T., Smith, J.L. & Maliszewski, C.R. Generation of murine dendritic cells from flt3-ligand-supplemented bone marrow cultures. *Blood* **96**, 3029-39 (2000).
12. Xu, Y., Zhan, Y., Lew, A.M., Naik, S.H. & Kershaw, M.H. Differential development of murine dendritic cells by GM-CSF versus Flt3 ligand has implications for inflammation and trafficking. *Journal of Immunology* **179**, 7577-84 (2007).
13. Lutz, M.B. & Rossner, S. Factors influencing the generation of murine dendritic cells from bone marrow: the special role of fetal calf serum. *Immunobiology* **212**, 855-62 (2007).
14. Menges, M. et al. IL-4 supports the generation of a dendritic cell subset from murine bone marrow with altered endocytosis capacity. *Journal of leukocyte biology* **77**, 535-43 (2005).
15. De Temmerman, M.L. et al. mRNA-Lipoplex loaded microbubble contrast agents for ultrasound-assisted transfection of dendritic cells. *Biomaterials* **32**, 9128-9135 (2011).
16. Zhang, Z.P., Guo, Y.J. & Feng, S.S. Nanoimmunotherapy: application of nanotechnology for sustained and targeted delivery of antigens to dendritic cells. *Nanomedicine* **7**, 1-4 (2012).
17. De Haes, W. et al. Lipoplexes carrying mRNA encoding Gag protein modulate dendritic cells to stimulate HIV-specific immune responses. *Nanomedicine* **8**, 77-87 (2013).
18. Van Lint, S., Heirman, C., Thielemans, K. & Breckpot, K. mRNA: From a chemical blueprint for protein production to an off-the-shelf therapeutic. *Human vaccines & immunotherapeutics* **9** (2013).
19. Van Meirvenne, S. et al. Efficient genetic modification of murine dendritic cells by electroporation with mRNA. *Cancer Gene Therapy* **9**, 787-797 (2002).
20. Lutz, M.B. & Schuler, G. Immature, semi-mature and fully mature dendritic cells: which signals induce tolerance or immunity? *Trends in Immunology* **23**, 445-449 (2002).
21. Van Lint, S., Thielemans, K. & Breckpot, K. mRNA: delivering an antitumor message? *Immunotherapy* **3**, 605-7 (2011).
22. Platt, C.D. et al. Mature dendritic cells use endocytic receptors to capture and present antigens. *Proceedings of the National Academy of Sciences of the United States of America* **107**, 4287-4292 (2010).
23. Lutz, M.B. IL-3 in dendritic cell development and function: a comparison with GM-CSF and IL-4. *Immunobiology* **209**, 79-87 (2004).

24. O'Neill, H.C. & Wilson, H.L. Limitations with in vitro production of dendritic cells using cytokines. *Journal of leukocyte biology* **75**, 600-603 (2004).
25. Wells, J.W., Darling, D., Farzaneh, F. & Galea-Lauri, J. Influence of interleukin-4 on the phenotype and function of bone marrow-derived murine dendritic cells generated under serum-free conditions. *Scandinavian Journal of Immunology* **61**, 251-259 (2005).
26. Kalantari, T. et al. Generation of large numbers of highly purified dendritic cells from bone marrow progenitor cells after co-culture with syngeneic murine splenocytes. *Experimental and Molecular Pathology* **94**, 336-342 (2013).
27. Li, G.B. & Lu, G.X. Adherent cells in granulocyte-macrophage colony-stimulating factor-induced bone marrow-derived dendritic cell culture system are qualified dendritic cells. *Cellular Immunology* **264**, 4-6 (2010).
28. Lutz, M.B. et al. Differential functions of IL-4 receptor types I and II for dendritic cell maturation and IL-12 production and their dependency on GM-CSF. *Journal of Immunology* **169**, 3574-3580 (2002).
29. Yamaguchi, Y., Tsumura, H., Miwa, M. & Inaba, K. Contrasting effects of TGF-beta 1 and TNF-alpha on the development of dendritic cells from progenitors in mouse bone marrow. *Stem Cells* **15**, 144-153 (1997).
30. Schlosser, E. et al. TLR ligands and antigen need to be coencapsulated into the same biodegradable microsphere for the generation of potent cytotoxic T lymphocyte responses. *Vaccine* **26**, 1626-1637 (2008).
31. Zaks, K. et al. Efficient immunization and cross-priming by vaccine adjuvants containing TLR3 or TLR9 agonists complexed to cationic liposomes. *Journal of Immunology* **176**, 7335-7345 (2006).
32. Lee, Y.R. et al. Biodegradable Nanoparticles Containing TLR3 or TLR9 Agonists Together with Antigen Enhance MHC-restricted Presentation of the Antigen. *Archives of Pharmacal Research* **33**, 1859-1866 (2010).
33. Gilboa, E. & Vieweg, J. Cancer immunotherapy with mRNA-transfected dendritic cells. *Immunological Reviews* **199**, 251-263 (2004).
34. Grunebach, F., Muller, M.R., Nencioni, A. & Brossart, P. Delivery of tumor-derived RNA for the induction of cytotoxic T-lymphocytes. *Gene Therapy* **10**, 367-374 (2003).
35. Nair, S.K. et al. Induction of primary carcinoembryonic antigen (CEA)-specific cytotoxic T lymphocytes in vitro using human dendritic cells transfected with RNA. *Nature biotechnology* **16**, 364-369 (1998).

3

Chapter 3

Design and evaluation of theranostic perfluorocarbon particles for simultaneous antigen-loading and ^{19}F MRI tracking of dendritic cells

This chapter is published as:

Heleen Dewitte[1], Bart Geers[1], Sayuan Liang[2], Uwe Himmelreich[2], Jo Demeester[1], Stefaan C. De Smedt[1] and Ine Lentacker[1]. Design and evaluation of theranostic perfluorocarbon particles for simultaneous antigen-loading and ^{19}F-MRI tracking of dendritic cells. *Journal of Controlled Release* **169**, 141-9 (2013).

[1]Laboratory for General Biochemistry and Physical Pharmacy, Faculty of Pharmaceutical Sciences, Ghent University, Ottergemsesteenweg 460, 9000 Ghent, Belgium

[2]Biomedical MRI Unit, Department of Imaging and Pathology, Faculty of Medicine, KU Leuven, O&N I Herestraat 49/505, 3000 Leuven, Belgium

ABSTRACT

Perfluorocarbon (PFC) particles are currently on the rise as cell labeling agents for ^{19}F MRI tracking of dendritic cell (DC)-based vaccines. In this work, we design theranostic PFC particles for single-step loading of DCs with both antigenic protein and a liquid PFC for ^{19}F MRI detection of the antigen-loaded cells. Upon addition to DCs *in vitro*, the antigen-loaded PFC particles are efficiently internalized, resulting in the intracellular presence of up to 40 pmol ^{19}F atoms per cell. At the same time, the DCs become loaded with antigenic proteins that can be efficiently processed, without important effects on cell viability or altering the DC's phenotype and the cell's capacity to respond to danger signals. In addition, DCs containing antigen-loaded PFC particles are capable of inducing extensive proliferation of antigen-specific $CD8^+$ T cells *in vitro*. Importantly, the antigen-coated PFC particles allow *in vitro* ^{19}F MRI-based detection of the antigen-containing DCs with detection limits as low as 10^3 cells μl^{-1}. The dual-modality characteristics of the designed particles could assure that only those DCs that have taken up the antigen, and hence are responsible for an immune response, are traceable *via* ^{19}F MRI. Taken together, these novel dual-modality particles represent an interesting strategy in the development of a traceable DC vaccine.

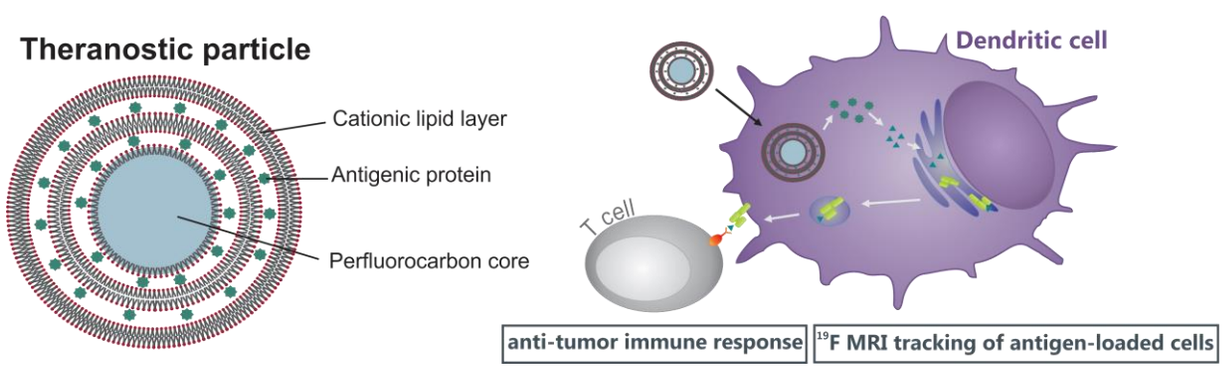

INTRODUCTION

As described in **Chapter 1**, for the production of current dendritic cell (DC)-based vaccines, DCs are currently modified *ex vivo* to present tumor associated antigens and initiate anti-tumor immune responses[1, 2]. These cellular vaccines are mostly injected subcutaneously, after which the antigen-laden DCs should be capable to reach the lymph nodes in order to present their antigens to naïve T cells. However, different studies in both mouse[3, 4] and man[5, 6] have demonstrated that upon injection, merely low percentages (in general <5%) of DCs are capable of reaching the draining lymph nodes, whereas most of the transplanted cells are retained at the injection site[3, 6, 7]. Even if the DCs are injected *intranodally*, in this way circumventing migratory problems, de Vries et al. discovered that in only half of the cases the DCs were correctly injected, despite ultrasound-guided injections by experienced radiologists[8].

Thus, one of the strategies to improve vaccinations with *ex vivo* generated cellular vaccines, would be to make them traceable. Ideally, this would be done by designing a theranostic particle that allows simultaneous delivery of tumor antigens and a contrast agent for high-resolution tracking of the antigen-loaded cells after administration *in vivo*. One technique that could be particularly interesting for this application, is magnetic resonance imaging (MRI), as it allows high-resolution imaging without making use of radioactive labels. In clinical ^{1}H MRI imaging, contrast agents based on lanthanide chelates or superparamagnetic nanoparticles have been used[9-12]. However, intrinsic contrast from the host tissue and contrast generated by those agents can be mistaken. To overcome this disadvantage, fluorine (^{19}F) MRI emerged as a powerful tool to locate transplanted cells, such as *ex vivo* modified DCs. By using the ^{19}F nuclei instead of ^{1}H, MR images can be obtained without background signal from the host tissue, enabling unambiguous identification and quantification of contrast agent-labeled cells[13]. In addition, anatomic information can be retained by also acquiring a ^{1}H MR image of the same subject.

As contrast agents for ^{19}F MRI, perfluorocarbons (PFCs) have been proposed. As described in **Chapter 1**, they are metabolically inert, offer a high density of ^{19}F nuclei per molecule and have well-defined safety profiles[11, 12, 14-16]. Due to their very low surface tension, liquid PFCs usually remain cohesive, and are therefore difficult to formulate into stable emulsions. To overcome this hurdle, different lipid and polymer coats have been designed to stabilize the PFC droplets in an aqueous environment[17-19].

However, the application of such particles has remained limited to mere imaging, which implies that besides the regular antigen-loading of the cells, a separate modification of the DCs with ^{19}F MRI contrast agents is required. In this way, the vaccine production becomes more labor-intensive, and there is no guarantee that the cells that are detected *in vivo* are in fact loaded with antigens and thus capable of inducing antigen-specific immune responses.

Therefore, we aim to design theranostic particles that can be applied in DC vaccination. Theranostics are multimodal particles that combine the delivery of therapeutic agents and a diagnostic functionality[20, 21]. In the case of DC vaccines, such particles would ideally modify the cells with antigens and at the same time, allow *in vivo* tracing of the antigen-loaded cells during their migration to the lymph nodes. This would assure that exclusively those DCs that have taken up the antigen and hence are responsible for an immunologic response are detected. Evidence of efficient migration could then be used as a first predictor of the vaccine efficacy. The present study aims to design and evaluate layer-by-layer antigen-coated PFC particles for single-step delivery of antigenic protein and ^{19}F MRI contrast agents to DCs.

MATERIALS AND METHODS

Preparation and characterization of PFC particles

Cationic PFC particles were prepared by mixing 63.7% DOTAP (1,2-dioleoyl-3-trimethylammonium-propane) (Avanti Polar Lipids, Alabaster, AL, USA), 24.5% DOPE (1,2-Dioleoyl-*sn*-Glycero-3-Phosphoethanolamine) (Lipoid, Ludwigshafen, Germany), 2% DSPE-PEG(2000) (1,2-distearoyl-*sn*-glycero-3-phosphoethanolamine-N-[amino polyethyl-ene glycol)-2000]) (Avanti Polar Lipids) and 9.8% cholesterol (Sigma-Aldrich, Bornem, Belgium), all dissolved in chloroform, in a round-bottom flask. After evaporation of the chloroform under nitrogen, the resulting lipid film was hydrated in a 1:2:7 mixture of glycerol, propanediol and distilled water to obtain a clear solution with a final lipid concentration of $1.4x10^{-3}$ mmol ml^{-1}. For fluorescent labeling of the lipids, CholEsteryl BODIPY® FL C12 (1%, Molecular Probes, Invitrogen, Merelbeke, Belgium) was added to the chloroform lipid mixture. To prepare PFC particles, 40 µl of either perfluorohexane (PFH, F2 chemicals, Preston, UK) or perfluoro-15-crown-5-ether (PFCE, Exfluor Research Corporation, Round Rock, Tx, USA) was emulsified in the presence of excess lipid solution by means of high-frequency shaking in a CapMix™ device (3M-ESPE, Diegem, Belgium). The produced particles were then centrifuged for 1min at 1000*g* in order to spin down the largest particles. Particle size was evaluated on the smaller particle fraction, using a Beckman-coulter Multisizer 4 (Beckman-coulter, Brea, CA, USA) equipped with a 20 µm aperture tube.

Antigen-loading of PFC particles

Cationic PFC particles were washed three times with dH_2O to remove unincorporated lipids. Then, particles were electrostatically loaded with negatively charged ovalbumin (OVA, a routinely used model antigen) by adding an aqueous OVA solution (1 mg ml^{-1}, Sigma-Aldrich). Repeated washing steps were performed to remove excess OVA before adsorbing an additional lipid layer. This process was repeated to load multiple layers of alternating cationic lipids and anionic protein onto the particles. The efficiency of this loading process was assessed *via* zeta potential measurements using a Malvern Zetasizer nano-ZS (Malvern Instruments Ltd, Worcestershire, UK). To determine the amount of OVA that could be adsorbed onto the PFH particles, the liquid PFH was first evaporated by placing the particles into a water bath at 90°C for 20min. Then, the OVA content of the resulting OVA solution was measured using a micro BCA assay (Thermo Fisher Scientific, Rockford, USA) according to the manufacturer's specifications. By loading the PFC particles with Alexa Fluor® 647-labeled OVA (Molecular Probes), the loaded PFC particles could be visualized by confocal microscopy.

Dendritic cell culture

Primary murine bone marrow-derived DC (BM-DC) cultures were generated from C57BL/6 mice. Female C57BL/6 mice were purchased from Janvier (Le Genest Saint Isle, France) and housed in an SPF facility according to the regulations of the Belgian law and the local Ethical Committee. Mice were euthanized and bone marrow was flushed from the hind limbs. Red blood cells were lysed (Pharm Lyse Buffer, BD Biosciences) and the collected cells were seeded in bacteriological petri dishes (Falcon, VWR, Haasrode, Belgium) at $2x10^6$ cells ml^{-1} in 10 ml. The cell culture medium used was RPMI 1640 (Gibco-Invitrogen, Merelbeke, Belgium) supplemented with FBS (5%, Hyclone, Pierce, Rockford, IL, USA), penicillin/streptomycin/L-glutamine (1%, Gibco-Invitrogen), β-mercaptoethanol (50 μM, Gibco-Invitrogen) and GM-CSF (20 ng ml^{-1}, Peprotech, Rock Hill, NJ). On day 3 of the culture, an additional 10 ml complete culture medium containing GM-CSF (40 ng ml^{-1}) was added. On day 6, all cells were collected by centrifugation (7min at 400*g*) and resuspended in fresh culture medium at 10^6 cells ml^{-1}. Next, the cells were seeded in well plates allowing them sufficient time to loosely adhere to the well surface before treatment on day 7 after the start of the culture.

Microscopy

Confocal microscopy images of OVA-loaded PFC particles, their uptake by DCs and subsequent OVA processing into peptides were recorded using a Nikon C1si confocal laser scanning module attached to a motorized Nikon TE2000-E inverted microscope (Nikon Benelux, Brussels, Belgium). For cell experiments, day 6 DCs were seeded in 35 mm MatTek glass bottom culture dishes (MatTek Corporation, MA, USA) 1 day before addition of PFC particles and confocal imaging using an oil immersion objective lens (Plan Apo 60X 1.4 NA oil immersion objective lens). For PFC particle uptake experiments, the cytoplasm of live cells was stained by incubating the cells for 15min in culture medium supplemented with CellTracker™ Green (50 μM, Molecular Probes). DC nuclei were stained using Hoechst 3342 (Molecular Probes).

Sample preparation for transmission electron microscopy (TEM) was performed as follows: After 1 h incubation of DCs with OVA-loaded PFC particles, the cells were pelleted in BEEM® capsules (Structure probe, Inc., West Chester, USA) and fixated in glutaraldehyde (2%, Sigma Chemical Co., St. Louis, MO). Subsequently, the cells were postfixated in osmiumtetraoxide (2%, Laborimpex, Brussels, Belgium) after which the cells were dehydrated in an ascending series of ethanol and finally embedded in epoxyresin at 60°C. The resulting blocks were cut into 60 nm sections and stained with uranyl acetate and lead citrate (both Laborimpex). TEM images were recorded using the TEM JEM 1200 EX II (JEOL, Tokyo, Japan).

Cytotoxicity assay

Cell viability was evaluated 24h after addition of OVA-PFC particles to DCs using an MTT assay (Cell Proliferation Kit I, Roche Diagnostics, Vilvoorde, Belgium) according to the manufacturer's specifications.

^{19}F NMR spectroscopy

The produced particles were suspended in deuterated water (0.5 ml total volume) and transferred to a 5 mm NMR tube (Wilmad, Vineland, NJ, USA). 5-Fluorocytosine or sodium fluoride (4-10 mM final concentration) were added as an internal chemical shift and concentration reference. NMR spectroscopy experiments were carried out using a 400 MHz Bruker Avance II NMR spectrometer (Bruker Biospin, Rheinstetten, Germany) equipped with a 5 mm broadband probe operating at 376.50 MHz for ^{19}F NMR spectroscopy. The following acquisition parameters were used: spectral width 200 ppm, relaxation delay 5s, number of acquisitions 128 to 1024, and acquisition of 64k data points. Chemical shift was referenced to 5-fluorocytosine at -172.4 ppm. The temperature was maintained at 37ºC for all measurements.

^{19}F NMR signals were quantified relative to 5-fluorocytosine or NaF by integration after phase and baseline correction using the manufacturer's software (Topsin, Bruker Biospin, Rheinstetten, Germany). T_1 relaxation times were calculated from inversion recovery experiments. T_2 relaxation times were determined from *Carr-Purcell-Meiboom-Gill* (CPMG) experiments. Other parameters were as described previously[22, 23].

^{19}F MRI detection of OVA-PFC particle loaded DCs

For *in vitro* detection of DCs containing OVA-loaded PFCE particles, phantoms were used that consist of Eppendorf tubes filled with 10^4 to 10^7 cells ml^{-1} suspended in agar (1% in saline, Invitrogen). In addition to the tubes of interest, Eppendorf tubes filled with NaF (25-100 mM solutions) were used as concentration and chemical shift references for ^{19}F MRI and ^{19}F NMR spectroscopy. All MR images were acquired using a Bruker Biospec 9.4 Tesla small animal MR scanner (Bruker Biospin, Ettlingen, Germany; horizontal bore, 20 cm) equipped with actively shielded gradients (600 mT m^{-1}). A purpose-built radio-frequency transmit-receive coil tunable to the ^{1}H (400.34 MHz) and ^{19}F (376.64 MHz) frequencies was used for all phantom experiments. After acquisition of a positioning scan, 2D multi-slice or 3D ^{1}H and ^{19}F gradient echo MR images (FLASH) were acquired using identical parameters (except for the frequency) for both nuclei. Acquisition parameters were as following for 3D MRI: isotropic resolution of 600 μm^3, repetition time (TR)=100 ms, echo time (TE)=5.9 ms, FLASH sequence (30° flip angle), field-of-view (FOV) 60x60x60 mm, number of averages 1 to 120; for 2D MRI: slices of 1-2 mm thickness, 600 µm in plane resolution, TR=100 ms, TE=5.8 ms, number of averages 8 to 64, matrix 96x96 data points, FOV 60x60 mm, FLASH sequence (30° flip angle). Acquisition frequencies were 376.652 MHz (^{19}F) and 400.325 MHz (^{1}H). The effective spectral bandwidth for ^{19}F MRI was 50 kHz. Images were analyzed using Paravision 5.1 (Bruker Biospin, Ettlingen, Germany).

Proteolytic processing of OVA by DCs

To investigate to what extent the uptake of OVA-loaded particles leads to effective OVA processing by the DCs, PFC particles were loaded with DQ™ OVA (Molecular Probes). Due to the extensive loading of the protein with BODIPY® dyes, the fluorescence of intact DQ™ OVA is highly quenched. Upon proteolytic digestion of the protein, the green fluorescence drastically increases, making it possible to visualize its intracellular degradation. Analysis of the green fluorescent signal upon DQ™ OVA proteolysis was performed 24h after particle addition to the DCs, using both confocal microscopy and flow cytometry. For FACS analysis, DCs were washed with Flow buffer (PBS (Gibco, Invitrogen) supplemented with BSA (1%) and azide (0.1%, Sigma-Aldrich) and surface stained for the DC marker CD11c-APC (eBioscience,

Vienna, Austria) for 30min at 4°C. FACS analysis was performed using a FACSCalibur™ (BD Pharmingen, Erembodegem, Belgium) and data were analyzed with CellQuest™ software.

Phenotype of OVA-PFC-particle loaded DCs

The influence of uptake of OVA-loaded PFC particles on the DC phenotype was investigated by quantifying up-regulation of the maturation markers CD40 and CD86 on the DC surface. 24h after particle uptake, DCs were washed with flow buffer. Then, the cells were surface stained for the DC marker CD11c-APC in combination with staining for either CD40-FITC or CD86-FITC (both BD Pharmingen) for 30min at 4°C. Untreated DCs and DCs cultured in the presence of *Escherichia coli*-derived lipopolysaccharide (1 µg ml^{-1} LPS, Sigma-Aldrich) served as negative and positive controls respectively.

T cell proliferation assay

In order to assess the efficiency of OVA-PFC-particle loaded DCs to prime antigen-specific CD8+ T cells, an *in vitro* OT-I proliferation assay was performed. In this assay, OVA-PFCE-particle-loaded DCs were co-cultured with carboxyfluorescein succinimidyl ester (CFSE)-labeled naïve OT-I cells, which have a transgenic T cell receptor that recognizes the MHC-I restricted OVA-peptide SIINFEKL. The DCs were first incubated for 2h with either OVA-loaded PFCE particles, unloaded PFCE particles (as a negative control), or the SIINFEKL peptide as a positive control (Eurogentec, Seraing, Belgium). Then, the cells were matured for 4h with LPS, washed, and seeded per 10^4 DCs in a U-bottom 96 well plate, for co-incubation with 10^5 CFSE-labeled OT-I cells (derived from the spleens of OT-I transgenic mice, Charles River). After 5 days, the cells were collected, surface stained for CD8-APC (BD Pharmingen) and analyzed by flow cytometry.

Statistical analysis

Statistical analysis was performed using GraphPad software (la Jolla, CA, USA). All data are presented as mean ± standard deviation (SD). A one-way ANOVA followed by Bonferroni multiple comparison was performed to determine statistically significant differences between datasets. *p*-values <0.05 were regarded significant.

RESULTS

Characterization and antigen-loading of PFC particles

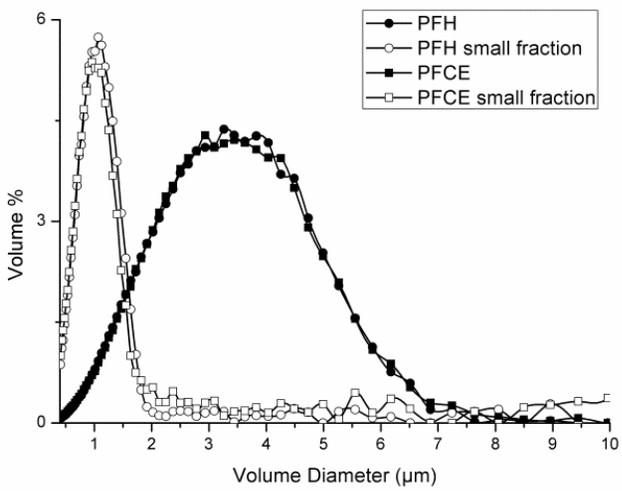

Figure 1. Size distribution of PFH and PFCE particles.

The size of PFC and PFCE particles was measured by coulter counter both immediately after production (PFH and PFCE) and after removal of the largest particles by centrifugation (PFH small fraction and PFCE small fraction). As a result, the mean volume diameter decreased from 2.96 ± 1.38 µm to 1.21 ± 1.28 µm for PFH particles and from 2.96 ± 1.40 µm to 1.42 ± 1.84 µm for PFCE particles.

As described in the materials and methods section, PFH and PFCE particles with a net positive surface charge could be prepared by high-frequency mixing of the liquid PFC with a cationic lipid mixture. By including 2% polyethylene glycol (PEG) modified lipids in the particle coat, formation of particle aggregates could be avoided. In order to remove the largest particles, the samples were briefly centrifuged (1min at 1000*g*). The average volume diameters of the remaining particles, as determined by coulter counter measurements, was 1.21 ± 1.28 µm for PFH particles and 1.42 ± 1.84 µm for PFCE particles (**Figure 1**). The presence of the stabilizing cationic lipid layer around the particles resulted in a positive zeta potential of 50.3 ± 3.80 mV for PFH particles and 67.5 ± 4.84 mV for PFCE particles.

These cationic particles were loaded with OVA *via* electrostatic interactions, as schematically depicted in **Figure 2A**. Effective antigen loading could be demonstrated by means of confocal microscopy (**Figure 2B**), where Alexa Fluor® 647-labeled OVA (red) is clearly present around PFC particles of which the lipid membrane was labeled with CholEsteryl BODIPY® FL C12 (green).

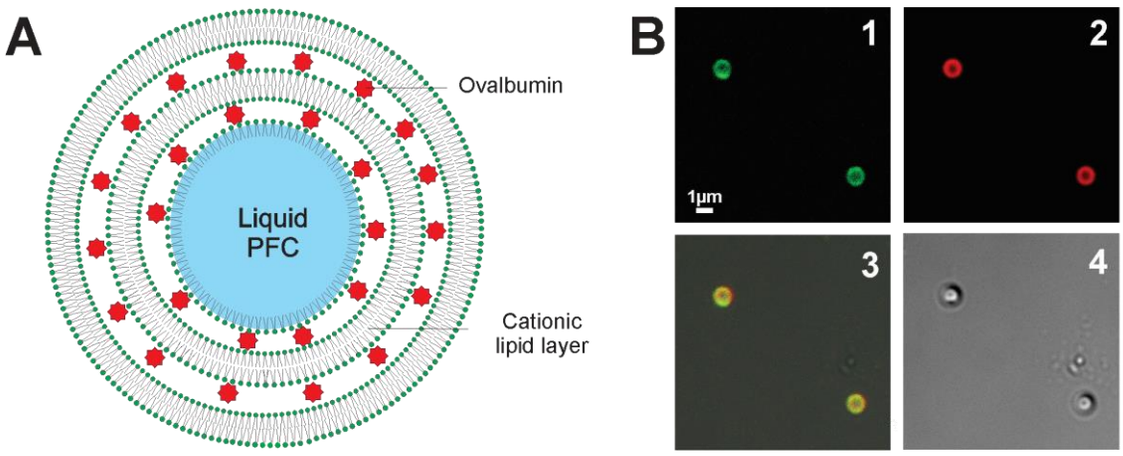

Figure 2. OVA loading of PFC particles.

(A) Schematic representation of a particle with a liquid PFC core, surrounded by alternating layers of cationic lipids and anionic OVA. (B) Confocal images of PFC particles stabilized by a green fluorescent lipid layer and loaded with red fluorescent OVA: (1) fluorescently labeled cationic PFC particles, (2) red fluorescent OVA, (3) merged image, (4) transmission.

To increase the amount of protein that could be loaded onto the particles, a layer-by-layer principle was applied[24], adsorbing alternating layers of cationic lipids and anionic protein around the liquid particle core. The effective presence of each of these additional layers was confirmed by zeta potential measurements demonstrating alternating positive and negative surface charges of the particle, as represented for PFH particles in **Figure 3**. The amount of OVA that could be loaded onto these PFH particles was 1.87 ± 0.26 µg per layer of OVA for 100 µl particles.

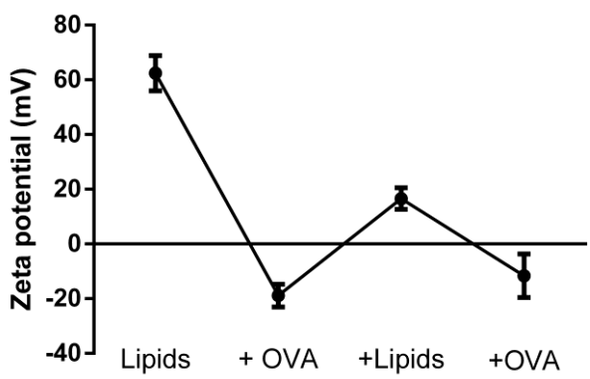

Figure 3. Zeta-potential measurements of OVA-loaded PFH particles.

PFH particles coated with cationic lipids show a positive zeta potential. Upon adsorption of negatively charged OVA, the zeta potential reverses. This can be repeated to produce particles coated with multiple layers of alternating lipids and OVA (*n*=3).

^{19}F NMR spectroscopic evaluation of OVA-loaded PFC particles

^{19}F NMR spectroscopy of the produced PFH and PFCE particles confirmed the integrity of the fluorinated compounds. For quantification purposes, 5-fluorocytosine or NaF of known concentration was added. The determined concentration of the stock solutions was 100 mM for the PFCE particles (the concentration of equivalent fluorine atoms was 2 M), and 80 mM for the PFH particles (the concentration of equivalent fluorine atoms was 0.48 mM for the two equivalent CF_3-groups). Furthermore, the chemical shift as well as the T_1 and T_2 relaxation times for both types of particles were determined and can be found in **Table 1**.

Table 1. ^{19}F NMR parameters of the prepared PFH and PFCE particles.

Incorporated PFC	^{19}F chemical shift (ppm)	T1 relaxation time (ms)	T2 relaxation time (ms)
PFH	-85ppm, -125ppm, -129ppm	1450 ± 150	400 ± 50
PFCE	-96ppm	1000 ± 100	350 ± 50

These data already imply the advantages of using PFCE particles over PFH particles. First of all, in PFH the fluorine is distributed over three signals, representing the chemically equivalent CF_2/CF_3 groups. This results in a maximum of six ^{19}F atoms for the two equivalent CF_3 groups that contribute to the signal at 85 ppm. In contrast, for PFCE twenty equivalent fluorine atoms make up the signal at 96 ppm which results in a higher sensitivity per molecule. In addition, the presence of multiple fluorine frequencies in PFH can lead to ghosting artifacts in MR images, depending on the selected ^{19}F MRI frequency and bandwidth.

Uptake of OVA-loaded PFC particles by DCs

Confocal microscopy was used to determine the intracellular presence of OVA-loaded PFC particles in murine BM-DCs after particle addition *in vitro*. Within merely 30min, all of the adherent DCs showed clear internalization of large numbers of red fluorescent OVA-loaded PFCE particles (**Figure 4**). Images also indicate that upon particle ingestion, OVA is released from the particles and is distributed over the entire DC cytoplasm.

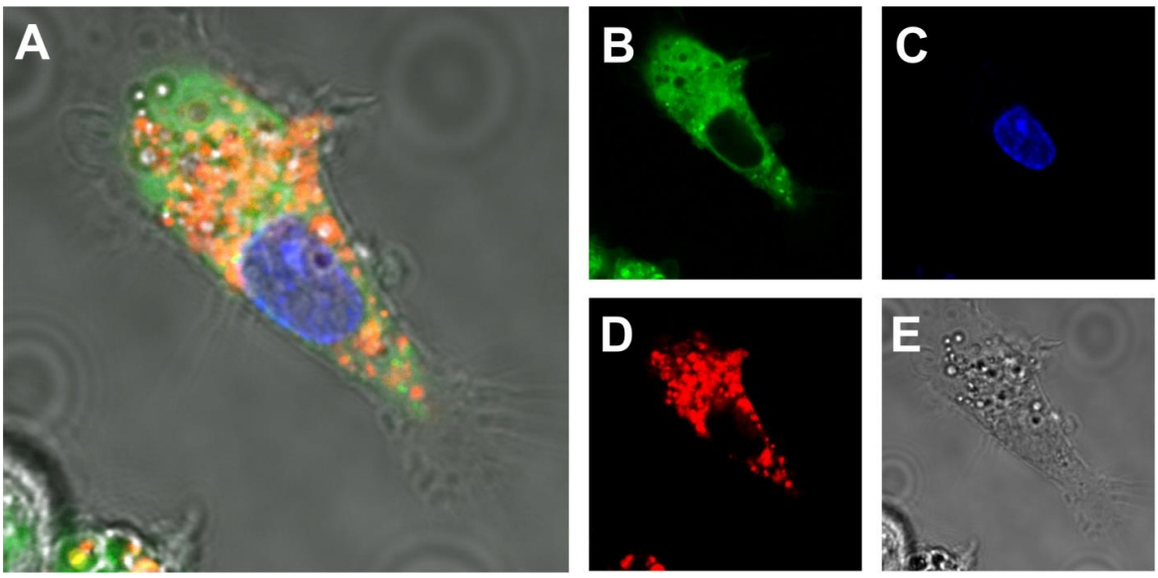

Figure 4. Uptake of OVA-loaded PFC particles by DCs.

OVA-loaded PFCE particles were added to murine BM-DCs. After 1h, particle uptake was evaluated via confocal microscopy. Images show (A) merged image, (B) CellTracker™ green cytoplasmic stain, (C) Hoechst nucleus stain, (D) red fluorescent OVA and (E) transmission.

More detailed information on the intracellular distribution of OVA-loaded PFC particles was obtained through TEM analysis of DC samples after 1h of PFCE particle loading. The images confirm the intracellular presence of spherical particles, as depicted in **Figure 5**. Non-loaded cells served as negative controls.

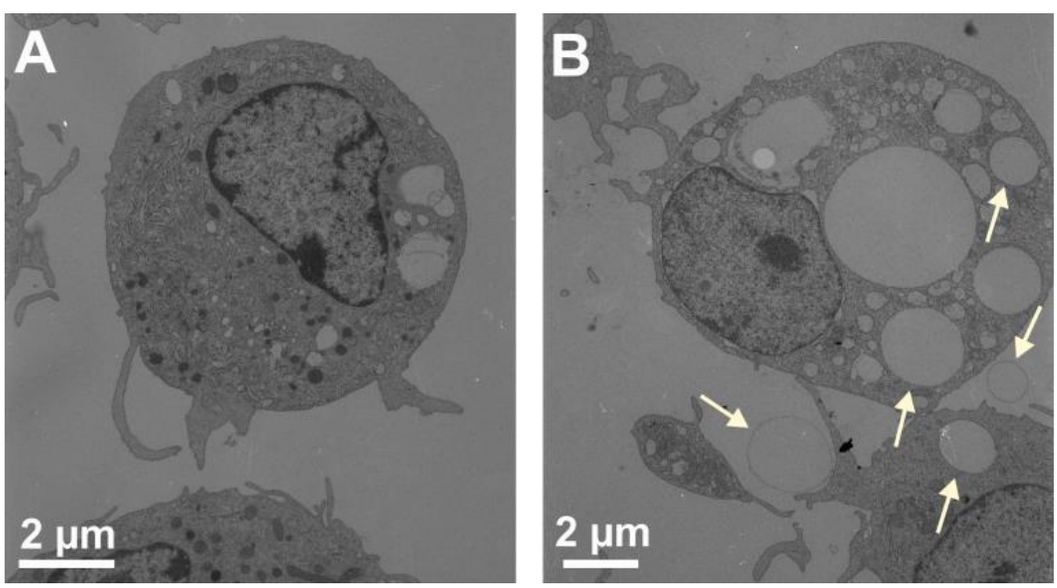

Figure 5. Transmission electron microscopy.

DCs were either (A) unloaded or (B) incubated with OVA-loaded PFCE particles for 1h prior to fixation and preparation for TEM imaging. In the latter image, both internalized and external PFCE particles can be observed (indicated with white arrows).

DC viability after addition of OVA-loaded PFC particles

In order to use these particles in DC vaccination, particle uptake by the cells should not compromise their viability. To determine the potential toxic effects of the OVA-loaded PFC particles on DCs, an MTT assay was performed 24h after addition of different PFC particles at different concentrations to the cells. The data, as shown in **Figure 6**, demonstrate a limited dose-dependent cytotoxic effect that occurs starting from a dose of 240 particles per cell when the particles are loaded with OVA. For the highest particle load (300 particles per DC), cell viability was 86.0 ± 5.2% for OVA-loaded PFCE particles and 79.9 ± 5.3% for OVA-loaded PFH particles. In general, cell viability is lower when unloaded particles are used compared to OVA-loaded particles, which can likely be attributed to the cationic surface charge of these unloaded particles.

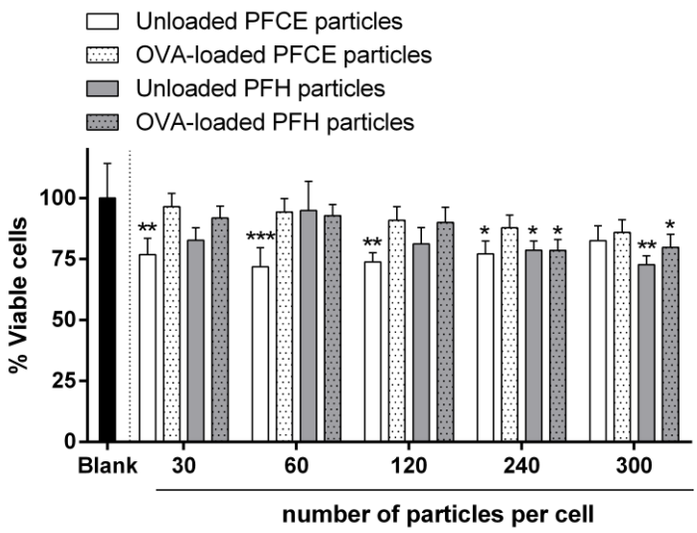

Figure 6. Viability of DCs after uptake of OVA-loaded PFCE and PFH particles.
Viability of DCs 24h after uptake of either unloaded or OVA-loaded PFCE and PFH particles was assessed using an MTT assay. Untreated cells served as a blank. Asterisks indicate statistically significant differences compared to blank.
(n=4, * p<0.05, ** p<0.01, ***p<0.005)

^{19}F MRI on OVA-PFC-particle loaded DCs

After uptake of OVA-loaded PFC particles by DCs, the detectability limits for the PFC-containing cells were determined by ^{19}F MRI. For this, DCs were cultured in the presence of PFC particles overnight and suspended in 1% agarose at different cell densities. Vials containing different cell densities and a control vial containing 100 mM NaF were put in a sample holder. Intracellular fluorine concentrations were estimated by using ^{19}F NMR spectroscopy of the different vials and the reference tubes (see **Figure 7**). For the PFCE-containing particles,

the intracellular fluorine concentration was estimated to be 40 pmol per cell. The detectability limit for PFCE-particle loaded DCs was estimated at 1000 cells μl^{-1} and 250 cells μl^{-1} for a 40min and 3h acquisition, respectively. Cells loaded with PFH particles were more difficult to detect. This could be attributed to the presence of three peaks in the ^{19}F NMR spectrum, each representing a lower number of chemically equivalent fluorine atoms. This resulted in a merely low concentration of 1 pmol of equivalent ^{19}F atoms per cell for the two CF_3-groups of PFH particles and a substantially higher detection limit of 10^4 cells μl^{-1}, which required a 9h acquisition time. It goes without saying that such long acquisition times will not be clinically applicable. Taken together, PFCE particles allow higher sensitivity detection of antigen-loaded DCs, at shorter acquisition times, which makes them preferable for the intended use.

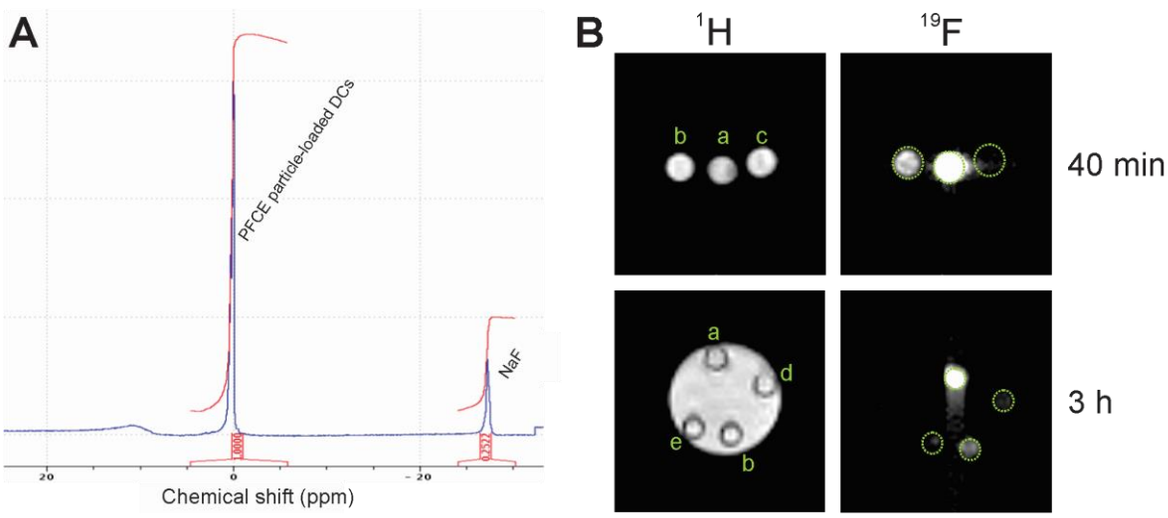

Figure 7. ^{19}F MR on PFCE particle-loaded DCs.

After 24h loading of DCs with PFCE particles, the cells were collected and suspended in 1% agarose at different concentrations. (A) ^{19}F NMR spectrum of PFCE particle-loaded cells compared to 100 mM NaF. (B) ^{1}H MRI and corresponding ^{19}F MRI of tubes filled with labeled cells suspended in agar. Top row: tubes with (a) 10 000 cells μl^{-1}; (b) 1000 cells μl^{-1} and (c) 100 cells μl^{-1}, acquired for 40min (number of averages = 10). Bottom row: tubes containing (a) 10 000 cells μl^{-1}; (b) 1000 cells μl^{-1}; (d) 500 cells μl^{-1} and (e) 250 cells μl^{-1} were put in an agar block (hyperintense background on ^{1}H MRI) and acquired for approximately 3h (number of averages = 32).

OVA processing upon uptake of OVA-loaded PFC particles by DCs

Besides introducing liquid PFCs for ^{19}F MRI imaging, we aimed to simultaneously load DCs with antigens for vaccination purposes. This means that the particle-mediated uptake of the antigenic protein should result in presentation of antigenic peptides in specialized molecules, called major histocompatibility complexes (MHCs) at the DC surface. This requires intracellular processing of the delivered antigen. To test if this

occurs using this method, cationic PFC particles were loaded with DQ™ OVA. Due to the extensive labeling of this OVA with BODIPY® dyes, the fluorescence of the intact protein is quenched. Upon intracellular proteolysis of DQ™ OVA, the quenching is relieved, causing a drastic increase in green fluorescence intensity. The intracellular green fluorescence due to processed DQ™ OVA was evaluated 24h after particle uptake by the DCs via both confocal microscopy and flow cytometry. Given that exploratory experiments revealed a significant increase in DC granularity after particle uptake, DCs incubated with unloaded PFC particles served as negative controls.

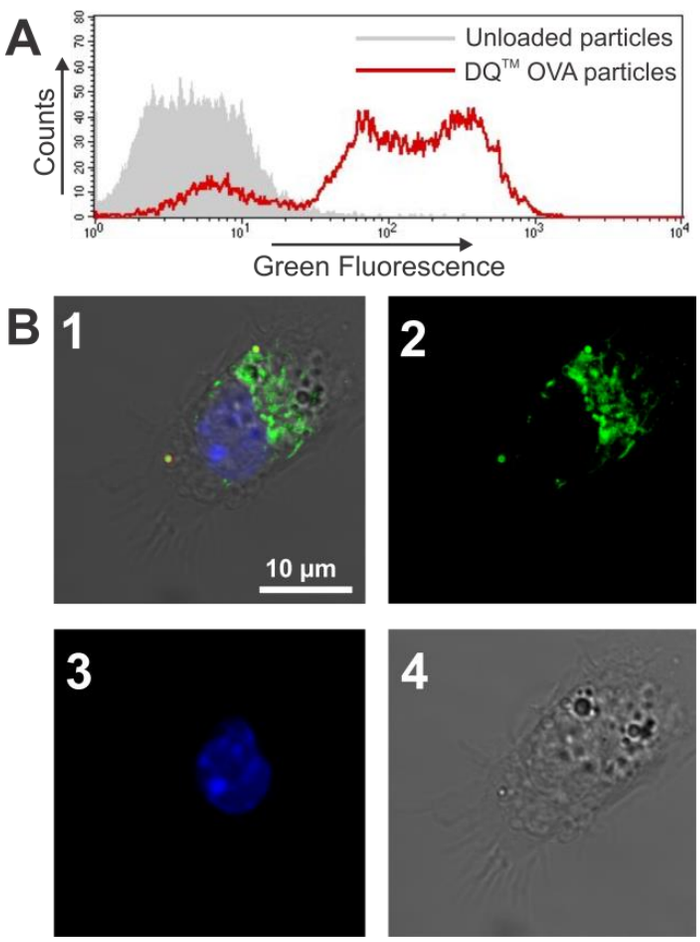

Figure 8. DQ™ OVA processing upon particle uptake by DCs.
24h after uptake of DQ™ OVA loaded PFC particles by DCs, antigen processing was evaluated by means of flow cytometry and confocal microscopy. (A) shows a representative histogram for the detection of green fluorescence in $CD11c^+$ DCs after uptake of unloaded or DQ™ OVA-loaded particles. The confocal images in (B) represent (1) overlay, (2) green fluorescence due to intracellular processing of DQ™ OVA, (3) Hoechst nucleus stain and (4) transmission.

Flow cytometric analysis, as seen in **Figure 8A**, revealed a 30-fold increase in mean green fluorescence intensity upon ingestion of DQ™ OVA particles, compared to unloaded particles. Further analysis demonstrated that the portion of cells that exhibit low green

fluorescence were also low in granularity, and did most likely not contain PFC particles. These data were confirmed by confocal images (**Figure 8B**), showing clear intracellular presence of green fluorescence due to processed DQ^{TM} OVA in DCs with internalized particles. This provides a proof of concept that the OVA introduced into DCs via OVA-loaded PFC particles can still be released from the particles and enter the natural pathway of intracellular antigen processing.

Phenotype of OVA-PFC-particle loaded DCs

When using materials for modification of DCs, it is crucial to consider the effects on the DC phenotype. Upon encounter of danger signals, such as pathogen-associated molecular patterns (PAMPs), the DCs mature, which results in a shift in function from antigen-sampling to antigen-presentation[25]. Since mature DCs are responsible for induction of immune responses, whereas immature and semi-mature DCs are mainly linked to suppression of immune responses and immune tolerance, it is essential that the ability of immature DCs to respond to maturation-stimuli and undergo such a phenotypic switch should not be hampered by the materials used in the vaccine development[26].

To evaluate the effect of particle uptake on the DC maturation status, immature DCs were incubated with OVA-loaded PFC particles. Additionally, a part of these samples was exposed to lipopolysaccharide (LPS), a known PAMP and maturation stimulus, 2h after particle addition. In this way, the influence of particle loading on the capacity of the cells to respond to maturation stimuli was assessed. After 24h incubation at 37°C, the cells were surface stained for the DC marker CD11c and the maturation markers CD40 and CD86. The samples were then analyzed by means of flow cytometry.

The results in **Figure 9** show that the uptake of OVA-loaded PFC particles by DCs does not induce an increase in expression of both maturation markers tested, indicating that the DCs do not recognize any danger signals associated with particle uptake. Moreover, DCs that were exposed to LPS 2h after particle uptake, showed up-regulation of both surface markers in a similar way to unloaded LPS-treated DCs. This demonstrates that the particle-loaded DCs are not phenotypically altered due to the intracellular presence of the particles, and preserve their capacity to respond to maturation-stimuli.

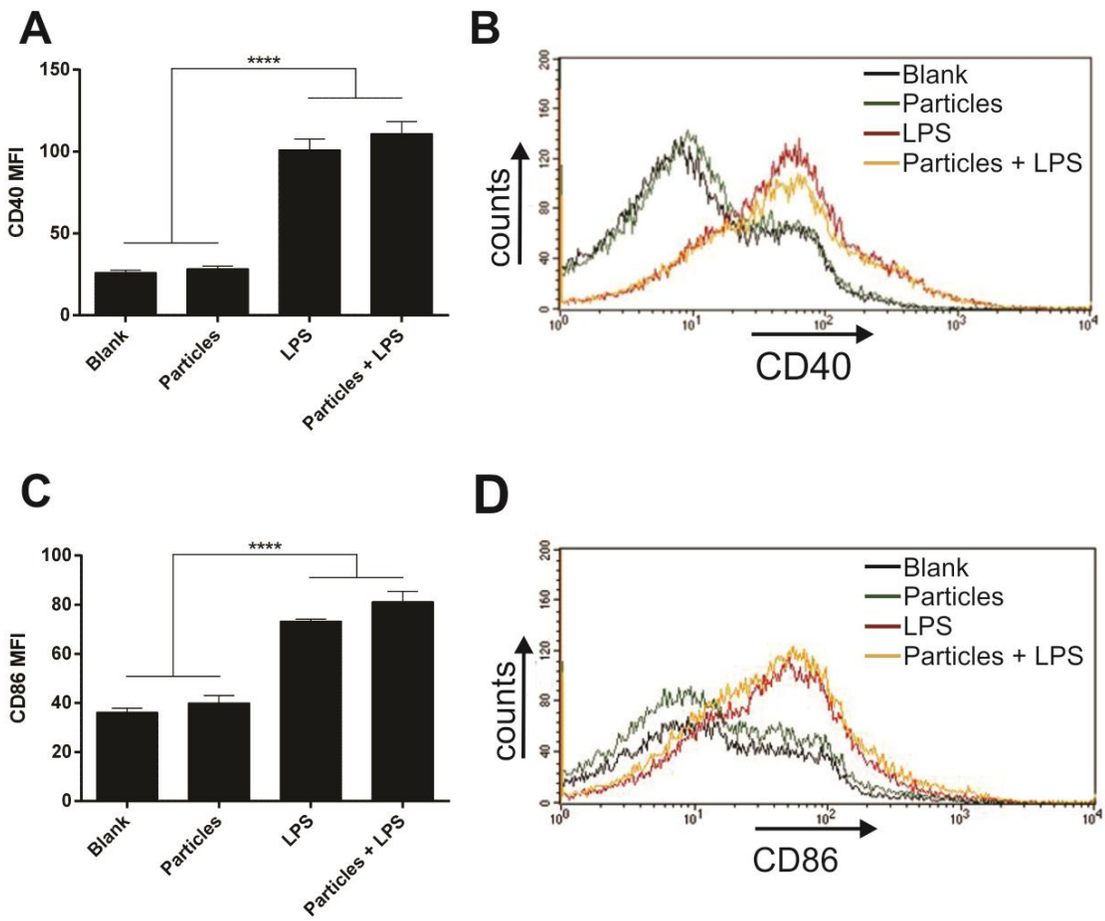

Figure 9. Maturation status of DCs after uptake of OVA-loaded PFC particles.
24h after uptake of OVA-loaded PFC particles by DCs, the cells were surface stained for the DC marker CD11c in addition to the maturation markers CD40 and CD86. (A) Graphic representation of CD40 mean fluorescence intensity (MFI) with (B) a representative histogram. (C) Graphic representation of CD86 MFI with (D) a representative histogram. (*n*=3, **** *p*<0.001).

T cell activation and proliferation by OVA-PFC-particle loaded DCs

In order to assess the potential of OVA-PFC-particle loaded DCs to efficiently present OVA-derived peptides in MHC-I to $CD8^+$ T cells, an *in vitro* OT-I proliferation assay was performed. OT-I cells carry a transgenic CD8 T cell receptor which specifically recognizes the MHC-I restricted OVA peptide SIINFEKL. If these naïve CFSE-labeled T cells are activated by mature DCs that present SIINFEKL in the context of MHC-I, these cells will become activated and start to proliferate, resulting in daughter cells that contain less CFSE and therefore exhibit lower green fluorescence intensities compared to non-proliferated cells. The results, as shown in **Figure 10**, demonstrate that DCs that were incubated with different amounts of OVA-loaded PFCE particles are capable of inducing up to 86.5% proliferation of antigen-specific $CD8^+$ T cells, compared to merely 8.9% proliferation when unloaded PFCE-loaded particles (at 60 particles per DC) were used. Interestingly, no statistically significant differences in OT-I

proliferation could be detected between the highest particle concentration and the SIINFEKL positive control. These data prove that uptake of OVA-loaded PFCE particles by DCs results in efficient antigen presentation, resulting in activation and extensive proliferation of antigen-specific $CD8^+$ T cells.

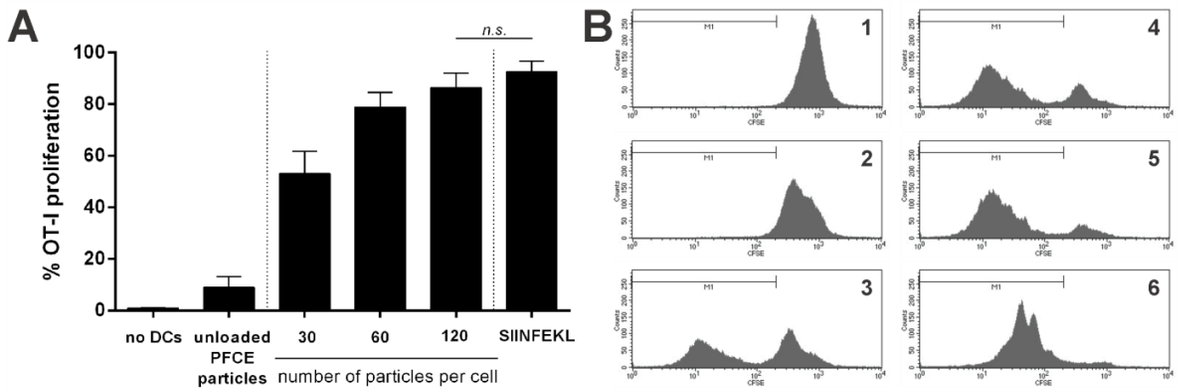

Figure 10. Induction of OT-I proliferation by OVA-PFCE particle loaded DCs.
(A) Graphic representation of the percentage of proliferating OT-I cells after 5 days of co-incubation with DCs. (B) Representative histograms for (1) OT-I cells that were not co-cultured with DCs, OT-I cells co-cultured with (2) DCs containing 60 unloaded PFCE particles per cell, (3) 30 OVA-loaded PFCE particles per cell, (4) 60 OVA-loaded PFCE particles per cell, (5) 120 OVA-loaded PFCE particles per cell or (6) DCs that were loaded with the SIINFEKL peptide, as a positive control. (n=4, *n.s.* = p>0.05)

DISCUSSION

Previous research has shown that the effectiveness of DC vaccines has been partially linked to their *in vivo* localization and the cells' migratory capacities[3, 5, 27, 28]. Therefore we intended to design a theranostic particle for single-step antigen- and PFC-loading of DCs, to allow specific tracing of antigen-containing DCs via ^{19}F MRI. This way, detection of these antigen-presenting cells in the lymph nodes, could be a first feedback on vaccine efficacy. We were able to demonstrate the efficient production of cationic PFC particles, with mean diameters around 0.9 µm that can be electrostatically loaded with multiple layers of OVA. Upon addition of these antigen-loaded particles to *in vitro* cultured BM-DCs, fast and extensive internalization was observed. This efficient uptake makes the use of additional transfection agents, as suggested in previous reports on PFC particles for DC labelling, redundant and consequently simplifies the DC modification[11]. The mild dose-independent cytotoxic effects that were observed 24h after particle uptake can presumably be attributed to the incorporation of a cationic lipid in the particle coating, since liquid PFCs, the other main particle compounds, are well-known to be inert, non-allergenic and non-toxic as they have already been intensively used as artificial oxygen carriers in the clinic[16]. Importantly, the OVA-PFC particle loaded DCs proved

to be very efficient in activating antigen-specific $CD8^+$ T cells, and inducing their proliferation *in vitro*. This indicates that both the antigen dose as well as the means of antigen delivery result in effective T cell priming. Moreover, these results show that the antigen-particle modified DCs are still capable of exerting their crucial role in the induction of immune responses.

It should be noted that in literature, most PFC particles used for cell labelling are nano-sized, with mean particle diameters ranging from 100 to 560 nm[11, 29, 30]. The presented particles were purposefully designed with larger average diameters as this offers several advantages regarding both the antigen-presenting as well as the ^{19}F MRI imaging of the particle-loaded cells. First of all, it was shown that phagosomes are competent organelles in antigen cross-presentation. In this process, phagocytosed exogenous antigens can escape from the phagosomes through a phagosome-to-cytosol pathway and can, as a result, be presented in MHC class I instead of class II on the DC surface. In this way, presentation of exogenous peptides to $CD8^+$ T cells (via MHC-I) can occur, resulting in activation and proliferation of anti-tumor cytotoxic T lymphocytes[31, 32]. In order to promote phagocytic uptake of the antigens, they can be coupled to larger-size particles, seeing as phagocytosis is generally accepted to be the main uptake mechanism for particles >0.5 µm. Therefore, the 0.9 µm antigen-coated PFC particles are expected to be an ideal antigen-delivery vehicle for induction of effective anti-tumor immune responses. Secondly, Tran and Shen recently investigated the effect of particle size and phagosomal pH on cross-presentation efficiency. They found that larger antigen-containing particles (e.g. antigens bound to 0.5 µm and 3 µm beads) resulted in a more neutral phagosomal pH, preventing complete intraphagosomal degradation of the immunogenic peptides, and hence promoting cross-presentation[33]. This is also confirmed by the results of the *in vitro* T cell proliferation assay, where efficient antigen processing and presentation in MHC-I was shown to lead to extensive proliferation of antigen-specific $CD8^+$ T cells. In addition, PFC particle size was also reported to influence the ^{19}F signal. By increasing the particle size by a factor 4.3, a 26.8-fold augmentation of the ^{19}F MR signal amplitude could be detected[30]. As a result, the larger diameter we used for these theranostic particles, is expected to positively influence both antigen-delivery and immunogenicity, as well as ^{19}F MRI traceability. This was also demonstrated by the acquired data showing the fast particle uptake, antigen distribution and proteolytic processing as well as sensitive detection of the particle-loaded cells via ^{19}F MRI.

With regards to this imaging modality, particles containing a PFCE core are preferable over PFH-containing particles. Indeed, PFCE particles exhibit one single ^{19}F NMR signal, representing 20 equivalent fluorine atoms which allows particle detection at high sensitivity and without potential chemical shift artefacts[29]. The number of fluorine spins that could be detected per PFCE-particle-loaded DC was estimated at $2.4x10^{13}$ (corresponding to 40 pmol ^{19}F spins per cell), which is comparable to previous reports on lipid-coated and PLGA-coated PFCE particles for cell tracking[11, 29, 34]. For applications in DC vaccines, the detectability threshold of

1000 cells μl^{-1} for a 40min acquisition is sufficient for future *in vivo* studies, since current protocols make use of intradermal or intranodal injections of at least 10^5 DCs in both mice and man. Even low percentages of migrating cells should then still be detectable by the presented method. Especially in case of intranodal vaccination strategies, unambiguous pinpointing of the injected antigen-loaded cells in an anatomical context should be feasible. In addition, the development in synthesis of new PFCs and the improvement of ^{19}F MRI methods is still ongoing.

To be applicable in DC vaccination, the effects of OVA-loaded PFC particle uptake on the DC phenotype are of key importance. We discovered that OVA-loaded PFC particle uptake did not induce up-regulation of DC maturation markers CD40 or CD86, nor did particle uptake interfere with the ability of the cells to undergo maturation upon stimulation with PAMPs. Previous literature regarding this DC maturation topic has been contradictory. The commercial agent CS-1000 (Celsense Inc., USA) was tested and found to have no influence on the expression of the maturation markers CD80, CD86 and CD83 on human monocyte-derived DCs,[14] nor on CD80 and MHC-II expression on murine BM-DCs[11]. Waiczies et al. on the other hand, reported a significant increase in the expression of both CD80 and CD86 when murine BM-DCs were loaded with larger (560 nm) surfactant-coated PFCE particles compared to smaller (130 nm to 365 nm) particles[30]. In contrast, our layer-by-layer antigen-coated PFC particles do not induce any changes in the DC phenotype. Moreover, complete maturation of DCs after particle uptake is not hindered, and the OVA-PFC-particle loaded DCs can induce extensive proliferation of antigen-specific $CD8^+$ T cells *in vitro*. This represents a major advantage, as it allows complete control over the DC maturation process during the further development of an effective DC vaccine based on these OVA-loaded PFC particles. Maturation could then be provoked by either providing a separate potent maturation stimulus after particle ingestion by the DCs, or the OVA-loaded PFC particles could be equipped with a layer of adsorbed anionic PAMPs (e.g. CpG DNA). Such a particle could make it possible to, in one single step, deliver antigen, a maturation stimulus and a ^{19}F MRI contrast agent to DCs.

CONCLUSIONS

Although PFC particles have been designed in many different forms, equipped with targeting ligands or drugs and were produced to serve various purposes, to our knowledge, this is the first report on a theranostic PFC particle for single-step loading of DCs with both antigenic protein and a ^{19}F MRI contrast agent. The particle consists of a liquid PFC core and can be equipped with multiple adsorbed layers of antigen. Upon *in vitro* modification of DCs with these particles, the antigen-loaded cells can be imaged via ^{19}F MRI and are capable of processing the particle-associated antigen which results in efficient activation and proliferation of antigen-specific $CD8^+$ T cells. Importantly, particle uptake does not compromise cell viability and does not temper with the cell's phenotypical properties.

ACKNOWLEDGEMENTS

The authors would like to express their gratitude to Prof.dr. Ria Cornelissen and Leen Pieters for their help with the transmission electron microscopy. Furthermore, we would like to thank Rein Verbeke for his assistance with the experimental work, and Dr. Roosmarijn Vandenbroucke and Elien Van Wonterghem for their help with the animal handling. The authors would also wish to acknowledge Prof.dr. Karine Breckpot and Cleo Goyvaerts for their assistance with the OT-I proliferation assays.

Heleen Dewitte is a doctoral fellow of the Institute for the Promotion of Innovation through Science and Technology in Flanders, Belgium (IWT-Vlaanderen). Ine Lentacker is a postdoctoral fellow of the Research Foundation-Flanders, Belgium (FWO-Vlaanderen). Uwe Himmelreich acknowledges financial support from the EC FP7-NMP Vibrant (228933), EC FP7 Health-2011-278850 (INMiND) and the KU Leuven PF IMIR.

REFERENCES

1. Steinman, R.M. & Dhodapkar, M. Active immunization against cancer with dendritic cells: the near future. *International Journal of Cancer* **94**, 459-473 (2001).
2. Figdor, C.G., de Vries, I.J.M., Lesterhuis, W.J. & Melief, C.J.M. Dendritic cell immunotherapy: Mapping the way. *Nature Medicine* **10**, 475-480 (2004).
3. Goldberg, B. et al. Contrast-enhanced ultrasound imaging of sentinel lymph nodes after peritumoral administration of Sonazoid in a melanoma tumor animal model. *Journal of ultrasound in medicine : official journal of the American Institute of Ultrasound in Medicine* **30**, 441-453 (2011).
4. Goldberg, B., Merton, D., Liu, J.-B., Murphy, G. & Forsberg, F. Contrast-enhanced sonographic imaging of lymphatic channels and sentinel lymph nodes. *Journal of ultrasound in medicine : official journal of the American Institute of Ultrasound in Medicine* **24**, 953-965 (2005).
5. Verdijk, P. et al. Limited Amounts of Dendritic Cells Migrate into the T-Cell Area of Lymph Nodes but Have High Immune Activating Potential in Melanoma Patients. *Clinical Cancer Research* **15**, 2531-2540 (2009).
6. Yang, W. & Goldberg, B. Microbubble contrast-enhanced ultrasound for sentinel lymph node detection: ready for prime time? *AJR. American journal of roentgenology* **196**, 249-250 (2011).
7. Morse, M.A. et al. Migration of human dendritic cells after injection in patients with metastatic malignancies. *Cancer Research* **59**, 56-58 (1999).
8. de Vries, I.J.M. et al. Magnetic resonance tracking of dendritic cells in melanoma patients for monitoring of cellular therapy. *Nature Biotechnology* **23**, 1407-1413 (2005).
9. Schwarz, S. et al. Synthetic and biogenic magnetite nanoparticles for tracking of stem cells and dendritic cells. *Journal of Magnetism and Magnetic Materials* **321**, 1533-1538 (2009).
10. Schwarz, S. et al. Polyelectrolyte coating of iron oxide nanoparticles for MRI-based cell tracking. *Nanomedicine-Nanotechnology Biology and Medicine* **8**, 682-691 (2012).
11. Ahrens, E.T., Feili-Hariri, M., Xu, H., Genove, G. & Morel, P.A. Receptor-mediated endocytosis of iron-oxide particles provides efficient labeling of dendritic cells for in vivo MR imaging. *Magnetic Resonance in Medicine* **49**, 1006-1013 (2003).
12. Himmelreich, U. et al. A responsive MRI contrast agent to monitor functional cell status. *Neuroimage* **32**, 1142-1149 (2006).
13. Himmelreich, U. & Dresselaers, T. Cell labeling and tracking for experimental models using Magnetic Resonance Imaging. *Methods* **48**, 112-124 (2009).
14. Sever, A. et al. Percutaneous removal of sentinel lymph nodes in a swine model using a breast lesion excision system and contrast-enhanced ultrasound. *European Radiology* **22**, 545-550 (2012).
15. Helfer, B.M. et al. Functional assessment of human dendritic cells labeled for in vivo (19)F magnetic resonance imaging cell tracking. *Cytotherapy* **12**, 238-250 (2010).
16. Krafft, M.P. Fluorocarbons and fluorinated amphiphiles in drug delivery and biomedical research. *Advanced Drug Delivery Reviews* **47**, 209-228 (2001).
17. Ahrens, E.T., Flores, R., Xu, H.Y. & Morel, P.A. In vivo imaging platform for tracking immunotherapeutic cells. *Nature Biotechnology* **23**, 983-987 (2005).
18. Bonetto, F. et al. A novel (19)F agent for detection and quantification of human dendritic cells using magnetic resonance imaging. *International Journal of Cancer* **129**, 365-373 (2011).
19. Srinivas, M. et al. Customizable, multi-functional fluorocarbon nanoparticles for quantitative in vivo imaging using F-19 MRI and optical imaging. *Biomaterials* **31**, 7070-7077 (2010).
20. Mura, S. & Couvreur, P. Nanotheranostics for personalized medicine. *Advanced Drug Delivery Reviews* **64**, 1394-1416 (2012).
21. Janib, S.M., Moses, A.S. & MacKay, J.A. Imaging and drug delivery using theranostic nanoparticles. *Advanced Drug Delivery Reviews* **62**, 1052-1063 (2010).
22. Malaisse, W.J. et al. F-19-heptuloses as tools for the non-invasive imaging of GLUT2-expressing cells. *Archives of Biochemistry and Biophysics* **517**, 138-143 (2012).

23. Waschke, D., Leshch, Y., Thimm, J., Himmelreich, U. & Thiem, J. Synthesis of Fluorinated Ketoheptoses as Specific Diagnostic Agents. *European Journal of Organic Chemistry* **2012**, 948-959 (2012).
24. Decher, G., Eckle, M., Schmitt, J. & Struth, B. Layer-by-layer assembled multicomposite films. *Current Opinion in Colloid & Interface Science* **3**, 32-39 (1998).
25. Moser, M. Dendritic cells in immunity and tolerance - Do they display opposite functions? *Immunity* **19**, 5-8 (2003).
26. Reis e Sousa, C. Essay - Dendritic cells in a mature age. *Nature Reviews Immunology* **6**, 476-483 (2006).
27. MacKay, J.A. & Li, Z. Theranostic agents that co-deliver therapeutic and imaging agents? Preface. *Advanced Drug Delivery Reviews* **62**, 1003-1004 (2010).
28. Srinivas, M., Boehm-Sturm, P., Figdor, C.G., de Vries, I.J. & Hoehn, M. Labeling cells for in vivo tracking using 19F MRI. *Biomaterials* **33**, 8830-8840 (2012).
29. Srinivas, M. et al. Customizable, multi-functional fluorocarbon nanoparticles for quantitative in vivo imaging using 19F MRI and optical imaging. *Biomaterials* **31**, 7070-7077 (2010).
30. Waiczies, H. et al. Perfluorocarbon Particle Size Influences Magnetic Resonance Signal and Immunological Properties of Dendritic Cells. *PLoS ONE* **6** (2011).
31. Houde, M. et al. Phagosomes are competent organelles for antigen cross-presentation. *Nature* **425**, 402-406 (2003).
32. Kovacsovicsbankowski, M. & Rock, K.L. A Phagosome-to-cytosol Pathway for Exogenous antigens Presented on MHC Class-I Molecules. *Science* **267**, 243-246 (1995).
33. Tran, K.K. & Shen, H. The role of phagosomal pH on the size-dependent efficiency of cross-presentation by dendritic cells. *Biomaterials* **30**, 1356-1362 (2009).
34. Bonetto, F. et al. A large-scale 19F MRI-based cell migration assay to optimize cell therapy. *NMR in Biomedicine* **25**, 1095-1103 (2012).

Chapter 4

mRNA-loaded microbubble contrast agents for ultrasound-assisted transfection of dendritic cells

This chapter is published as:

Marie-Luce De Temmerman[1,*], Heleen Dewitte[1,*], Roosmarijn E. Vandenbroucke[2], Bart Lucas[1], Claude Libert[2], Jo Demeester[1] Stefaan C. De Smedt[1], Ine Lentacker[1,§] and Joanna Rejman[1,§] mRNA-lipoplex loaded microbubble contrast agents for ultrasound-assisted transfection of dendritic cells. *Biomaterials* **32**, 9128-9135 (2011).

[*]Both authors contributed equally to this work

[§]Both senior authors contributed equally to this work

[1]Laboratory for General Biochemistry and Physical Pharmacy, Faculty of Pharmaceutical Sciences, Ghent University, Ottergemsesteenweg 460, 9000 Ghent, Belgium

[2]Inflammation Research Center, VIB, Technologiepark 927, 9052 Ghent, Belgium

ABSTRACT

Cancer immunotherapy aims to selectively recognize and eliminate cancer cells. One way to achieve this, is by loading dendritic cells (DCs) with tumor-associated antigens (TAAs), for example by transfecting the DCs with mRNA encoding a TAA. Here we demonstrate transient transfection of DCs *in vitro* using mRNA-loaded microbubbles in combination with ultrasound. We were able to attach mRNA-lipoplexes (*i.e.* complexes of mRNA with cationic lipids) to the surface of lipid microbubbles. When adding these mRNA-loaded microbubbles to primary murine DCs *in vitro* and exposing them to ultrasound, we observed fast-onset ultrasound-triggered transfection in up to 24% of the DCs, with maximal expression levels around 8h after ultrasound application. Interestingly, when looking at the DC maturation status, transfection with mRNA-loaded microbubbles and ultrasound induced a slight but significant shift in the expression level of maturation markers (CD40 and CD86). However, further maturation in the presence of additional maturation stimuli was not affected. Thus, our results demonstrate that mRNA-loaded microbubbles can serve as an applicable and safe tool for efficient mRNA-transfection of cultured DCs.

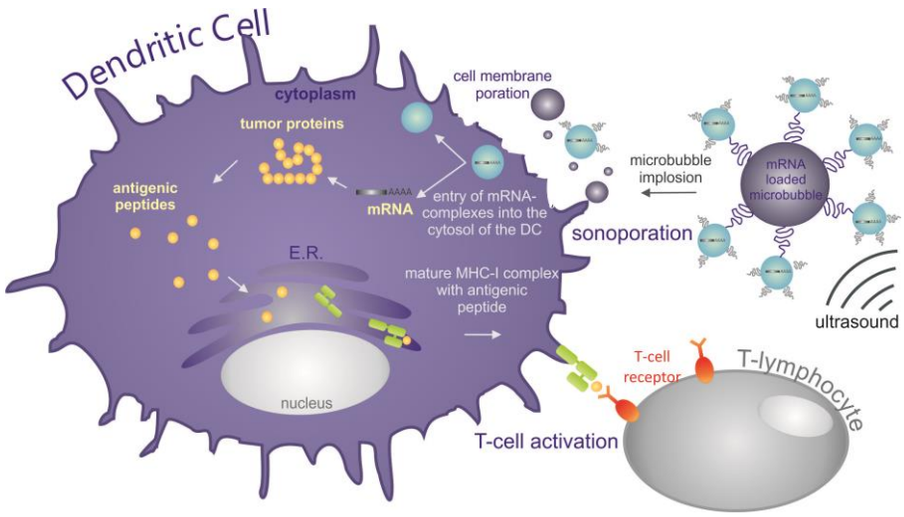

INTRODUCTION

In **Chapter 3**, we showed that theranostic perfluorocarbon particles could be used for simultaneous loading of dendritic cells (DCs) with antigens and ^{19}F MRI contrast agents. This way, cellular vaccines based on these particle-loaded DCs can allow high-resolution tracking of the injected antigen-presenting cells *in vivo*. However, this strategy still focuses on the generation of *ex vivo* DC vaccines. As described in **Chapter 1**, several important drawbacks limit the effectiveness of these *ex vivo* generated vaccines, such as patient-specificity, the fact that "artificial" DCs are used and the high costs associated with the cumbersome vaccine production steps. Hence, there is a growing interest in delivery systems that can target antigens to DCs *in vivo.*

To address this issue, we propose the use of theranostic microbubbles for ultrasound-guided and ultrasound-triggered antigen delivery to DCs. As introduced in **Chapter 1**, it is without doubt that the combination of microbubbles with ultrasound has become an established value in diagnostic medicine. Moreover, their emerging use as theranostics for image-guided and ultrasound-triggered delivery of a plethora of small and large molecules adds to their versatility. New microbubble designs, improved transducers, novel *in vivo* targets, and diverse therapeutic approaches are currently under investigation, so we are only at the beginning of exploring their full potential.

Importantly, when translating the mechanisms of action and current knowledge on microbubbles and ultrasound to the requirements for delivery systems to target DCs *in vivo*, three important facts point towards the potential use of microbubbles and ultrasound for this purpose. First of all, drug- and gene-loaded microbubbles can be used for sonoporation-mediated delivery to various targets *in vivo* and *in vivo*[1-4]. Thus, maybe it could be possible to design a loaded microbubble that could deliver tumor antigens antigen and immune adjuvants to DCs *in vivo*. Secondly, there is convincing evidence that commercially available microbubbles can drain to the lymphatics and end up in the lymph nodes after interstitial injection[5-11]. This implies that these microbubbles can reach the core location of immune response induction, and one of the main homing regions of DCs *in vivo*. Thus, microbubbles can reach their target cells *in vivo*. Thirdly, microbubbles can be imaged via contrast-enhanced ultrasound (CEUS) and have potential as theranostics. This way, the vaccination could become an image-guided therapy where the antigen-loaded microbubbles are followed during their migration to the lymph nodes. Moreover, their disappearance after delivery of the high-intensity ultrasound bursts required for microbubble implosion and antigen transfer, can also be visualized using CEUS[12, 13]. Bundling these concepts gave rise to the idea of using microbubbles as a potential means of locally delivering antigens and adjuvants to DCs in the

lymph nodes under ultrasound-guidance. Whether or not this has potential, will be the topic of investigation in the chapters to follow.

Once the delivery vehicle is chosen, the next step is to select the source of tumor antigens that will be introduced into the DCs. In recent years, the focus of research has shifted from peptide and protein loading of DCs towards genetic approaches, where DNA or RNA is delivered into isolated DCs[14-16]. Translation of the proteins by the DC itself is attractive as it paves the way to antigen presentation in both MHC-II and MHC-I. Moreover, these strategies hold the potential to introduce multiple epitopes, ultimately yielding an immune response against the broad antigenic repertoire of the tumor. As compared to DNA-based approaches, RNA-based vaccination presents several advantages. Firstly, RNA does not integrate into the genome, rendering its application much safer. Secondly, while in non-dividing cells, the nuclear envelope represents a serious obstacle for the delivery of DNA into the nucleus, this obviously does not apply to RNA[17]. Finally, although RNA generates only transient protein expression, this should be adequate for antigen processing and presentation by DCs.

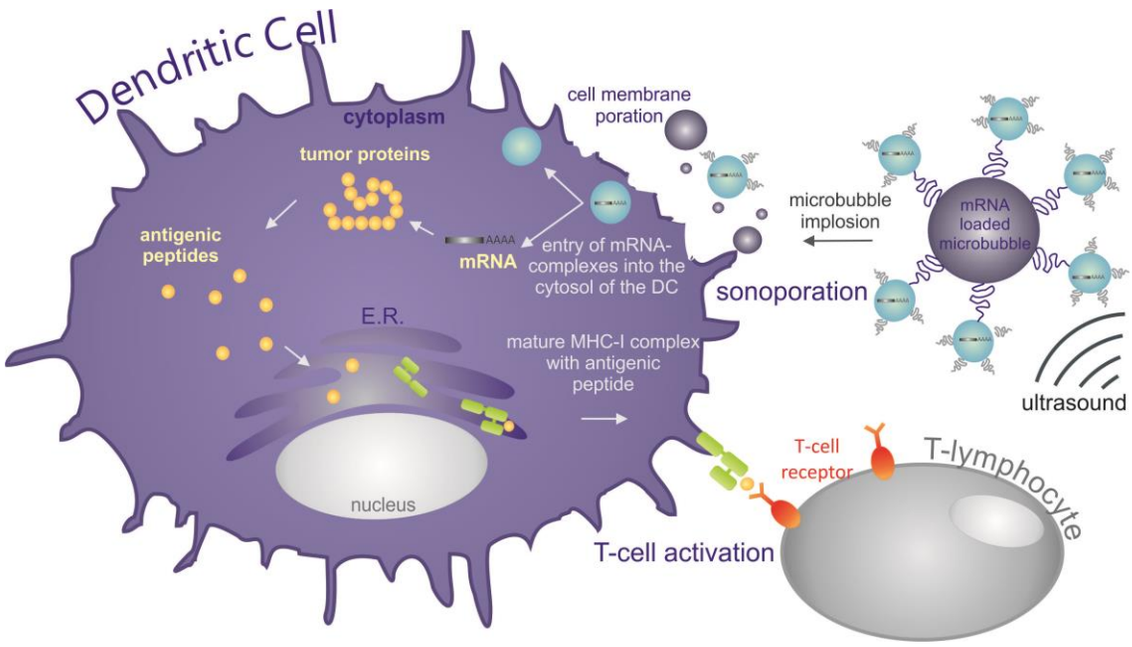

Figure 1. Schematic image of ultrasound-triggered mRNA-transfection of DCs. When mRNA-loaded microbubbles are exposed to ultrasound in the presence of DCs, the microbubbles will implode, leading to the local formation of pores in the DC membrane, as well as in local release of mRNA-lipoplexes from the surface of the imploding microbubble. As a result, the mRNA-lipoplexes can be taken up through the created pores and immediately enter into the DC cytoplasm. Upon mRNA translation, antigenic protein is produced, and processed into peptide fragments which can be loaded onto MHC molecules and presented to T cells.

Thus, the specific aims of this study were (a) to evaluate the potential of ultrasound-responsive microbubbles loaded with mRNA-complexes to transfect DCs, (b) to measure the levels and kinetics of marker protein production following transfection, and (c) to reveal the impact of ultrasound treatment on the viability and maturation status of DCs. A schematic overview of the concept of mRNA-loaded microbubbles and ultrasound for mRNA delivery to DCs in light of cancer immunotherapy, is presented in **Figure 1**.

MATERIALS AND METHODS

Cell culture

Primary DC cultures were generated from the bone marrow of C57BL/6 mice. Female C57BL/6 mice were purchased from Janvier (Le Genest Saint Isle, France) and housed in a specified pathogen-free facility according to the regulations of the Belgian law and the local Ethical Committee. Mice were sacrificed and bone marrow was flushed out of the femur and tibia. After red blood cell lysis (Pharm Lyse Buffer, BD Biosciences), cells were seeded at a density of $5x10^5$ cells ml^{-1} in OptiCells™ (Nunc, Thermo Scientific, Aalst, Belgium) and incubated at 37°C in 5% CO_2. The cell culture medium was RPMI-1640 (Gibco-Invitrogen, Merelbeke, Belgium) supplemented with 5 % FCS (Hyclone, Pierce, Rockford, IL, USA), 1% penicillin / streptomycin (Gibco-Invitrogen, Merelbeke, Belgium), 1% L-glutamine (Gibco-Invitrogen, Merelbeke, Belgium) and 50 μM β-mercaptoethanol (Gibco-Invitrogen, Merelbeke, Belgium) and contained also 10 ng ml^{-1} IL-4 (Peprotech, Rock Hill, NJ) and 10 ng ml^{-1} granulocyte macrophage colony-stimulating factor (GM-CSF, Peprotech, Rock Hill, NJ). At day 2 and 6 of culture, the non-adherent cells were collected by centrifugation, resuspended in fresh culture medium and seeded to the same OptiCell™. The cells were treated 7 days after seeding.

Messenger RNA

To produce mRNA by *in vitro* transcription, plasmids encoding luciferase and enhanced green fluorescent protein (eGFP) were purified using a QIAquick PCR purification kit (Qiagen) and linearized using *Dra* I restriction enzyme (plasmid encoding firefly luciferase) or *Spe* I (plasmid encoding eGFP). Linearized plasmids were used as templates for the *in vitro* transcription reaction using the T7 mMessage mMachine kit (Ambion). mRNAs were purified by DNase I digestion and precipitated with LiCl. This was followed by washing with 70% ethanol. The produced mRNAs were both capped and polyadenylated. The mRNA concentration was determined by measuring the absorbance at 260 nm. mRNAs were stored in small aliquots at -80°C at a concentration of 1 μg $μl^{-1}$.

Bioluminescence assay

All cells were removed from OptiCells™ and collected by centrifugation. After removing the culture medium, the cells were washed once with PBS (Gibco/Invitrogen, Merelbeke, Belgium). Subsequently, 100 µl of Cell Culture Lysis Reagent (Promega, Leiden, The Netherlands) was added. After incubation for 30min, the samples were centrifuged (12,000 rpm at 4°C for 5min) and 40 µl aliquots of the supernatants were transferred to a 96-well plate. Luciferase activity of each sample was assayed in a GloMax™ 96 Luminometer (Promega, Leiden, The Netherlands). 100 µl of the substrate solution was added to each well and the emitted light was measured over a 10s period. A standard Bradford assay was employed to determine the protein content of each sample (Biorad, Nazareth Eke, Belgium). The results are expressed as relative light units (RLU) per milligram of protein.

Lipoplexes

If not indicated differently, liposomes were composed of 42.5 % DOTAP (1,2-dioleoyl-3-trimethylammonium-propane), 42.5% DOPE (1,2-dioleoyl-*sn*-glycero-3-phosphoethanolamine) and 15% DSPE-PEG-2000-biotin [1,2-distearoyl-*sn*-glycero-3-phosphoethanol-amine-N-[biotinyl(polyethylene glycol)-2000] (all from Avanti Polar Lipids, Alabaster, AL). This was done by transferring the appropriate amounts of lipids, dissolved in $CHCl_3$ into a round-bottom flask. The $CHCl_3$ was evaporated under nitrogen and the resulting lipid film was rehydrated in RNase-free water (Ambion, Lennik, Belgium). The resulting DOTAP/DOPE/PEG liposomes were sonicated. The total lipid concentration in these liposomes was 1 mg ml^{-1}. Fluorescently labeled liposomes were obtained by incorporation of 1% NBD-PE (phosphatidylethanolamine-N-(7-nitro-1,3-benzoxadiol-4-yl)) (Avanti Polar Lipids, Alabaster, AL).

Preparation and characterization of biotinylated microbubbles

Microbubbles were prepared starting from a solution of a mixture of DPPC (1,2-dipalmitoyl-*sn*-glycero-3-phosphocholine) (Lipoid, Ludwigshafen, Germany) and DSPE-PEG-biotin [1,2-distearoyl-*sn*-glycero-3-phosphoethanolamine-N-[biotin(polyethylene glycol)-2000] (Avanti Polar Lipids, Alabaster, AL) in a 1:2:7 glycerol-propyleneglycol-H_2O solvent (Sigma-Aldrich, Bornem, Belgium). The molar ratio of the lipids in the lipid solutions was 85:15. The lipid solution was prepared as follows. Appropriate aliquots of both lipids, dissolved in $CHCl_3$, were transferred to a round bottom flask. After $CHCl_3$ evaporation, the lipid film was dissolved in a 1:2:7 glycerol-propyleneglycol-H_2O mixture to obtain a clear solution with a final lipid concentration of $4.6x10^{-4}$ mmol ml^{-1}. Aliquots of this lipid solution were transferred to 2.5 ml chromatography vials, the headspace of which was filled with C_4F_{10} gas (F2 chemicals, Preston, UK). Finally, microbubbles were obtained by high-frequency shaking of the lipid solution in a

Capmix™ device (3M-ESPE, Diegem, Belgium) during 15s. The size and the concentration of the microbubbles in the dispersion (*i.e.* number of microbubbles per ml) were determined with a Beckman-coulter Multisizer 4 (Beckman-coulter, Brea, CA).

Transfection

mRNA encoding luciferase or eGFP was complexed with cationic liposomes and the resulting complexes were attached to the microbubble surface via avidin-biotin interaction, as shown in Fig. 2A. The cells were transfected 7 days after seeding. Different amounts of DOTAP/DOPE/PEG liposomes were dispersed in 50 µl of OptiMem® (Invitrogen, Merelbeke, Belgium). This solution was mixed with 50 µl of mRNA solution in OptiMem®. After 10min of incubation at RT, 900 µl of OptiMem® was added. Subsequently, the mixture was added to the microbubble solution in OptiMem®. After a short incubation of the cells with mRNA-loaded microbubbles, ultrasound was applied (Sonitron 2000, Artison, Inola, OK, USA) (1 MHz, 2 W cm^{-2} corresponding to a peak negative pressure of 800 kPa, 20% duty cycle (2ms on, 8ms off), 30s total insonation time per OptiCell™).

BM-DC staining for flow cytometric analysis and confocal microscopy

Transfected cells were surface stained for CD11c following the manufacturer's protocols and instructions (BD Pharmingen, Erembodegem, Belgium). Briefly, cells were surface stained for CD11c-APC or CD11c-FITC (both BD Pharmingen) for 1h at 4°C. Cells were washed twice and resuspended in flow buffer (PBS containing 1% BSA and 0.1% azide) for flow cytometric analysis or confocal microscopy.

Dendritic cell maturation

The effect of the mRNA-lipoplex loaded microbubbles and ultrasound application on the DC maturation status was assessed by evaluating up-regulation of the maturation surface markers CD40 and CD86. Briefly, following transfection the cells were transferred to 24 well plates and cultured with or without addition of *Escherichia coli*-derived lipopolysaccharide (LPS, 1 µg ml^{-1}, Sigma Aldrich, Bornem, Belgium) to the culture medium. 24h after exposure of DCs to mRNA-lipoplexes, microbubbles and/or ultrasound, the cells were washed with flow buffer and incubated on ice for 30min with 5% goat serum in PBS. Then cells were stained for CD11c-FITC in combination with staining for CD40-PE or CD86-PE (all BD Pharmingen) for 1h on ice, followed by washings with flow buffer. Untreated and LPS stimulated cells were used as negative and positive controls respectively.

Flow cytometric analysis

Flow cytometric data were acquired using a FACSCalibur™ flow cytometer (BD Pharmingen) and data were analyzed using CellQuest™ software. In all experiments, DCs were identified based on their CD11c-APC or CD11c-FITC surface staining. Intracellular localization of mRNA-lipoplexes was determined by using fluorescently labeled liposomes. Transfection efficiency was evaluated by measuring eGFP expression in gated DCs.

Confocal Microscopy

Confocal microscopy images of mRNA-loaded microbubbles and transfected DCs were recorded using a Nikon C1si confocal laser scanning microscopy module (CLSM) attached to a motorized Nikon TE2000-E inverted microscope (Nikon Benelux, Brussels, Belgium). A sample of microbubbles or cell suspension was placed on a cover glass and analyzed with CLSM using a water immersion objective lens (Plan Apo 60X, NA 1.2, collar rim correction, Nikon).

Toxicity assay

Cytotoxicity was evaluated 24h after transfection of DCs in OptiCells™ using a SYTOX® green nucleic acid stain (Molecular Probes/Invitrogen, Merelbeke, Belgium). 24h after treatment, the cells were washed in HEPES buffer and nuclei of non-viable cells were stained with a 45 nM SYTOX® green solution for 30min on ice. Prior to flow cytometric analysis, samples were diluted in flow buffer.

RESULTS

Characterization of microbubbles loaded with mRNA-lipoplexes

To avoid degradation by nucleases and to achieve sustained circulation time *in vivo* nucleic acids-based drugs are often complexed with cationic lipids and modified with polyethylene glycol (PEG). The latter also serves to prevent complex clearance by the reticuloendothelial system[18] thus enhancing the chance of uptake by the target cells.

As described in the material and methods section, mRNA-lipoplexes were prepared by mixing mRNA with DOTAP/DOPE liposomes. The resulting lipoplexes were attached to microbubbles via biotin-avidin-biotin bridges as schematically depicted in **Figure 2A**. To be responsive to ultrasound frequencies used for diagnostic imaging (1-5 MHz) and enable microbubble implosion, microbubbles should ideally have a diameter between 1 and 7 µm[19]. We determined the size of microbubbles by coulter counter measurements. The mean volume

diameter of microbubbles employed in this study was 4.4 ± 1.6 µm (consistent with a mean number diameter of 2.3 ± 1.2 µm), which meets these requirements. The effective binding of mRNA-lipoplexes to microbubbles was demonstrated by confocal microscopy. As shown in **Figure 2B** fluorescently labelled mRNA-lipoplexes clearly mark the bubble surface.

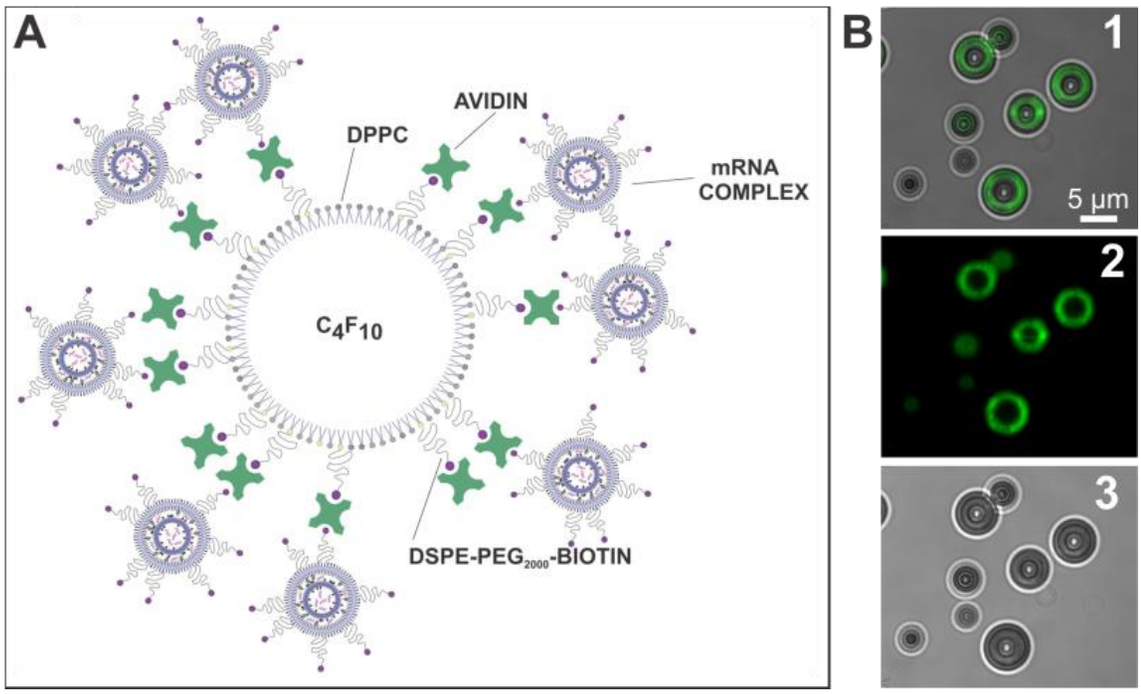

Figure 2. mRNA-lipoplex-loaded microbubbles.

(A) Schematic representation of an mRNA-loaded microbubble. To generate mRNA-loaded microbubbles, mRNA was complexed with cationic liposomes consisting of DOTAP, DOPE and DSPE-PEG-biotin. The resulting mRNA-lipoplexes were loaded onto the microbubble surface via avidin-biotin interactions. (B) Confocal micrographs of avidinylated microbubbles after incubation with fluorescently labelled biotinylated mRNA-lipoplexes: (1) overlay; (2) fluorescently labelled mRNA-lipoplexes; (3) transmission.

Ultrasound-triggered delivery of mRNA-lipoplexes

To investigate whether mRNA-loaded microbubbles could be used for the intracellular delivery of mRNA-lipoplexes to DCs, DCs were incubated with microbubbles loaded with fluorescently labelled mRNA-lipoplexes and exposed to ultrasound. 15min after ultrasound application, the cells were collected, surface stained for CD11c and analyzed by flow cytometry. As shown in **Figure 3**, over 50% of DCs contained fluorescently labelled mRNA-lipoplexes. By contrast, negligible uptake of complexes (<1%) was observed if cells were incubated with free mRNA-lipoplexes or lipoplex-loaded microbubbles without application of ultrasound.

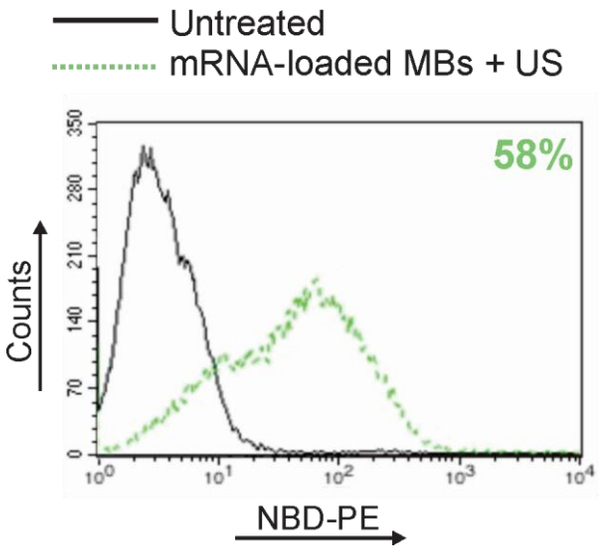

Figure 3. Intracellular localisation of fluorescently labelled mRNA-lipoplexes. Fluorescently labeled mRNA-lipoplexes, containing 1% NBD-PE, were attached to the microbubbles (MBs) and added to DCs. 15min after ultrasound exposure, the cells were thoroughly washed to remove non-internalized complexes, which was followed by anti-CD11c-APC surface staining and flow cytometric analysis.

The insignificant uptake of free mRNA-lipoplexes by DCs can be explained by the high degree of PEGylation (15-20%) of the complexes used in this study. It is known that such a hydrophilic coating reduces uptake of the complexes because it shields their positive charge thereby preventing interactions with the negatively charged cell surface[20]. Moreover, it has been demonstrated that PEGylated particles, taken up by the cells via endocytosis, get trapped in the endo-lysosomal compartment, which impedes their release into the cytosol[21]. One possible way to overcome this problem, is to deliver PEGylated particles directly into the cytosol as achieved by ultrasound-assisted delivery. Our group has shown that microbubble implosion creates temporary cell membrane perforations and at the same time pushes the complexes through such pores[22].

Transfection efficiency of mRNA-lipoplex loaded microbubbles

To assess the ability of mRNA-lipoplex loaded microbubbles to transfect DCs, an mRNA encoding luciferase was employed. The expression kinetics were characterized by determining the levels of luciferase at different time points. For this reason we used firefly luciferase mRNA as this is known to have a very rapid intracellular turnover with a half-life of 3h[23]. As shown in **Figure 4**, significant protein expression occurs as early as 30min after mRNA-delivery. Maximal levels of luciferase were detected 8h after ultrasound application. Upon longer incubation, protein levels gradually declined. Furthermore, no luciferase activity was detected when only mRNA-lipoplexes were added to the cells, consistent with the insignificant uptake of mRNA-lipoplexes by the DCs if neither microbubbles nor ultrasound were applied. This proves that

mRNA transfection of DCs can indeed be triggered by means of ultrasound and thus opens possibilities towards an image-guided spatiotemporally controlled vaccination system, as will be discussed later on.

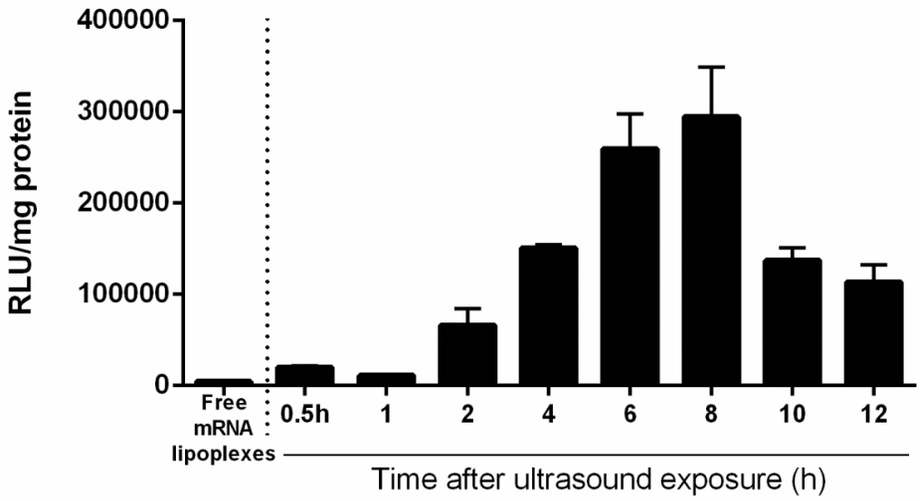

Figure 4. Transfection efficiency of mRNA lipoplex-loaded microbubbles.
mRNA encoding luciferase was complexed with DOTAP/DOPE/PEG lipoplexes and added to microbubbles after which ultrasound was applied. Levels of luciferase activity in DCs at different time points after ultrasound exposure were assayed by measuring bioluminescence. Graphs are summaries of two independent experiments at *n*=3. Transfection efficiency of free PEGylated mRNA lipoplexes was assayed 2h after addition to the cells.

In addition to measuring total levels of protein expression, we evaluated the number of transfected cells. To that end, DCs were transfected with complexes carrying eGFP mRNA. The percentage of DCs expressing eGFP was evaluated 24h after transfection by means of flow cytometry. The influence of the transfection protocol on the background fluorescence signal of the DCs was verified by using mRNA encoding luciferase. Application of ultrasound in combination with mRNA-loaded microbubbles resulted in transfection of up to 24% of the DCs (**Figure 5A**). Ultrasound-assisted transfection of DCs with free mRNA-lipoplexes did not result in transfection (<1%; data not shown). These results were confirmed by confocal analysis of transfected DCs. **Figure 5B** shows surface stained DCs (anti-CD11c-APC) expressing eGFP.

These transfection data provide proof of concept for the use of mRNA-loaded microbubbles to transfect DCs. Although 50% of DCs were shown to contain mRNA-complexes after this treatment (Figure 3), only 24% of the cells expressed eGFP (Figure 5A). This may be due to the incomplete release of the mRNA from the lipoplexes.

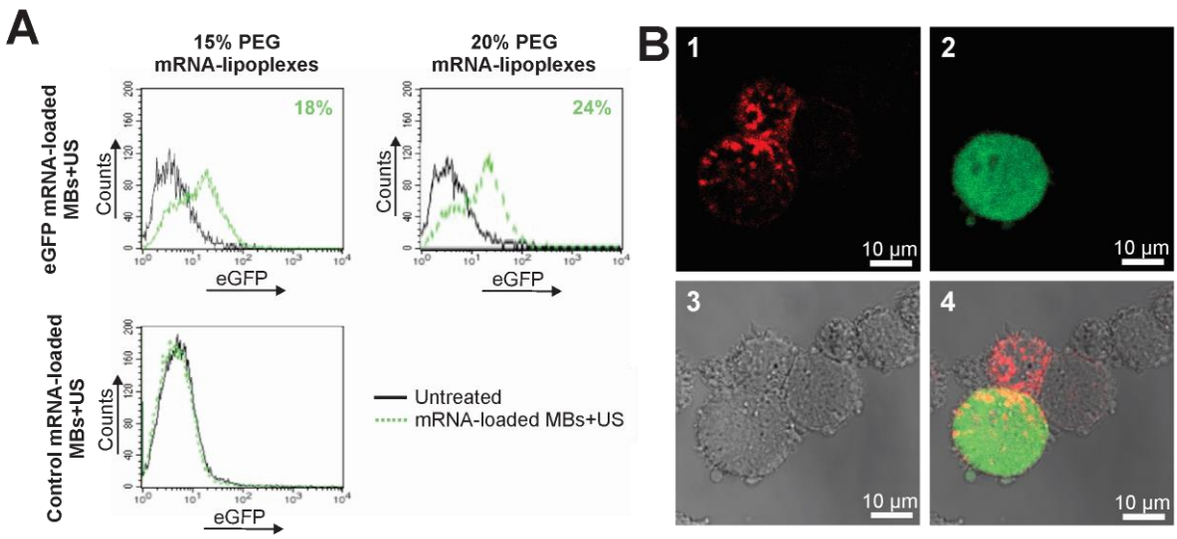

Figure 5. Transfection efficiency of mRNA-loaded microbubbles.

(A) mRNA encoding eGFP was complexed with DOTAP/DOPE/PEG liposomes (15% or 20% PEG) and added to microbubbles (MBs) and ultrasound was applied. As a control, DCs were transfected with luciferase mRNA. CD11c$^+$ DCs were analyzed for eGFP expression by flow cytometry 24h after transfection. (B) Confocal images of DCs after transfection with mRNA lipoplex-loaded microbubbles and ultrasound. (1) overlay; (2) CD11c-APC stain; (3) eGFP expression; (4) transmission.

mRNA electroporation has been shown to achieve transfection efficiencies of up to 70% for DCs[24]. However, Grünebach et al. proved that high transfection efficiencies are not essential to elicit effective T cell responses. They even succeeded in eliciting antigen-specific cytotoxic T cell (CTL) responses with low to hardly detectable (<1%) transfection efficiencies[25]. Several suggestions explaining this phenomenon were brought forward. Firstly, the CTL assay is possibly more sensitive than flow cytometry in detecting low levels of antigen. Secondly, not all antigenic peptides that are recognized by CTLs are necessarily derived from biologically functional proteins. Even protein fragments translated from damaged mRNA could be processed into antigenic peptides that can elicit CD8$^+$ T cells. Taking all this together, we may conclude that the transfection results obtained with mRNA-loaded microbubbles and ultrasound are likely to be sufficient for effective stimulation of the immune system.

Cell via*bility of DCs following ultrasound exposure*

The potential of mRNA delivery by means of ultrasound can be properly evaluated only if potentially toxic effects on the cells are taken into consideration. To assess the effect of the mRNA-complexes, microbubbles and ultrasound on DC viability, we utilized a SYTOX® green nucleic acid stain. Flow cytometric analysis indicated a survival of 84% of the cells after exposure to mRNA-lipoplex loaded microbubbles, 85% after exposure to unloaded microbubbles combined with ultrasound and 79% after addition of mRNA-loaded microbubbles with ultrasound application (**Figure 6**). This corresponds with data reported by Suzuki et al. and indicates that most of the DCs are indeed able to completely restore the ultrasound-induced cell membrane damage within 24h[26]. The percentage of dead cells after sonoporation is comparable to that resulting from electroporation, where 80-90% viability has been reported for human monocyte-derived DCs, depending on the physical parameters used[25, 27]. Moreover, the 85% toxicity observed when unloaded bubbles were used in combination with ultrasound correlates with prior results of our group on other cell types[28]. This indicates that DCs are not particularly sensitive to sonoporation-induced damage.

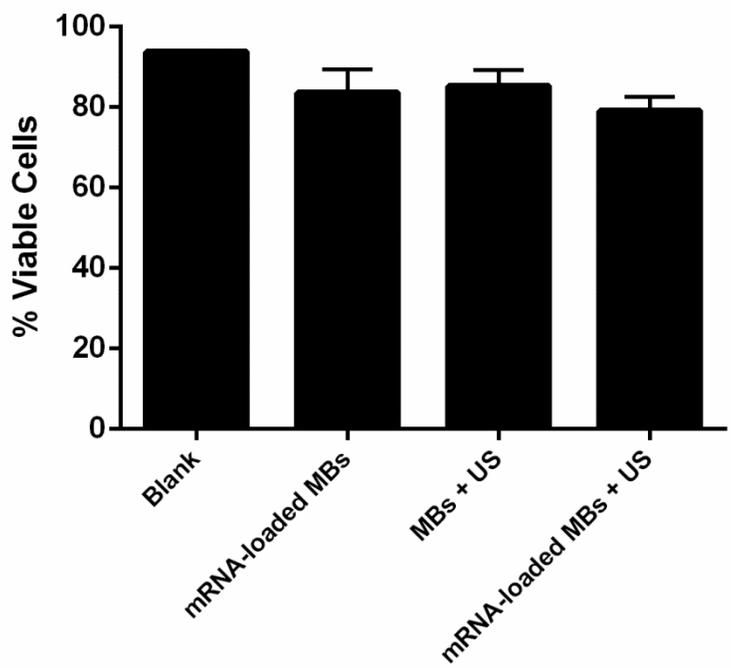

Figure 6. Cell viability.

DCs were exposed to mRNA-loaded microbubbles or microbubbles (MBs) and ultrasound (US) or mRNA-loaded microbubbles and ultrasound. After treatment, cells were stained with SYTOX® green nucleic acid stain to identify dead cells. (*n*=3)

Maturation status of transfected DCs

In the context of DC-based vaccination strategies, the DC maturation status should be taken into consideration. This is a series of changes in the DC phenotype, shifting DC function from antigen-sampling to antigen-presentation. As a result, this maturation process is crucial for the ability of DCs to prime naive T cells[29, 30]. We determined whether the mRNA-loaded microbubbles and the ultrasound treatment have an influence on DC maturation. To that end, DCs were evaluated with respect to the expression of the co-stimulatory markers (CD40 and CD86) 24h after transfection. Moreover, we investigated the susceptibility of treated DCs to additional maturation stimuli. Therefore, DCs were cultured in the absence or presence of a maturation stimulus (lipopolysaccharide, LPS), added immediately after transfection.

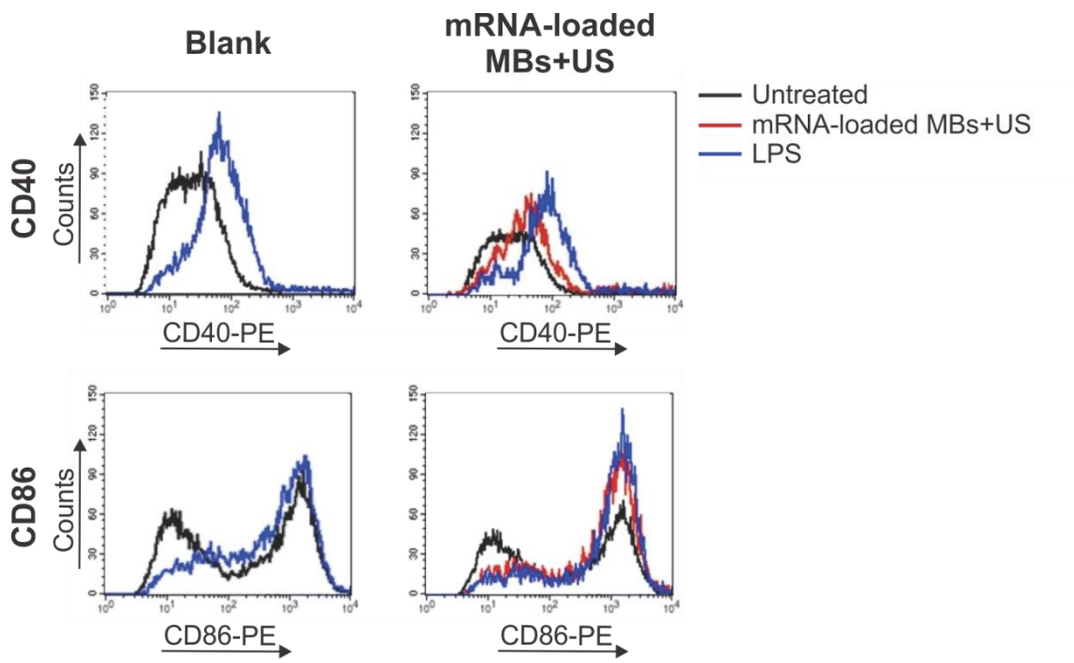

Figure 7. Maturation of DCs.

Representative histograms illustrating phenotypic maturation of DCs in response to mRNA-loaded microbubbles (MBs) and ultrasound (US). 24h after transfection, DCs were stained for the DC marker CD11c and maturation markers CD40 or CD86 and assessed by flow cytometry. Untreated DCs and LPS-stimulated DCs served as negative and positive controls, respectively.

An overview of the phenotypic maturation of DCs in response to mRNA-loaded microbubbles and ultrasound is given in **Figure 7**. In the absence of additional maturation signals, transfection of immature DCs with mRNA-loaded microbubbles and ultrasound application induced only a minor shift in the expression level of CD40 and a slightly higher increase of CD86, compared to that in the untreated cells. However, in the presence of the activation stimulus LPS, cells were able to further mature as shown by a significant up-regulation of CD40 expression. We take this to indicate that the transfection procedure did not

negatively affect the capacity of DCs to respond to pathogen-associated molecular patterns (PAMPs) and to become activated. Immature DCs exposed to either ultrasound or microbubbles did not express higher levels of CD40 and CD86, while LPS stimulation of these cells induced expression of these markers. Taken together, these observations indicate that the slight phenotypical changes in DC maturation status were solely due to the mRNA-complexes which had been delivered and that the transfection procedure itself did not induce phenotypical changes in the treated DCs.

DISCUSSION

We were able to show that mRNA-lipoplexes can be attached to the surface of ultrasound-responsive microbubbles via biotin-avidin-biotin bridges. Secondly, we demonstrated an effective uptake of mRNA-lipoplexes by DCs resulting in a significant expression of luciferase and eGFP by DCs after ultrasound-triggered transfection with mRNA-loaded microbubbles, without compromising DC viability and maturation capacities. In 2009 Suzuki and colleagues reported on the use of microbubbles and ultrasound to pulse DCs with ovalbumine[26]. They showed that this resulted in MHC-I presentation and the development of a strong $CD8^+$ T cell response. These results are very encouraging as this indicates that the combination of microbubbles and ultrasound can be a powerful vaccination tool. We believe that, compared to the system proposed by Suzuki et al. for vaccination purposes, the development of an mRNA-loaded microbubble offers several advantages. Firstly, when considering the use of autologous tumor-derived antigens, even small tumor samples may yield sufficient amounts of mRNA, while for protein extraction relatively large tumor samples are required. Moreover, co-transfection with mRNA encoding maturation stimuli could be possible, leading to enhanced cytokine signaling, thus strengthening the desired immune response[31].

The most important outcome of our findings is that ultrasound-assisted transfection of DCs might eliminate the need of *ex vivo* procedures in the development of a DC vaccine, as we will elaborate below. This is important because besides the problems of costs and labor-intensiveness of current DC vaccination procedures, it has been suggested that the capacity of the *in vitro* cultured and transfected DCs to migrate to the lymph nodes is sub-optimal[32]. To address this drawback, the DC vaccine has been injected intranodally[33, 34]. Alternatively, *in vivo* transfection of DCs could be considered. The latter is particularly interesting, considering that currently used *ex vivo* generated monocyte-derived DCs are subject to debate. It has become more and more clear that this type of DCs merely represents one of the many subsets that can be found *in vivo*. As it remains unclear which particular DC subtypes are responsible for the most efficient CTL priming, it would be advantageous to transfect several of these DC subtypes in an *in vivo* setting[30, 35]. For this purpose, the ideal location would be the lymph nodes, as these organs are populated by large numbers of both resident and migratory DCs. In this connection,

it has been reported that intranodal delivery of naked pDNA resulted in an important increase of vaccine immunogenicity[36, 37]. Although this is a promising observation, the unprotected DNA is rapidly cleared and still has to make its way across the plasma membrane, avoid lysosomal degradation and cross the barrier of the nuclear membrane before it can be transcribed and translated into an antigenic protein. Therefore, this approach is obviously amenable to substantial improvement.

Microbubbles and ultrasound could provide a possible solution, allowing an increase in transfection efficiency of intranodally located DCs. We care to stress here that besides the *in vitro* proof presented in the present work, satisfactory transfection efficiencies with microbubbles and ultrasound have been shown also *in vivo*[38, 39]. Furthermore, our suggestion to use microbubbles for intranodal DC transfection is supported by the consideration that microbubbles have already been used clinically as ultrasound contrast agents in the lymphatics, and more specifically, as means to visualize sentinel lymph node metastases[7, 10]. This would imply that a non-invasive intradermal injection of the mRNA-loaded microbubbles would be sufficient to obtain intranodal localization of the nucleic acids. Intranodal location of the microbubbles – and hence of the mRNA – can easily be visualized as the presence of the bubbles will be revealed by enhanced ultrasound contrast. This way, the complete vaccination procedure could be divided into a first phase of low intensity ultrasound, allowing microbubble visualization and a second phase, where the ultrasound intensity is increased to cause microbubble collapse and subsequent DC transfection.

CONCLUSIONS

Our results demonstrate that mRNA-loaded microbubbles can be used as an efficient ultrasound-triggered transfection tool for DCs, without compromising cell viability or DC maturation capacities. These findings are especially important in the context of a possible *in vivo* use of this technique. Needless to say that direct *in vivo* transfection of DCs would not only eliminate the need for costly *ex vivo* DC handling and transfection, but it could also allow transfection of several DC subsets which would broaden the generated immune response. The feasibility of this approach will further be explored in the following chapters.

ACKNOWLEDGEMENTS

Heleen Dewitte is a doctoral fellow of the Institute for the Promotion of Innovation through Science and Technology in Flanders, Belgium (IWT-Vlaanderen). Ine Lentacker is a postdoctoral fellow of the Research Foundation-Flanders, Belgium (FWO-Vlaanderen). The support of both these institutions is gratefully acknowledged. We would also like to thank this institution for granting the BRAINSTIM project. This research was funded through the FWO research Grant G.0187.11.

REFERENCES

1. Bekeredjian, R., Grayburn, P.A. & Shohet, R.V. Use of ultrasound contrast agents for gene or drug delivery in cardiovascular medicine. *Journal of the American College of Cardiology* **45**, 329-335 (2005).
2. Ferrara, K., Pollard, R. & Borden, M. Ultrasound microbubble contrast agents: Fundamentals and application to gene and drug delivery. *Annual Review of Biomedical Engineering* **9**, 415-447 (2007).
3. Geers, B., Dewitte, H., De Smedt, S.C. & Lentacker, I. Crucial factors and emerging concepts in ultrasound-triggered drug delivery. *Journal of Controlled Release* **164**, 248-255 (2012).
4. Newman, C.M. & Bettinger, T. Gene therapy progress and prospects: ultrasound for gene transfer. *Gene Therapy* **14**, 465-75 (2007).
5. Goldberg, B.B. et al. Contrast-enhanced ultrasound imaging of sentinel lymph nodes after peritumoral administration of Sonazoid in a melanoma tumor animal model. *Journal of ultrasound in medicine : official journal of the American Institute of Ultrasound in Medicine* **30**, 441-53 (2011).
6. Goldberg, B.B., Merton, D.A., Liu, J.B., Murphy, G. & Forsberg, F. Contrast-enhanced sonographic imaging of lymphatic channels and sentinel lymph nodes. *Journal of ultrasound in medicine : official journal of the American Institute of Ultrasound in Medicine* **24**, 953-65 (2005).
7. Goldberg, B.B. et al. Sentinel lymph nodes in a swine model with melanoma: contrast-enhanced lymphatic US. *Radiology* **230**, 727-34 (2004).
8. Sever, A. et al. A novel approach to identify sentinel lymph nodes using microbubbles and contrast enhanced ultrasound in preoperative breast cancer patients. *Journal of Clinical Oncology* **27** (2009).
9. Sever, A., Jones, S., Weeks, J., Mills, P. & Jones, P. Successful outpatient identification of the sentinel lymph node with ultrasound using microbubbles in breast cancer patients: final results. *British Journal of Surgery* **97**, 28-28 (2010).
10. Sever, A.R. et al. Preoperative Sentinel Node Identification With Ultrasound Using Microbubbles in Patients With Breast Cancer. *American Journal of Roentgenology* **196**, 251-256 (2011).
11. Sever, A.R., Mills, P., Jones, S.E., Mali, W. & Jones, P.A. Sentinel node identification using microbubbles and contrast-enhanced ultrasonography. *Clinical Radiology* **67**, 687-694 (2012).
12. Burns, P.N. Harmonic imaging with ultrasound contrast agents. *Clinical Radiology* **51**, 50-55 (1996).
13. Lindner, J.R. Microbubbles in medical imaging: current applications and future directions. *Nature Reviews Drug Discovery* **3**, 527-532 (2004).
14. Boczkowski, D., Nair, S.K., Snyder, D. & Gilboa, E. Dendritic cells pulsed with RNA are potent antigen-presenting cells in vitro and in vivo. *Journal of Experimental Medicine* **184**, 465-472 (1996).
15. Kirk, C.J. & Mule, J.J. Gene-modified dendritic cells for use in tumor vaccines. *Human Gene Therapy* **11**, 797-806 (2000).
16. Ponsaerts, P., Van Tendeloo, V.F.I. & Berneman, Z.N. Cancer immunotherapy using RNA-loaded dendritic cells. *Clinical and Experimental Immunology* **134**, 378-384 (2003).
17. Tavernier, G. et al. mRNA as gene therapeutic: how to control protein expression. *Journal of Controlled Release* **150**, 238-247 (2011).
18. Eliyahu, H., Servel, N., Domb, A.J. & Barenholz, Y. Lipoplex-induced hemagglutination: potential involvement in intravenous gene delivery. *Gene Therapy* **9**, 850-858 (2002).
19. Schutt, E.G., Klein, D.H., Mattrey, R.M. & Riess, J.G. Injectable microbubbles as contrast agents for diagnostic ultrasound imaging: the key role of perfluorochemicals. *Angewandte Chemie-International Edition* **42**, 3218-3235 (2003).
20. Song, L.Y. et al. Characterization of the inhibitory effect of PEG-lipid conjugates on the intracellular delivery of plasmid and antisense DNA mediated by cationic lipid liposomes. *Biochimica Et Biophysica Acta-Biomembranes* **1558**, 1-13 (2002).
21. Shi, F.X. et al. Interference of poly(ethylene glycol)-lipid analogues with cationic-lipid-mediated delivery of oligonucleotides; role of lipid exchangeability and non-lamellar transitions. *Biochemical Journal* **366**, 333-341 (2002).

22. Lentacker, I. et al. Ultrasound exposure of lipoplex loaded microbubbles facilitates direct cytoplasmic entry of the lipoplexes. *Molecular Pharmaceutics* **6**, 457-467 (2009).
23. Rejman, J., Tavernier, G., Bavarsad, N., Demeester, J. & De Smedt, S.C. mRNA transfection of cervical carcinoma and mesenchymal stem cells mediated by cationic carriers. *Journal of Controlled Release* **147**, 385-391 (2010).
24. Van Meirvenne, S. et al. Efficient genetic modification of murine dendritic cells by electroporation with mRNA. *Cancer Gene Therapy* **9**, 787-797 (2002).
25. Grunebach, F., Muller, M.R., Nencioni, A. & Brossart, P. Delivery of tumor-derived RNA for the induction of cytotoxic T-lymphocytes. *Gene Therapy* **10**, 367-374 (2003).
26. Suzuki, R. et al. A novel strategy utilizing ultrasound for antigen delivery in dendritic cell-based cancer immunotherapy. *Journal of Controlled Release* **133**, 198-205 (2009).
27. Van Tendeloo, V.F.I. et al. Highly efficient gene delivery by mRNA electroporation in human hematopoietic cells: superiority to lipofection and passive pulsing of mRNA and to electroporation of plasmid cDNA for tumor antigen loading of dendritic cells. *Blood* **98**, 49-56 (2001).
28. Lentacker, I., Geers, B., Demeester, J., De Smedt, S.C. & Sanders, N.N. Design and Evaluation of Doxorubicin-containing Microbubbles for Ultrasound-triggered Doxorubicin Delivery: Cytotoxicity and Mechanisms Involved. *Molecular Therapy* **18**, 101-108 (2010).
29. Sousa, C.R. Essay - dendritic cells in a mature age. *Nature Reviews Immunology* **6**, 476-483 (2006).
30. Villadangos, J.A. & Schnorrer, P. Intrinsic and cooperative antigen-presenting functions of dendritic-cell subsets in vivo. *Nature Reviews Immunology* **7**, 543-555 (2007).
31. Bonehill, A. et al. Single-Step Antigen Loading and Activation of Dendritic Cells by mRNA Electroporation for the Purpose of Therapeutic Vaccination in Melanoma Patients. *Clinical Cancer Research* **15**, 3366-3375 (2009).
32. Morse, M.A. et al. Migration of human dendritic cells after injection in patients with metastatic malignancies. *Cancer Research* **59**, 56-58 (1999).
33. Lambert, L.A. et al. Intranodal immunization with tumor lysate-pulsed dendritic cells enhances protective antitumor immunity. *Cancer Research* **61**, 641-646 (2001).
34. Bedrosian, I. et al. Intranodal administration of peptide-pulsed mature dendritic cell vaccines results in superior CD8+ T-cell function in melanoma patients. *Journal of Clinical Oncology* **21**, 3826-3835 (2003).
35. Nestle, F.O., Farkas, A. & Conrad, C. Dendritic-cell-based therapeutic vaccination against cancer. *Current Opinion in Immunology* **17**, 163-169 (2005).
36. Maloy, K.J. et al. Intralymphatic immunization enhances DNA vaccination. *Proceedings of the National Academy of Sciences of the United States of America* **98**, 3299-3303 (2001).
37. Tagawa, S.T. et al. Phase I study of intranodal delivery of a plasmid DNA vaccine for patients with Stage IV melanoma. *Cancer* **98**, 144-154 (2003).
38. Taniyama, Y. et al. Development of safe and efficient novel nonviral gene transfer using ultrasound: enhancement of transfection efficiency of naked plasmid DNA in skeletal muscle. *Gene Therapy* **9**, 372-380 (2002).
39. Vannan, M. et al. Ultrasound-mediated transfection of canine myocardium by intravenous administration of cationic microbubble-linked plasmid DNA. *Journal of the American Society of Echocardiography* **15**, 214-218 (2002).

Chapter 5

The potential of antigen and TriMix sonoporation using mRNA-loaded microbubbles for ultrasound-triggered cancer immunotherapy

This chapter is published as:

Heleen Dewitte[1], Sandra Van Lint[2], Carlo Heirman[2], Kris Thielemans[2], Stefaan C. De Smedt[1], Karine Breckpot[2,*] and Ine Lentacker[1,*]. The potential of antigen and TriMix sonoporation using mRNA-loaded microbubbles for ultrasound-triggered cancer immunotherapy. *Journal of Controlled Release*, **194**, 28-36 (2014).
(DOI: 10.1016/j.jconrel.2014.08.011)

[*]Both senior authors contributed equally to this work

[1]Laboratory for General Biochemistry and Physical Pharmacy, Faculty of Pharmacy, Ghent University, Ottergemsesteenweg 460, 9000 Ghent, Belgium.

[2]Laboratory of Molecular and Cellular Therapy, Department of Biomedical Sciences, Medical School of the Vrije Universiteit Brussel (VUB), Laarbeeklaan 103, 1050 Jette, Belgium.

ABSTRACT

Dendritic cell (DC)-based cancer vaccines, where the patient's own immune system is harnessed to target and destroy tumor tissue, has emerged as a potent therapeutic strategy. In the development of such DC vaccines, it is crucial to load the DCs with tumor antigens, and to simultaneously activate them to become more potent antigen-presenting cells. For this, we report on microbubbles, loaded with both antigen mRNA as well as immunomodulating TriMix mRNA, which can be used for the ultrasound-triggered transfection of DCs. *In vivo* experiments with in vitro sonoporated DCs, show the effective induction of antigen-specific T cells, resulting in specific lysis of antigen-expressing cells. Especially in a therapeutic setting, sonoporation with TriMix has an important added value, resulting in a significant reduction of tumor outgrowth and a marked increase in overall survival. What is more, complete tumor regression was observed in 30% of the antigen+TriMix DC vaccinated animals, which also displayed long-term antigen-specific immunological memory. As a result, DC sonoporation using microbubbles loaded with a combination of antigen and TriMix mRNA can elicit powerful immune responses *in vivo*, and might serve as a potential tool for further *in vivo* DC vaccination applications.

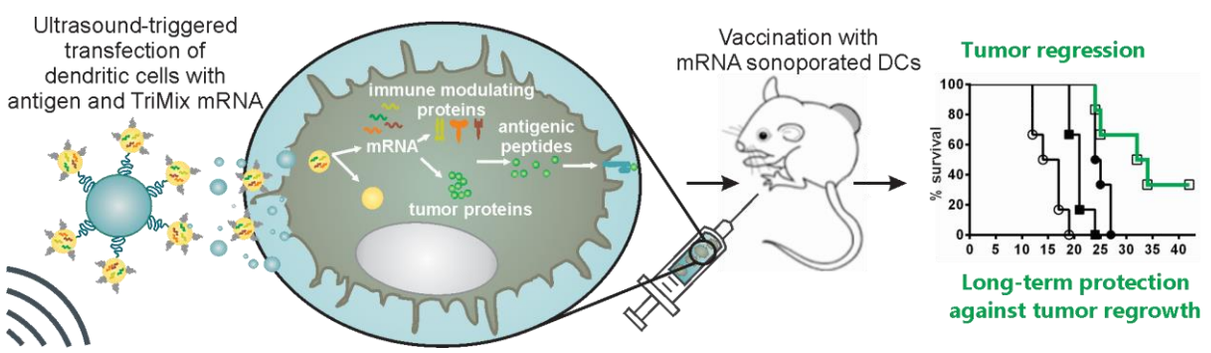

INTRODUCTION

Since its discovery in the early 70s by Noble Prize winner Ralph M. Steinman, the dendritic cell (DC) came to be known as nature's adjuvant[1] (**Chapter 1**). Its unique capacity to present antigens and initiate antigen-specific T cell responses, makes the DC an interesting target in cancer immunotherapy. In order to produce effective DC-based vaccines, two major requirements need to be satisfied. Firstly, the immune system should be able to discriminate between healthy tissue and cancer cells. For this, it is crucial to load DCs with cancer-specific tumor associated antigens (TAAs)[2, 3]. Upon presentation of these TAAs in major histocompatibility complexes (MHCs) on the DC surface, TAA-specific immune responses can be mounted. Secondly, DCs should receive additional stimulation to become fully mature antigen-presenting cells that can provide the necessary co-stimulatory signals to activate antigen-specific T cells.

In **Chapter 4**, we showed that by using mRNA-loaded microbubbles, we could induce fast and efficient, ultrasound-triggered mRNA-loading of murine bone marrow-derived DCs *in vitro*, without important negative repercussions on the DC viability and capacity to respond to maturation stimuli[4]. Thus, this strategy uses mRNA as a source of antigen, and microbubbles for ultrasound-triggered antigen delivery.

With respect to the second requirement, it is essential that the DCs undergo a process called "maturation" in order for antigen-presentation to effectively result in T cell activation. Maturation is initiated when DCs encounter "*danger*" signals, such as toll like receptor (TLR) agonists, causing them to shift in phenotype and function from antigen-capturing to antigen-presenting cells[5]. This is an absolute necessity for a DC-based cancer vaccine to be successful, as it is now clear that mature DCs are capable of inducing immunity against the presented antigens (*i.e.* stimulation of effector T cells), whereas their immature counterparts will rather induce tolerance (*i.e.* T cell anergy and regulatory T cells)[6]. The main reason for this is that immature DCs lack co-stimulatory molecules required for effective T cell activation[7]. Therefore, it is crucial to deliver not only antigens to DCs, but also maturation stimuli to ensure optimal immune activation by the DC vaccine.

In this study, we aimed to evaluate the capacity of mRNA-sonoporated DCs to induce immune responses *in vivo*. Moreover, to address the second DC vaccine requirement, we aimed to obtain both antigen-loading and stimulation of maturation by a single step sonoporation. This is important, as we previously reported that mRNA sonoporation without inclusion of additional immune stimulants merely induces partial maturation of the DCs. Therefore, we performed sonoporations with antigen mRNA and TriMix mRNA. TriMix is a mixture of 3 mRNAs, encoding CD40-ligand, a constitutively active form of TLR4 and CD70 (a co-stimulatory molecule required for effective $CD8^+$ T cell priming)[8]. Co-delivery of these 3

nucleic acid sequences was already shown to modulate the DCs' functionality, resulting in APCs that display a more mature, T cell activating phenotype[9]. Previous studies have demonstrated the superiority of TriMix over other, more conventional, maturation stimuli after intranodal injection of TAA and TriMix mRNA in tumor-bearing mice[10]. Also in a clinical setting, vaccination with DCs electroporated with TAA and TriMix mRNA lead to the induction of durable antitumor responses in a chemorefractory melanoma patient[11, 12]. On the basis of these results, we evaluated the potential of simultaneous delivery of TAA mRNA and TriMix via microbubbles and ultrasound to induce potent antitumor immune responses in mice, as schematically depicted in **Figure 1A**.

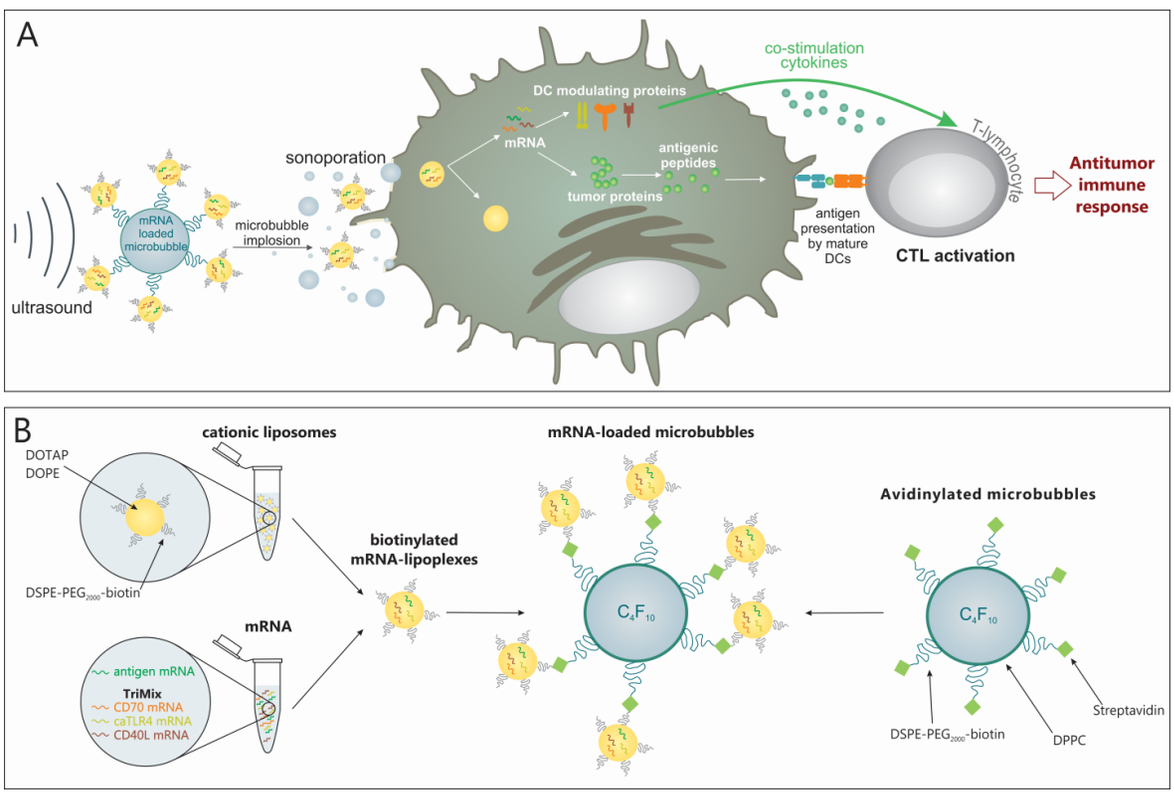

Figure 1. mRNA sonoporation of DCs using mRNA-loaded microbubbles and ultrasound.

(A) Schematic representation of the use of mRNA-loaded microbubbles, which implode upon exposure to ultrasound and sonoporate the DCs. As a result, both antigen and DC modulating proteins are produced by the DC, which can lead to antigen presentation and T cell activation. (B) Schematic representation of the production of mRNA-loaded microbubbles. Antigen and TriMix mRNA are premixed and complexed to biotinylated cationic liposomes. The resulting mRNA-lipoplexes can then be attached to the surface of avidinylated lipid microbubbles.

MATERIALS AND METHODS

Cell culture and mice

Primary murine bone marrow-derived DC (BM-DC) cultures were generated from C57BL/6 mice. Female C57BL/6 mice were purchased from Harlan (Gannat, France) and housed in an SPF facility according to the regulations of the Belgian law and the local Ethical Committee. Mice were sacrificed and bone marrow was flushed from the hind limbs. After red blood cell lysis (Pharm Lyse Buffer, BD Biosciences, Erembodegem, Belgium), the collected cells were seeded in 100 mm not TC-treated polystyrene culture dishes (Corning®, Amsterdam, The Netherlands) at $2x10^6$ cells ml^{-1} in 15 ml. The cell culture medium used was RPMI 1640 (Gibco-Invitrogen, Merelbeke, Belgium) supplemented with penicillin/streptomycin/L-glutamine (1%, Gibco-Invitrogen), β-mercaptoethanol (50 µM, Gibco-Invitrogen), 5% FetalClone™ I (FCI, 5%, HyClone™) and recombinant murine GM-CSF (20 ng ml^{-1}, Peprotech, Rock Hill, NJ). On day 3 of the culture, an additional 15 ml complete culture medium containing GM-CSF (40 ng ml^{-1}) was added. On day 5, all cells were collected by centrifugation (5min at 300*g*), resuspended in the appropriate culture medium at $5x10^5$ cells ml^{-1} and seeded per 10 ml in OptiCells™ (Nunc, Thermo Scientific, Aalst, Belgium) for sonoporation the next day.

The mouse melanoma cell line MO4 (kindly provided by K. Rock, University of Massachusetts Medical Center) and the T cell lymphoma E.G7-OVA (obtained from the American Type Culture Collection, Rockville, MD, USA) were cultured at 37°C in a humidified 5% CO_2 atmosphere in RPMI 1640 medium (Sigma-Aldrich, Diegem, Belgium) supplemented with 5% FCI, 100 U ml^{-1} penicillin, 100 µg ml^{-1} streptomycin, 2 mM L-glutamine, 1 mM sodium pyruvate and nonessential amino acids (Sigma-Aldrich).

C57BL/6 and OT-I mice for *in vivo* experiments were ordered from Charles River (L'Arbresle, France) and housed in SPF facilities according to the regulations of the Belgian law and the local Ethical Committee.

Messenger RNA

The vector, pST1 was provided by U. Sahin (Johannes-Gutenberg University, Mainz, Germany). The vectors pGEM-li80tOVA, pST1-eGFP-bis, pST1-caTLR4, pST1-mouse CD40-L and pST1-mouse CD70 were previously described[8, 10, 13]. Before *in vitro* transcription, pGEM and pST1 vectors were linearized with the restriction enzymes *Spe* I and *Sap* I, respectively. All enzymes were purchased from Fermentas (Vilnius, Lithuania). The *in vitro* transcription of mRNA and its subsequent quality control were performed as previously described[13].

In vitro mRNA sonoporation

Lipid microbubbles loaded with mRNA-lipoplexes were prepared as described previously[4]. A schematic representation of the material production is shown in **Figure 1B**. Briefly, perfluorobutane (F2 chemicals, Preston, UK) microbubbles stabilized by a lipid coat consisting of DPPC (1,2-dipalmitoyl-*sn*-glycero-3-phosphocholine) (Lipoid, Ludwigshafen, Germany) and DSPE-PEG-biotin [1,2-distearoyl-*sn*-glycero-3-phosphoethanolamine-N-[biotin(polyethylene glycol)-2000] (Avanti Polar Lipids, Alabaster, AL) in a 85:15 molar ratio were prepared. These biotinylated microbubbles were subsequently coated with avidin (Cell Sciences, Canton, USA), to allow coupling to biotin-containing mRNA lipoplexes. The mRNA lipoplexes were prepared by mixing mRNA with cationic liposomes consisting of 48.75% DOTAP (1,2-dioleoyl-3-trimethylammonium-propane), 48.75% DOPE (1,2-dioleoyl-*sn*-glycero-3-phosphoethanolamine) and 2.5% DSPE-PEG-2000-biotin [1,2-distearoyl-*sn*-glycero-3-phosphoethanol-amine-N-[biotinyl(polyethylene glycol)-2000] (all Avanti Polar Lipids), at a cationic lipid-to-mRNA charge (N/P) ratio of 8 in OptiMem® (Gibco Invitrogen). When multiple mRNAs were used, these were first pre-mixed in a 1:1 ratio prior to complexation to the cationic liposomes. The resulting mRNA-lipoplexes (corresponding to 10 µg mRNA when GFP or OVA were used alone, or 40 µg when co-sonoporations with TriMix were performed) were incubated with the microbubbles for 5 min prior to use. After injection of mRNA lipoplex-loaded microbubbles in the OptiCells™, ultrasound was applied using a Sonitron 2000 (Artison, Inola, USA) (1 MHz, 2 W cm^{-2} corresponding to a peak negative pressure of 800 kPa, 20% duty cycle (2ms on, 8ms off), 30s total insonation time per OptiCell™).

BM-DC antibody staining and flow cytometric analysis

To evaluate the impact of mRNA sonoporation on the transfection efficiency and DC phenotype, the mRNA sonoporated cells were collected 24h or 48h after ultrasound application. The cells were washed and surface stained with anti-CD11c-APC (BM-DC marker, Affymetrix eBioscience, Vienna, Austria) and anti-CD40-PE (Affymetrix), anti-CD86-PE (BD biosciences) or anti-CD70-PE (Affymetrix) for 45min at 4°C in the dark. After washing, the cells were resuspended in FACS buffer (phosphate buffered saline (PBS, Gibco-invitrogen), supplemented with 5% bovine serum albumin (BSA, Sigma-Aldrich)) and analyzed using a FACSCalibur™ (BD) equipped with CellQuest™ software.

Vaccination of mice with mRNA sonoporated DCs

After *in vitro* mRNA sonoporation, the DCs were incubated for 2h at 37°C in the OptiCells™. Then, all the cells (both the cells in suspension as well as the cells that grow adherent to the OptiCell™ membranes) were collected, and washed twice with PBS. Finally, the cells were resuspended at $2x10^6$ cells ml^{-1} in PBS, of which 50 µl was injected subcutaneously into the flank of the mice.

In vivo T cell proliferation assay

In order to assess the potential of mRNA sonoporated DCs to efficiently induce proliferation of antigen-specific T cells, an *in vivo* OT-I proliferation assay was performed. This assay uses OVA as a model antigen, and is based on adoptive transfer of OT-I cells, which carry a transgenic CD8 T cell receptor which specifically recognizes the MHC-I restricted OVA peptide SIINFEKL. For this, spleens from OT-I mice were processed into a single-cell suspension. After red blood cell lysis, $CD8^+$ T cells were isolated via magnetically activated cell sorting, using a MACS CD8a T cell isolation kit (MACS Miltenyi, Leiden, The Netherlands) according to the manufacturer's instructions. The collected $CD8^+$ T cells were fluorescently labeled using carboxyfluorescein diacetate succinimidyl ester (CFSE, Molecular probes, 10 µM in PBS supplemented with 0.1% BSA) for 15min at 37°C. After washing the cells with RPMI medium, the cells were resuspended at $1x10^8$ cells ml^{-1} in PBS. All mice received 200 µl of this CFSE-labeled OT-I cell suspension i.v. via tailvein injection. The next day, the mice received subcutaneous injections with PBS (negative control) or mRNA sonoporated DCs, as described previously. 5 days after vaccination, the mice were sacrificed and the inguinal lymph nodes were collected. After 30min digestion of the nodes in liberase TL (100 µl, Roche, Vilvoorde, Belgium), a single-cell suspension was prepared. Half of the cells were used for flow cytometric analysis of proliferation (using a FACSCanto flow cytometer with FACSDiva™ software, BD Biosciences). On the other half of the suspension, a $CD8^+$ T cell sort was performed. The resulting cells were resuspended at $2x10^6$ cells ml^{-1} in RPMI medium and seeded per 100 µl in a round-bottom 96 well plate for restimulation. To this extent, day 6 BM-DCs were loaded with 1 µg ml^{-1} SIINFEKL peptide (Eurogentec, Seraing, Belgium) for 30min at 37°C. After washing, 100 µl SIINFEKL-pulsed DCs, suspended at $2x10^5$ cells ml^{-1} were added to the OT-I cells in the 96 well plates for 24h at 37°C.

In vivo cytotoxic T lymphocyte assay

To investigate the potential of mRNA sonoporated DCs to induce antigen-specific cytotoxic T lymphocyte (CTL) responses, an *in vivo* CTL assay was performed using an OVA model. For this, 5 days after vaccination with mRNA sonoporated DCs, the vaccinated mice were challenged i.v. with both target cells and control cells in a 1:1 ratio. The injected cells were splenocytes of untreated C57BL/6 mice that were either labeled with CFSE at low intensity ($CFSE^{lo}$ control cells, $5x10^6$ cells per injection), or labeled with CFSE at high intensity and additionally pulsed with the peptide SIINFEKL ($CFSE^{hi}$ target cells, $5x10^6$ cells per injection). The next day, the mice were sacrificed, inguinal lymph nodes were collected, processed into a single-cell suspension, and analyzed for CFSE staining via flow cytometry using a BD FACSCanto. Mice injected subcutaneously with PBS served as non-immunized controls. The percentage specific lysis of target cells was calculated using the following formula:

$$\%\ specific\ lysis = 1 - \frac{(\%CFSE^{hi}/\%CFSE^{lo})_{immunized}}{(\%CFSE^{hi}/\%CFSE^{lo})_{non-immunized}} \times 100\%$$

In vivo therapeutic vaccination experiments

The therapeutic potential of mRNA sonoporated DCs to reduce tumor growth was evaluated by performing therapeutic vaccinations in tumor-bearing mice. For this, C57BL/6 received a subcutaneous injection of $3x10^5$ MO4 or E.G7-OVA tumor cells (suspended in PBS) in the flank. 10 days after tumor inoculation, when the lesions were palpable, the mice were randomized in different treatment groups based on tumor volume, and vaccinated with mRNA sonoporated DCs. A second therapeutic vaccination was performed at day 13 or 14 after tumor cell injection. Tumor growth was measured every other day using a caliper. When the tumor volume exceeded 1500 mm^3, the mice were euthanized via cervical dislocation. Animals that completely rejected their tumors were rechallenged with $3x10^5$ E.G7-OVA tumor cells, and subsequently with $3x10^5$ MO4 cells. As controls for the rechallenge study, naïve (non-vaccinated) C57BL/6 were used.

ELISA measurements

Supernatants of mRNA sonoporated DCs were screened for the presence of IL-10 and IL-12p70. Supernatants of DC and T cell co-cultures were assayed for IFNγ. Cytokine measurements were performed via ELISA (all Ready-SET-Go!® ELISA kits, Affymetrix) according to the manufacturer's instructions.

Statistical analysis

A one-way ANOVA followed by a Bonferroni multiple comparison test, was carried out (GraphPad software, la Jolla, CA, USA). Sample sizes and number of times experiments were repeated are indicated in the figure legends. The results are shown in column graphs as mean ± standard deviation. The number of asterisks in the figures indicates the statistical significance as follows: *p<0.05; **p<0.01; ***p<0.001. Survival was visualized in a Kaplan-Meier plot. Differences in survival were analyzed by the log-rank (Mantel-Cox) test.

RESULTS

Transfection efficiency and phenotype of mRNA sonoporated DCs

In our previous report, we demonstrated that sonoporation could be used for ultrasound-triggered transfection of primary DCs with mRNA *in vitro*. In addition, the sonoporation procedure as such, without the use of additional maturation stimuli, was shown to readily induce a small but significant shift in the expression of the DC maturation markers CD40 and CD86[4]. However, compared to a positive control where the DCs' TLR4 was stimulated by incubation with bacteria-derived lipopolysaccharide (LPS), this maturation was merely partial. As complete DC maturation is warranted for effective immunostimulation, this prompted us to include additional stimuli to further increase the expression of co-stimulatory markers. Therefore, we included TriMix mRNA in the antigen mRNA-containing lipoplexes. We evaluated the effect of TriMix inclusion on the transfection efficiency as well as the DC phenotype, by analyzing the expression of 3 molecules involved in T cell activation by DCs 24h after sonoporation with either reporter mRNA alone (GFP) or in combination with TriMix (GFP+TriMix).

In accordance with our previous report, the results in **Figure 2** indicate satisfactory transfection with GFP mRNA, resulting in 19% GFP-expressing DCs 24h after sonoporation. Inclusion of TriMix results in a decrease in transfection efficiency to 11%. With regards to the DC phenotype, we observed a significant up-regulation of CD86 and CD40 expression in the GFP group compared to blank. The effects on CD70 expression are less pronounced. Sonoporation with GFP+TriMix, lead to a slight but significant additional increase in the expression of CD40, CD86 and CD70 over sonoporation with GFP mRNA alone. However, the expression levels of these surface molecules after GFP+TriMix sonoporation are still significantly lower in comparison to an LPS-stimulated positive control.

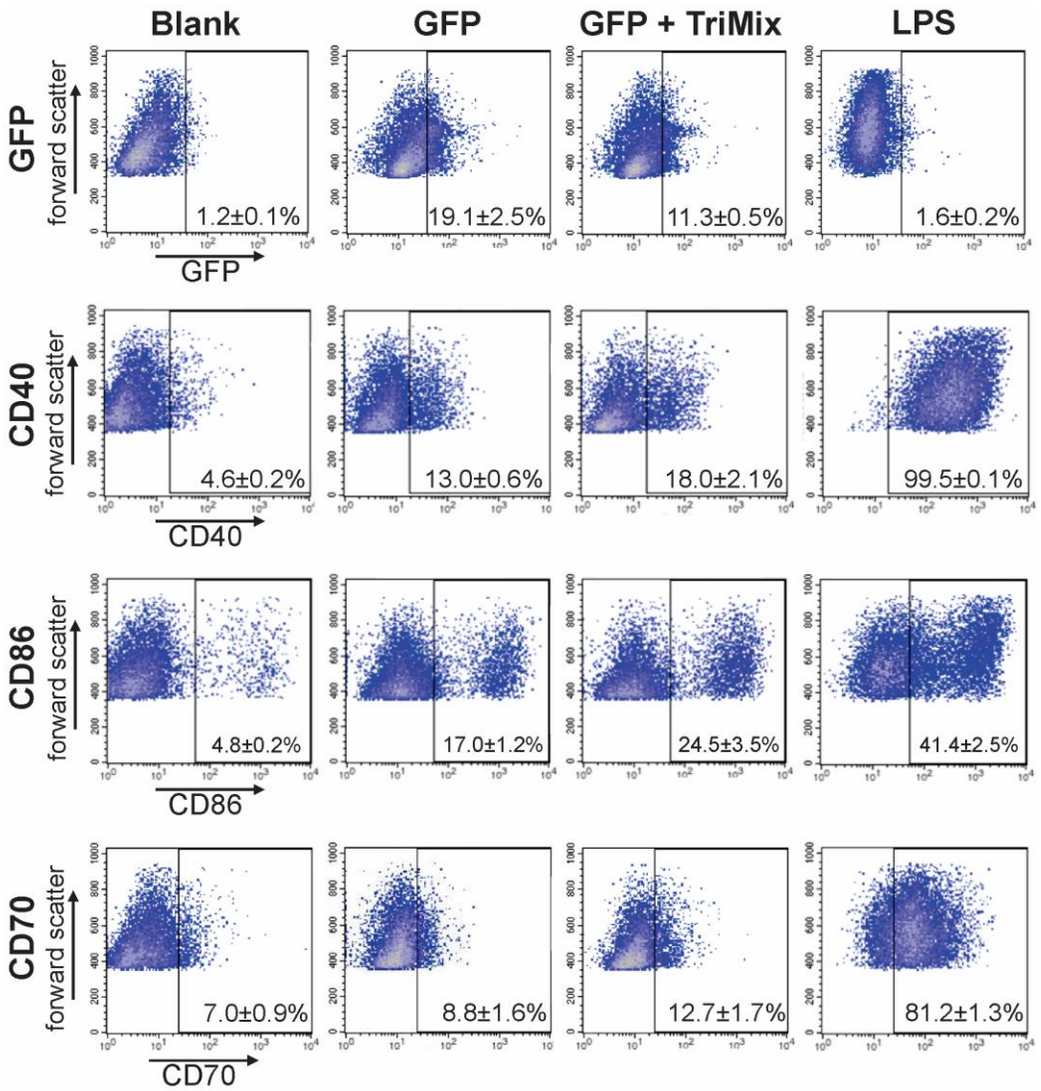

Figure 2. Transfection efficiency and phenotypical analysis of DCs after mRNA sonoporation.

24h after treatment of the DCs by sonoporation with GFP mRNA alone (GFP) or in combination with TriMix (GFP+TriMix), the cells were analyzed for the expression of GFP and different maturation markers (CD40, CD86 and CD70). DCs were gated based on CD11c staining. Untreated cells and LPS-stimulated cells served as negative and positive controls, respectively (*n*=3).

Similar observations can be made when looking at the levels of immune stimulating (IL-12p70) and immune suppressive (IL-10) cytokines that are produced by the mRNA sonoporated DCs 24h after treatment (**Figure 3**). Sonoporation with GFP mRNA alone resulted in a significant increase in IL-10, but not IL-12p70 secretion. For both cytokines, inclusion of TriMix into the mRNA lipoplexes surrounding the microbubbles results in higher cytokine production. But still, the concentrations are significantly lower than when LPS was applied to induce maturation of the DCs.

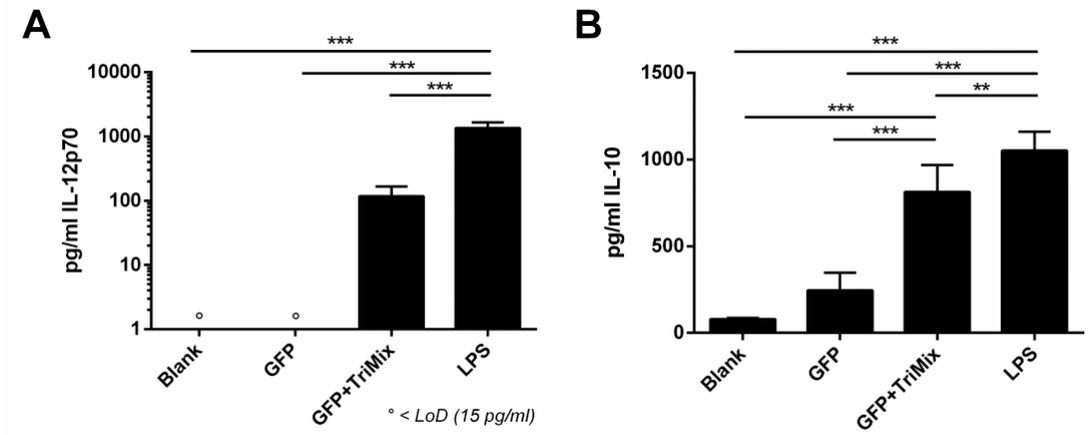

Figure 3. Cytokine production by mRNA sonoporated DCs.

The amounts of cytokines produced by untreated DCs (blank), DCs sonoporated with GFP mRNA alone, or in combination with TriMix (GFP+TriMix) and DCs that were matured with LPS were measured 24h after cell treatment. Figures show graphical representations of the levels of (A) IL-12p70 and (B) IL-10. Graphs are summaries of 2 independent experiments at n=3, **p<0.01, ***p<0.001.

In vivo induction of antigen-specific T cell proliferation by mRNA sonoporated DCs

To assess the impact of mRNA sonoporation on the capacity of DCs to prime antigen-specific $CD8^+$ T cells, we performed an *in vivo* T cell proliferation study using chicken ovalbumin (OVA) as a model antigen. This makes use of an adoptive transfer of OT-I cells, which are transgenic T cells that carry a CD8 T cell receptor that specifically recognizes the OVA-derived peptide SIINFEKL when presented in MHC-I. 24h after adoptive OT-I cell transfer, tumor-free mice were vaccinated with mRNA sonoporated DCs, and the percentage proliferating OT-I cells was evaluated 5 days later. Results were normalized to the background signal in mice that received PBS instead of DCs. As demonstrated in **Figure 4A**, no unspecific OT-I proliferation was observed in the negative control group that received DCs sonoporated with GFP mRNA (3 ± 3%). When vaccination was performed with DCs sonoporated with antigen mRNA alone (OVA), this resulted in 31 ± 16% proliferation of OVA-specific $CD8^+$ T cells, indicating efficient intracellular processing and presentation of OVA by the mRNA sonoporated DCs without additional stimulation of maturation. When OVA sonoporation was combined with phenotype-modulating stimuli, either by 2h incubation of the sonoporated DCs with LPS (OVA/LPS as a positive control) or by sonoporation with OVA and TriMix mRNA (TriO), antigen-specific T cell proliferation increased to respectively 41 ± 15% and 48 ± 19%. Although there is a trend towards more extensive proliferation in the OVA/LPS and TriO groups, the observed differences were not statistically significant (p>0.05).

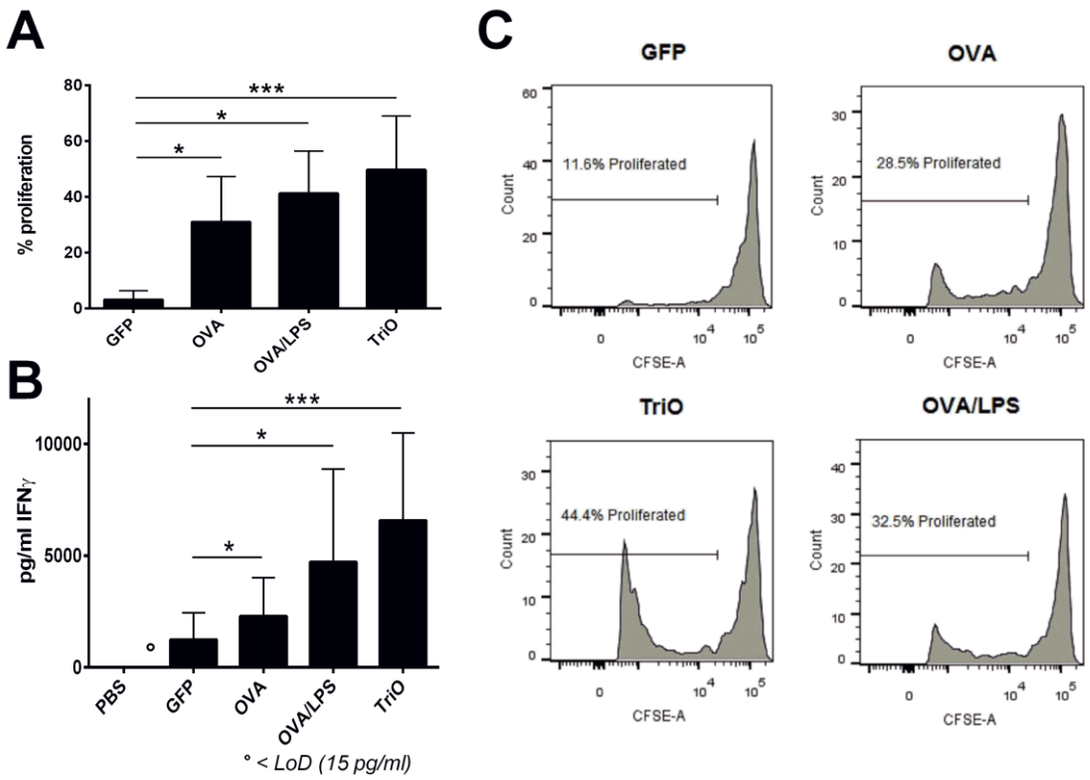

Figure 4. *In vivo* proliferation of antigen-specific T cells.

1 day after adoptive OT-I transfer, mice were vaccinated with DCs sonoporated with GFP mRNA (negative control), OVA mRNA alone (OVA) or in combination with TriMix (TriO), or OVA-sonoporated DCs that were matured with LPS (OVA/LPS). Read-out was performed 24h later. Graphs show (A) percentages proliferating OT-I cells normalized to the background that was detected in mice that received a PBS injection. (B) levels of IFNγ measured 24h after restimulation of proliferated OT-I cells with peptide-pulsed DCs. Graphs are summaries of 2 independent experiments at n=3, *p<0.05, ***p<0.001. Representative histograms for the percentage proliferating OT-I cells are provided in (C).

In addition, we evaluated the functionality of the proliferating T cells, by performing a re-stimulation with peptide. For this, a fraction of the proliferated OT-I cells were co-cultured in a 10:1 ratio with DCs that were pulsed with SIINFEKL peptide. 24h later, the response of these restimulated T cells to the antigen-presenting DCs was evaluated by measuring the levels of IFNγ, an important mediator of CTL responses, in the co-culture supernatant. The results in **Figure 4B** display a similar trend to the proliferation results: T cells activated by DCs that received OVA mRNA via sonoporation produce significantly larger amounts of IFNγ compared to those stimulated with DCs sonoporated with GFP mRNA. After additional maturation by LPS incubation or sonoporation with TriMix, a trend towards higher IFNγ levels was observed.

In vivo cytotoxic T cell response induction by mRNA sonoporated DCs

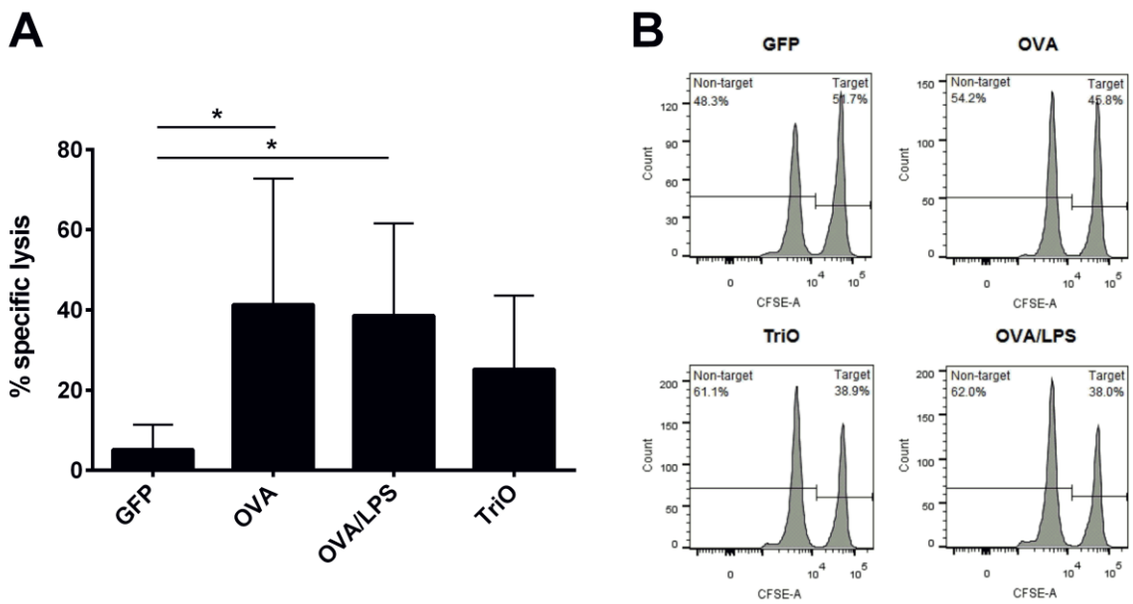

Figure 5. *In vivo* cytotoxic T cell assay.

5 days after vaccination of mice with DCs sonoporated with GFP mRNA (negative control), OVA mRNA alone (OVA) or in combination with TriMix (TriO), or OVA-sonoporated DCs that were matured with LPS (OVA/LPS), mice were challenged with target cells and non-target cells in a 1:1 ratio. The next day, the percentage of antigen-specific lysis of target cells compared to non-target cells was measured. (A) Graphs are summaries of 3 independent experiments at n=3, *p<0.05. Representative histograms showing the relative distribution of target to non-target cells (as used for the calculation of the percentage target-specific lysis) are provided in (B).

Besides the capacity to stimulate antigen-specific T cells to proliferate, mRNA sonoporated DCs should be able to activate $CD8^+$ T cells to cause antigen-specific lysis of target cells. To evaluate this, an *in vivo* CTL assay was performed, again using OVA as a model antigen. For this, tumor-free mice were vaccinated with mRNA sonoporated DCs and 5 days later, the animals were challenged with allogenic splenocytes that were either untreated (non-target cells) or pulsed with SIINFEKL peptide (target cells). The next day, the ratio of target cells versus non-target cells was studied as a measure for antigen-specific lysis. The results, as represented in **Figure 5**, show 41 ± 31% OVA-specific lysis of target cells when mice were vaccinated with DCs sonoporated with OVA mRNA. LPS-induced maturation of the DCs after sonoporation (OVA/LPS), could not further increase this percentage (39 ± 23%). Unexpectedly, DCs sonoporated with TriO were markedly less efficient in inducing antigen-specific lysis

(25 ± 18%). Based on the proliferative potential of TriO DCs as well as on their capacity to stimulate IFNγ-producing $CD8^+$ T cells, more extensive CTL responses were expected.

Therapeutic vaccinations with mRNA-sonoporated DCs

Immune induction is a complex orchestrated response that relies on numerous synergistic components of both cellular and humoral immunity. Moreover, tumor-mediated suppression of immune responses, regulated by various immunosuppressive cell types such as myeloid-derived suppressor cells and regulatory T cells (T_{regs}) that reside in the tumor microenvironment, could potentially limit the therapeutic benefits of DC-based immunotherapy[14, 15]. Therefore, the impact of cancer vaccines can only truly be evaluated when all these different players are taken into account. For that reason, we assessed the potential of DCs sonoporated with antigen and TriMix mRNA in a therapeutic setting. For this, we examined the effect of vaccination with *ex vivo* mRNA sonoporated DCs in mice with pre-existing tumors. We initially opted for an OVA-expressing B16 melanoma model (MO4). 10 days after tumor inoculation in the flank, tumors were palpable and the animals were randomized into 3 treatment groups based on the tumor volume (as shown in **Figure 6A**).

Subsequently, the animals were given a subcutaneous injection with either DCs sonoporated with GFP mRNA (DC GFP, negative control, *n*=9), OVA mRNA (DC OVA, *n*=9), or sonoporated with TriMix and OVA mRNA (DC TriO, *n*=8). A second vaccination was performed 3 days later. When measuring tumor growth as a function of time, we observed a significant slow-down of tumor outgrowth in the DC OVA, and especially in the DC TriO group compared to the DC GFP group (**Figure 6**). This was translated in a prolongation of median survival of 41% and 82% for DC OVA and DC TriO respectively. This indicates that antigen mRNA sonoporated DCs can induce potent antitumor immune responses *in vivo*, which can further be boosted by sonoporation with DC-modulating TriMix mRNA.

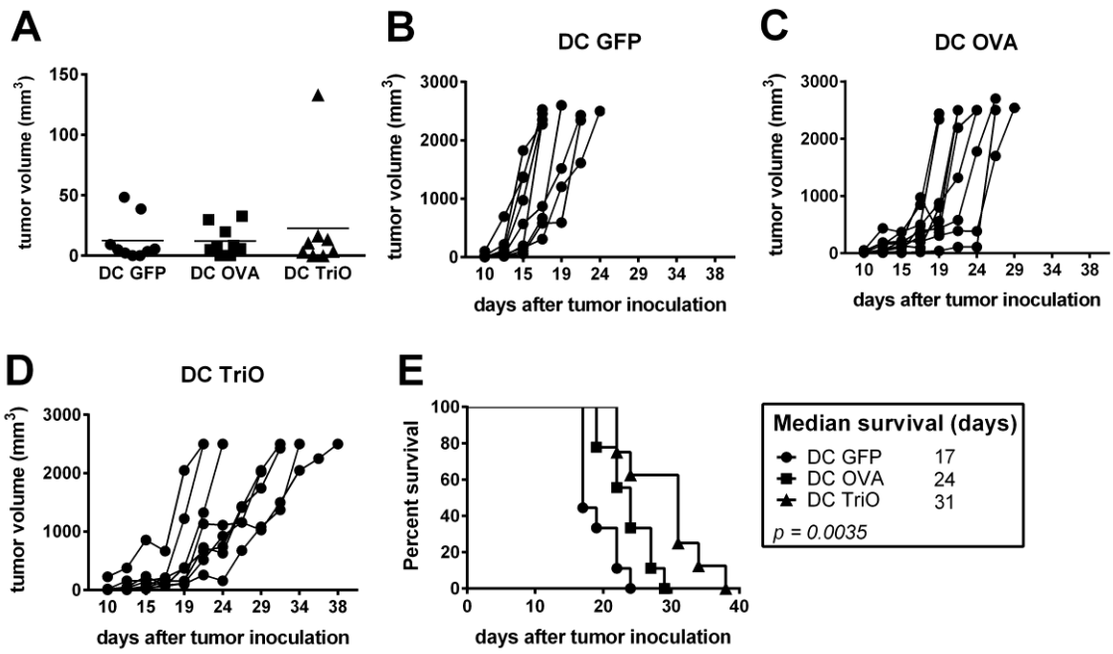

Figure 6. Therapeutic vaccination of MO4-bearing mice with mRNA sonoporated DCs.

10 and 13 days after inoculation with MO4 melanoma cells, mice were randomized in three treatment groups based on tumor volume as shown in (A) Then, the animals received therapeutic vaccinations with mRNA sonoporated DCs. Graphs show tumor growth as a function of time for mice vaccinated with DCs sonoporated with (B) GFP mRNA (control), (C) OVA mRNA and (D) OVA mRNA and TriMix (DC TriO). A Kaplan-Meier survival curve is shown in (E).

These therapeutic vaccination experiments were repeated in a different tumor model, expressing the same antigen. For this, mice were inoculated with E.G7-OVA, which are OVA-expressing lymphoma cells. Randomization was done based on tumor volume at day 10 after tumor inoculation (as shown in **Figure 7A**). Once more, two therapeutic vaccinations were performed at 10 and 14 days after tumor inoculation. In addition to the three treatment groups described in the previous experiment, we included a group that received OVA mRNA sonoporated DCs that were additionally matured with LPS for 2h prior to injection (DC OVA/LPS) (*n*=6 in all groups). This way, we aimed to compare the therapeutic effects of TriMix sonoporation to the use of a known and potent maturation inducer.

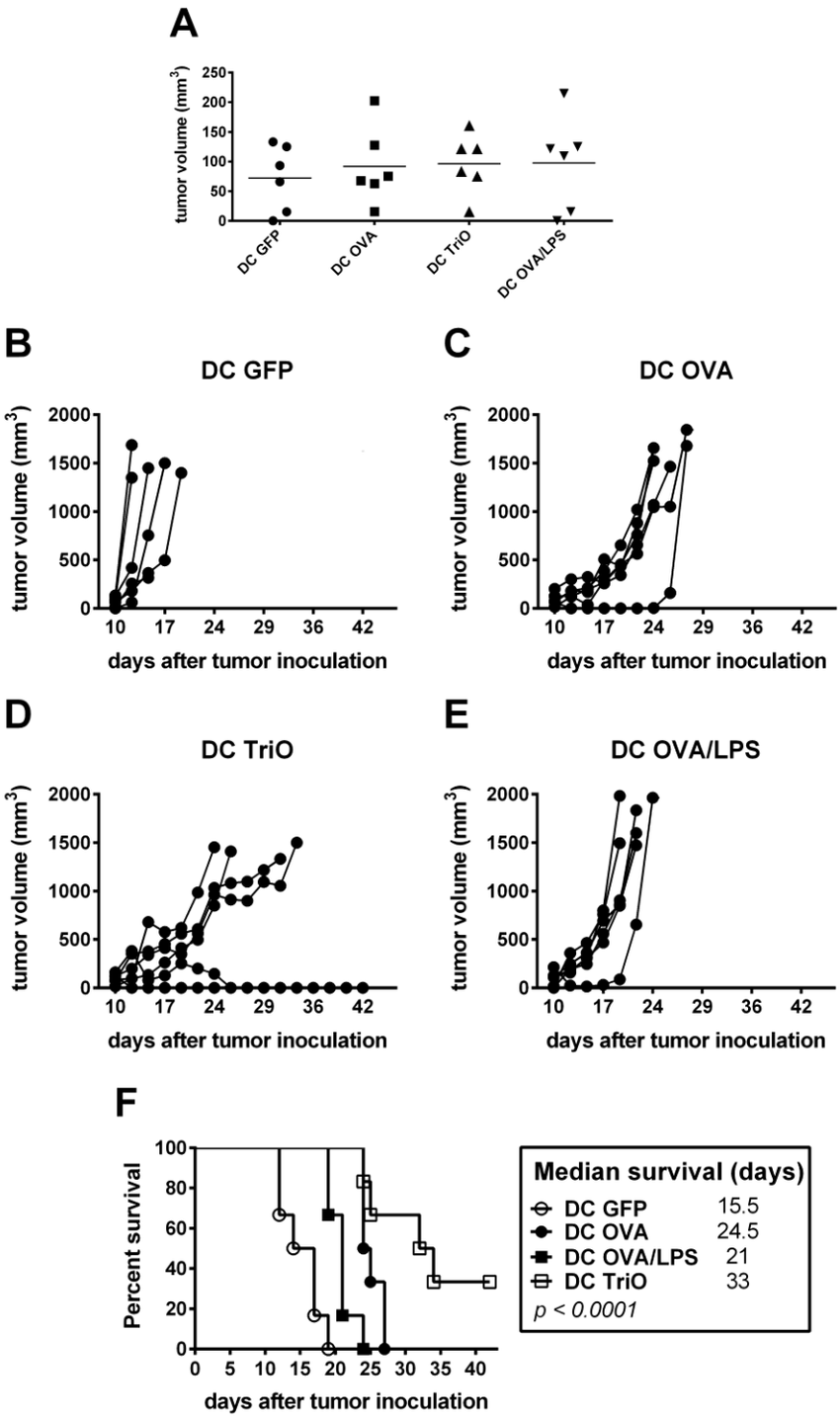

Figure 7. Therapeutic vaccination of E.G7-OVA-bearing mice with mRNA sonoporated DCs.

10 and 14 days after inoculation of mice with E.G7-OVA lymphoma cells, mice were randomized in three treatment groups based on tumor volume as shown in (A) Then, the animals received therapeutic vaccinations with mRNA sonoporated DCs. Graphs show tumor growth as a function of time for mice vaccinated with DCs sonoporated with (B) GFP mRNA (control), (C) OVA mRNA, (D) OVA mRNA and TriMix (DC TriO) and (E) OVA mRNA followed by a 2h maturation with LPS (DC OVA/LPS). A Kaplan-Meier survival curve is shown in (F).

In accordance to the previous experiment, the tumor growth curves in **Figure 7** indicate that sonoporation with antigen results in a significant delay of tumor outgrowth, resulting in a 58% increase in median survival. Interestingly, the slow-down of tumor growth was markedly shorter-lived in the DC OVA/LPS group compared to their unstimulated counterparts (DC OVA). This resulted in merely 35% prolongation of median survival of animals in the DC OVA/LPS group compared to the DC GFP group. In contrast, stimulation of antigen presentation by sonoporation with OVA and TriMix mRNA, resulted in a pronounced effect on tumor growth: median survival was more than doubled (212% increase), and complete tumor regression was observed in 2/6 animals in the DC TriO group.

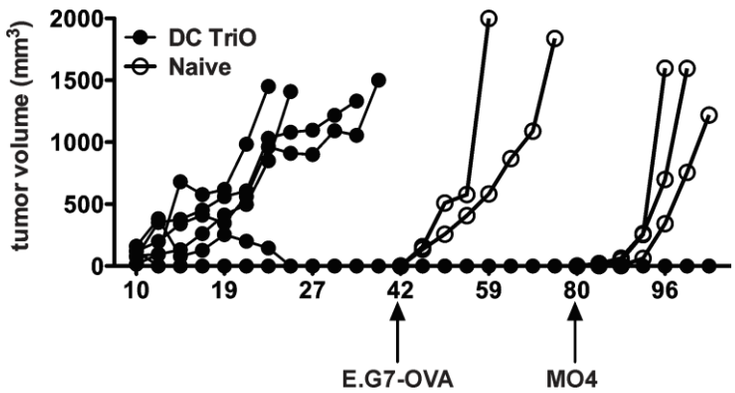

Figure 8. Rechallenge of tumor-free DC TriO treated mice.

The two E.G7-OVA challenged mice that showed complete tumor regression after two vaccinations with DC TriO, were rechallenged with E.G7-OVA and MO4 tumor cells on day 42 and day 80 after initial tumor inoculation, respectively. As controls, naïve, non-vaccinated mice were injected with the same tumor load.

These surviving animals, as well as two naïve control mice, were rechallenged with E.G7-OVA tumor cells 42 days after the first tumor inoculation. This to evaluate whether durable antitumor immunity was induced by the vaccinations. Indeed, in comparison to the control mice where rapid tumor growth was observed, the DC TriO vaccinated mice were protected against a second injection with the same tumor (**Figure 8**). To prove that this protective immunity is antigen-specific, we challenged these animals with a different tumor (MO4 melanoma instead of the initial lymphoma) that expresses the same antigen. Once more, no tumor growth could be detected in the DC TriO vaccinated animals in contrast to 3 naïve control mice. Thus, vaccination with DC TriO can induce antigen-specific immunological memory that is capable of protecting tumor-free survivors against tumor recurrence.

DISCUSSION

In continuation of our previous report on the use of mRNA-loaded microbubbles and ultrasound for the transfection of DCs *in vitro*[4], we further investigated if antigen transfer into DCs via mRNA sonoporation could result in the induction of antitumor immune responses. For this, it is crucial to not only deliver antigen mRNA to the DCs, but also to induce a shift in activity of these cells, in order to make them more effective in antigen presentation to naïve T cells. This should in turn result in protection against tumor growth. To allow this antigen-loading and maturation to occur simultaneously, we included TriMix into the mRNA-lipoplexes that surround the microbubbles, and performed sonoporations with four mRNA sequences in total.

First of all, we were able to show that sonoporation with multiple mRNAs is feasible. Upon sonoporation with GFP mRNA and TriMix, both GFP expression as well as a slight but significant up-regulation of maturation marker expression by DCs were observed. However, sonoporation with TriMix leads to a reduction in the percentage of GFP-expressing cells, which is probably due to limitations in the amount of mRNA that can be loaded onto the microbubble surface. For sonoporation with TriMix, a four-fold increase in total amount of mRNA, and therefore in amount of mRNA-lipoplexes is required. However, the number of binding spaces on the bubble surface is limited[16]. Therefore, it is likely that in the TriMix conditions, complete microbubble saturation occurs, resulting in the presence of a substantial portion of free mRNA-lipoplexes in the medium. In our previous reports, we demonstrated that the highest transfection efficiencies could be reached when the lipoplexes are physically attached to the microbubbles and not just co-delivered[17, 18]. For that reason, sonoporation with multiple mRNAs could lead to a lower protein expression. In addition, there is the possibility that the co-transfection with multiple RNAs results in competition for mRNA translation. This theory is supported by the observations of Chen et al., who also reported a drop in transfection efficiency when two mRNAs were co-electroporated in DCs compared to electroporation of each of these mRNAs alone[19]. This was also reported by Bonehill and colleagues who showed that upon electroporation of DCs with TriMix the number of mRNA-expressing DCs was always slightly decreased when two or three mRNAs were co-electroporated, in comparison to the electroporation of each mRNA alone[8]. This might indicate that there is a limit to the amount of mRNA that can be transferred into the cells. This raises the question whether this reduced transfection efficiency could limit the use of antigen mRNA and TriMix sonoporation. To answer this, it is important to take the therapeutic studies performed with TriO sonoporated DCs into account. These confirm that a higher transfection efficiency does not necessarily result in more potent immune responses. Indeed, DCs sonoporated with antigen mRNA alone, which allows higher antigen expression, result in less powerful immune responses, even after additional LPS-maturation, compared to TriO sonoporated DCs, where the amount of antigen that is produced by the DCs is lower. This discrepancy between transfection efficiency and

immunogenicity was previously reported by Grünebach et al., who postulated that it is important to realize that T cell receptors can detect antigens at much higher sensitivity than any routinely used analytical instrument in the lab[20]. In addition, T cell activation does not only depend on the presence of the antigen. Only when the antigens are presented to T cells by fully functional and mature DCs, can this result in effective T cell activation[6].

Thus, it is crucial to obtain antigen-loaded DCs with a mature phenotype. In accordance to our previous reports, mRNA sonoporation as such, without incorporation of additional immune stimulants, readily results in a distinct up-regulation of maturation marker expression at the DC surface. This in contrast to mRNA electroporation, which is considered the golden standard for mRNA transfer into DCs *in vitro*, where no effects on the DC maturation status were observed[8, 13]. Two possible mechanisms might explain this sonoporation-induced maturation. First of all, sonoporation is a physical transfection method, where pores are created as a result from shear forces and violent microbubble movements[21]. DCs are known to be sensitive to shear forces, and can already up-regulate maturation markers upon stress due to pipetting and centrifugation[22]. Thus, the shear stress induced by sonoporation could contribute to the observed phenotypical changes. In addition, sonoporation was reported to influence Ca^{2+} signaling within cells[21, 23]. Importantly, increased intracellular Ca^{2+} concentrations were also reported as one of the early events after LPS stimulation of mouse bone marrow-derived DCs[24]. Another possibility is direct triggering of innate immune responses by the cationic lipids (in this case DOTAP) within the mRNA lipoplexes, via TLR4 ligation. This, charge-related TLR activation was previously reported for DOTAP-containing lipoplexes as well as for various cationic polymers that are routinely used as transfection reagents[25, 26]. Likely, the observed effects are caused by a combination of these different mechanisms.

Much to our surprise, this limited maturation induced by antigen sonoporation alone already rendered the cells capable of inducing potent T cell proliferation, CTL responses and antitumor immune effects in tumor-free animals *in vivo*. Therefore, it was crucial to evaluate whether or not sonoporation with TriMix had an added value on the induced immune responses. By looking at the relative maturation marker expression and cytokine production by mRNA sonoporated DCs *in vitro*, it would appear that the contribution of TriMix is limited, especially in comparison to maturation by LPS as a positive control. A possible explanation for this could be the transfection efficiency that can be obtained with mRNA sonoporation. Although this technique allows substantial transfection of DCs, its efficiency is still relatively low in comparison to electroporation, where over 90% of the DCs can be transfected with mRNA. Indeed, with mRNA electroporation, TriMix does cause a significant up-regulation of maturation markers and cytokine expression, as previously reported by Bonehill et al.[9]. In addition, based on the results obtained in the OT-I proliferation assay and the *in vivo* CTL assay, it would appear that TriO sonoporation works fine to enhance the quantity of antigen-specific $CD8^+$ T lymphocytes (*i.e.*

numbers of proliferating cells), but at a first glance, their quality (*i.e.* cytolytic activity) is not as good as when OVA or OVA/LPS are used. However, it should be noted that these experiments were performed in naïve, healthy mice and not in tumor-bearing animals. In the latter, it was obvious that TriO sonoporation was superior and resulted in the most pronounced slowdown of tumor outgrowth and prolongation of median survival. Importantly, TriO DCs could even induce complete regression in 30% of the vaccinated animals, resulting in long-lasting protection against (re)challenges with tumor cells that express the vaccine antigen (in this case OVA).

A possible explanation for this discrepancy between immune responses observed in healthy versus tumor-bearing animals, is the existence of pre-vaccination antitumor immune responses. It was shown by Germeau and colleagues that large numbers of antitumor T cells are already present within melanoma patients prior to vaccination with tumor antigens. However, these natural pre-vaccine immune responses are often too weak to result in tumor rejection or even a reduction in tumor growth, due to the various immune suppressive mechanisms that occur within the tumor microenvironment[27]. Vaccination can then aid in boosting these spontaneous immune responses, either by aiding to overcome tumor-induced immune suppression, by re-activating anergic tumor-reactive T cells at the tumor site, or by inducing new antitumor CTL clonotypes (probably due to additional antigen release from attacked tumor cells)[2, 28]. This priming of the immune system by a growing tumor could explain why the immunogenicity of the mRNA sonoporated DCs was more pronounced in a therapeutic setting.

As to the question what could explain the superiority of TriMix over LPS in the therapeutic vaccination experiment, there are a number of possible causes. In essence, it is important to always keep in mind that immune responses are regulated in a complex manner, involving numerous different cell types. As discussed earlier, the effectiveness of a DC vaccine is not only determined by its capacity to induce effector $CD8^+$ T cells. Major factors that limit the potency of cancer vaccines are the hostile tumor microenvironment and the presence of T_{regs} that counteract CTL activity[29]. Therefore, undermining these immunosuppressive mechanisms might be the key to successful cancer vaccines. Interestingly, previous research by Pen et al. exposed TriMix as a potential tool in subverting T_{reg} effects. They demonstrated that $CD8^+$ T cells that were preactivated by TriMix electroporated DCs were protected against T_{reg} suppression. What was more, TriMix electroporated DCs could reprogram T_{regs} towards a Th1 phenotype, thus reinforcing cellular immunity against the tumor[30]. Based on these observations, it is quite likely that in the therapeutic vaccination setting, the superior antitumor effects of TriO DCs could be, at least partially, attributed to a reduction of T_{reg}-mediated immune suppression. Of course, many other cell types are involved in the regulation of antitumor immunity, and the effects of TriMix on these different cells is not yet known. For instance, it might be possible that TriMix transfected DCs could stimulate natural killer (NK) cells, which act synergistically with

CTLs and were recently reported to mount antigen-specific responses that can lead to long-term memory[31-34].

We reported that the transfection efficiencies that can be reached with mRNA sonoporation are significantly lower than when mRNA is electroporated into DCs, however it should be noted that the importance of mRNA sonoporation as a transfection technique lies within its possible *in vivo* applicability[35, 36]. Commercially available microbubble contrast agents were shown to migrate to the tumor-draining lymph nodes upon intradermal injection around the tumor of breast cancer patients[37]. This makes them useful to identify and localize sentinel lymph nodes in a non-invasive manner, using contrast-enhanced ultrasound imaging (CEUS). In addition, their lymphatic uptake is particularly interesting, since lymph nodes harbor large numbers of immune cells, including a substantial fraction of DCs[38, 39]. Therefore, microbubbles could be used for image-guided *in vivo* vaccination. The immunotherapy could then consist of a subcutaneous injection of mRNA-loaded microbubbles, of which the migration to the draining lymph nodes could be visualized using CEUS. Once the microbubbles and hence the mRNA are localized within the lymph nodes, higher intensity ultrasound pulses could induce localized microbubble implosion, resulting in spatiotemporally controlled delivery of both antigen mRNA and immunomodulating TriMix to intranodal DCs. This could allow a minimally invasive vaccination procedure that could substantially reduce the costs and laborious procedures that are currently associated with the production of *ex vivo* generated DC vaccines. Of course, this will require a thorough optimization of microbubble and mRNA dosages and ultrasound parameters, as these greatly influence the transfection efficiency with microbubbles and ultrasound *in vivo*[40].

CONCLUSIONS

Taken together, DCs that were sonoporated with antigen mRNA via mRNA loaded microbubbles and ultrasound can induce potent antigen-specific immune responses *in vivo*. Sonoporation with TriMix, to further modulate the DC's antigen-presenting functionality, could be used to further augment immunity. Especially in a therapeutic setting, vaccination with antigen and TriMix mRNA sonoporated DCs resulted in a significant reduction in tumor growth, leading to a marked increase in overall survival and long-lasting antigen-specific protection against tumor recurrence. Therefore, sonoporation could be a useful tool in the future development of *in vivo* DC vaccines.

ACKNOWLEDGEMENTS

The authors would like to thank Elsy Vaeremans and Petra Roman for their help with the mRNA production. Heleen Dewitte is a doctoral fellow of the Institute for the Promotion of Innovation through Science and Technology in Flanders, Belgium (IWT-Vlaanderen). Ine Lentacker and Karine Breckpot are postdoctoral fellows of the Research Foundation-Flanders, Belgium (FWO-Vlaanderen). This project was funded through the FWO grant G016513N.

REFERENCES

1. Steinman, R.M. & Cohn, Z.A. Identification of a Novel Cell Type in Peripheral Lymphoid Organs of Mice. *Journal of Experimental Medicine* **137**, 1142-1162 (1973).
2. Coulie, P.G., Van den Eynde, B.J., van der Bruggen, P. & Boon, T. Tumour antigens recognized by T lymphocytes: at the core of cancer immunotherapy. *Nature reviews. Cancer* **14**, 135-46 (2014).
3. Wayteck, L., Breckpot, K., Demeester, J., De Smedt, S.C. & Raemdonck, K. A personalized view on cancer immunotherapy. *Cancer letters* (2013).
4. De Temmerman, M.L. et al. mRNA-Lipoplex loaded microbubble contrast agents for ultrasound-assisted transfection of dendritic cells. *Biomaterials* **32**, 9128-9135 (2011).
5. Reis e Sousa, C. Dendritic cells in a mature age. *Nature reviews. Immunology* **6**, 476-83 (2006).
6. Lutz, M.B. & Schuler, G. Immature, semi-mature and fully mature dendritic cells: which signals induce tolerance or immunity? *Trends in Immunology* **23**, 445-449 (2002).
7. Steinman, R.M., Hawiger, D. & Nussenzweig, M.C. Tolerogenic dendritic cells. *Annual Review of Immunology* **21**, 685-711 (2003).
8. Bonehill, A. et al. Enhancing the T-cell stimulatory capacity of human dendritic cells by co-electroporation with CD40L, CD70 and constitutively active TLR4 encoding mRNA. *Molecular therapy : the journal of the American Society of Gene Therapy* **16**, 1170-80 (2008).
9. Bonehill, A. et al. Single-Step Antigen Loading and Activation of Dendritic Cells by mRNA Electroporation for the Purpose of Therapeutic Vaccination in Melanoma Patients. *Clinical Cancer Research* **15**, 3366-3375 (2009).
10. Van Lint, S. et al. Preclinical Evaluation of TriMix and Antigen mRNA-Based Antitumor Therapy. *Cancer Research* **72**, 1661-1671 (2012).
11. Van Nuffel, A.M.T. et al. Intravenous and intradermal TriMix-dendritic cell therapy results in a broad T-cell response and durable tumor response in a chemorefractory stage IV-M1c melanoma patient. *Cancer Immunology Immunotherapy* **61**, 1033-1043 (2012).
12. Wilgenhof, S. et al. A phase IB study on intravenous synthetic mRNA electroporated dendritic cell immunotherapy in pretreated advanced melanoma patients. *Annals of Oncology* **24**, 2686-2693 (2013).
13. Van Meirvenne, S. et al. Efficient genetic modification of murine dendritic cells by electroporation with mRNA. *Cancer Gene Therapy* **9**, 787-797 (2002).
14. Motz, G.T. & Coukos, G. Deciphering and Reversing Tumor Immune Suppression. *Immunity* **39**, 61-73 (2013).
15. Gabrilovich, D.I. & Nagaraj, S. Myeloid-derived suppressor cells as regulators of the immune system. *Nature Reviews Immunology* **9**, 162-174 (2009).
16. Geers, B. et al. Self-assembled liposome-loaded microbubbles: The missing link for safe and efficient ultrasound triggered drug-delivery. *Journal of controlled release : official journal of the Controlled Release Society* **152**, 249-56 (2011).
17. Lentacker, I., Geers, B., Demeester, J., De Smedt, S.C. & Sanders, N.N. Design and Evaluation of Doxorubicin-containing Microbubbles for Ultrasound-triggered Doxorubicin Delivery: Cytotoxicity and Mechanisms Involved. *Molecular Therapy* **18**, 101-108 (2010).
18. Lentacker, I. et al. Ultrasound Exposure of Lipoplex Loaded Microbubbles Facilitates Direct Cytoplasmic Entry of the Lipoplexes. *Molecular Pharmaceutics* **6**, 457-467 (2009).
19. Chen, J. et al. Generation of CTL responses against pancreatic cancer in vitro using dendritic cells co-transfected with MUC4 and survivin RNA. *Vaccine* **31**, 4585-4590 (2013).
20. Grunebach, F., Muller, M.R., Nencioni, A. & Brossart, P. Delivery of tumor-derived RNA for the induction of cytotoxic T-lymphocytes. *Gene Therapy* **10**, 367-374 (2003).
21. Lentacker, I., De Cock, I., Deckers, R., De Smedt, S.C. & Moonen, C.T. Understanding ultrasound induced sonoporation: Definitions and underlying mechanisms. *Advanced Drug Delivery Reviews* **72**, 49-64 (2014).
22. Lutz, M.B. & Rossner, S. Factors influencing the generation of murine dendritic cells from bone marrow: The special role of fetal calf serum. *Immunobiology* **212**, 855-862 (2007).

23. Fan, Z., Kumon, R.E., Park, J. & Deng, C.X. Intracellular delivery and calcium transients generated in sonoporation facilitated by microbubbles. *Journal of Controlled Release* **142**, 31-39 (2010).
24. Shumilina, E., Huber, S.M. & Lang, F. Ca2+ signaling in the regulation of dendritic cell functions. *American Journal of Physiology-Cell Physiology* **300**, C1205-C1214 (2011).
25. Vasievich, E.A., Chen, W. & Huang, L. Enantiospecific adjuvant activity of cationic lipid DOTAP in cancer vaccine. *Cancer Immunology Immunotherapy* **60**, 629-638 (2011).
26. Chen, H. et al. The promotion of type 1 T helper cell responses to cationic polymers in vivo via toll-like receptor-4 mediated IL-12 secretion. *Biomaterials* **31**, 8172-80 (2010).
27. Germeau, C. et al. High frequency of antitumor T cells in the blood of melanoma patients before and after vaccination with tumor antigens. *The Journal of experimental medicine* **201**, 241-8 (2005).
28. Lurquin, C. et al. Contrasting frequencies of antitumor and anti-vaccine T cells in metastases of a melanoma patient vaccinated with a MAGE tumor antigen. *The Journal of experimental medicine* **201**, 249-57 (2005).
29. Bonertz, A. et al. Antigen-specific Tregs control T cell responses against a limited repertoire of tumor antigens in patients with colorectal carcinoma. *Journal of Clinical Investigation* **119**, 3311-3321 (2009).
30. Pen, J.J. et al. Modulation of regulatory T cell function by monocyte-derived dendritic cells matured through electroporation with mRNA encoding CD40 ligand, constitutively active TLR4, and CD70. *Journal of Immunology* **191**, 1976-83 (2013).
31. Karimi, K. et al. Enhanced antitumor immunity elicited by dendritic cell vaccines is a result of their ability to engage both CTL and IFN gamma-producing NK cells. *Molecular Therapy* **16**, 411-418 (2008).
32. Van Elssen, C.H.M.J., Oth, T., Germeraad, W.T.V., Bos, G.M.J. & Vanderlocht, J. Natural Killer Cells: The Secret Weapon in Dendritic Cell Vaccination Strategies. *Clinical Cancer Research* **20**, 1095-1103 (2014).
33. Marcus, A. & Raulet, D.H. Evidence for Natural Killer Cell Memory. *Current Biology* **23**, R817-R820 (2013).
34. Paust, S. & von Andrian, U.H. Natural killer cell memory. *Nature Immunology* **12**, 500-508 (2011).
35. Xie, A. et al. Ultrasound-mediated vascular gene transfection by cavitation of endothelial-targeted cationic microbubbles. *JACC. Cardiovascular imaging* **5**, 1253-62 (2012).
36. Nomikou, N., Tiwari, P., Trehan, T., Gulati, K. & McHale, A.P. Studies on neutral, cationic and biotinylated cationic microbubbles in enhancing ultrasound-mediated gene delivery in vitro and in vivo. *Acta biomaterialia* **8**, 1273-80 (2012).
37. Sever, A.R. et al. Preoperative Sentinel Node Identification With Ultrasound Using Microbubbles in Patients With Breast Cancer. *American Journal of Roentgenology* **196**, 251-256 (2011).
38. Randolph, G.J., Angeli, V. & Swartz, M.A. Dendritic-cell trafficking to lymph nodes through lymphatic vessels. *Nature Reviews Immunology* **5**, 617-628 (2005).
39. Henri, S. et al. The dendritic cell populations of mouse lymph nodes. *Journal of Immunology* **167**, 741-748 (2001).
40. Newman, C.M. & Bettinger, T. Gene therapy progress and prospects: ultrasound for gene transfer. *Gene Therapy* **14**, 465-75 (2007).

Chapter 6

Theranostic mRNA-loaded microbubbles in the lymphatics of dogs: implications for drug delivery

This chapter is published as:

Heleen Dewitte[1,*], Katrien Vanderperren[2,*], Hendrik Haers[2], Emmelie Stock[2], Luc Duchateau[3], Myriam Hesta[4], Jimmy H. Saunders[2], Stefaan C. De Smedt[1], and Ine Lentacker[1]. Theranostic mRNA-loaded microbubbles in the lymphatics of dogs: implications for drug delivery. *Theranostics* **5**, 97-109 (2015).

[*]Both authors contributed equally to this work

[1]Laboratory for General Biochemistry and Physical Pharmacy, Faculty of Pharmacy, Ghent University, 9000 Ghent, Belgium

[2]Department of Veterinary Medical Imaging and Small Animal Orthopaedics, Faculty of Veterinary Medicine, Ghent University, 9820 Merelbeke, Belgium

[3]Department of Comparative Physiology and Biometrics, Faculty of Veterinary Medicine, Ghent University, 9820 Merelbeke, Belgium

[4]Department of Animal Nutrition, Faculty of Veterinary Medicine, Ghent University, Heidestraat 19, 9820 Merelbeke, Belgium

ABSTRACT

Microbubbles have shown potential as intralymphatic ultrasound contrast agents while nanoparticle-loaded microbubbles are increasingly investigated for ultrasound-triggered drug and gene delivery. To explore whether mRNA-nanoparticle loaded microbubbles could serve as theranostics for detection and mRNA transfer to the lymph nodes, we investigate the behavior of unloaded and mRNA-loaded microbubbles using contrast-enhanced ultrasound imaging after subcutaneous injection in dogs. Our results indicate that both types of microbubbles are equally capable of rapidly entering the lymph vessels and nodes upon injection, and novel, valuable and detailed information on the lymphatic structure in the animals could be obtained. Furthermore, additional observations were made regarding the dynamics of microbubble lymph node uptake. Importantly, neither the microbubble migration distance within the lymphatics, nor the observed contrast signal intensity was influenced by mRNA-loading. Although further optimization of acoustic parameters will be needed, this could represent a first step towards ultrasound-guided, ultrasound-triggered intranodal mRNA delivery using these theranostic microbubbles.

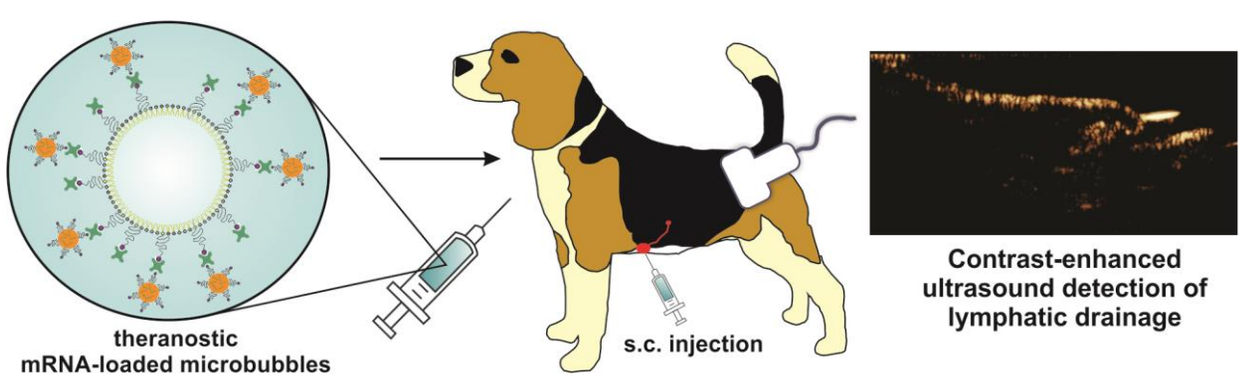

INTRODUCTION

Over the years, microbubbles have gained popularity as contrast agents for ultrasound imaging, as described in **Chapter 1**. When injected intravenously, these microbubbles remain within the vasculature where they increase the echogenicity of blood. In this way, enhanced contrast between blood and soft tissues can be achieved. This has led to the FDA and EMA approval of various microbubble contrast agents for echocardiography (e.g. Definity®, SonoVue®, Sonazoid® and Optison®)[1]. Ever since, new applications for these contrast agents are under investigation, including their potential to enhance contrast in the lymphatics. For this, the microbubbles are injected intradermally (i.d.) or subcutaneously (s.c.), after which they drain to the lymphatics and accumulate in the lymph nodes. This is particularly interesting, since studies in tumor-bearing animals as well as in human breast cancer patients showed that peritumoral i.d. and s.c. injection of microbubbles results in their drainage to the sentinel lymph node (SLN)[2-7]. This lymph node is especially important, as it is the first node to come in contact with tumor material, making it most vulnerable to metastasis. Therefore, SLN detection, biopsy and removal are routine procedures in oncology to detect and remove disseminated tumor cells[8, 9]. Currently used standard methods for SLN detection are the injection of blue dyes which aid to localize the SLN visually during surgery, or via scintigraphy after injection of radiolabeled dyes[8, 10]. However, these procedures both come with their limitations, resulting in an ongoing search for novel SLN mapping modalities, such as microbubble contrast-enhanced ultrasound imaging (CEUS), which could represent a non-radioactive, non-invasive and potentially more patient-friendly alternative[11, 12].

In addition to these clinical applications, microbubbles are also under preclinical investigation as potential drug- and gene-delivery agents. When microbubbles are exposed to ultrasound, their gas core starts cavitating, *i.e.* continuously expands and shrinks. When the amplitude of the applied ultrasound waves is augmented, this cavitation can become unstable, eventually causing the microbubbles to implode. Both stable cavitation as well as microbubble implosion can affect neighboring cells, by either stimulating endocytosis or by the formation of temporary pores in the cell membranes[13]. Both mechanisms can be used for ultrasound-triggered delivery of drugs and genes *in vitro* and *in vivo*[14-16].

In the previous chapters, we reported on the design of microbubbles that can be loaded with mRNA-nanoparticles and therefore have potential applications in cancer immunotherapy[17]. The results in **Chapter 4** indicated that it is indeed possible to induce ultrasound-triggered transfection of dendritic cells (DCs) *in vitro*, without interfering with their potential to respond to maturation stimuli[17]. Furthermore, in **Chapter 5** we expanded this concept by loading the microbubbles with lipoplexes containing both antigen as well as adjuvant mRNA. When mRNA-sonoporated DCs were injected as vaccines, we showed the onset of potent antitumor immune

responses and the induction of long-term immunological memory[18]. However, for these mRNA-loaded microbubble vaccines to have potential for *in vivo* transfection of DCs, it is crucial that they can be present within the anatomical locations where large numbers of DCs are present: the lymph nodes.

Therefore, we investigated if these nucleic-acid loaded bubbles can reach the lymph nodes after s.c. injection, and if this can be monitored with CEUS. For this, we performed a crossover study where both unloaded and mRNA-loaded microbubbles were injected s.c. in dogs. Using CEUS, we determined (a) which injection site resulted in optimal lymphatic microbubble appearance, (b) if there were differences in kinetics and lymph node contrast-enhancement for both types of microbubbles and (c) to what extent the nucleic acid-loaded microbubbles could have potential as intralymphatic theranostics.

MATERIALS AND METHODS

mRNA and mRNA-lipoplexes

Luciferase mRNA was produced by *in vitro* transcription from pBlue-Luc-A50 plasmids. The plasmids were purified using a QIAquick PCR purification kit (Qiagen, Venlo, The Netherlands) and linearized using *Dra* I restriction enzymes (Promega, Leiden, The Netherlands). Linearized plasmids were used as templates for the *in vitro* transcription reaction using the T7 mMessage mMachine kit (Ambion, Life Technologies, Ghent, Belgium). The resulting capped and polyadenylated mRNAs were purified by DNase I digestion, LiCl precipitation and washed with 70% ethanol. The mRNA concentration was determined by measuring the absorbance at 260 nm. mRNA was stored in small aliquots at -80°C at a concentration of 1 µg μl^{-1}.

mRNA lipoplexes were prepared by complexing the mRNA to cationic liposomes. For this, liposomes were prepared consisting of 48.75% DOTAP (1,2-dioleoyl-3-trimethylammonium-propane), 48.75% DOPE (1,2-dioleoyl-*sn*-glycero-3-phosphoethanolamine, both Avanti Polar Lipids) and 2.5% DSPE-PEG3400-biotin [1,2-distearoyl-*sn*-glycero-3-phosphoethanol-amine-N-[biotinyl(polyethylene glycol)-3400] (Laysan Bio Inc., Arab, Alabama). Fluorescently labeled mRNA-lipoplexes were prepared by incorporating 1% CholEsteryl-BODIPY® FL C12 (Avanti Polar Lipids). The appropriate amounts of lipids (dissolved in chloroform) were transferred to a round-bottom flask, and the chloroform was evaporated under nitrogen. Subsequently, the resulting lipid film was hydrated in RNase-free water (Ambion) to obtain a final lipid concentration of 1 mg ml^{-1}. The resulting cationic liposomes were sonicated for 15min in a bath sonicator (Branson Ultrasonics, Dansbury, USA). Then, the cationic liposomes were mixed with mRNA in OptiMem® (Gibco Invitrogen) to obtain mRNA-lipoplexes at a cationic lipid-to-mRNA charge (N/P) ratio of 8.

Unloaded and mRNA-loaded microbubbles

Lipid microbubbles loaded with mRNA-lipoplexes were prepared as described previously[17]. Briefly, perfluorobutane (F2 chemicals, Preston, UK) microbubbles stabilized by a lipid coat consisting of DPPC (1,2-dipalmitoyl-*sn*-glycero-3-phosphocholine) (Lipoid, Ludwigshafen, Germany) and DSPE-PEG3400-biotin [1,2-distearoyl-*sn*-glycero-3-phosphoethanolamine-N-[biotin(polyethylene glycol)-3400] in a 85:15 molar ratio were prepared as follows. Appropriate aliquots of both lipids, dissolved in chloroform, were transferred to a round-bottom flask. After chloroform evaporation, the lipids was dissolved in a 1:2:7 glycerol-propyleneglycol-H_2O mixture to obtain a clear solution with a final concentration of $4.6x10^{-4}$ mmol ml^{-1}. Aliquots of this lipid solution were transferred to 2.5 ml chromatography vials and the vial headspace was filled with perfluorobutane gas (F2 chemicals, Preston, UK). In order to form microbubbles, the vials were shaken at high-frequency in a Capmix™ device (3M-ESPE, Diegem, Belgium) for 15s. Microbubbles were avidinylated by first performing washing steps to remove excess lipids, after which the microbubbles were incubated with avidin (Cell Sciences, Canton, USA) for 5min. Then, the bubbles were washed to remove excess avidin and the final bubble cake was redispersed in a sterile, endotoxin- and nuclease-free 5% glucose solution (Sigma-Aldrich, Diegem, Belgium). 5min prior to injection, 150 µl avidinylated bubbles were mixed with either 100 µl OptiMem® (for the unloaded bubbles) or 100 µl mRNA-lipoplexes (for the mRNA-loaded microbubbles, corresponding to 10 µg mRNA per injection).

Microbubble characterization

The size distribution and concentration of mRNA-loaded microbubbles was determined via coulter counter measurements using a Beckman-coulter Multisizer 4 (Analis SA, Suarlée, Belgium). Confocal microscopy was performed to evaluate the loading of the microbubbles with fluorescently labeled mRNA-lipoplexes. This was done using a Nikon C1si confocal laser scanning module attached to a motorized Nikon TE2000-E inverted microscope (Nikon, Brussels, Belgium), and a Plan Apo 60X 1.4 NA oil immersion objective lens (Nikon).

Dogs

Six healthy research beagles (3 spayed females, 1 intact female and 1 castrated male and 1 intact male) were used in this experiment. All procedures were performed in accordance with the Ethical committee guidelines of Ghent University (2014/31). The mean age of the animals was 7 years, and body weight ranged from 9.7 kg to 15.4 kg with a mean of 10.8 kg. Dogs were healthy based on physical findings and routine laboratory data.

Contrast-enhanced ultrasound imaging

For CEUS experiments, the animals were sedated by intravenous injection of a combination of Butorphanol (Dolorex®, 0.4 mg kg^{-1}) and Acepromazine (Placivet®, 0.04 mg kg^{-1}). Once sedated, the animals were manually restrained in dorsal recumbency and received a s.c. injection of microbubbles. First, different injection sites in the caudal abdomen and inguinal region were evaluated based on contrast migration to choose the optimal location for further experiments. After injection of 250 µl microbubbles, the contrast timer was started and the injection site was massaged during 1min. After this, continuous CEUS imaging was performed with contrast-specific software using a 12-5 MHz linear transducer (L12-5) of a Philips iU-22 US scanner (Philips Medical systems, Bothell, Wa) for at least 6min. Mechanical index (MI) was set at a low level (MI=0.08) to achieve microbubble resonance with production of harmonic frequencies. Machine settings such as overall gain (80%), time gain compensation, depth (2.5 cm), frame rate (10 Hz) persistence (off) and dynamic range were set at the same value for every examination. Only one focal spot was used, set at the lowest level of the image. Destruction of intranodal microbubbles was performed at the end of the imaging period by setting the acoustic power at the highest level (MI=0.61). Multiple subsequent bursts were delivered until the echo intensity stabilized.

This study was performed using a crossover design, with all dogs receiving 2 injections of both unloaded and mRNA-loaded microbubble formulations, on 2 injection sites (in the left and right abdominal region) at 2 different time points separated by a 2 week wash-out period, resulting in a total of 24 injections (12 with unloaded bubbles and 12 with mRNA loaded bubbles, **Table 1**).

Table 1. Design of the crossover CEUS study.

Day	Dogs	Microbubble injections
Week 1, day 1	1, 2, 3	Left: unloaded microbubbles Right: mRNA-loaded microbubbles
Week 1, day 2	4, 5, 6	Left: mRNA-loaded microbubbles Right: unloaded microbubbles
2 week wash-out		
Week 3, day 1	1, 2, 3	Left: mRNA-loaded microbubbles Right: unloaded microbubbles
Week 3, day 2	4, 5, 6	Left: unloaded microbubbles Right: mRNA-loaded microbubbles

Image analysis

Image analysis was performed using QLAB quantification software (Philips) and ImageJ. Microbubble migration distances were calculated as a linear distance between the injection site and the most distant microbubble contrast signal. Measurements were performed by 2 independent, blinded observers. Maximal echo intensities were measured using ImageJ at different timepoints after injection on a region of interest (ROI) within the lymphatics (i.e. within the enhanced lymph nodes or within the lymph vessels when no lymph node enhancement could be observed). Analysis of burst destruction of intranodal microbubbles was performed by drawing a ROI over the lymph node of interest, after which the mean echo intensity was studied as a function of time using the QLAB quantification software. In the figures, time is indicated in min:s on the CEUS images, and the depth scale bar is shown at the right-hand side of the corresponding B-mode images (the distance between two ticks is 5 mm in all images). In the figures, time is indicated in min:s on the CEUS images, and the depth scale bar is shown at the right-hand side of the corresponding B-mode images (the distance between two ticks is 5 mm in all images).

Statistical analysis

The migration distance and the maximal echo intensity was compared between the loaded and unloaded bubbles by a mixed model with dog as random effect and period and bubble type as categorical fixed effects, using the F-test at the 5% significance level. The contrast echo intensity over time was compared between the loaded and unloaded bubbles by a mixed model with dog as random effect and period, time, bubble type and the interaction

between time and bubble type as categorical fixed effects, using the F-test at the 5% significance level.

Within and between observer variability was determined by estimating the within and between observer variances for a same assessment (*i.e.*, the same dog, side, bubble type and period) by the restricted maximum likelihood procedure (REML). These estimated variances were next used to determine the range in which 95% of the differences between two measurements of the same observers and two different observers are contained. SAS version 9.3 was used for all analyses.

RESULTS

Characterization of unloaded and mRNA-loaded microbubbles

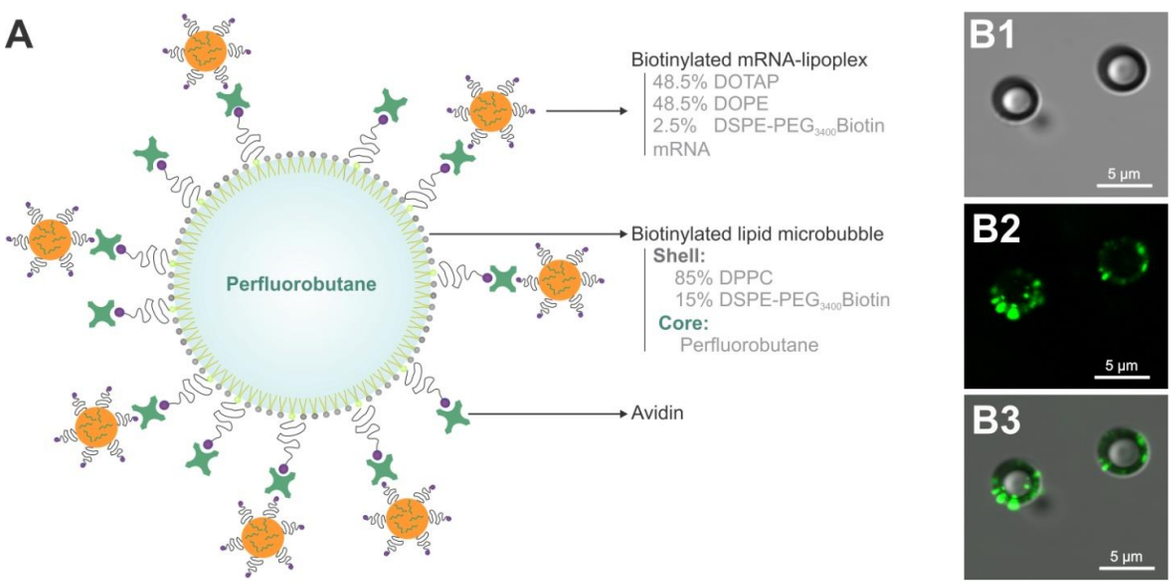

Figure 1. Characterization of mRNA-loaded microbubbles.

(A) Graphical representation of the mRNA-loaded microbubble composition. (B) Confocal micrographs of microbubbles loaded with fluorescently labeled mRNA-lipoplexes: (B1) transmission, (B2) green fluorescent mRNA-lipoplexes, (B3) overlay.

mRNA-lipoplex loaded microbubbles were prepared by first complexing the mRNA to cationic liposomes, to form mRNA-lipoplexes in which the mRNA is protected against degradation. These mRNA-lipoplexes are then attached to the surface of avidinylated lipid microbubbles, as shown in **Figure 1A**. To demonstrate effective loading, we performed confocal microscopy on microbubbles that were loaded with fluorescently labeled mRNA-lipoplexes. As demonstrated in **Figure 1B**, the mRNA-lipoplexes are clearly present around the microbubble surface, and we did not observe any aggregation. The size and concentration of the microbubble preparations was determined via coulter counter measurements. The unloaded microbubbles had a mean number diameter of 2.48 ± 1.57 µm. Attachment of mRNA-lipoplexes

did not significantly alter the mean diameter (1.93 ± 1.25 µm). The concentration of the microbubble preparations was 2.68 ± 0.86 x 10^9 bubbles ml^{-1}.

Factors influencing intralymphatic CEUS

Based on previous experiments studying the lymphatic drainage of SonoVue® microbubbles by Goldberg et al.[7], we performed s.c. injections of both unloaded and mRNA-loaded microbubbles in dogs. When performing these experiments, we observed a number of factors that influenced the observed CEUS signals.

First of all, we noticed important differences in the migration of the microbubbles depending on the injection site. When the microbubbles were injected in the groin, close to the inguinal lymph node, no lymphatic uptake of the contrast agents could be observed. The reasons for this are probably dual. First of all, lymphatic uptake occurs through a passive process that depends on the interstitial pressure at the injection site. Hence, regions such as the groin, where the skin is loose and the interstitial pressure is low, are not preferable[19]. In addition to pressure-related differences, some tissues such as the mammary regions of female dogs, contain a more developed lymph vessel network. In accordance to this, initial s.c. injections of the contrast agents in the loose skin of the abdominal region, did not result in migration of the contrast agents from the injection site. This despite the fact that the microbubbles were injected at a distance of merely 20 mm from the inguinal lymph node, as indicated by palpation and B-mode ultrasound imaging. On the other hand, injection around the dog's nipple resulted in extensive microbubble drainage in all female dogs, as shown in **Figure 2**. Migration from the injection site was seen for all injections with both unloaded (8/8) and mRNA-loaded (8/8) microbubbles in the female dogs, and after most of the injections around the nipples of the male dogs (4/4 for the unloaded bubbles and 2/4 for the mRNA-loaded bubbles). This is not unexpected, as the mammary regions accommodate a vast network of lymph vessels that lead to multiple clusters of lymph nodes close to the mammary glands, as well as more distant gastric and mesenteric lymph nodes, depending on the location of the mammary gland (e.g. axillary versus inguinal mammary glands)[20]. Based on these observations, further injections were performed s.c. around the left and right nipple of the inguinal mammary gland.

Besides the effects of the injection site, inter-animal variation in the mammary gland lymphatic network also played a role. In male dogs, the mammary glands are markedly less developed compared to females, which also results in a less dense lymphatic network and fewer intramammary nodes. Moreover, the male dogs clearly showed a less thick subcutaneous fat layer (*i.e.* where the lymph vessels and nodes are located) compared to all females, as evidenced by the B-mode images in Figure A2, B2 and C2. As a result, contrast agent migration after injection was less pronounced in the males compared to the females. In the intact male,

injection next to the testicles resulted in more distant microbubble migration when compared to injection around the mammary glands, which therefore represented a valuable alternative to injection around the mammary glands. Beside these gender-related factors, we also observed differences between spayed and intact females. After microbubble injection in the intact female, the lymphatic structures were visible as a vast network with multiple nodes and vessels extending more deeply into the subcutaneous fat pad (Figure 2C, observed for all injections with both unloaded and mRNA-loaded microbubbles). Such a branched lymph network could not be observed in any of the 3 spayed females.

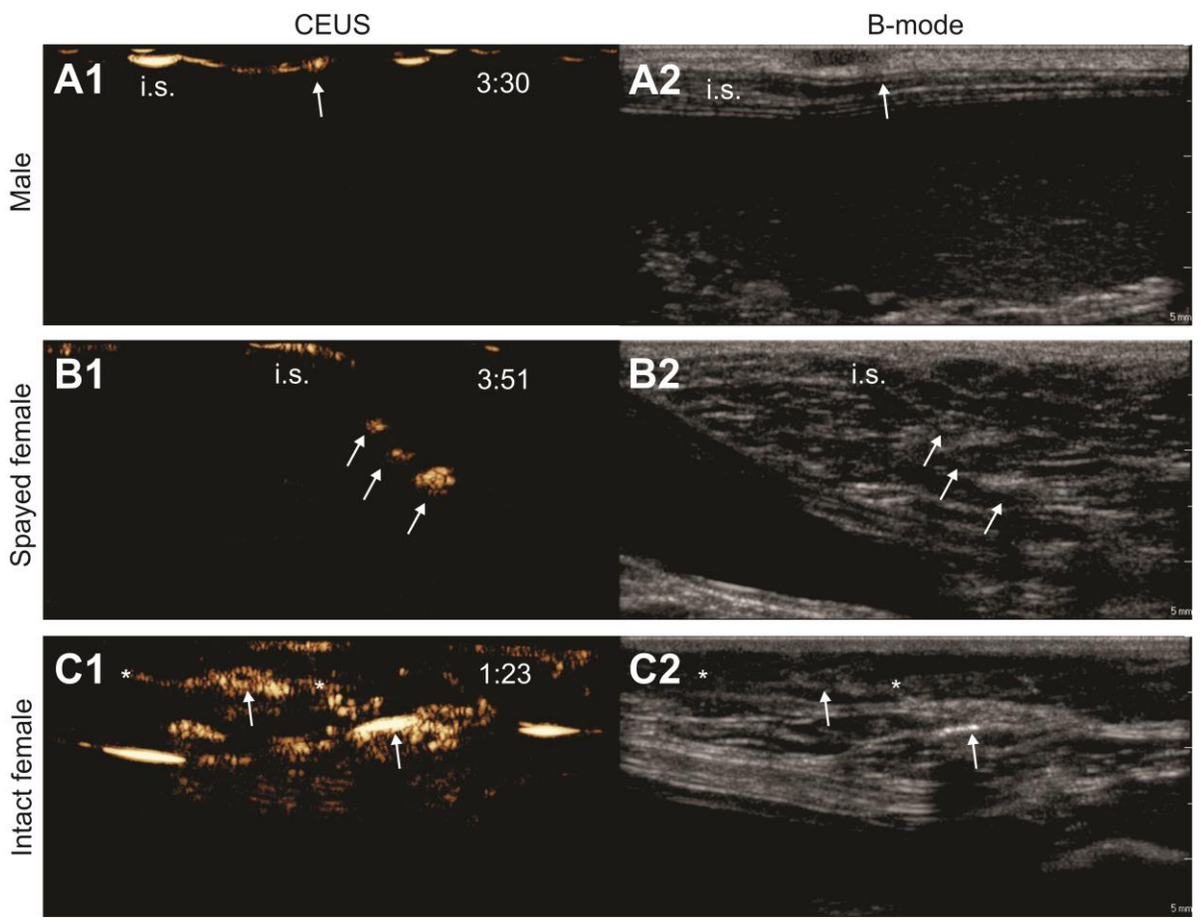

Figure 2. Influence of animal properties on the lymphatic CEUS images.

CEUS images obtained after s.c. injection of unloaded microbubbles around the mammary glands of a male dog (A1), a spayed female dog (B1) and an intact female dog (C1). Respective B-mode images are shown in A2, B2 and C2. The injection site is indicated as "i.s." (The injection site for images C1 and C2 is out of the field-of-view), arrows indicate the accumulation of microbubbles in the lymph nodes and lymph vessels are pointed out with asterisks. Time after microbubble injection is noted on the CEUS images (in min:s).

Of course, this inter-animal variation makes it more difficult to fully exclude anatomical bias when comparing the lymphatic drainage of unloaded and mRNA-loaded microbubbles. The crossover design used for this study, where all dogs receive s.c. injections with both unloaded and mRNA-loaded microbubbles in the nipples of both the left- and the right caudal

mammary gland, was used to take this variability into account and allow a better comparison of both microbubble types.

Lymphatic network visualization

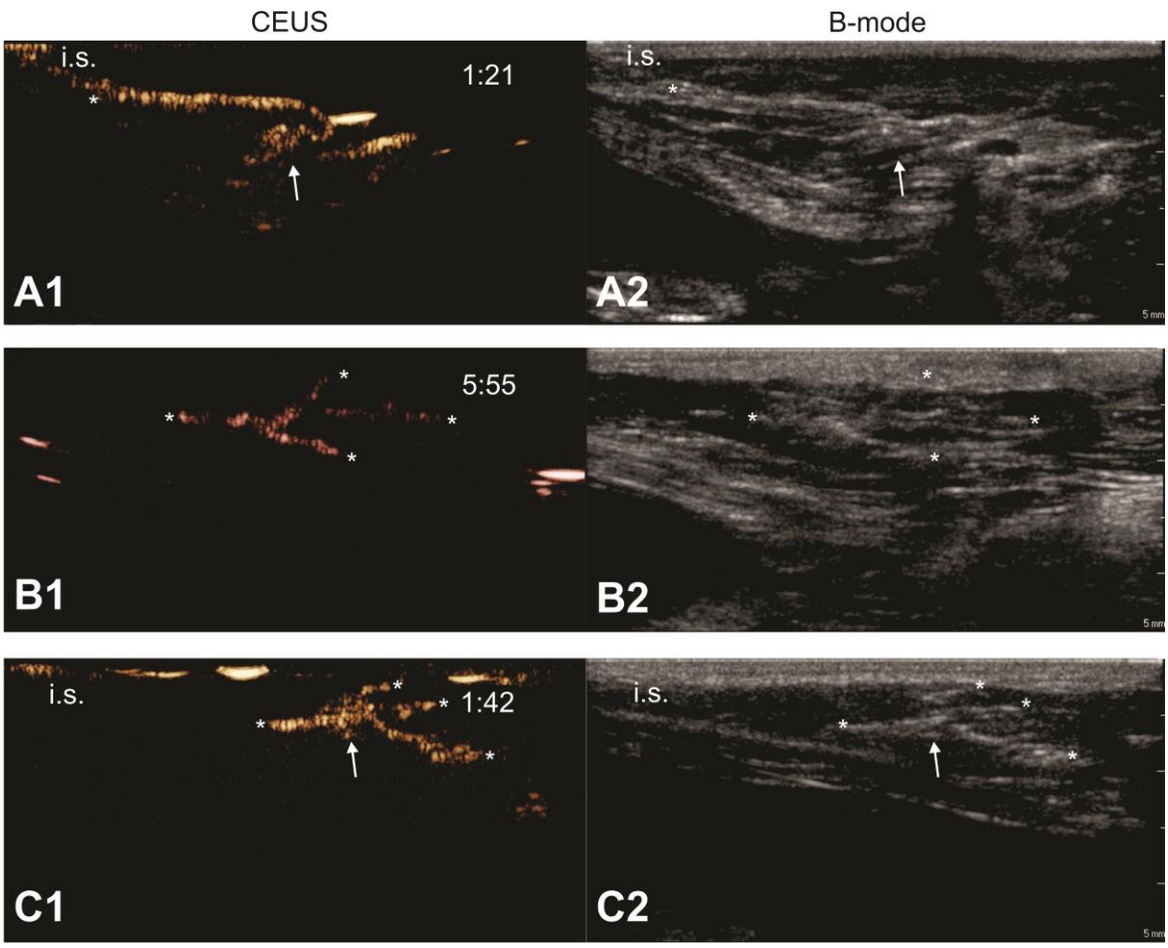

Figure 3. Contrast agent migration from the injection site into the lymph vessels and nodes.

Upon microbubble injection, unidirectional transport of microbubbles away from the injection site, through an afferent lymph vessel into a draining lymph node can be observed with CEUS (A1). Image (B1) shows the trafficking of microbubble contrast signal through branched lymph vessels. In (C1), the CEUS image shows a lymph node connected to one afferent lymph vessel and 3 efferent lymph vessels that take the contrast agents further away from the injection site. Corresponding B-mode images are shown in (A2), (B2) and (C2), respectively. Images were obtained after injection of mRNA-loaded microbubbles in different female dogs. The injection site is marked as “i.s.” (unless outside of the field-of-view), arrows indicate lymph nodes and asterisks point out lymph vessels. Time after microbubble injection is noted in min:s.

After microbubble injection and massaging of the injection site, the migration of the contrast agent was observed unidirectional, with the contrast agents leaving the injection site at only one end in the spayed females and the males, as exemplified in **Figure 3A**. In the intact female, microbubble migration occurred both cranially as well as caudally. The migrating contrast agents were followed through the lymph vessels towards draining lymph nodes (Figure 3B and 3C). Importantly, in none of the injections (0/24) was blood pool contrast enhancement observed, indicating that the microbubbles were restricted to the interstitium, the lymph vessels and the lymph nodes. Moreover, when the contrast agents were injected on one side (either left or right) of the animal, contrast signal was only observed on that same side of the animal. No contrast crossing over the midline of the dogs was noted in any of the cases. One or multiple lymph nodes could be identified using CEUS after 9/12 injections of both unloaded and mRNA-loaded microbubbles, and the size of the enhanced lymph nodes ranged from 1.6 to 7.0 mm.

Interestingly, CEUS imaging revealed detailed information on the lymphatic anatomy: in accordance to previous reports, CEUS could pinpoint the location of the lymph nodes, and provide information on the number of afferent and efferent lymph vessels[5]. In addition, we could observe different patterns of contrast agent presence with the nodes. Some lymph nodes, such as the one shown in **Figure 4A**, are completely filled with contrast agent, whereas others rather exhibit a “hollow” appearance, with contrast material only appearing at the outer rim of the node, as shown by the yellow arrows in **Figure 4B** and **4C**. This can be explained by the fact that afferent lymph vessels can either directly discharge their content into the draining lymph nodes, or the afferent lymph vessels run through or over the nodes, without effectively discharging the lymph within the node[21].

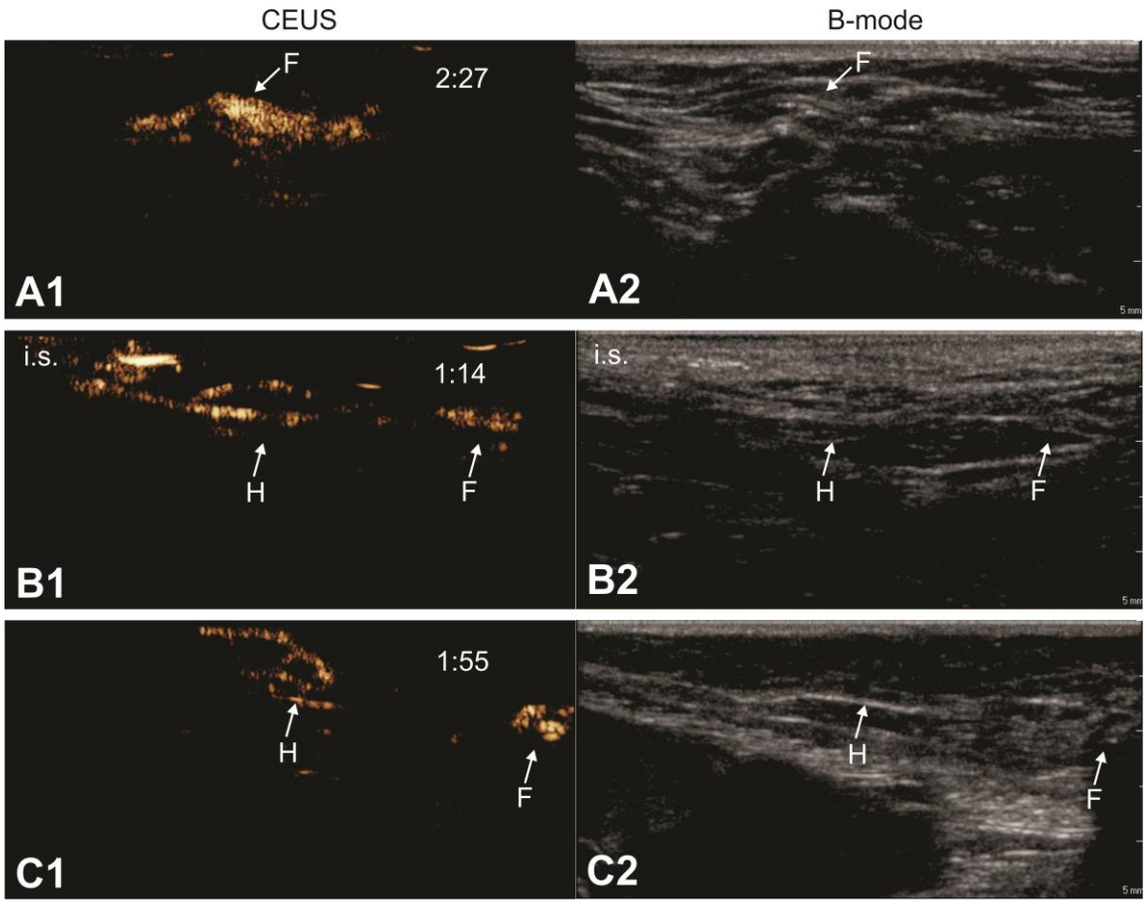

Figure 4. Lymph node anatomy observed by CEUS.

CEUS can be used to identify the relation between afferent lymph vessels and draining lymph nodes. Lymph vessels either distribute their content within the lymph node ("filled" nodes, A1-A2) or they go around the lymph nodes without discharging its contents into the node ("hollow" nodes, B1-B2 and C1-C2). In the latter scenario, we always observed a node with a "hollow" appearance (indicated as "H"), followed by a more distant "filled" node (indicated as "F"). Images were obtained from 3 different animals. Where possible, the injection site is pointed out as "i.s.". Time after microbubble injection is noted on the CEUS images (in min:s).

Lymphatic CEUS using mRNA-loaded microbubbles versus unloaded microbubbles.

In this study, we compared the CEUS images after s.c. injection of unloaded and mRNA-loaded microbubbles, using three main scoring criteria: (a) the migration distance of the contrast agents from the injection site within the lymphatics, (b) the maximal intensity of the contrast signal and (c) the stability of the contrast agents in the lymph vessels and nodes over time.

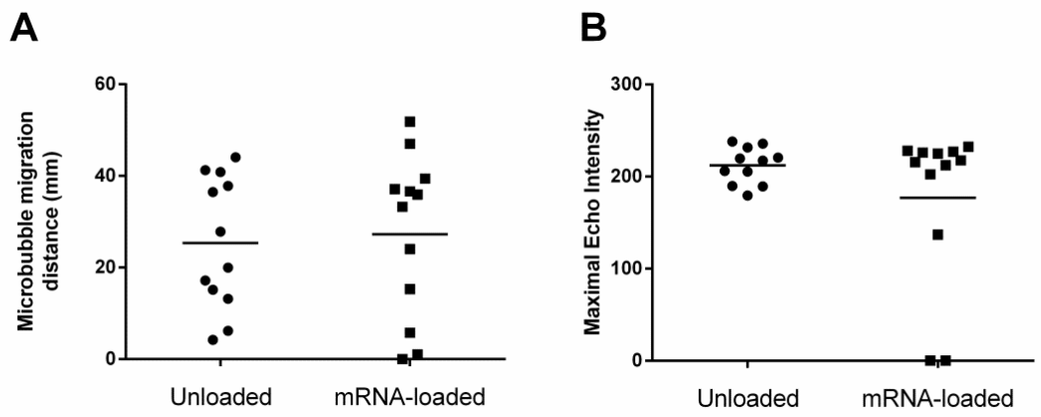

Figure 5. Maximal migration distance and maximal echo intensity of mRNA-loaded and unloaded microbubbles.

Scatterplots show (A) the linear migration distance of unloaded and mRNA-loaded microbubbles from the injection site and (B) the maximal echo intensity within the lymphatics for both microbubble types. For both parameters, no statistically significant differences between unloaded and mRNA-loaded microbubbles could be detected.

With regard to the first parameter, the migration distance, we could detect microbubble migration from the injection site for all injections with unloaded microbubbles (12/12), and in 10/12 cases after mRNA-loaded microbubble injections. The two injections that did not result in contrast agent drainage were observed in the male dogs (one in the castrated male and one in the intact male). The microbubble migration distance (calculated linearly from the injection site) was on average 24.7 ± 13.7 mm for unloaded microbubbles and 29.0 ± 19.0 mm for mRNA-loaded microbubbles (**Figure 5A**). No significant differences could be observed between for migration distances of loaded and unloaded bubbles, with a mean difference equal to 4.33 (95% CI: [-4.55; 13.22]). It should be noted that even though these results were analyzed based on injections of unloaded and mRNA-loaded microbubbles within the same mammary gland, variation based on the exact injection site cannot be excluded, even though injections were always performed caudally from the nipple by the same person. For instance, it was shown by Goldberg et al. that injection sites that were merely 1 cm apart in distance, could result in drainage to a different lymph node, which can obviously impact the microbubble migration distance that was observed[6]. As the exact injection site was not marked at the time of the first imaging session, variation related to the injection site location cannot be fully excluded. The variation between repeated measurements of the same observer was 23.9, and the extra variation due to different observers was 9.0 for loaded bubbles, leading to somewhat larger 95% intervals for differences between two measurements of two different observers as compared to the same observer. On the other hand, for the unloaded microbubbles, the variation due to repeated observations of the same observer was 16.7, and there was no extra

variation due to different observers, resulting in the same 95% intervals for differences between two measurements of two different observers as compared to the same observer.

In addition to migration distance measurements, we compared the maximal echo intensity that we could obtain within the lymphatics after injection of unloaded and mRNA-loaded microbubbles. As for the migration distance, we could not observe significant differences in lymphatic contrast enhancement between both types of bubbles (**Figure 5B**), with a mean difference between loaded and unloaded bubbles equal to -2.56 (95% CI: [-15.04; 9.91]). Moreover, when the contrast echo intensity was evaluated as a function of time, we could observe relatively long-term contrast agent stability within the lymphatics. In all cases where contrast migration was observed, the microbubbles could still be clearly detected 6 min after microbubble injection. There was merely a slight decay of the echo intensity over this period, and we could not detect significant differences between both types of microbubbles (**Figure 6**).

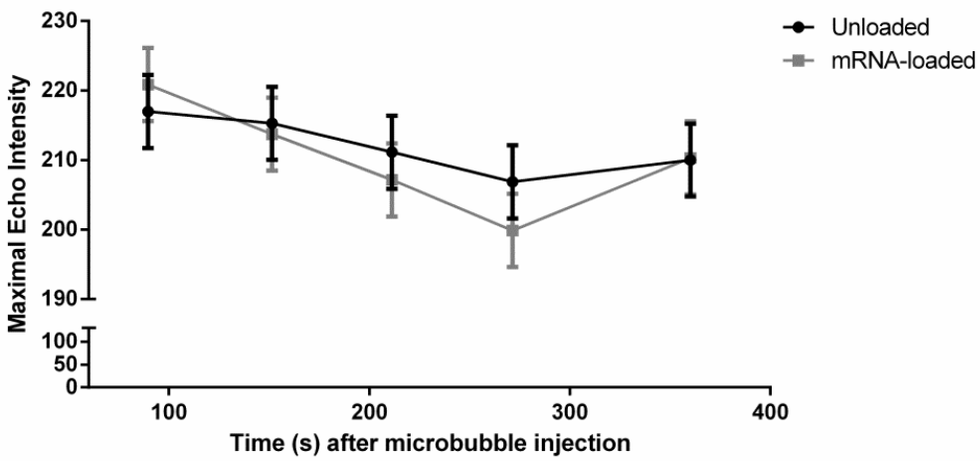

Figure 6. Intralymphatic stability of unloaded and mRNA-loaded microbubbles. The maximal echo intensity was followed as a function of time for both unloaded and mRNA loaded microbubbles. A slow reduction in maximal echo intensity was observed over the 6min imaging period. No significant differences could be detected between unloaded and mRNA-loaded microbubbles.

Keeping in mind the final aim of the mRNA loaded microbubbles, namely the ultrasound-triggered delivery of mRNA to DCs that reside within the lymph nodes, we tested whether intranodal mRNA-loaded microbubbles could indeed be imploded by applying higher-intensity ultrasound bursts. For this, we used the scanner's preset burst function (at a MI of 0.61), and looked at the decrease in mean echo contrast intensity within the lymph node. As shown in **Figure 7**, with each burst, the microbubble echo intensity was reduced, reaching a minimum after 6 bursts.

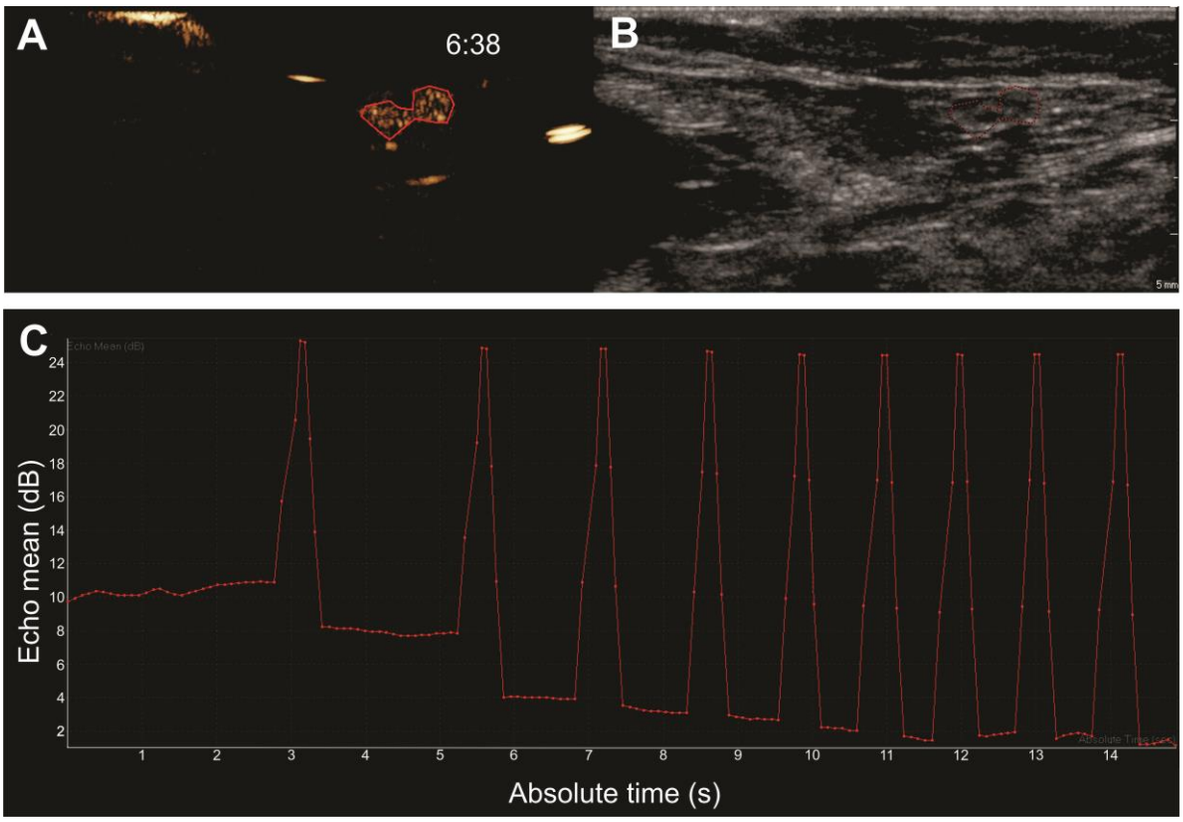

Figure 7. Burst destruction of intranodal microbubbles.

After visualization of microbubble drainage, the scanner's burst function was used to destroy the microbubbles within the lymphatics. Images show (A) a CEUS image with a ROI around a lymph node filled with mRNA-loaded microbubbles and (B) the corresponding B-mode image. Burst analysis is represented in (C) where each burst is visible as a peak in echo mean (in dB), followed by a reduction of the contrast echo mean. Time after microbubble injection is noted on the CEUS images (in min:s).

DISCUSSION

In recent years, drug- and gene loaded microbubbles emerged as interesting theranostics after intravenous injection. This, however, is the first report on the development of theranostic mRNA-loaded microbubbles for lymphatic imaging and lymph node detection after s.c. injection. When taken together with our previous research on transfections with these microbubbles, this paves the way for ultrasound-guided microbubble-assisted drug delivery to intranodal cells. To explore this, we aimed to compare unloaded and mRNA-loaded microbubbles with respects to the lymphatic uptake and contrast enhancement in the lymph nodes upon s.c. injection in dogs.

The lipid microbubbles used in this study could be loaded with mRNA-lipoplexes, and had mean diameters around 2.5 µm, which is comparable to the size of commercially available microbubbles. Lipoplex-loading did not significantly alter the mean microbubble diameter. Our imaging results indicated that despite animal-related variation, both types of microbubbles could be detected within the lymph nodes within 1min after s.c. injection around the mammary glands.

How exactly the microbubbles are transported from the interstitium to the lymph vessels remains controversial, as it goes against the current view of ideal particle properties for lymphatic uptake. It is generally considered that particles between 10 and 100 nm in size result in the best lymphatic uptake[19]. Although the appearance of 1 µm particles in the draining lymph nodes was also observed, their uptake efficiency and speed was significantly reduced, and a large fraction of the injected particles was retained at the injection site[22]. In the case of our microbubbles we could observe fast and extensive microbubble uptake into the lymph vessels and draining nodes, despite their larger size. The rapid uptake of microbubbles into the lymphatic system is not well understood. A first explanation could be found within the other physicochemical properties of the microbubble contrast agents we injected. Besides particle size, lipophilicity and the presence of surface modifications that give stealth properties to injected particles, were also reported to positively impact their lymphatic drainage[22]. Therefore, the presence of the lipid coat in both the microbubbles and the mRNA-lipoplexes could aid to promote microbubble uptake into the lymph vessels. In addition, the microbubbles as well as the mRNA lipoplexes contain lipids that are conjugated to polyethylene glycol (PEG, 15 mol.% and 2.5 mol.% for bubbles and lipoplexes, respectively), which is known to protect the particles against uptake by phagocytes. Thus, their premature clearance is reduced, resulting in enhanced drainage to the lymphatics. On the other hand, Goldberg et al. proposed a cell-mediated uptake mechanism after s.c. injection of Sonazoid® in pigs[6]. They performed electron microscopy on isolated lymph nodes after contrast agent injection, and observed the presence of vacuoles in the intranodal phagocytic cells, which could imply that the microbubbles are first ingested by cells, which then transport them from the interstitium to the lymph vessels and draining lymph nodes. However, this cellular transport through the lymphatics is only likely for microbubbles that are easily phagocytosed. A study by Yanagisawa et al. pointed out that microbubble phagocytosis by primary liver cells was highly dependent on the microbubble composition. Indeed, the authors demonstrated that over 99% of the Sonazoid® microbubbles were rapidly phagocytosed by primary liver cells, which can likely be attributed to their shell composition[23]. Sonazoid® consists of egg phosphatidyl serine, which is recognized by macrophages and thus enhances phagocytic uptake[24, 25]. In contrasts, anionic Imavist® microbubbles (where the anionic charges reduces microbubble contact with cell membranes) and PEGylated SonoVue® microbubbles were merely for 0% or 7.3% phagocytosed, respectively. As our microbubbles are also PEGylated (by inclusion of 15% DSPE-PEG(3400)-biotin), and no specific targets for macrophage recognition are present, it is unlikely that our microbubbles were carried into the lymphatics inside of cells. (For an overview of the shell composition of commercially available microbubbles, we refer to Table 4 in **Chapter 1**.)

Upon s.c. injection, we could observe clear migration of unloaded and mRNA-loaded microbubbles from the injection site into the lymph vessels and the draining lymph nodes. Moreover, our CEUS images nicely correspond to previous reports on the lymphatic drainage

of microbubbles, which indicates that the observed structures were indeed lymph nodes[5-7, 26, 27]. The imaging options that are associated with these mRNA-loaded microbubbles could have implications for mRNA delivery as well as for diagnostic purposes. Firstly, the mRNA-loaded microbubbles could provide information on the anatomical features of draining lymph nodes. To our knowledge, this is the first report where CEUS was shown to discriminate between the two different types of connection of lymph vessels to lymph nodes (*i.e.* the "hollow" nodes and the "filled" lymph nodes)[21]. The impact of this might be dual. First of all, from our perspective of future mRNA delivery to intranodal DCs, it would be a major advantage to be able to discriminate between situations where the afferent lymph vessels discharge the mRNA-loaded bubbles within the core of the lymph node ("filled" nodes) versus lymph vessels that merely run over the surface of the lymph nodes, thus bypassing the actual node, resulting in the absence of a microbubble signal in the center of the node ("hollow" nodes). Only in the first scenario will the mRNA-loaded bubbles be able to reach the intranodal DCs, and is DC transfection with mRNA via sonoporation possible. Therefore, delivery of high-intensity ultrasound pulses to induce microbubble implosion and mRNA delivery, should only be performed in the lymph nodes that exhibit the "filled" appearance. Other than for ultrasound-guided drug delivery, this anatomical information could also have benefits with regards to SLN detection. In a tumor setting, the SLN will be the first lymph node that encounters material that directly originates from the tumor, such as disseminating tumor cells. However, if the first lymph node after the tumor has the "hollow" characteristics, this means that the tumor cells do not enter within the node, making it less likely that this node would be populated with tumor cells[21]. Therefore, lymph node biopsies to detect lymph node metastasis could best be performed in the first node in which the content of the tumor-draining lymph vessels are actually discharged. CEUS-guided identification of the first "filled" SLN could therefore have an added value to reduce the chance of false negatives in SLN biopsies. Of note, other imaging possibilities such as 3D CEUS imaging, could enable improved visualization of the lymphatic drainage and improve variability in measurements.

When comparing mRNA-loaded microbubbles with unloaded microbubbles, we could not observe statistically significant differences with regards to migration distance, mean contrast intensity and the stability of both contrast agents in the lymphatics. As the size distribution of both types of bubbles did not significantly differ, this was not entirely unexpected. In addition, experiments on similar nanoparticle-loaded lipid microbubbles by Luan et al. demonstrated that the shell elasticity of individual unloaded and liposome-loaded microbubbles was nearly the same[28]. The effects of liposome-loading that was observed by the authors were mainly on the microbubble shell viscosity (which was higher for liposome-loaded microbubbles) and thus on the ultrasound-induced microbubble vibrations. Taken together, the impact on these acoustical differences between both types of bubble populations is expected to be limited with respect to contrast-enhancement. However, it is likely that for molecular imaging and therapeutic

purposes, which often involve only a single microbubble or a few microbubbles in a given volume, these differences will need to be addressed: liposome-loaded microbubbles exhibited a higher pressure threshold for microbubble vibration, which might indicate that the pressures that will be needed to implode these bubbles in order to locally deposit the mRNA, also need to be higher. This could already be expected based on the burst-destruction of the intranodal mRNA-loaded microbubbles. Using the preset “burst” function on the clinical scanner, the microbubble contrast signal is maximally reduced by 50%, indicating an incomplete intranodal microbubble destruction. Only after 6 bursts the mean echo reaches a minimum. On this basis, the transducer that was used in this study (12-5 MHz linear) is probably not ideal for microbubble destruction that could allow effective sonoporation and mRNA transfection. Other clinical transducers that can emit lower frequencies, which are closer to the resonance frequency of the microbubbles and can emit higher powers (and thus higher MIs), could be better suited. In any case, *in vivo* optimization of the various ultrasound parameters such as acoustic pressure, pulse duration and number of pulses, will be required for this purpose[13].

CONCLUSION

In conclusion, we were able to show that homemade unloaded as well as mRNA-loaded microbubbles efficiently reach the lymph vessels and nodes upon s.c. injection in dogs. Loading of the microbubbles with mRNA-lipoplexes had no significant effect on the distance of microbubble migration from the injection site, nor on the intensity of the observed contrast signals. This shows that theranostic mRNA-loaded microbubbles could have potential for the ultrasound-guided, ultrasound-triggered intranodal delivery of mRNA. However, further research is needed for the optimization of acoustic parameters to most effectively sonoporate target cells of interest.

ACKNOWLEDGEMENTS

Heleen Dewitte is a doctoral fellow of the Institute for the Promotion of Innovation through Science and Technology in Flanders, Belgium (IWT-Vlaanderen). Katrien Vanderperren and Ine Lentacker are postdoctoral fellows of the Research Foundation-Flanders, Belgium (FWO-Vlaanderen). This project was funded through the FWO grant G016513N. The authors would also like to thank Prof.dr. Jean-Paul Remon for providing the animals, and Prof.dr. Mike Averkiou and Ying Luan for the helpful discussions.

REFERENCE LIST

1. Lindner, J.R. Microbubbles in medical imaging: current applications and future directions. *Nature Reviews Drug Discovery* **3**, 527-532 (2004).
2. Sever, A., Jones, S., Weeks, J., Mills, P. & Jones, P. Successful outpatient identification of the sentinel lymph node with ultrasound using microbubbles in breast cancer patients: final results. *British Journal of Surgery* **97**, 28-28 (2010).
3. Sever, A.R. et al. Preoperative Sentinel Node Identification With Ultrasound Using Microbubbles in Patients With Breast Cancer. *American Journal of Roentgenology* **196**, 251-256 (2011).
4. Sever, A.R., Mills, P., Jones, S.E., Mali, W. & Jones, P.A. Sentinel node identification using microbubbles and contrast-enhanced ultrasonography. *Clinical Radiology* **67**, 687-694 (2012).
5. Goldberg, B.B. et al. Contrast-enhanced ultrasound imaging of sentinel lymph nodes after peritumoral administration of Sonazoid in a melanoma tumor animal model. *Journal of ultrasound in medicine : official journal of the American Institute of Ultrasound in Medicine* **30**, 441-53 (2011).
6. Goldberg, B.B., Merton, D.A., Liu, J.B., Murphy, G. & Forsberg, F. Contrast-enhanced sonographic imaging of lymphatic channels and sentinel lymph nodes. *Journal of ultrasound in medicine : official journal of the American Institute of Ultrasound in Medicine* **24**, 953-65 (2005).
7. Goldberg, B.B. et al. Sentinel lymph nodes in a swine model with melanoma: contrast-enhanced lymphatic US. *Radiology* **230**, 727-34 (2004).
8. Chakera, A.H., Drzewiecki, K.T., Ingvar, C., Steiniche, T. & Hesse, B. Sentinel node imaging. *Current Medical Imaging Reviews* **2**, 341-346 (2006).
9. Swartz, M.A. & Skobe, M. Lymphatic function, lymphangiogenesis, and cancer metastasis. *Microscopy Research and Technique* **55**, 92-99 (2001).
10. Keshtgar, M.R. & Ell, P.J. Sentinel lymph node detection and imaging. *European Journal of Nuclear Medicine* **26**, 57-67 (1999).
11. Yang, W.T. & Goldberg, B.B. Microbubble Contrast-Enhanced Ultrasound for Sentinel Lymph Node Detection: Ready for Prime Time? *American Journal of Roentgenology* **196**, 249-250 (2011).
12. Zhang, F., Niu, G., Lu, G.M. & Chen, X.Y. Preclinical Lymphatic Imaging. *Molecular Imaging and Biology* **13**, 599-612 (2011).
13. Lentacker, I., De Cock, I., Deckers, R., De Smedt, S.C. & Moonen, C.T. Understanding ultrasound induced sonoporation: Definitions and underlying mechanisms. *Advanced Drug Delivery Reviews* **72C**, 49-64 (2014).
14. Xie, A. et al. Ultrasound-mediated vascular gene transfection by cavitation of endothelial-targeted cationic microbubbles. *JACC. Cardiovascular imaging* **5**, 1253-62 (2012).
15. Nomikou, N., Tiwari, P., Trehan, T., Gulati, K. & McHale, A.P. Studies on neutral, cationic and biotinylated cationic microbubbles in enhancing ultrasound-mediated gene delivery in vitro and in vivo. *Acta biomaterialia* **8**, 1273-80 (2012).
16. Geers, B., Dewitte, H., De Smedt, S.C. & Lentacker, I. Crucial factors and emerging concepts in ultrasound-triggered drug delivery. *Journal of controlled release : official journal of the Controlled Release Society* **164**, 248-55 (2012).
17. De Temmerman, M.L. et al. mRNA-Lipoplex loaded microbubble contrast agents for ultrasound-assisted transfection of dendritic cells. *Biomaterials* **32**, 9128-9135 (2011).
18. Dewitte, H. et al. The potential of antigen and TriMix sonoporation using mRNA-loaded microbubbles for ultrasound-triggered cancer immunotherapy. *Journal of Controlled Release* **194**, 28-36 (2014).
19. Oussoren, C. & Storm, G. Liposomes to target the lymphatics by subcutaneous administration. *Advanced Drug Delivery Reviews* **50**, 143-156 (2001).
20. Patsikas, M.N. et al. The lymph drainage of the neoplastic mammary glands in the bitch: A lymphographic study. *Anatomia Histologia Embryologia-Journal of Veterinary Medicine Series C* **35**, 228-234 (2006).
21. Tanis, P.J., Nieweg, O.E., Olmos, R.A.V. & Kroon, B.B.R. Anatomy and physiology of lymphatic drainage of the breast from the perspective of sentinel node biopsy. *Journal of the American College of Surgeons* **192**, 399-409 (2001).

22. Swartz, M.A. The physiology of the lymphatic system. *Advanced Drug Delivery Reviews* **50**, 3-20 (2001).
23. Yanagisawa, K., Moriyasu, F., Miyahara, T., Yuki, M. & Iijima, H. Phagocytosis of ultrasound contrast agent microbubbles by Kupffer cells. *Ultrasound in Medicine and Biology* **33**, 318-325 (2007).
24. Callahan, M.K., Williamson, P. & Schlegel, R.A. Surface expression of phosphatidylserine on macrophages is required for phagocytosis of apoptotic thymocytes. *Cell Death and Differentiation* **7**, 645-653 (2000).
25. Sontum, P.C. Physicochemical characteristics of Sonazoid (TM), a new contrast agent for ultrasound imaging. *Ultrasound in Medicine and Biology* **34**, 824-833 (2008).
26. Gelb, H.R., Freeman, L.J., Rohleder, J.J. & Snyder, P.W. Feasibility of Contrast-Enhanced Ultrasound-Guided Biopsy of Sentinel Lymph Nodes in Dogs. *Veterinary Radiology & Ultrasound* **51**, 628-633 (2010).
27. Lurie, D.M., Seguin, B.D., Schneider, P.D., Verstraete, F.J. & Wisner, E.R. Contrast-assisted ultrasound for sentinel lymph node detection in spontaneously arising canine head and neck tumors. *Investigative radiology* **41**, 415-421 (2006).
28. Luan, Y. et al. Acoustical Properties of Individual Liposome-Loaded Microbubbles. *Ultrasound in Medicine and Biology* **38**, 2174-2185 (2012).

Summary, conclusions & future perspectives

SUMMARY

In the early 1970's, Ralph M. Steinman discovered a novel cell type in the lymphoid organs of mice: the dendritic cells (DCs). This was quickly regarded a scientific breakthrough, as these cells were identified as the missing link between antigens and antigen-specific T cell responses. This crucial finding not only resulted in a (posthumous) Nobel Prize in Medicine for Ralph M. Steinman in 2011, it also ushered in a new era in cancer immunotherapy. From then on researchers started exploiting DCs by loading them with tumor antigens *in vitro* to turn them in to cellular vaccines that could aid to harness our immune system in the battle against cancer.

Chapter 1 comprises two main sections that explain the key principles of this thesis. Firstly, it provides an overview of how DCs can trigger antitumor immunity, and how they can be utilized in DC-based vaccination. Unfortunately, several drawbacks associated with these patient-specific, laborious and costly vaccines have moderated the initial enthusiasm. Hence, researchers started shifting their focus: instead of collecting cells and modifying them *ex vivo*, it would be beneficial to target DCs *in situ* as this could allow the production of off-the-shelf vaccines. This change in strategy has brought material scientists and immunologists closer together in their joint search for biomaterials (e.g. nano- and microparticles or implantable scaffolds) that could deliver tumor antigens to DCs *in vivo*. One of the most important pitfalls in particulate vaccine developments that the exclusive delivery of tumor antigens to DCs will not suffice to evoke powerful and durable antitumor immunity *in vivo*. In order to transform antigen-laden DCs into potent antigen-presenting cells, they require additional stimuli that are ideally co-delivered with the antigenic material. Therefore, we presented an overview of different nano- and micromaterials that fulfill this requirement. In the second part of this chapter, we focused on an interesting group of biomaterials that merge therapy and diagnostic imaging into a single compound. These *theranostics* are a hot topic these days, as they provide real-time feedback on the treatment effects. We briefly highlighted two diagnostic imaging techniques that do not require the use of ionizing radiation: fluorine magnetic resonance imaging (^{19}F MRI) and ultrasonography. For both techniques, the development of theranostic particles is on the rise. In case of ^{19}F MRI, highly fluorinated perfluorocarbons can be imaged at a negligible tissue background. Alternatively, ultrasonography is an inexpensive imaging technique in which enhanced contrast can be obtained by using microbubbles. Interestingly, their unique response to ultrasound waves not only makes them interesting contrast agents. Their potential use

reaches far beyond imaging alone. In response to higher intensity ultrasound waves, these microbubbles can implode, which temporarily permeates neighboring cell membranes. Thus, by designing theranostic microbubbles loaded with drugs or genes, ultrasound-guided, ultrasound-triggered enhanced drug and gene delivery may be established. When combining the insights from the immunotherapy point of view and the multifunctionality of theranostics, the aim of this thesis is to design immunotheranostics: imageable carriers that could assist in DC-mediated cancer vaccination.

In the development of agents for therapeutic imaging, the initial screening of novel materials is performed *in vitro*, on model DCs that are often derived from the bone marrow of mice. However, there is a large variety in the protocols that are used to obtain these bone marrow-derived DCs (BM-DCs). **Chapter 2** investigates the impact of 2 variables on the BM-DC immunobiology and the cells' response to nanoparticlulate vaccines. We showed that different combinations of bovine serum and cytokines can result in cultures with extensive differences in purity, yield and phenotype. Especially the maturation status of the DCs was affected, as indicated by maturation marker expression and cytokine production. This is crucial, since more mature cells have a reduced endocytic capacity. Indeed, the uptake of mRNA-lipoplexes, as a model particulate vaccine, was clearly reduced in more mature BM-DC models. When looking more deeply into transfection efficiency and T cell activation, we also observed extensive model-related variation despite the use of identical nanoparticles. In this way, we were able to expose an important bias of the model cells on the functional outcome of a particulate vaccine.

In **Chapter 3**, we reported on the design and evaluation of a first particle for therapeutic imaging that allows the simultaneous loading of DCs with antigenic protein and a ^{19}F MRI contrast agent. For this, we developed a *layer-by-layer* particle consisting of a liquid perfluorocarbon core, surrounded by multiple alternating layers of cationic lipids and negatively charged antigenic protein. These particles were rapidly ingested by BM-DCs *in vitro*, resulting in efficient antigen presentation and activation of antigen-specific T cells. Besides this capacity to deliver antigens to DCs, the particle-loaded DCs could be imaged via ^{19}F MRI at low detection limits (down to 10^3 cells μl^{-1}). This strategy could be interesting in the development of *ex vivo* generated DC vaccines, as one of the hurdles in these vaccines is the poor migration of the antigen-containing cells from the injection site to the draining lymph nodes, where antigen-presentation to T cells occurs. Using these particles, selective and non-invasive tracking of DCs that have taken up the antigen and are able to induce antitumor immune responses, could be possible.

This strategy, however, still requires DC precursor isolation, *ex vivo* antigen-loading and injection of DCs as vaccines. In order to address this, we explored other paths that could allow targeting antigens towards DCs *in vivo*. For this, we developed mRNA-loaded microbubbles as immunotheranostics for ultrasonography. As described in **Chapter 4**, we designed lipid microbubbles that could be loaded with mRNA-lipoplexes via avidin-biotin linkages. When these microbubbles were exposed to ultrasound in the presence of BM-DCs *in vitro*, this resulted in transfection efficiencies up to 24%. Of note, ultrasound-triggered transfection did not affect the DCs' potential to respond to maturation stimuli, making these microbubbles a promising tool for the safe transfer of antigen-mRNA to DCs.

Based on this proof of concept, we further improved the potential of these immunotheranostics (**Chapter 5**). As we already highlighted in Chapter 1, it is important to co-deliver antigen and immune stimuli to DCs in order for a cancer vaccine to be truly effective. In case of the mRNA-loaded microbubbles, this was achieved by loading them with multiple mRNAs. On the one hand, we used mRNA that is translated into tumor associated antigens, and on the other hand, we used TriMix, an mRNA cocktail that will modulate the DCs' functionality. Co-sonoporation with these four mRNAs resulted in acceptable transfection efficiencies and moderately increased the expression of maturation markers and the production of cytokines by the DCs. When these sonoporated DCs were injected as a vaccine, we observed extensive proliferation of antigen-specific T cells, which led to specific lysis of antigen-expressing target cells. Most importantly, in a therapeutic setting where tumor-bearing mice were vaccinated with sonoporated DCs, we observed a significant reduction in tumor outgrowth in the animals that were vaccinated with antigen mRNA, but especially in the animals that received both antigen and TriMix mRNA. In the latter group, complete tumor regression could even be observed in 30% of the vaccinated animals. Moreover, these animals displayed long-term antigen-specific immunological memory. These results clearly show the potential of mRNA sonoporation for cancer vaccination, especially when it is used to co-deliver antigen and immunostimulatory mRNA.

The results above illustrate that the way DCs are modulated using immunotheranostics results in the generation of highly immunogenic cells. However, the full potential of these mRNA-loaded microbubbles lies within the possibility to directly deliver the antigen and immunostimulatory mRNA to DCs *in vivo*. The ideal location where this should occur, are the lymph nodes, as these harbor large numbers of immature DCs and these are the anatomical sites where antigen presentation to T cells occurs. Therefore, in **Chapter 6**, we performed a study in dogs, to investigate whether mRNA-loaded microbubbles are capable of reaching the lymph nodes after subcutaneous injection. Using contrast-enhanced ultrasound imaging (CEUS), we observed that already within 1min after injection, mRNA-loaded microbubbles can be detected within the lymph nodes. The ultrasound contrast provided by these microbubbles

provided detailed information on the lymph node anatomy, which could be of value for further *in vivo* sonoporation experiments.

GENERAL CONCLUSIONS

Taken together, the results in this thesis show that therapeutic imaging can indeed be used for cancer immunotherapy and, as such, gained the status of *"immunotherapeutic imaging"*. We developed two different biomaterials that could deliver antigens to DCs *in vitro*. Moreover, using the microbubble approach, we showed the simultaneous delivery of antigen and immunostimulating mRNA, which markedly improved the therapeutic outcome in tumor-bearing mice. Lastly, and most importantly, mRNA-loaded microbubbles can reach the lymph nodes of larger animals, which brings them to the key anatomical site of interest for immunotherapy. The image feedback information provided by these contrast agents on the lymphatic anatomy underpins their interesting role as immunotheranostic agents.

FUTURE PERSPECTIVES

Are we there yet? Unfortunately, the answer is no. We have merely made our first steps towards a potentially potent immunotherapeutic strategy. The promising results that we were able to show here, definitely warrant further investigation. Firstly, although we have collected convincing evidence that theranostics such as microbubbles can be used to transfect DCs *in vitro*, generate highly immunogenic DC vaccines, and that they can reach the DCs within the lymph nodes *in vivo*, we still need to investigate whether *in vivo* ultrasound-guided and ultrasound-triggered delivery of antigen and adjuvant mRNA is feasible. Without a doubt, the key challenge there will be to identify the ideal ultrasound parameters needed to burst the mRNA-loaded bubbles and deliver the mRNA to the DCs intranodally.

An additional feature that will certainly need to be addressed, is immune suppression. It should be kept in mind that immunotherapy does not end with the induction of an antitumor T cell response. Increasing evidence indicates that during tumor development, a growth-supporting micro-environment is created, harboring a plethora of immune suppressive cell types (e.g. regulatory T cells and myeloid-derived suppressor cells) which allow the tumor to escape from immune recognition and block effector immune cells at the tumor site. Therefore, even if using intelligent antigen- and adjuvant-delivery strategies results in the effective proliferation of antitumor CTLs, in all likelihood, a major fraction of these cells might become trapped within the tumor microenvironment without exerting their tumor-killing effects. Finding ways to overcome this tumor-mediated immune suppression will likely become a leading topic of investigation.

Lastly, it is probably safe to say that the future lies in the art of combining. Several established cancer treatments, such as chemotherapy and thermal tumor ablation have been shown to induce immunogenic cell death. In this process, tumor antigens and additional immunostimulatory signals (e.g. danger-associated molecular patterns, DAMPs) are released from the dying tumor cells. This, in turn, attracts and activates DCs. Thus, in a way, the stimulation of immunogenic cell death can turn tumor cells into an auto-vaccine. Hence, by merging these established treatments with immunotherapy, we could tackle the tumor from different angles.

Samenvatting, besluiten & toekomstperspectieven

SAMENVATTING

In het begin van de jaren ’70 ontdekte Ralph. M. Steinman een nieuw celtype in de lymfeweefsels van muizen: de dendritische cellen (DC’s). Al snel werd dit beschouwd als een belangrijke wetenschappelijke doorbraak. DC’s vormen immers de *missing link* tussen antigenen en antigen specifieke T-cel responsen. In 2011 werd Ralph M. Steinman voor deze ontdekking geëerd met een (postume) Nobelprijs. Het ophelderen van de werking van DC’s en hun cruciale rol in het opwekken van immuniteit kondigden een nieuw tijdperk aan in het domein van kanker immunotherapie. Door DC’s *in vitro* te beladen met tumor antigenen, en deze zo om te vormen tot cellulaire vaccins, slaagden wetenschappers er in ons immuunsysteem in te schakelen in de strijd tegen kanker.

Hoofdstuk 1 bestaat uit twee delen die de belangrijke thema’s die in dit werk aan bod komen, toelichten. Het eerste deel focust op immunotherapie, meer specifiek op de werking van DCs en hoe ze kunnen gemodificeerd worden tot krachtige antikanker DC-vaccins. Ondanks de succesverhalen gepubliceerd werden, blijft DC-vaccinatie te kampen hebben met een aantal nadelen. Zo zijn deze *ex vivo* gegenereerde vaccins steeds patiënt specifiek en het omslachtige en arbeidsintensieve productieproces leidt tot een hoge kost per vaccin. Om dit te verbeteren, is men sinds kort beginnen zoeken naar methodes om DC’s *in vivo* te moduleren en zo een kant-en-klaar vaccin te maken dat bij een grotere patiëntenpopulatie kan worden gebruikt. Deze koerswijziging bracht al snel wetenschappers van verschillende achtergronden, materiaalkundigen en immunologen, samen in een vereende zoektocht naar biomaterialen (bijv. nano- en micropartikels of implantaten) die tumorantigenen kunnen aanleveren aan DC’s *in vivo*. De belangrijkste valkuil bij het ontwikkelen van dergelijke partikelvaccines is dat het uitsluitend afleveren van tumorantigenen niet zal volstaan om een effectief kankervaccin te ontwikkelen. Naast de belading met antigen, moet de DC er namelijk ook toe worden aangezet het antigeen materiaal efficiënt te gaan presenteren om zo antigen specifieke T-cellen te activeren. Voor deze omvorming van antigen opnemende naar antigen presenterende cellen zijn extra stimulansen nodig die idealiter simultaan met de antigenen worden afgeleverd. De verschillende nano- en micromaterialen die aan deze vereisten voldoen, worden hier samengevat. Het tweede deel van dit hoofdstuk legt de focus op een bijzonder interessante groep biomaterialen die therapeutische en diagnostische eigenschappen samenbrengen in één enkel partikel. Deze *theranostische* materialen hebben het voordeel dat ze via medische

beeldvorming *real-time* feedback verschaffen tijdens en/of kort na de behandeling. We lichten specifiek twee beeldvormingstechnieken uit waarbij geen ioniserende straling wordt gebruikt, en waarvoor steeds meer theranostica worden ontwikkeld: fluor magnetische resonantie beeldvorming (^{19}F MRI) en echografie. Als contraststoffen voor ^{19}F MRI worden sterk gefluorineerde perfluorocarbonen gebruikt, gezien deze aan hoge signaal-ruisverhouding in beeld kunnen gebracht worden. Een andere techniek is de echografie, een goedkope medische beeldvormingsmethode waar microbubbels voor verbeterd contrast kunnen zorgen. De unieke trillingsrespons van microbubbels op ultrasone golven, maakt ze uiterst geschikt als contraststoffen en biedt tegelijk nog heel wat andere mogelijkheden. Wanneer de amplitude van de ultrasone golven toeneemt, kunnen microbubbels imploderen, wat via verschillende mechanismen kan zorgen voor een tijdelijke porievorming in naburige celmembranen. Hier kan gebruik van worden gemaakt door de microbubbels te beladen met geneesmiddelen of genen en zo ultrasound-geleide ultrasound-geïnduceerde gen- of geneesmiddelafgifte rechtstreeks doorheen de poriën tot in het cytoplasma van de cel, mogelijk te maken. Door de nieuwste inzichten op vlak van kanker-immunotherapie en de multifunctionaliteit van theranostica te bundelen, kwam het idee om *immunotheranostica* te ontwerpen. Dit zijn biomaterialen die niet-invasief gevolgd kunnen worden via medische beeldvorming en een rol kunnen spelen in DC vaccinatie tegen kanker.

Tijdens de ontwikkeling van deze immunotheranostica wordt steeds eerst een *in vitro* screening uitgevoerd op model-DC's die veelal verkregen worden uit het beenmerg van muizen. Er bestaan echter erg veel verschillende protocollen om deze beenmerg-afgeleide DC's (BM-DC's) te verkrijgen. Daarom onderzoekt **Hoofdstuk 2** wat de impact is van twee variabelen op de BM-DC immunobiologie en de respons van deze cellen op nanopartikel-vaccins. We konden aantonen dat wanneer verschillende combinaties van kalfsserum en cytokines werden gebruikt, dit leidde tot BM-DC culturen die sterk verschillend waren op vlak van zuiverheid, opbrengst en fenotype. Het effect was het meest uitgesproken op de maturatiestatus van de cellen. Dit is van cruciaal belang, aangezien meer mature cellen doorgaans een verminderde endocytose-capaciteit vertonen. Zo werd wanneer mRNA-lipoplexen (als model partikelvaccins) werden gebruikt, een beduidend lagere partikelopname vastgesteld in de BM-DC modellen met een meer matuur fenotype. Door dieper in te gaan op de transfectie-efficiëntie en de capaciteit van de antigen-beladen BM-DC's om T-cellen te activeren, konden we ook hier een uitgesproken modelgerelateerde variatie waarnemen, ondanks het feit dat telkens identieke nanopartikels werden gebruikt. Deze resultaten toonden aan dat het type model BM-DC dat wordt gebruikt, een belangrijke invloed kan hebben op de functionele uitkomst van een partikelvaccin.

Hoofdstuk 3 beschrijft het ontwerp en de evaluatie van een eerste immunotheranostisch partikel voor de simultane belading van DC's met antigenen en met een ^{19}F MRI contraststof. Deze partikels bestaan uit een kern van vloeibaar perfluorocarbon die omgeven wordt door meerdere afwisselende lagen kationische lipiden en negatief geladen antigene eiwitten. De antigen-beladen perfluorocarbonpartikels werden snel opgenomen door BM-DC's *in vitro* wat leidt tot efficiënte antigenpresentatie en activering van antigen specifieke T-cellen. Tegelijk met de afgifte van antigenen aan de DC's, werden de cellen gemerkt met het perfluorocarbon, wat toelaat de partikel-beladen DC's via ^{19}F MRI in beeld te brengen aan een lage detectielimiet (tot 10^3 cellen μl^{-1}). Deze strategie kan mogelijk interessant zijn voor het ontwikkelen van *ex vivo* aangemaakte DC-vaccins. Het is immers zo dat de beperkte migratie van de antigen-beladen DC's vanuit de injectieplaats naar de lymfeknopen, waar antigenpresentatie aan T-cellen plaatsvindt, een gekend probleem is bij dergelijke cellulaire vaccins. Deze immunotheranostische partikels kunnen het mogelijk maken om selectief en niet-invasief de antigen-beladen DC's die in staat zijn een antitumor immuunrespons op te wekken, te traceren *in vivo*.

Deze aanpak blijft echter steunen op de isolatie van DC precursoren, *ex vivo* antigenbelading en injectie van de gemodificeerde cellen als vaccins. Om dit aan te pakken, werd onderzocht of het mogelijk is een detecteerbaar materiaal te ontwikkelen dat de antigenen naar de DC's kan brengen *in vivo*. Hiervoor werden mRNA-beladen microbubbels aangemaakt als immunotheranostica voor contrast-echografie. **Hoofdstuk 4** beschrijft de ontwikkeling van lipide-gestabiliseerde microbubbels die konden beladen worden met mRNA-lipoplexen via avidine-biotine bruggen. Wanneer deze microbubbels bestraald werden met ultrasound in de nabijheid van BM-DC's *in vitro*, leidde dit tot expressie van het mRNA in 24% van de cellen. Belangrijk hierbij is dat de ultrasound-geleide transfectie geen impact heeft op de maturatiecapaciteit van de DC's, wat van deze microbubbels een veelbelovend materiaal maakt voor de veilige afgifte van antigen-mRNA aan DC's.

Op basis van deze *proof of concept* wordt de mogelijke toepassing van deze immunotheranostica verder uitgewerkt in **Hoofdstuk 5**. Zoals eerder aangehaald in Hoofdstuk 1, kan een DC-vaccin pas echt efficiënt zijn wanneer het antigen tegelijk met de nodige immuunadjuvantia aan de cellen wordt aangeleverd. Voor de mRNA-beladen microbubbels wordt dit mogelijk gemaakt door de bubbels te beladen met meerdere mRNA sequenties. Zo wordt enerzijds mRNA gebruikt dat codeert voor tumorantigenen, en anderzijds TriMix mRNA, een mRNA cocktail die de werking van de DC's zal moduleren. Co-sonoporatie met deze vier mRNA's resulteert in een aanvaardbare transfectie-efficiëntie en een matig maturatie-effect. Wanneer de gesonoporeerde DC's als vaccin worden geïnjecteerd, veroorzaakt dit een duidelijke proliferatie van antigen specifieke T-cellen, wat leidt tot specifieke vernietiging van antigen-expresserende doelwitcellen. Nog belangrijker is het effect in een

therapeutisch kader. Wanneer tumordragende muizen worden gevaccineerd met gesonoporeerde DC's, stellen we een significante vertraging van de tumorgroei vast wanneer werd gesonoporeerd met antigen mRNA. Wanneer tegelijk gesonoporeerd werd met antigen en TriMix mRNA, is dit effect nog meer uitgesproken. In deze laatste groep resulteert dit zelfs in volledige tumorregressie en langdurig antigen specifiek immunologisch geheugen in 30% van de gevaccineerde dieren. Deze resultaten leveren bewijs van het potentieel van mRNA sonoporatie voor immunotherapie, in het bijzonder wanneer het wordt gebruikt om tegelijk antigen mRNA en immuunstimulerend mRNA af te leveren.

Bovenstaande resultaten tonen dat DC-modulatie m.b.v. microbubbels als immuno-theranostica aanleiding geeft tot sterk immunogene cellen *in vitro*. Het grote voordeel van deze mRNA-beladen microbubbels ligt echter in de mogelijkheid om het antigen en immuunstimulerend mRNA rechtstreeks in te brengen in DC's *in vivo*. De locatie bij uitstek waar dit zou moeten gebeuren, is in het lymfeklierweefsel. Hier zijn namelijk grote aantallen DC's aanwezig en dit zijn tevens de anatomische regio's waar antigenpresentatie aan T-cellen zich voordoet. Daarom wordt in **Hoofdstuk 6** een studie uitgevoerd om na te gaan of mRNA-beladen microbubbels tot in de lymfeknopen geraken na subcutane injectie in honden. Op contrast-echografie kan amper 1 minuut na injectie al een groot aantal mRNA-beladen microbubbels gedetecteerd worden in de lymfeknopen. Het contrastsignaal van de microbubbels levert tegelijk gedetailleerde informatie over de anatomie van het lymfesysteem, wat van belang kan zijn voor verdere *in vivo* sonoporatie-experimenten.

ALGEMENE BESLUITEN

De resultaten die in dit doctoraal onderzoek werden behaald wijzen er op dat theranostics effectief kunnen gebruikt worden voor kankerimmunotherapie. Ze kunnen dus de status krijgen van immunotheranostics. Er werden twee verschillende biomaterialen ontwikkeld die antigenen kunnen afleveren aan DC's *in vitro*. De techniek op basis van microbubbels maakt het bovendien mogelijk om tegelijk antigen en immuunstimulerend mRNA af te leveren, wat duidelijk een positief therapeutisch effect heeft in tumordragende muizen. Een laatste en erg belangrijke vaststelling is dat de mRNA-beladen microbubbels de lymfeknopen kunnen bereiken in grotere proefdieren. Dit brengt ze naar de optimale anatomische regio voor immunotherapie. Daarenboven leveren de gedetailleerde beelden van de contrast echografieën extra bewijs van het mogelijk belang van mRNA-beladen microbubbels als immunotheranostica.

TOEKOMSTPERSPECTIEVEN

Betekent dit dat we de oplossing gevonden hebben? Helaas niet… Dit zijn slechts de eerste stappen in een lange zoektocht naar een mogelijk interessant immuno-therapeuticum. De resultaten in deze thesis vragen zeker om verder en meer diepgaand onderzoek. Een eerste belangrijke punt hierbij is dat de resultaten die we hier konden voorleggen, werden behaald na het *in vitro* sonoporeren van de DC's. We moeten dus nog steeds onderzoeken hoe we dit kunnen vertalen naar een *in vivo* setting. Zonder twijfel wordt het optimaliseren van de ultrasoundparameters om de microbubbels te imploderen en zo het mRNA af te leveren aan intranodale DCs *in vivo*, een van de belangrijkste uitdagingen in dit verder onderzoek.

Een belangrijke stoorzender in elke vorm van immunotherapie is immuun-onderdrukking. Immunotherapie eindigt namelijk niet bij het opwekken van een antitumor T-cel respons. Integendeel, er zijn steeds meer aanwijzingen van het ontstaan van een immunosuppressieve en tumor bevorderende micro-omgeving binnenin het tumorweefsel. Deze herbergt een grote diversiteit aan onderdrukkende immuuncellen (bijv. regulatoire T-cellen en myeloid-derived suppressor cellen) die de tumor helpen te ontkomen aan vernietiging door het immuunsysteem en die effector antitumor immuuncellen lamleggen t.h.v. de tumor. Dus zelfs wanneer intelligente antigen- en adjuvant-afgiftesystemen ontwikkeld worden die een sterke activering van antitumor T-cellen induceren, zal een groot deel van deze cellen naar alle waarschijnlijkheid vastgehouden worden in de tumor micro-omgeving zonder dat ze hun tumor dodende functie kunnen uitoefenen. Het zoeken naar manieren om deze tumor gemedieerde immuunsuppressie tegen te gaan, wordt zeker een belangrijk onderzoeksonderwerp in de toekomst.

Ten slotte kunnen we met zekerheid stellen dat er toekomst zit in combinatietherapie. Bij vaak toegepaste kankerbehandelingen zoals chemotherapie en hitte-ablatie, werd al aangetoond dat ze immunogene celdood veroorzaken. Tijdens dit proces worden tumorantigenen en bijkomende immuunstimulerende signalen (zoals danger-associated molecular patterns, DAMP's) vrijgesteld vanuit de stervende tumorcellen. Deze zorgen op hun beurt voor de aantrekking en activering van DC's. Zo zal het induceren van immunogene celdood de tumorcellen als het ware omvormen tot een auto-vaccin. Door deze standaardbehandelingen te combineren met een extra stimulatie van het immuunsysteem via immunotherapie, zou het mogelijk kunnen worden de tumor tegelijk vanuit verschillende hoeken aan te vallen.

Appendix A

Report on experiments performed at the University of Virginia (UVa):

The potential of doxorubicin-loaded microbubbles for ultrasound-guided, ultrasound-triggered tumor treatment *in vivo*

These experiments were performed at the Lab of Prof.dr. Alexander Klibanov, during a 1 month research visit (June 2011) to the University of Virginia (UVa), Charlottesville, Virginia, USA.

ABSTRACT

Theranostic microbubbles have previously shown potential for various applications. Recently, a formulation where liposome-loaded microbubbles were produced through a self-assembly process was developed. In this study we aimed to evaluate this formulation *in vivo*. Experiments performed in tumor-bearing mice indicate that these doxorubicin (DOX)-liposome loaded microbubbles can be used to obtain detailed information on the tumor perfusion by contrast-enhanced ultrasound imaging. Moreover, when therapeutic ultrasound was applied to locally burst the microbubbles and allow enhanced DOX delivery, a trend towards a reduction in tumor outgrowth was observed. Although further research is warranted to fully assess the theranostic features of this microbubble formulation, these experiments already provide a first indication of their potential *in vivo*.

INTRODUCTION

In 2011, a strategy for the production of self-assembled liposome-loaded microbubbles was developed in our group[1]. The formulation, as shown in **Figure 1** makes use of maleimide-containing liposomes that are added to a microbubble precursor solution. The latter consists of the basic lipid component of the microbubbles, DPPC, and DSPE-PEG-SPDP, a lipid that is equipped with a PDP moiety via a polyethylene glycol (PEG) spacer. When this resulting solution is mixed in the presence of perfluorobutane gas, liposome-loaded microbubbles are formed. Such an *in vial* formulation abrogates the washing steps that are needed for avidin-biotin linking of liposomes to microbubbles. As a result, this type of formulations could be an important step forward in bringing drug-loaded microbubbles from bench to bedside.

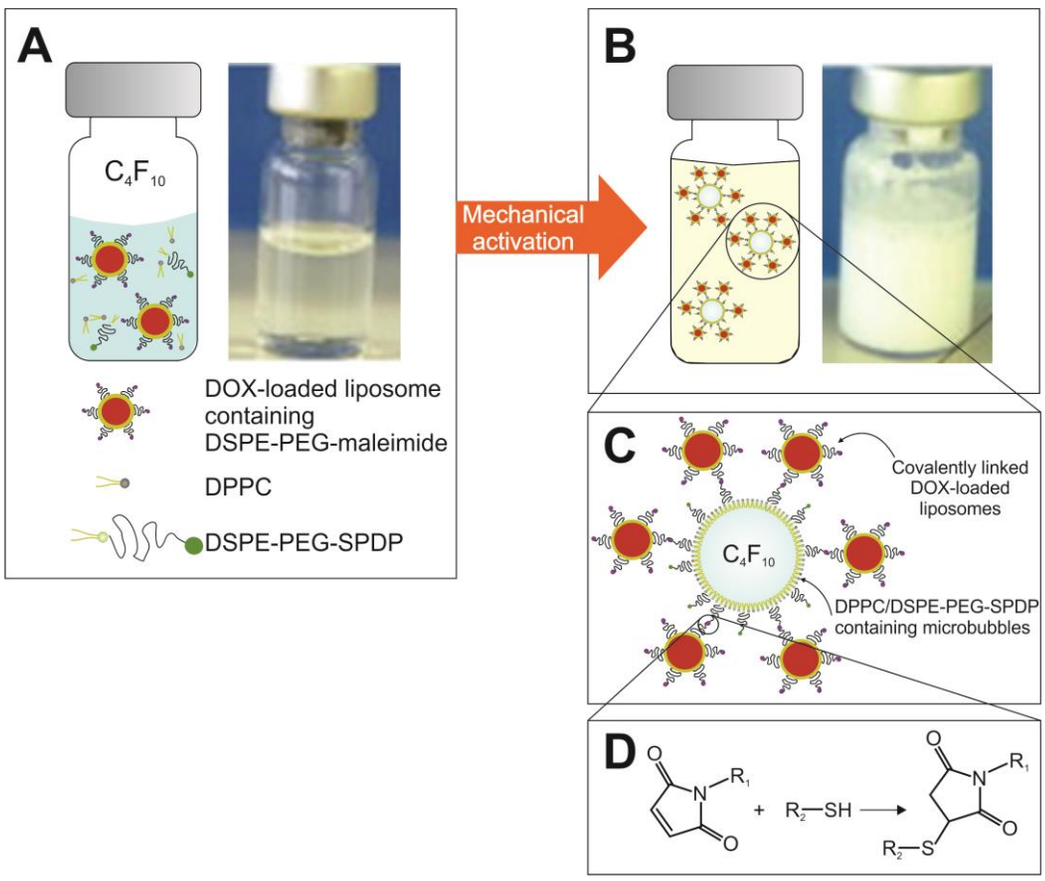

Figure 1. Schematic representation of self-assembly liposome-loaded microbubbles.

(A) Doxorubicin (DOX)-loaded maleimide-liposomes were added to a solution of microbubble lipids that contain DSPE-PEG-SPDP. The vial's headspace was filled with perfluorobutane gas. (B) By mechanical agitation, lipid-coated microbubbles are formed, that are loaded with DOX-loaded liposomes as schematically depicted in (C). In (D), the chemical reaction between the maleimide on the liposomes and the PDP on the microbubbles is clarified. Image adjusted from Geers et al.[1]

After extensive *in vitro* characterization of the microbubbles, the aim of these experiments was to evaluate the potential of this new liposome-loaded microbubble formulation *in vivo*. More specifically, we prepared microbubbles loaded with doxorubicin (DOX)-containing liposomes, and tested whether intravenous injection of these microbubbles, followed by local ultrasound application at the site of the tumor, could result in enhanced antitumor effects. For this, we collaborated with Prof.dr. Alexander Klibanov at the University of Virginia (UVa, Charlottesville, Virginia, USA), who has extensive experience with the *in vivo* application of ultrasound-assisted microbubble therapeutics[2-4].

MATERIALS AND METHODS

Doxorubicin containing liposomes

Liposomes were loaded with DOX via an active loading system, as previously described by Haran and colleagues[5]. Briefly, liposomes were prepared via the proliposome technique[6], by first dissolving DOPC (1,2-dioleoyl-*sn*-glycero-3-phosphocholine, Avanti Polar Lipids, Alabaster, AL, USA), Cholesterol (Sigma, St. Louis, MO) and DSPE-PEG3400-maleimide (Shearwater, Mill Creek, WA, USA) in a 50:35:15 molar ratio in absolute ethanol (at 60°C). Then, ammonium citrate (0.5 M, at 60°C) was added to obtain a weight ratio 100:80:200 of lipids:EtOH:ammonium citrate. The so formed pre-liposomes are rapidly diluted with pre-heated ammonium citrate while vortexing, resulting in a final lipid concentration of 16 mg ml^{-1}. Then, the liposomes were sized via extrusion through a 200 nm polycarbonate filter, and unencapsulated ammonium citrate was removed in three washing steps. Active loading of DOX into the liposomes was performed by adding DOX (10 mg ml^{-1} in saline, Bedford Laboratories™, Bedford, OH, USA), and allowing overnight loading at 60°C. Excess DOX was again removed in three washing steps. The resulting DOX-loaded liposomes were resuspended in saline and the final DOX concentration was measured via absorbance spectroscopy.

Liposome-loaded microbubbles

Microbubbles were prepared starting from a solution of a mixture of 65 mol.% DPPC (1,2-dipalmitoyl-*sn*-glycero-3-phosphocholine, Avanti Polar Lipids) and 35 mol.% DSPE-PEG2000-SPDP (Avanti Polar lipids) in a 1:2:7 glycerol-propyleneglycol-H_2O solvent. For this, appropriate aliquots of both lipids, dissolved in $CHCl_3$, were transferred to a round-bottom flask. After $CHCl_3$ evaporation, the lipid film was dissolved in a 1:2:7 glycerol-propyleneglycol-H_2O mixture to obtain a clear solution with a final lipid concentration of $2x10^{-4}$ mmol ml^{-1}. 500 µl aliquots of this lipid solution were transferred to 2.5 ml chromatography vials, the headspace of which was filled with C_4F_{10} gas (F2 chemicals, Lancashire UK). Then, TCEP (Tris(2-carboxyethyl)phosphine hydrochloride, a thiol-free reducing agent) and DOX-liposomes

(corresponding to 355 µg DOX) were added per vial. Finally, DOX-liposome loaded microbubbles were obtained by high-frequency shaking of the lipid solution in a Vialmix™ device (Lantheus Medical Imaging, Billerica, MA, USA) during 15s. The concentration of the microbubbles in the dispersion were determined with a Beckman-coulter Multisizer 3 (Beckman-coulter, Brea, CA).

Cells and mice

MC38 murine colon carcinoma cells were provided by Dr. J. Schlom (National Institute of Health), and maintained in DMEM with 10% Fetal Calf Serum, 1% Penicillin/Streptomycin and 1% sodium pyruvate.

All animal experiments were conducted in accordance with the animal guidelines of the Animal Care and Use Committee (ACUC) of the UVa. Female C57BL/6 mice (weight ~30 g) were anesthetized using isoflurane, and the hair of the left hind leg was removed using Nair shaving crème. After this, they were inoculated subcutaneously with $5x10^4$ MC38 cells in the left hind leg. Treatment was started 5 days after tumor inoculation. Tumor growth was monitored at least every other day.

Therapeutic regimen

5 and 8 days after tumor inoculation, the mice received treatments with either DOX-liposome loaded microbubbles and ultrasound or free DOX-loaded liposomes. For this, the mice were anesthetized using isoflurane and placed on a heating pad. Their tumor-bearing hind leg was placed over an absorbing rubber pad to avoid reflection of the ultrasound waves. The center of the tumor was marked as the starting point for ultrasound application. Mice receive a retro-orbital injection of 100 µl of either the *in* via*l* prepared DOX-liposome loaded microbubbles, washed DOX-liposome loaded microbubbles (to remove unattached DOX-liposomes) or free DOX-liposomes (without bubbles). Then, ultrasound application and contrast-enhanced ultrasound imaging (CEUS) were performed as depicted in **Figure 2**.

Briefly, the rushing in and ultrasound-triggered destruction of DOX-loaded microbubbles was visualized using an Acuson Sequoia clinical scanner (Siemens medical solutions, Malvern, PA, USA) equipped with a 15L8-S (linear array transducer, 15-8 MHz operating frequency) in cadence pulsed sequencing (CPS) mode (Figure 2B). All images were recorded at a frequency of 14 MHz at low mechanical index (MI=0.19). Under US imaging, higher intensity ultrasound pulses were given to locally burst the microbubbles within the tumor, using a therapy and imaging probe system (TIPS, Philips Research, Briarcliff, NY, USA), which has a focused transducer consisting of an eight element linear array (Figure 2C)[7]. Pulses of 10,000 cycles were given at a frequency of 1.2 MHz, a wave amplitude of 2 MPa (corresponding to a MI=1.8)

and at a pulse repetition frequency (PRF) of 10 Hz. During ultrasound application, the TIPS scanned over the tumor area, following 8 coordinates that form a square spiral of 6x6 mm, for a total of 13 loops (Figure 2D). The duration of one loop was about 15s, followed by a 10s period where the ultrasound was switched off to allow replenishment of the tumor vasculature with microbubbles.

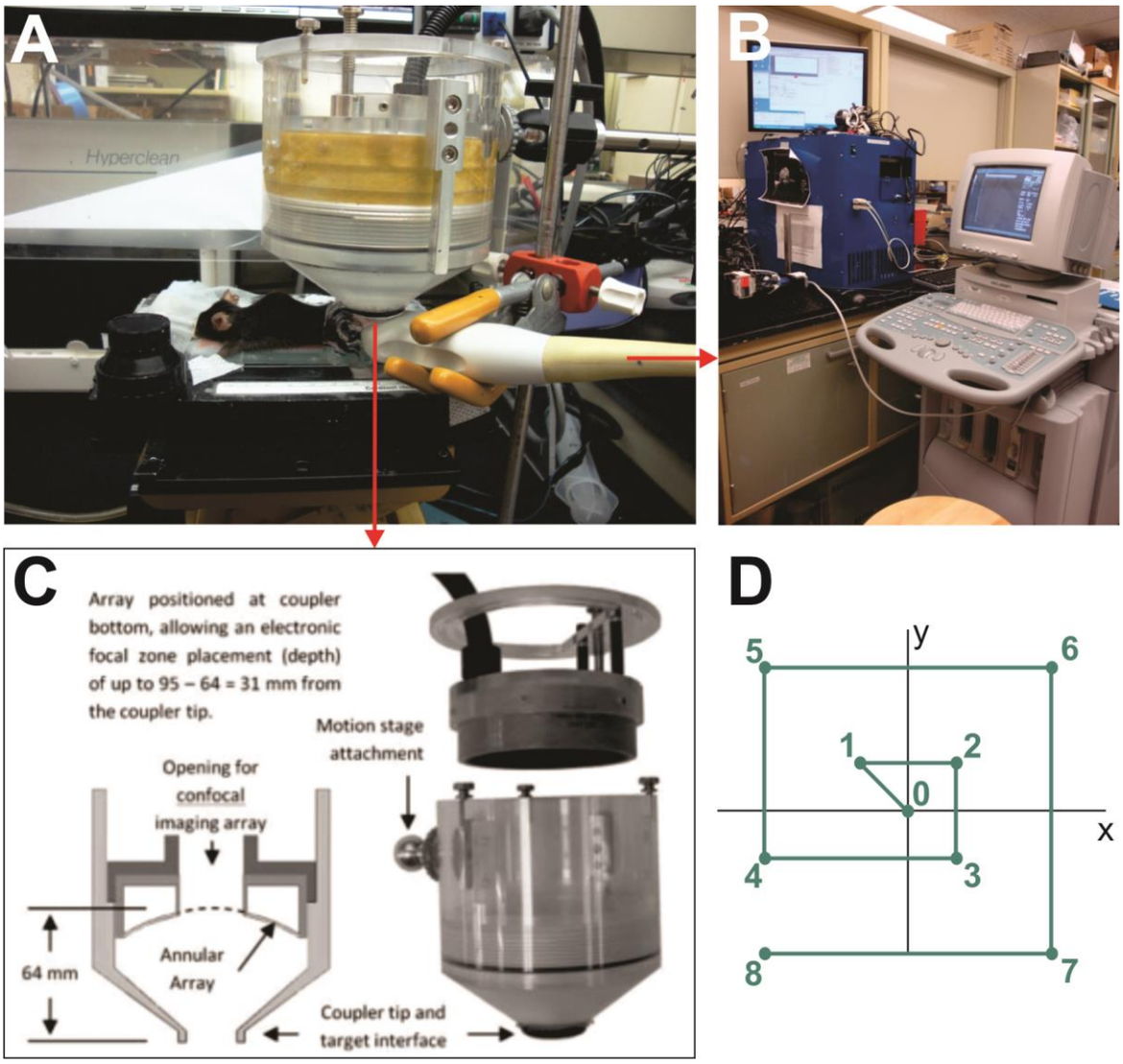

Figure 2. Experimental set-up.

(A) Photograph of the experimental set-up where the mouse is positioned on a heating pad, with the tumor-bearing hind leg placed on an absorbing rubber. The tumor is imaged in CEUS mode via an imaging probe connected to an Acuson Sequoia scanner (B). Simultaneously, higher intensity therapeutic ultrasound is applied using a TIPS therapy probe as shown in (C). Therapeutic ultrasound was applied at 8 different points over the tumor area. The treatment scan plan is depicted in (D). Image (C) was reproduced from Seip et al.[7]

After two days of treatment (at day 5 and day 8 after tumor inoculation), tumor growth was followed as a function of time. Animals were euthanized when tumor volumes reached 1500 mm^3 or when humane end-points were reached.

RESULTS

Preparation and characterization of DOX-liposome loaded microbubbles

After preparation of the DOX-liposomes, as described in the materials and methods section, the DOX content was measured via absorbance spectroscopy. This revealed a DOX encapsulation of 0.71 mg DOX per ml liposomes. These liposomes were added to a microbubble-precursor solution in order to prepare liposome-loaded microbubbles. The resulting DOX-LPS loaded microbubbles were allowed to float for 1min to remove the fraction of larger microbubbles in the vial. If needed, washing steps were performed to remove unbound DOX-liposomes. An overview of the DOX and microbubble concentrations that were administered this way, is provided in **Table 1**.

Table 1. Overview of DOX and microbubbles doses for injection.

Days after tumor inoculation	In vial formulation	Washed microbubbles	Free DOX-liposomes
5	82 µg DOX $3.9x10^6$ bubbles	18.9 µg DOX $8x10^6$ bubbles	82 µg DOX *No microbubbles*
8	86 µg DOX $8.6x10^8$ bubbles	21 µg DOX $5.37x10^8$ bubbles	86 µg DOX *No microbubbles*

CEUS imaging during tumor treatment

The theranostic DOX-liposome loaded microbubbles were imaged prior and during ultrasound treatment via CEUS. B-mode images recorded prior to microbubble injection show the outline of the tumor, and the presence of a region where the echogenicity is lower. When switching to the CPS CEUS mode, only reflections at the skin surface are visible. Rapidly after retro-orbital injection of the DOX-liposome loaded microbubbles, their rushing in at the tumor site was detected. Here too, a dark region where no microbubble contrast appears is observed, at the same anatomical location as in the previous B-mode images. Likely, this poorly vascularized region is a necrotic core within the tumor volume. 1min after microbubble injection, the therapeutic ultrasound was applied, which resulted in immediate and complete destruction of the microbubbles within the tumor. After one full round of ultrasound expose, partial

replenishment of the tumor volume with microbubbles could be observed during the 10s delay period. However, due to the relatively low concentrations of microbubbles used in these experiments, this only occurred until after the second therapeutic ultrasound application. After this, no further replenishment could be detected in the CEUS images. An example of ultrasound B-mode and CEUS images that could be obtained during animal treatment, is provided in **Figure 3**. Notably, due to the lower microbubble concentrations in the washed microbubble preparations, a less intense CEUS signal was received from the intratumoral washed microbubbles.

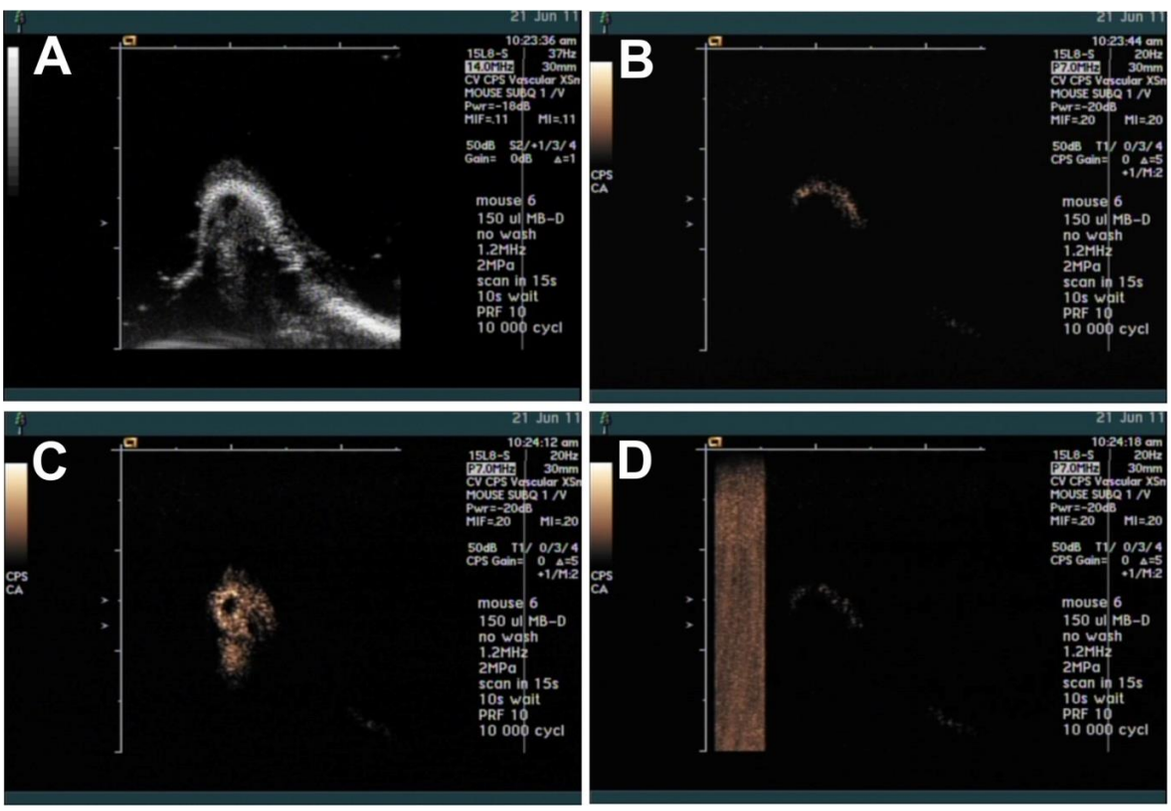

Figure 3. Ultrasound imaging of the DOX-liposome loaded microbubbles.
Prior to injection with DOX-liposome loaded microbubbles, the tumor was imaged with in B-mode (A) and CPS mode (B). Microbubbles were injected during imaging, and one maximal tumor enhancement was reached (C), the therapy probe was used to burst the bubbles at the tumor site. As a result, the non-linear echoes derived from the DOX-liposome loaded microbubble contrast agents disappeared, as shown in (D).

Effect of DOX-liposome loaded microbubble treatment on tumor growth

To assess the therapeutic potential of DOX-liposome loaded microbubbles, different treatment groups were compared. Firstly, we made a comparison between groups that received DOX-liposome loaded microbubble formulations where the excess free DOX-liposomes were washed away, either with or without ultrasound application. As shown in **Figure 4A**, the delivery of these washed formulations results in a reduction in tumor growth compared to control.

Additional application of ultrasound to enhance local DOX delivery at the tumor site resulted in a more pronounced slowdown of tumor outgrowth. However, none of the differences observed were statistically significant, which is likely the result of the low dosage of DOX that could be delivered in this way.

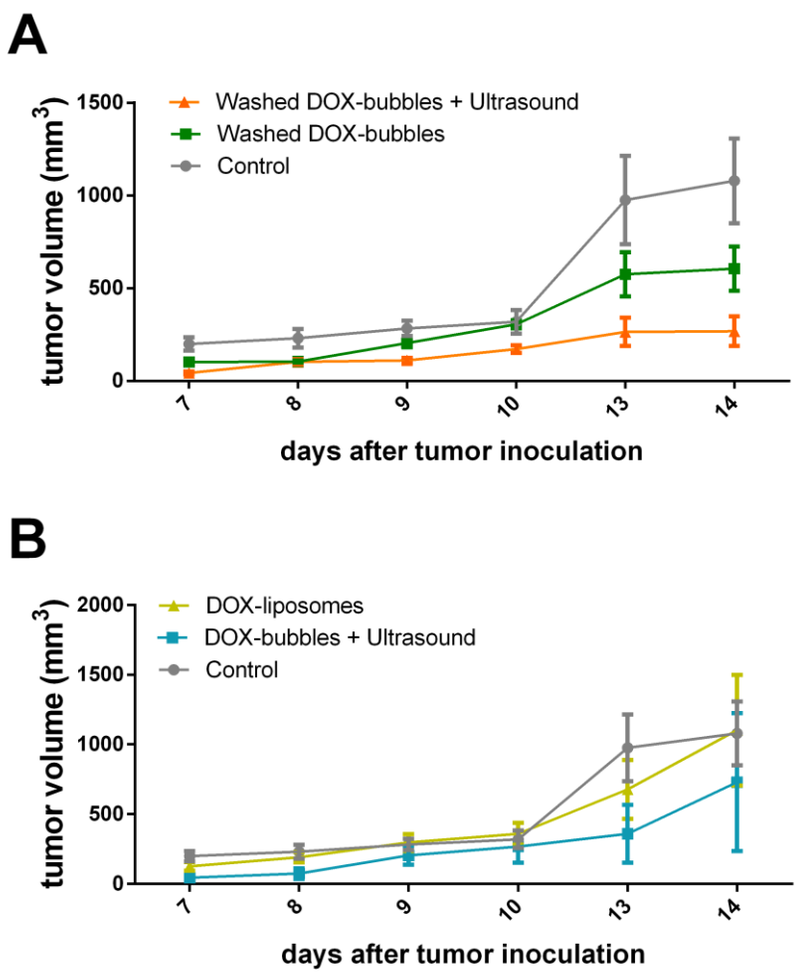

Figure 4. Therapeutic effect of DOX-liposome loaded microbubbles and ultrasound application.

The antitumor effects of washed and unwashed (*in vial*) formulations of DOX-liposome loaded microbubbles were compared in the presence or absence of ultrasound application. (A) provides a graphical representation of tumor growth as a function of time for animals treated with washed DOX-liposome loaded microbubbles with or without ultrasound application. In (B), the tumor growth for the *in vial*, unwashed DOX-liposome loaded microbubble formulation with therapeutic ultrasound is shown compared to an equal dose of free DOX-liposomes (without microbubbles). Untreated tumor-bearing animals served as controls. Results are shown as mean ± standard error mean.

When microbubbles were injected straight from the vial, without additional washing steps, there is still a fraction of free DOX-liposomes present. Therefore, we compared the effects of the delivery of equal doses of DOX, either via DOX-liposome loaded microbubbles and ultrasound or via free DOX-liposomes (without microbubbles or ultrasound). As shown in **Figure 4B**, delivery of a DOX dose of ~2.7 mg kg^{-1} body weight packaged in liposomes, did not result in an improved outcome when compared to untreated mice. However, when an equal dose of DOX was delivered via DOX-liposome loaded microbubbles and ultrasound, a slight reduction in tumor growth could be observed. Although the DOX doses that were delivered with the *in vial* formulation were about four times higher than in the experiments with the washed microbubbles, the observed differences were not statistically significant.

DISCUSSION & CONCLUSIONS

In the described experiments, we were able to show that theranostic DOX-liposome loaded microbubbles could indeed be detected intratumorally by means of CEUS imaging after intravenous injection. However, there are a number of limitations that need to be reported with respect to this study, that make it difficult to interpret the therapeutic effects of the different formulations.

Firstly, the first aim of this research visit was to inject DOX-liposome loaded microbubble formulations that were prepared in Ghent. This would allow optimal comparison to previously obtained *in vitro* results. However, transportation from Ghent to the USA clearly affected the quality of the microbubble preparations, resulting in a significantly lower microbubble concentration, and substantial leakage of DOX from the liposomes. This prompted the *in situ* preparation of new samples at UVa, where not all the materials and instruments were present to prepare these samples in optimal conditions. This resulted in lower DOX-encapsulation efficiencies in comparison to the formulations prepared in Ghent, as well as in substantially reduced microbubble quality (lower concentrations and a relatively larger size distribution). This way, the DOX doses were 10 times lower (for the washed microbubble formulations) and about 4 times lower (for the *in* via*l* formulation) than the 10 mg kg^{-1} doses that are normally required for effective treatment[8]. Although intratumoral DOX delivery via microbubbles and ultrasound triggering could be more efficient in comparison to intravenous injection of free DOX, the ability to deliver higher doses of DOX at the tumor site would surely augment the therapeutic effects.

Secondly, the time we had to perform these experiments was limited, and it only allowed us to perform two experiments in tumor-bearing mice. Due to sample instability during the first experiment, we could not combine the results of multiple experiments to enlarge the overall sample number and increase statistical power.

Overall, these experiments do point towards improved delivery of the chemotherapeutic DOX by attaching DOX-loaded liposomes to microbubbles and locally applying therapeutic ultrasound. However, to fully assess their potential as theranostics in cancer treatment, further experiments are necessary.

ACKNOWLEDGEMENTS

We would like to thank Prof.dr. Alexander (Sasha) Klibanov for the opportunity to perform these experiments at his lab. Furthermore, we would like to acknowledge Dr. Bill Shi from Philips Research USA for his helpful assistance in programming the TIPS scanning patterns, and Talent Shevchenko for the support with animal handling and the *in vivo* experiments.

REFERENCES

1. Geers, B. et al. Self-assembled liposome-loaded microbubbles: The missing link for safe and efficient ultrasound triggered drug-delivery. *Journal of controlled release : official journal of the Controlled Release Society* **152**, 249-56 (2011).
2. Hernot, S. & Klibanov, A.L. Microbubbles in ultrasound-triggered drug and gene delivery. *Advanced Drug Delivery Reviews* **60**, 1153-1166 (2008).
3. Hernot, S. et al. Nanobody-coupled microbubbles as novel molecular tracer. *Journal of Controlled Release* **158**, 346-353 (2012).
4. Tlaxca, J.L. et al. Ultrasound-based molecular imaging and specific gene delivery to mesenteric vasculature by endothelial adhesion molecule targeted microbubbles in a mouse model of Crohn's disease. *Journal of Controlled Release* **165**, 216-225 (2013).
5. Haran, G., Cohen, R., Bar, L.K. & Barenholz, Y. Transmembrane Ammonium-Sulfate Gradients in Liposomes Produce Efficient and Stable Entrapment of Amphipathic Weak Bases. *Biochimica Et Biophysica Acta* **1151**, 201-215 (1993).
6. Rengel, R.G. et al. High efficiency entrapment of superoxide dismutase into mucoadhesive chitosan-coated liposomes. *European Journal of Pharmaceutical Sciences* **15**, 441-448 (2002).
7. Seip, R. et al. Targeted ultrasound-mediated delivery of nanoparticles: on the development of a new HIFU-based therapy and imaging device. *IEEE transactions on bio-medical engineering* **57**, 61-70 (2010).
8. Keith, W.N., Mee, P.J. & Brown, R. Response of mouse skin tumors to doxorubicin is dependent on carcinogen exposure. *Cancer Research* **50**, 6841-7 (1990).

Curriculum Vitae

PERSONALIA

Name	Dewitte
First names	Heleen Ann Elisabeth
Nationality	Belgian
Place of birth	Brugge (Bruges)
Date of birth	09/04/1987
Private address	Achilles Musschestraat 123A 9000 Gent
Telephone	+32 (0)498 45 23 05
Professional address	Laboratory for General Biochemistry and Physical Pharmacy, Faculty of pharmaceutical sciences, Ghent university Ottergemsesteenweg 460 9000 Gent Belgium
Telephone	+32 (0)9 264 83 60
Email	Heleen.Dewitte@UGent.be
Websites	https://www.biofys.ugent.be https://www.researchgate.net/profile/Heleen_Dewitte

DEGREES

June 2010	Ghent University, Ghent, Belgium Master in Drug Development – Pharmaceutical Sciences with great distinction. At the proclamation, Heleen was awarded the "Prize of the Bank of Breda" Master thesis: "*The evaluation of Doxil®-loaded PLLA-PFO polymer microbubbles for ultrasound-guided cancer treatment*", under supervision of Dr.apr. Ine Lentacker and the promotership of Prof.dr.apr. Jo Demeester of the Ghent Research Group on Nanomedicines of Ghent University, Belgium.
June 2008	Ghent University, Ghent, Belgium Bachelor in Pharmaceutical Sciences with distinction.
June 2005	St. Lodewijkscollege, Bruges, Belgium High school degree (Ancient Greek & Mathematics)

PREVIOUS WORK EXPERIENCES

August (2005-2014)	Volunteer at the MAfestival, Bruges, Belgium
August 2010	Summer work as a pharmacist in Pharmacy Bruggepharma, Koningin Astridlaan 204, 8200 Sint-Andries, Belgium
July 2007 & 2008	Summer job in Toxikon Europe NV, Romeinsestraat 12, 3001 Leuven, Belgium *Job description*: "Evaluation and implication of a GC-MS method for determination of epoxidized soybean oil (ESBO) as a leachable in pharmaceutical products."

LANGUAGES

Dutch:	Native language
English:	Fluent speaking and writing
French:	Good speaking and writing
Swedish:	Elementary proficiency
German:	Elementary proficiency

INTERNATIONAL PEER-REVIEWED PUBLICATIONS

Marie-Luce De Temmerman*, **Heleen Dewitte***, Roosmarijn E. Vandenbroucke, Bart Lucas, Claude Libert, Jo. Demeester, Stefaan C. De Smedt, Joanna Rejman*, Ine Lentacker*, mRNA-Lipoplex loaded microbubble contrast agents for ultrasound-assisted transfection of dendritic cells, Biomaterials, 32 (2011) 9128-9135. (**IF 2013 = 8.3**)
**equal contribution of first and last authors.*

Bart Geers, **Heleen Dewitte**, Stefaan C. De Smedt, Ine Lentacker, Crucial factors and emerging concepts in ultrasound-triggered drug delivery, Journal of Controlled Release, 164 (2012) 248–255. (**IF 2013 = 7.3**)

Heleen Dewitte, Bart Geers, Sayuan Liang, Uwe Himmelreich, Jo Demeester, Stefaan C. De Smedt, Ine Lentacker, Design and evaluation of theranostic perfluorocarbon particles for simultaneous antigen-loading and ^{19}F-MRI tracking of dendritic cells, J. Control. Release, 169 (2013) 141-149. (**IF 2013 = 7.3**)

Heleen Dewitte, Sandra Van Lint, Carlo Heirman, Kris Thielemans, Stefaan C. De Smedt, Karine Breckpot*, Ine Lentacker*, The potential of antigen and TriMix sonoporation using mRNA-loaded microbubbles for ultrasound-triggered cancer immunotherapy, J. Control. Release*,* 194 (2014) 28-36*.* (**IF 2013 = 7.3**)
**equal contribution.*

Heleen Dewitte*, Rein Verbeke*, Karine Breckpot, Roosmarijn E. Vandenbroucke, Claude Libert, Stefaan C. De Smedt, Ine Lentacker, Choose your models wisely: How different murine bone marrow-derived dendritic cell protocols influence the success of nanoparticulate vaccines *in vitro*, J. Control. Release*,* 195 (2014) 138-146*.* (**IF 2013 = 7.3**)
**equal contribution.*

Sandra Van Lint, Dries Renmans, Katrijn Broos, **Heleen Dewitte**, Ine Lentacker, Carlo Heirman, Karine Breckpot*, Kris Thielemans*, The ReNAissanCe of mRNA-based cancer therapy, Expert Rev Vaccines, *In press.* (**IF 2013 = 4.2**)
**equal contribution.*

Heleen Dewitte*, Katrien Vanderperren*, Hendrik Haers, Emmelie Stock, Luc Duchateau, Jimmy Saunders, Stefaan C. De Smedt, Ine Lentacker, Theranostic mRNA-loaded microbubbles in the lymphatics of dogs: implications for drug delivery, Theranostics, 5 (2015) 97-109. (**IF 2013 = 7.8**)
*equal contribution

Heleen Dewitte, Rein Verbeke, Karine Breckpot, Stefaan C. De Smedt, Ine Lentacker, Nanoparticle design to induce tumor immunity and oppose the immunosuppressive tumor microenvironment, Nano Today, *in press*. (**IF 2013 = 18.4**)

CONFERENCE PROCEEDINGS

Marie-Luce De Temmerman, **Heleen Dewitte**, Jo Demeester, Stefaan C. De Smedt, Ine Lentacker, Joanna Rejman, The use of mRNA-loaded microbubbles for ultrasound-assisted transfection of dendritic cells, Hum Gene Ther, 22 (2011) A82-A82. (**IF 2013 = 3.6**)

Heleen Dewitte, Sandra Van Lint, Stefaan C. De Smedt, Karine Breckpot, Ine Lentacker, mRNA sonoporation as a novel tool in dendritic cell-based cancer immunotherapy, Hum Gene Ther, 23 (2012) A92-A93. (**IF 2013 = 3.6**)

Ying Luan, Erik Gelderblom, Guillaume Lajoinie, Ilya Skachkov, **Heleen Dewitte**, Bart Geers, Ine Lentacker, Ton van der Steen, Michel Versluis, Nico de Jong, IEEE, Characterizing Ultrasound-controlled Drug Release by High-speed Fluorescence Imaging, 2012. (**IF 2013 = 1.8**)

Ying Luan, Guillaume Lajoinie, Erik Gelderblom, Ilya Skachkov, **Heleen Dewitte**, Ine Lentacker, Tom van Rooij, Hendrik Vos, Ton van der Steen, Michel Versluis, Nico de Jong, IEEE, Liposome Shedding from a Vibrating Microbubble on Nanoseconds Timescale, 2013 IEEE International Ultrasonics Symposium (IUS), (2013) 57-60. (**IF 2013 = 1.8**)

NATIONAL & INTERNATIONAL CONFERENCES WITH ORAL PRESENTATION

April 11th – 13nd 2011	2011 International Society for Therapeutic Ultrasound Symposium (ISTU), New York City, USA *"The Use of mRNA-loaded Microbubbles for Transfection of Dendritic Cells"*
May 11th – 12th 2011	15th Forum of Pharmaceutical Sciences, Spa, Belgium *"Ultrasound contrast agents in immunotherapy: The use of mRNA-loaded microbubbles for transfection of dendritic cells."*
January 19th-20th 2012	17th European Symposium on Ultrasound Contrast Imaging, Rotterdam, The Netherlands *"From contrast to cancer immunotherapy: exploring sonoporation-induced mRNA transfection of dendritic cells"*

September 19th 2012	Seminar on Inflammation & Vaccination, Merelbeke, Belgium ***"****mRNA sonoporation as a novel tool in dendritic cell-based cancer immunotherapy"*
November 9th 2012	Biopharmacy Day, Utrecht, The Netherlands ***"****mRNA sonoporation as a novel tool in dendritic cell-based cancer immunotherapy"*
January 17th-18th 2013	18th European Symposium on Ultrasound Contrast Imaging, Rotterdam, The Netherlands *"The bubble breakthrough in cancer immunotherapy"* **This presentation won the prize in the "Therapeutic use of microbubbles" competition**
July 17th – 18th 2013	Leeds Microbubble Consortium Annual Symposium, Leeds, UK *"The bubble breakthrough in cancer immunotherapy"*
February 4th 2014	OncoPoint II, Ghent, Belgium *"The bubble breakthrough in cancer immunotherapy: The use of mRNA sonoporation in dendritic cell-based cancer vaccination"* **This presentation was awarded with one of the "best presentation" prizes**
January 22nd-23rd 2015	20th European Symposium on Ultrasound Contrast Imaging, Rotterdam, The Netherlands "*Theranostic mRNA-loaded microbubbles in the lymphatics of dogs: implications for ultrasound-guided cancer vaccination"*
February 1st – 6th 2015	Hot topics in molecular imaging – Imaging inflammation, Les Houches, France *"Theranostic mRNA-loaded microbubbles for dendritic cell based cancer vaccination"*

NATIONAL & INTERNATIONAL CONFERENCES WITH POSTER PRESENTATION

January 19th – 21st 2011	16th European Symposium on Ultrasound Contrast Imaging, Rotterdam, The Netherlands. *"The Use of Ultrasound Contrast Agents in Cancer Immunotherapy: The Use of mRNA-loaded Microbubbles for Transfection of Dendritic Cells"* (nominated abstract for the "Young Investigators Award" poster prize)
April 11th – 13nd 2011	2011 International Society for Therapeutic Ultrasound Symposium (ISTU), New York City, USA. *"The Use of mRNA-loaded Microbubbles for Transfection of Dendritic Cells"* (Nominated abstract for the 2011 ISTU Student Competition)

April 4th – 6th 2012	12th European Symposium on Controlled Drug Delivery, Egmond aan Zee, The Netherlands. *"^{19}F-MRI-traceable Particles for Antigen Loading of Dendritic Cells"*
October 25th – 29th 2012	European Society of Gene and Cell Therapy (ESGCT) and Société Française de Thérapie Cellulaire et Génique (SFTCG) collaborative congress 2012, Versailles, France ***"**mRNA sonoporation as a novel tool in dendritic cell-based cancer immunotherapy"*
December 5th-6th 2012	Immunotherapies & Cancer Vaccines Conference, Brussels, Belgium ***"**mRNA sonoporation as a novel tool in dendritic cell-based cancer immunotherapy"*
May 14th-16th 2013	Cancer Immunotherapy (CIMT), Mainz, Germany *"The bubble breakthrough in cancer immunotherapy"*
May 30th 2013	Knowledge for Growth, Ghent, Belgium "The bubble breakthrough in cancer immunotherapy" **This poster was awarded the Knowledge for Growth poster prize.**
April 16th-18th 2014	13th European Symposium on Controlled Drug Delivery, Egmond aan Zee, The Netherlands. *"The bubble breakthrough in cancer immunotherapy: mRNA-sonoporation in dendritic cell-based cancer vaccination"* **This poster was awarded the Jan Feijen Poster prize.**
May 8th 2014	Knowledge for Growth, Ghent Belgium "*The bubble breakthrough in cancer immunotherapy*"
May 19th-20th 2014	Le Tours de Microbulles, Tours, France *"The bubble breakthrough in cancer immunotherapy: mRNA-sonoporation in dendritic cell-based vaccination"*

AWARDS AND PRIZES

June 2005	Prize of Ghent University (St. Lodewijkscollege, Bruges, Belgium)
September 2010	Prize of the Bank of Breda (Ghent University, Ghent, Belgium)
January 2013	Winner of the "Therapeutic use of microbubbles" competition (18th European Symposium on Ultrasound Contrast Imaging, Rotterdam, The Netherlands)
May 2013	2013 Knowledge for Growth poster award (Ghent, Belgium)
February 2014	"Best oral presentation" award (OncoPoint II (Ghent, Belgium)
April 2014	Jan Feijen poster prize (13th European Society of Controlled Drug Delivery symposium, Egmond aan Zee, The Netherlands)

INTERNATIONAL RESEARCH EXPERIENCE

June 2011	*In vivo* experiments with Doxorubicin-loaded microbubbles at the lab of Prof. Dr. A. Klibanov at University of Virginia (UVa, Charlottesville, VA, USA)

TEACHING ACTIVITIES

2010-2013	Tutor and lab instructor for the Pharmaceutical Bachelor Proof (FaBaP).
2011-2014	Supervisor of: Rein Verbeke, Master dissertation (Pharmaceutical Sciences – Drug Development, UGent). 19-F MRI traceable perfluorocarbon particles for antigen loading of dendritic cells. (2011-2012) Delphine Goethals, Bachelor dissertation (Medical Laboratory Techniques, KAHO Sint-Lieven). Aanmaak en evaluatie van therapeutische perfluorocarbon partikels voor siRNA therapie en kankervaccinatie. (2012-2013) Johan Van Ongeval, 1st Master dissertation (Biochemistry and Biotechnology, UGent). Analyse van transfectie-efficiëntie na niet-viraal gemedieerde gentransfer (microbubbles-sonoporatie) bij muis-dendritische cellen. (2013-2014) Philippe Giron, Master Dissertation (Biomedical Sciences, VUB). The use of cationic mRNA lipoplexes for transfection of immature dendritic cells. The road to efficient tumor antigen loading and maturation dendritic cells. (2013-2014)
2013-2015	Selected lectures on “mRNA vaccination” within the Biopharmacy Courses of Prof.dr.apr. Stefaan De Smedt.

SPECIALIST COURSES

May 5th – 6th 2011	Molecular Biology and Cytometry Course, Mol, Belgium
June 2011	Animal Research Orientation seminar and Rodent Biomethodology Workshop, University of Virginia (UVa), Charlottesville, Virginia
2011-2012	Laboratory Animal Science I & II (by Prof. Katleen Hermans) at Ghent University
September 3rd – 5th 2012	Applied Flow Cytometry Course (Joint organization by UGent, UA and VUB)

Dankwoord

Acknowledgements

"In this world, there are things you can only do alone,
and things you can only do with somebody else.
It's important to combine the two in just the right amount."

Haruki Murakami, After Dark

Als ik één iets met 100% zekerheid kan zeggen op het einde van deze 4 jaar, is het wel dat een doctoraat één van de dingen is die enkel maar in dichte samenwerking met andere mensen tot stand kunnen komen. En ik heb geluk gehad: de lijst met "te bedanken mensen" is lang.

Stefaan, als student was ik al onder de indruk van je begeesterde manier van lesgeven, waarbij je ons meetrok in je enthousiasme en continue verbazing over hoe alles ineen zit, en je ons leerde om alles in vraag te stellen en steeds kritisch na te denken. Net diezelfde manier van werken maakt je zo'n goeie promotor. Na elke Mondaymeeting (die overigens maar zelden echt op een maandag plaatsvond) had ik weer stof om over na te denken, soms wetenschappelijk, soms eerder filosofisch. Ik herinner me nog een moment in mijn eerste jaar, toen ik bubbels aan het maken was in het lab. Je kwam bij me staan, nam mijn vialtje bubbels over, hield dat tegen het licht en zei: "*Als je er eens bij stil staat hoe lang het duurt om zo'n kleine microbubbel te karakteriseren, probeer je dan maar eens voor te stellen hoe lang het zou duren om de hele wereld te karakteriseren*". En inderdaad... Het mysterie van de bubbels is nog niet helemaal opgehelderd, en toegegeven, ook de wereld snap ik nog niet helemaal, maar ik ben er wel mee bezig…

Karine, in je rol als hoofdondervrager op mijn IWT-verdediging was onze eerste ontmoeting er eentje van stress en angstzweet. Enkele maanden later kruisten onze wegen nog eens: na weken vruchteloos wachten op een recombinante T cel lijn waren we bij jullie gaan aankloppen. We kregen niet alleen de cellen, maar meteen ook een berg advies, en de

mogelijkheid om een *in vivo* assay bij jullie te komen doen. Al snel werd dat ene assay een hele reeks experimenten en zaten we tijdens incubatietijden te koffiekletsen, of gingen we na een lange dag in het lab iets eten (en drinken, uiteraard) in de Bibitor. In alle labs die ik intussen heb gezien, zie je maar zelden een prof nog *hands-on dirty labwork* doen, maar jij slaagde er altijd in tijd vrij te maken om samen miltjes te pletten, muizen te injecteren en FACS analyses te doen. Ik ben je enorm dankbaar voor alles wat je me hebt geleerd, je onuitputtelijke enthousiasme en wetenschappelijke kennis, de snelle en vrolijke e-mails met antwoorden op al mijn vragen, alle weekendwerk om tumoren te gaan opmeten, alle leuke momenten en gezellige babbels aan de VUB en op congres, en alle kansen die ik dankzij jou heb gekregen. Ik ben dan ook niet minder dan vereerd dat je bereid was om naast Stefaan ook mijn promotor te worden. Bedankt!

Ine, je was al mijn mentor tijdens mijn thesis en je passie voor bubbels is extreem besmettelijk. Je gaf me toen al de vrijheid om mijn project zelf in handen te nemen en al snel was er geen ontsnappen aan de *bubblebug* (de goeie variant, gelukkig). Je creativiteit in het bedenken van projecten en experimenten, en het vinden van niet-alledaagse oplossingen voor al even weinig alledaagse problemen is indrukwekkend. Je was er altijd om me advies te geven, knopen door te hakken, me op te peppen als dat nodig was, nieuwe contacten te leggen, of om leuke momenten te beleven op congres: celebrities spotten op Broadway, stoffenwinkels plunderen (tot grote ergernis van Bart en Roel die ongeduldig buiten stonden te wachten), gedeelde hotelkamers met een glazen badkamerdeur (blij dat je braaf aan de veilige kant van de kamer bleef)… Die ene keer bij je presentatie in Egmond aan Zee toen je hoogzwanger was van Janne en Stefaan al ongerust op zijn stoel aan het schuiven was in 't geval je hulp nodig zou hebben, sloeg iemand de nagel op de kop toen ze je een "*heroic woman*" noemde, want dat ben je, geen twijfel mogelijk. Ook op persoonlijk vlak zorgde die creatieve geest voor vonken. Onze gemeenschappelijke interesses in naaien, patronen tekenen, laser cutten en 3D-printen zorgden dat je al snel veel meer werd dan "*zomaar*" co-promotor. Bedankt voor de raad, de motivatie, de rondvliegende muizenpootjes, je eeuwige enthousiasme, de verhuishulp, de gezellige patroontekenavonden (in de les en nadien op café of bij jou thuis) en de inspiratie. Ik kan niet anders zeggen dan dat ik met mijn gat in de boter ben gevallen met een begeleider/co-promotor/mentor/vriendin als jij. Merci!

Ook de andere professoren in het lab in Gent, **Jo**, **Kevin** en **Katrien** zou ik graag bedanken voor de steun en raad, voor de wetenschappelijke input en voor het creëren van een lab waar ik zo veel ondersteuning en kansen heb gekregen.

Voor zij die het nog niet zouden weten: Labo Biochemie rules! Er zijn niet alleen de creatieve lunchpauzes (op een dag komen daar patenten uit voort, mark my words), cel lab meezingmomenten of helpende handen links en rechts, maar ook de (foute) lab party's en bijhorende verkleedsessies, lab weekendjes, uitstapjes, after-work feestjes en Fun on Friday die zorgden dat deze periode in het lab onvergetelijk is.

In elk lab zit één iemand op wie iedereen kan rekenen, die – soms zelfs in het bezit is van een Fiat multipla, maar dan moet je al érg veel geluk hebben – een draaiende kracht is binnen een lab en die voor al je kleine of grote, praktische of onnozele problemen altijd wel een oplossing vindt. **Bart**, je was altijd al een redder in nood, in het lab en daarbuiten. Bedankt voor de multi-multipla-verhuis samen met Ine, de pootjesleveringen, de vaste *3 Lousbergs en een portie kaas* op maandagavond, de vers-van-de-kip eitjes, de tips, goeie raad en vooral om je eeuwige en geduldige bereidheid om mij en alle andere mensen in het lab altijd met de glimlach te helpen.

Ook jullie, **Katharine** en **Ilse**, zijn mee verantwoordelijk voor het logistiek en administratief smooth sailing tijdens mijn doctoraat. Bedankt voor alle hulp, het scheppen van orde in de chaos en voor de gezellige babbels over reizen en andere leuke dingen.

Werken in een bureau waar je elke dag opgevrolijkt wordt door 3 fantastische vrouwen met wie je alles – soms zelfs té veel – kan delen, ervaringen kan uitwisselen (over wetenschap en andere dingen), kan discussiëren maar vooral veel stoom kan aflaten en onnozel mee kan doen, maakte van dit doctoraat een fantastische ervaring. **Lynn**, jij zat al in de bureau toen die nog bevolkt werd door dinosaurussen uit een ver vervlogen tijd. Je had altijd wel wat "spetterende" verhalen of gekke trucjes klaar, bent verantwoordelijk voor het introduceren van een aantal niet mis te verstane gebaren, was mijn melige partner in crime ("*Zeg dat je niet hoeft te gaan schat. Nee, nee nee!"*) en doet er altijd nog nét dat schepje bovenop. Op onze eerste werkuitstap samen kochten we uit pure miserie in Dessel (want noch daar, noch in Mol was een open frietkot te vinden) een slaatje en een zak chips in de Delhaize als avondeten. Gelukkig was er "*thuis*" om de zeden te verzachten… **Laura**, bedankt voor de etentjes na een lange dag experimenteren in het lab, voor de Moulin Rouge zangstonde in de straten van Versailles, de überdeskundige hulp met de T cellen, je vrolijkheid, je fantastische verkleed-outfits en collectie pruiken, en het aanzetten tot office-planking. **Joke**, de nieuwe en volledig door Ine DC democratisch verkozen vice-CPO, je bent een enorme aanwinst voor het lab én voor de bureau. Sfeer gegarandeerd! **Sangram**, I wish you all the best in your work and life. It must be a little tough to be the only man in an office filled with women, but hang on in there!

Ine, samen met "*grote Ine*" staan we intussen op het jaarlijkse ultrasoundcongres in Rotterdam gekend als "*The girls from Ghent*", en je bent een fantastische bubbelcollega! Jammer dat ik nog niet de eer gehad heb om door jou "*kaasgunstig*" verklaard te worden, maar wat niet is, kan natuurlijk nog komen…

Rein(tje), dankzij jouw sappig accent merkt niemand nog dat ik stiekem ook uit Brugge afkomstig ben. Je was al een crème van een thesisstudent, maar nu ook nog een fantastische collega, bierconnaisseur en opschenker van 70-jarige ex-playboybunny's met blauw haar. Kunnen samenwerken met iemand als jij is pure luxe.

Karen, Sosuke, je enthousiasme is grenzeloos, of het nu over octopi, whaaaalllles, hemelkijkers, koeienogen of autofagie gaat. Je dansmoves zijn té groovy voor woorden, je bent keistrak in je gouden morphsuit, je bent – dat geef ik grif toe – mijn meerdere in CTR en met jou en de Patron nieuwe bands spotten op pukkelpop is gewoon de max. Voor eens en voor altijd en *speciaal voor jou*: *Totoro Sosuke suki!!!*

Freya, je bent een superonesie, de ideale persoon om mee in een doos te kruipen of om samen een GSM mee te zoeken in de struiken, een dansmirakel en de indrukwekkendste Mega Mindy die ik ken!

Stephan, de experimenten die ik samen met jou gedaan hebben waren ongetwijfeld bij de plezantste die ik al gedaan heb (flow cytometrie was nog nooit zo plezant). Het feit dat je voor mij onlosmakelijk verbonden bent met een combinatie van kriek, wc-papier en de bijhorende dansmoves (met inbegrip van je overtuigende Harlem Shake interpretatie), kan daar natuurlijk ook wel voor iets tussen zitten.

Koen, met jou als Chief Party Officer is er nogal wat afgefeest binnen het lab. Afhankelijk van de situatie was je Zorro, schuurtalent Geordie, een topatleet, grote broer of zomaar een marginaal met nekmat en en/of movembermoustache.

Thomas en **Katrien**, jullie worden gemist… En hard… Bedankt voor de fotosessies en fotoshops (sommige staan voor eeuwig in mijn geheugen gegrift), het delen van gênante mascaramomenten, het niet zomaar opgeven toen we niet in de laserkaraoke binnen mochten, en alle hulp en tips over "how to defend your PhD", ik had me geen betere adviseurs kunnen wensen. Het moet gezegd: *You are The Hague*.

Koen, **Lotte**, **Eline**, **Elisa**, **Oliwia**, **Hua**, **George**, **Rita**, **Bart G**, **Broes**, **Dries**, bedankt voor: de schuine mopjes, de droge mopjes, de naturelle radioreclamestem, baking chips in the oven like a cake, je kletterende lach, being our very own biochemistry lab version of Psy, elucidating the liposome-mysteries, being a splendid & fun office-buddy, de korte en lange-

afstandshulp bij het bubbelen, het blijven organiseren van de traditionele burger & movie avonden, en de immer toevallige ontmoetingen op de gekste plaatsen.

I've been lucky to have a great number of collaborators in other universities in Belgium and beyond who've helped me with experiments, gave me the opportunity to expand my view and to get acquainted with new assays and techniques, or who've brightened up the evenings at conferences (Leeds, Rotterdam…). Prof.dr. **Uwe Himmelreich**, Prof.dr. **Sasha Klibanov**, Prof.dr. **Katrien Vanderperren**, **Roos**, **Sandra**, **Cleo**, **Emmelie**, **Hendrik**, **Sunil**, **Tim**, **Tom**, **Guillaume**, **Ying**, **Verya**, **Ilya**, and many, many more… Thanks!!

Zonder de steun van vrienden en familie, was dit boekje er wellicht nooit gekomen. Ik kon altijd op jullie rekenen, jullie waren altijd te vinden voor goeie raad, hulp, een gezellige avond na een lange dag, het maken van een fantastische illustratie bij dit boekje, of overheerlijk comfort food. **Mama** en **papa**, ik kan jullie niet genoeg bedanken voor alle kansen die ik van jullie gekregen heb. Jullie interesse en trots was altijd een enorme motivatie tijdens mijn studies en gedurende de afgelopen vier jaar. Jullie gaven me de mooiste cadeaus die ik ooit had kunnen krijgen: een warm, creatief, avontuurlijk nest, aangeboren nieuwsgierigheid, een passie voor reizen en een gezonde dosis relativeringsvermogen. Bedankt voor alles.

"*Luck is what happens to you when fate gets tired of waiting*". En er is een goeie dosis geluk nodig geweest om jou eerst op de trein en daarna op de reismarkt in Brugge tegen het lijf te lopen. **Bart**, ik wist meteen al dat ik met jou mijn avonturier gevonden had, en ik had gelijk. Elke dag weer verras je me, vul je me perfect aan, breng je het beste in mij naar boven en maak je van mij het gelukkigste kieken ter wereld. Bedankt om de platen op te leggen waarvan je weet dat ik er gelukkig van word, bedankt om met me te dansen in de keuken en te zingen op de fiets, bedankt voor de fantastische reis in Myanmar, het vrolijk *mingulaba*'en en de *liefde in tijden van Dengue*, bedankt om me mijn chaos te gunnen en me tegelijk ook een beetje structuur te geven, bedankt om altijd jezelf te zijn, maar bovenal: bedankt om samen met mij nieuwe plannen te maken en te dromen. Ik zie je graag, Bart, en ik kijk al uit naar onze volgende avonturen samen…

-Heleen-